工學博士學位論文

Fabrication of Graphene/Conducting Polymer Nanohybrid Materials and Their Sensor Applications

그래핀/전도성 고분자 나노하이브리드 물질의 제조 및 센서로의 응용

2016 年 2 月

서울大學校 大學院

化學生物工學部

朴 秦 煜

Fabrication of Graphene/Conducting Polymer Nanohybrid Materials and Their Sensor Applications

그래핀/전도성 고분자 나노하이브리드 물질의 제조 및 센서로의 응용

指導敎授: 張 正 植

이 論文을 工學博士 學位論文으로 提出함

2015 年 11 月

서울大學校 大學院

化學生物工學部

朴 秦 煜

朴 秦 煜의 工學博士 學位論文을 認准함

2015 年 11 月

委 員 長 _____ (인)

副委員長 _____ (인)

委 員 _____ (인)

委 員 _____ (인)

委 員 _____ (인)

Fabrication of Graphene/Conducting Polymer Nanohybrid Materials and Their Sensor Applications

by

Jin Wook Park

Submitted to the Graduate School of Seoul National University

in Partial Fulfillment of the Requirements

for the Degree of Doctor of Philosophy

February, 2016

Thesis Adviser: Jyongsik Jang

ABSTRACT

Graphene/conducting polymer (CP) nanohybrid materials have attracted considerable attention, due to their synergetic effects, including enhanced surface area, charge carrier mobility, thermal/electrical conductivity, and chemical/mechanical stability. To synthesize the graphene/CP nanohybrid materials for using in electronic device applications, covalent and non-covalent synthetic methods have been introduced. Contrary to non-covalent method, covalent functionalization requires time-consuming and harsh conditions, because it needs firstly to introduce functional group on the surface of graphene and CPs. On the other hand, non-covalent functionalization offers facile way to obtain graphene/CP nanohbyrid materials through secondary bonding interactions, such as π–π interactions. In-situ synthetic method, as one of the non-covalent synthetic method, is very promising and powerful tool to design graphene/CP nanohybrids owing to getting uniform nanohbyrid materials. Furthermore, the morphology and shape of the graphene/CP nanohybrids can be controlled by selectively designing the morphology of starting materials (graphene or CP materials).

In this study, various graphene/CP nanohbyrid materials are introduced by using in-situ synthetic method. The synthesized nanohybrid materials exhibit excellent electrical/chemical properties, enabling to be applied in sensor applications. Synergetic effects of graphene/CP nanohbyrid mateirals provide rapid response/recovery time, when using as a transducer in the sensing device. Furthermore, the enlarged surface area from graphene/CP nanohybrids can provide the improved interactions with target analytes, leading to the ultrasensitive sensing performance.

KEYWORDS: Graphene; conducting polymers (CP); nanohybrid materials; Field-effect transistor (FET); sensor applications

STUDENT NUMBER: 2013–30778

List of Abbreviations

CP : conducting polymer

PPy : polypyrrole

PANI : polyaniline

PT : polythiophene

PEDOT : poly(3,4-ethylenedioxylthiophene)

PF : polyfuran

PSe : polyselenophene

PPV : poly(para-phenylene vinylene)

RT : room temperature

NCP : nanoscaled conducting polymer

CNTs : carbon nanotubes

QDs : quantum dots

NPs : nanoparticles

NCs : nanocrystals

NFs : nanofibers

NRs : nanorods

NTs : nanotubes

1D : one-dimensional

SWCNT : single-walled carbon nanotbue

FET : filed-effect transistor

OLED : organic light emitting diode

PSS : poly(sodium 4-styrenesulfonate)

TPAPAM : triphenylamine-based poly-azomethine

PB^- : 1-pyrenebutyrate

EDLC : electric double layer capacitor

GO : graphene oxide

RGO : reduced graphene oxide

CPPy : carboxylated polypyrrole

DMT-MM : 4-(4,6-Dimethoxy-1,3,5-triazin-2-yl)-4-methyl-morpholinium chloride

EDOT : 3,4-ethylenedioxythiophene

PVDF : polyvinylfluoride

IDA : interdigitated array

S/N : signal-to-noise

GF : gauge factor

MO : methyl orange

PBS : phosphate-buffered solution

XRD : X-ray diffraction

FE-SEM : field emission-scanning electron microscope

TEM : transmission electron microscope

HRTEM: high resolution transmission electron microscope

ATR-FTIR : Attenuated total reflection-fourier transform infrared spectroscopy

AFM : Atomic Force Microscope

XPS : X−ray photoelectron spectra

TGA : Thermogravimetric analysis

CVD : chemical vapor deposition

GCE : glassy carbon electrode

List of Figures

Figure 1. Typical conducting polymer structures (undoped form).

Figure 2. Electronic band model of PPy: Neutral, Polaron, and Bipolaron state.

Figure 3. Structures of various important carbon nanomaterials: fullerene (C_{60}), single-walled carbon nanotube (SWCNT), multi-walled carbon nanotube (MWCNT), carbon nanohorn, graphene, few layer graphene and graphene oxide.

Figure 4. Photo image of rGO and graphene with PB^- materails.

Figure 5. Illustration of the process for preparation of rGO–PANI composites.

Figure 6. (a) Photograph of the all solid-state supercapacitor. (The inset is a schematic image of the solid-state supercapacitor.) (b) CV curves at 200mV s^{-1} with various bending angles and (c) galvanostatic charge−discharge curves at a current density of 4 A g^{-1} before (black) and after 100 bending cycles (red).

Figure 7. (A) Output voltage generation (human finger (B) touch and release response) from the ECE made with PVDF, 0.1Fe-RGO/PVDF,

0.5Fe-RGO/PVDF and 2.0Fe-RGO/PVDF nanocomposite films, and (C) schematic diagram for measuring the human finger response signal (voltage) for the Fe-RGO/PVDF film. Photograph of (D) the Fe-RGO/PVDF nanocomposite film and (E) a demonstration of the flexibility.

Figure 8. Illustration of IDA chemical sensing device.

Figure 9. Illustration of liquid-ion gated FET sensing device.

Figure 10. (a) Schematic of the assembly and operation of a flexible sensor layer sandwiched between thin PDMS supports (~500 μm thickness each). (b) Photograph showing the flexibility of the assembled sensor. Scale bar, 1 cm. (c) SEM image of a dense array of 50-nm radius nanohairs with AR = 10. Scale bar, 1 μm. (d) Schematic illustrations of the pressure, shear and torsion loads and their possible geometric distortions of the paired hairs. (e) Operation of a flexible sensor layer by means of recording of resistance change (Roff : unloading, Ron: loading).

Figure 11. A schematic illustration of the synthesis of rGO/PPy NT hybrids.

Figure 12. (a) SEM image shows PPy NTs. The inset shows a TEM image. Cross-sectional SEM images show (b) rGO and (c) rGO/PPy NTs. The inset indicates the magnification level. (d) A TEM image shows rGO/PPy NTs.

Figure 13. Raman spectra of GO, rGO, PPy, NT, and rGO/PPy NT composites.

Figure 14. ATR-FTIR spectra of (a) GO, rGO, PPy, NT, and rGO/PPy NT hybrids. A magnified view of the marked area in (a) is shown in (b).

Figure 15. X-ray diffractions of GO, rGO, PPy NT, and rGO/PPy NT hybrids.

Figure 16. (a) Current−voltage (I−V) curves of GO, rGO, PPy NTs, and rGO/PPy NTs composites and (b) rGO/PPy NTs composites at V_g from –2.0 to 0.4 V in 0.2-V steps (V_{sd}: 0 to 1.0 V in 0.2-V steps).

Figure 17. (a) Schematic diagram shows a liquid-ion-gated FET-type sensor. (Ag/AgCl reference electrode, R; platinum counter electrode, C; source and drain electrodes, S and D) (b) Real-time responses and (c) a calibration curve for H_2O_2 based on rGO, PPy NTs, and rGO/PPy NTs composites were measured at V_{sd} = 10 mV (V_g = 0.1

V) with H_2O_2 concentrations of 0.1 nM to 100 nM. Storage stability biosensor performance is shown in (d). Real-time responses to PBS, UA, AA, glucose, and H_2O_2 are shown in (e). (f) A histogram details the sensing performance to UA, AA, glucose, and H_2O_2.

Figure 18. Real-time responses for H_2O_2 based on rGO/PPy NTs composites were measrured at V_{sd} = 10 mV (V_g = 0.1 V) with H_2O_2 concentration of 10 pM to 100 pM.

Figure 19. Schematic illustration of the fabrication of rGO/C-PPy NT hybrid glucose sensing device.

Figure 20. (a) SEM image of the C-PPy NTs. The inset shows a TEM image. (b) Cross-sectional SEM images of the rGO layers and (c) the rGO/C-PPy NTs. (d) TEM image of rGO/C-PPy NTs.

Figure 21. ATR-FT-IR spectra of rGO, C-PPy NT, and rGO/C-PPy NT hybrids.

Figure 22. ATR-FT-IR spectra of PPy NT and C-PPy NT.

Figure 23. (a) X-ray diffraction patterns and (b) Raman spectra of GO, rGO, C-PPy NT, and rGO/C-PPy NTs.

Figure 24. Current−voltage ($I-V$) curves of C-PPy NTs, rGO, and rGO/C-PPy NT hybrids.

Figure 25. (a) A schematic diagram showing the liquid-ion-gated FET-type sensor, with a Ag/AgCl reference electrode, labeled R, platinum counter electrode, labeled C, and source and drain electrodes, labeled S and D. (b) The source–drain current of the biosensors as a function of V_{SD} at various values of V_G in the range from –1.0 to +1.0 V. (c) The real-time responses and (d) a calibration curve for glucose biosensor with and without the GOx enzyme, which were measured at V_{SD} = 10 mV and V_G = – 0.1 V, with glucose concentrations of 1 nM to 100 mM. (e) The real-time response to PBS, AA, UA, and glucose solutions.

Figure 26. Real-time responses to exposure to H_2O_2 based on rGO/C-PPy NTs with GOD aptamer measured at V_{SD} = 10 mV and V_G = – 0.1 V, with H_2O_2 concentrations in the range 1–100 mM.

Figure 27. The real-time responses towards glucose of the rGO/C-PPy NTs measured at V_{SD} = 10 mV and V_G = – 0.1 V, with glucose

concentrations of 100 pM and 1 nM.

Figure 28. The real-time response of the rGO/C-PPy NTs hybrid FET-based biosensor (a) after 50 repetitions, and (b) after one month. Both datasets were measured with at V_{SD} = 10 mV and V_G = – 0.1 V, and with a glucose concentration of 1 nM.

Figure 29. The schematic illustration of the synthesis of rGO-PF NT hybrids.

Figure 30. (a) SEM image of PF NTs; the inset is a TEM image. Cross-sectional SEM images of (b) rGO layers and (c) rGO-PF NTs. (d) TEM image of rGO/PF NTs.

Figure 31. (a) Raman, (b) X-ray diffraction patterns, and (c) ATR-FT-IR spectra of GO, rGO, PF, and rGO+PF NT hybrids.

Figure 32. (a) Current−voltage (I−V) curves of PF NTs, rGO, and rGO-PF NT hybrids and (b) rGO-PF NT composites at V_g from –1.0 to +0.6 V in 0.2-V steps (Vsd: 0 to 1.0 V in 0.2-V steps).

Figure 33. PF NTs at V_g from −1.0 to 0.4 V in 0.2-V steps (Vsd: 0 to 1.0 V in 0.2-V steps).

Figure 34. (a) A liquid-ion-gated FET-type sensor based on rGO-PF NTs.

(Ag/AgCl reference electrode, R; platinum counter electrode, C; source and drain electrodes, S and D) (b) Real-time responses and (c) a calibration curve for Hg^{2+} based on rGO, PF NTs; rGO-PF NT composites were measured at Vsd = 10 mV (V_g = – 0.1 V) with Hg^{2+} concentrations of 10 pM to 100 nM. (d) A histogram of the sensitivity of the rGO-PF NT composites to Hg^{2+}, Zn^{2+}, Ce^{2+}, Na^{+}, Ni^{2+}, Pb^{2+}, Cu^{2+}, Co^{2+}, Li^{+}.

Figure 35. Real-time responses for Hg^{2+} sensor based on rGO-PF NT composites measured at V_{sd} = 10 mV (V_g = - 0.1 V) with a Hg^{2+} concentration of 1 pM to 10 pM.

Figure 36. Real-time responses to Zn^{2+}, Ce^{2+}, Na^{+}, Ni^{2+}, Pb^{2+}, Cu^{2+}, Co^{2+}, Li^{+}, and Hg^{2+} measured at V_{SD}= 10 mV (V_g = - 0.1 V).

Figure 37. (a) Schematic illustration of the preparation of graphene–PSe nanocomposites FE-SEM images of (b) rGO and (c) rGO/PSe nanocomposites. (Insets are the TEM images of rGO and rGO/PSe nanohybrid materials.) (d) Typical STEM image of graphene–PSe nanohybrids. Corresponding elemental mapping images of (e) C

and (f) Se.

Figure 38. (a) Raman spectroscopy, (b) XRD patterns, and (c) ATR-FTIR spectra of GO, rGO, PSe, and rGO/PSe nanohybrids.

Figure 39. (a) Overall, (b) C 1s, and (c) Se 3d XPS profiles of rGO/PSe nanohybrids.

Figure 40. TGA curves of rGO, PSe, and rGO-PSe nanohybrid materials.

Figure 41. N_2 adsorption/desorption isotherms of PSe, rGO, and rGO/PSe nanohybrids.

Figure 42. Current−voltage ($I-V$) curves of PSe, RGO, and RGO-PSe nanohybrid materials.

Figure 43. (a) schematic illustration of RGO/PSe nanohybrid chemiresistive electrode. Optical microscopic images of fabricated electrode (b) before and (c) after RGO/PSe nanohybrid material coataing process.

Figure 44. (a) Real-time responses of PSe and RGO/PSe nanohybrid materials upon sequential exposure to NH_3 (0.01 to 10 ppm) and MeOH (1 to 100 ppm). (b) Real-time responses of PSe and RGO/PSe nanohybrid materials on periodic exposure to 10 ppm of

NH_3 and 100 ppm of MeOH. (c) Normalized resistance changes of PSe and RGO/PSe nanohybrids with periodic exposure to 10 ppm of NH_3 and 100 ppm of MeOH gases for 100 cycles. (d) Calibration curve of PSe and RGO/PSe nanohybrids as a function of NH_3 and MeOH concentration.

Figure 45. Sensing performance histrogram of RGO/PSe nanohybrid mateirals to 11 analytes: each analyte concentration was fixed at around 10 ppm.

Figure 46. Schematic diagram showing the fabrication process of E-skin based on graphene/V-PEDOT/P(VDF-HFP) nanohybrid device.

Figure 47. (a) AFM and (b) HR-TEM images of the single-layer graphene. (c) UV-Vis spectra of the graphene transferred onto the PDMS film. The inset shows a photograph of the flexible and transparent graphene film.

Figure 48. SEM image of the (a) graphene, (b) the vertically grown PEDOT (via VDP) nanofibers on the graphene, and (c) the fabricated P(VDF-HFP)/PEDOT/graphene films.

Figure 49. SEM images of V-PEDOT according to VDP reaction time (a) 0, (b) 15, (c) 30 min, and (d) 1h.

Figure 50. Raman spectra of graphene, P(VDF-HFP), PEDOT, and graphene/PEDOT/P(VDF-HFP) nanohybrid materials.

Figure 51. (a) Schematic diagram of the E-skin device. (b) Sensitivities to pressure with various stimuli. (c) Real-time change in resistance of the electronic skin devices as a function of the graphene, graphene/P(VDF-HFP), graphene/V-PEDOT/P(VDF-HFP), V-PEDOT, and V-PEDOT/P(VDF-HFP) material.

Figure 52. Resistance as a function of strain for graphene, graphene/V-PEDOT, graphene/P(VDF-HFP), and graphene/V-PEDOT/P(VDF-HFP) nanohybrid film.

Figure 53. Current–voltage (*I-V*) curves of graphene, graphene/PEDOT, and graphene/PEDOT/P(VDF-HFP) nanohybrids.

Figure 54. Real-time change in the resistance of the E-skin over more than 1000 loading cycles, with a cycle length of 2 s and an applied pressure of 30 Pa. The inset shows a magnified image in the red

rectangular region.

Figure 55. (a) Resistance as a function of time during motion of the hand from an outstretched to a clenched-fist position. (b) Resistance as a function of time while measuring the pulse in the wrist.

List of Tables

Table 1. Comparison of the performance of various H_2O_2 sensors.

Table 2. Determination of glucose concentration in real samples using the biosensors.

Table 3. Comparison of the mercury sensing performance of various sensor type devices.

Table 4. Comparison between the detection limit performances of our flexible strain sensor and those of strain sensors based on other materials.

Table 5. Comparison of the sheet resistance values based on graphene, graphene/V-PEDOT, and graphene/V-PEDOT/P(VDF-HFP) nanohybrids..

Table of Contents

Abstract ..... **i**

List of Abbreviations ..... **iii**

List of Figures ..... **vi**

List of Tables ..... **xvii**

Table of Contents ..... **xviii**

1. INTRODUCTION **1**

1.1. Background **1**

1.1.1. Conducting polymers 1

1.1.1.1. Polypyrrole (PPy) 3

1.1.1.2. Poly(3,4,- ethylenedioxythiophene) (PEDOT) 6

1.1.1.3. Polyfuran (PF) 7

1.1.1.4. Polyselenophene (PSe) 8

1.1.1.5. CP nanomaterials 9

1.1.1.5.1 1D CP nanomaterials 11

1.1.1.5.1.1 Self-degradation method 12

1.1.2. Graphene 13

1.1.3. Graphene/conducting polymer nanohybrid mateirals 16

1.1.3.1. Non-covalent graphene-CP nanohybrids 18

1.1.3.2. Covalent graphene-CP nanohybrids 26

1.1.4. Sensor application 28
1.1.4.1. Chemical sensor 30
1.1.4.1.1. Hazardous and toxic gases sensor 31
1.1.4.2. Liquid-ion gated FET-type biosensor 33
1.1.4.2.1. H_2O_2 FET-type biosensor 35
1.1.4.2.2. Glucose FET-type biosensor 37
1.1.4.2.3. Hg^{2+} FET-type biosensor 38
1.1.4.3. Piezotronic sensor 39

1.2. Objectives and Outlines 42
1.2.1. Objectives 42
1.2.2. Outlines 43

2. EXPERIMENTAL DETAILS 45

2.1. RGO/PPy NT hybrid materials 45
2.1.1. Fabrication of polypyrrole nanotube embedded reduced graphene oxide transducer for field-effect transistor-type H_2O_2 biosensor 45
2.1.1.1. Prepartation of PPy NTs 45
2.1.1.2. Prepratation of RGO/PPy NT hybrids 46
2.1.1.3. Fabrication of RGO/PPy NT composite FET sensor 47
2.1.1.4. Characterization of RGO/PPy NT hybrids 48

2.2. RGO/C–PPy NT hybrid materials 49
2.2.1. Fabrication of carboxylated polypyrrole nanotube wrapped graphene sheet transducer for field-effect

transistor-type glucose biosensor 49
2.2.1.1. Preparation of C–PPy NTs 49
2.2.1.2. Preparation of RGO/C–PPy NT hybrids 50
2.2.1.3. Fabrication of RGO/C–PPy NT composites FET sensor 51
2.2.1.4. Characterization of RGO/C–PPy NT hybrids 52

2.3. RGO/PF NT hybrid materials 53
2.3.1. Fabrication of reduced graphene oxide-polyfuran nanohybrid for High-performance Hg^{2+} FET-type sensors 53
2.3.1.1. Prepration of PF NTs 53
2.3.1.2. Prepration of RGO/PF NT hybrids 54
2.3.1.3. Fabrication of RGO/PF NT composite FET sensor 55
2.3.1.4. Characterization of RGO/PF NT hybrids 56

2.4. RGO/PSe nanohybrid materials 57
2.4.1. Fabrication of graphene/polyselenophene nanohybrid materials for highly sensitive and selective chemiresistive sensor 57
2.4.1.1. Preparation of RGO/PSe nanohybrid materials 57
2.4.1.2. Characterization of RGO/PSe nano hybrid materials 58

2.5. CVD graphene/PEDOT/P(VDF-HFP) nanohbyrid mateirals 59
2.5.1. Prepatation of CVD graphene/free-standing PEDOT nanofiber/P(VDF-HFP) nanohbyrid materials 59
2.5.1.1. Prepatation of CVD graphene/free-standing PEDOT

nanofiber/P(VDF-HFP) nanohbyrid materials 59
2.5.1.2. Characterization of CVD graphene/PEDOT/P(VDF-HFP) nanohybrid materials 61

3. RESULTS AND DISCUSSION 62

3.1. Fabrication of polypyrrole nanotube embedded reduced graphene oxide transducer for field-effect transistor-type H_2O_2 biosensor. 62

3.1.1. Fabrication of RGO/PPy NT hybrid materials 62
3.1.2. Electrical performance of RGO/PPy NT hybrid materials 70
3.1.3. FET-type H_2O_2 biosensor based on RGO/PPy NT hybrid materials 73

3.2. Fabrication of carboxylated polypyrrole nanotube wrapped graphene sheet transducer for field-effect transistor-type glucose biosensor 80

3.2.1. Fabrication of RGO/C–PPy NT hybrid materials 80
3.2.2. Electrical performance of RGO/C–PPy NT hybrid materials 88
3.2.3. FET-type glucose biosensor based on RGO/C–PPy NT hybrid material 91

3.3. Fabrication of reduced graphene oxide-polyfuran nanohybrid for High-performance Hg^{2+} FET-type sensors 100

3.3.1. Fabrication of RGO/PF NT hybrid materials 100

3.3.2. Electrical performance of RGO/PF NT hybrid materials 106
3.3.3. FET-type Hg^{2+} biosensor based on RGO/PF NT hybrid materials 110

3.4. Fabrication of graphene/polyselenophene nanohybrid materials for highly sensitive and selective chemiresistive sensor 117
3.4.1. Fabrication of RGO/PSe nanohybrid materials 117
3.4.2. Fabrication of chemiresistive sensor based on RGO/PSe nanohybrid materials 127
3.4.3. Chemiresistive sensing performance of the RGO/PSe nanohybrid film 130

3.5. Fabrication of graphene/free-standing nanofibrillar PEDOT/P(VDF-HFP) hybrid device for wearable and sensitive human motion detective piezo-resistive sensor 135
3.5.1. Fabrication of CVD graphene/free-standing nanofibrillar PEDOT/P(VDF-HFP) nanohbyrid devices 135
3.5.2. Sensing performance of E-skin device 143
3.5.3. Practical application of E-skin device 147

4. CONCLUSIONS 156

REFERENCES 162

국문초록 180

1. INTRODUCTION

1.1. Background

1.1.1. Conducting polymers

During several decades, π-conjugated conducting polymers (CPs) have actively investigated due to their unique and outstanding properties.[1−6] Since the discovery of polyacetylene in 1977, various kinds of CPs have been continuously studied, such as polypyrrole (PPy), polyaniline (PANI), polythiophene (PT), poly(3,4-ethylenedioxylthiophene) (PEDOT), polyfuran (PF), polyselenophene (PSe), and poly(para-phenylene vinylene) (PPV). CPs have polyconjugated system, consisting of alternating single (σ bond) and doulble (π bond) bonds, and these π-conjugated cahins regard as determining the mechanical and optoelectrical properties of conducting polymers. In general, the conjugated length, the intra-/inter-chain interaction, and the extent of disorder are the crucial parameters for the physical properties of CPs.

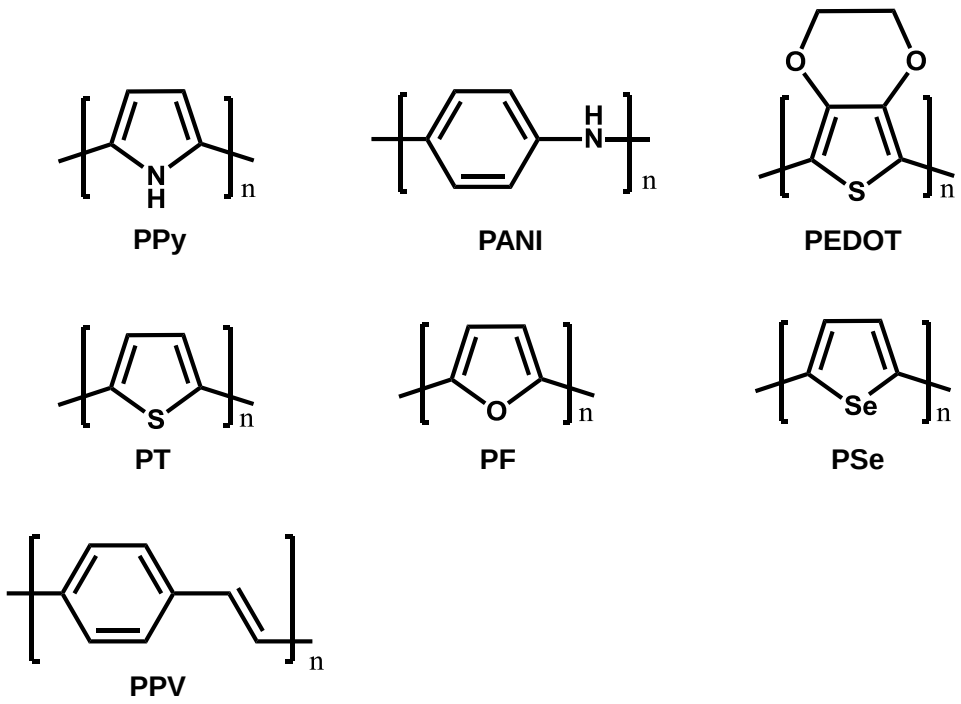

Figure 1. Typical conducting polymer structures (undoped form).

1.1.1.1. Polypyrrole (PPy)

Among of the CPs, polypyrrole (PPy), which was firstly synthesized in 1912, is the one of the most frequently used in practical applications, owing to excellent conductivity, biocompatibility, and good long-tem stability.[7–10] The structure and ability of charge transport of CPs are the key factors to determin the electrical conductivity. Charge transport relies on the charge carrier, which carries electric charges in electrical conductors. Charge carriers ared dividied two types: i) electron and ii) hole transport. This is determined by the spin number of the charge carriers. However, the charge carrier in PPy is spinless and has a positive sign, indicating that PPy does not have unpaired electron. To describe the electornic phenomena in PPy, new existence of the charge carrier finally indentified, called biploaron. The oxidation level of the PPy chains resolves the concentration of charge carrier in PPy. In neutral phase, the PPy has benzoniod-like structure, as shown in Figure 2. PPy, in neutral state, acts as an insulator because the bandgap is too wide for electrons in valence band to jump to conduction band at room temperature (RT) without any irritation. When oxidation reaction occurs in PPy structure, one electorn is removed from a neutral segment of PPy chain. To stabilize the state, electronic and structure rearrangement happen on the polymer backbone, resulting in formation of polaron. Two localized

electronic levels in the band gap was caused by the presence of the polaron on the chain. When another electron is extracted from the same segment of PPy chain, bipolaron (doubly charged state) was formed. A bipolaron, which is a pair of delocalized positive charges, extens over about four pyrrole rings (conjugation length). This conjugtation length depends on oxidation state, which means that the energy obtained by the distortion into bipolaron state is larger than the Coulomb repulsion between the two positive charges. However, the lower energy of bipolaron state is empty, indicating that the species has a spin of zero. A bipolaron enable to jump along the PPy chain through the reaarangemnt of double and single bonds in the PPy backbone structure. Thus, the PPy, in oxidized state, can transfer charge.

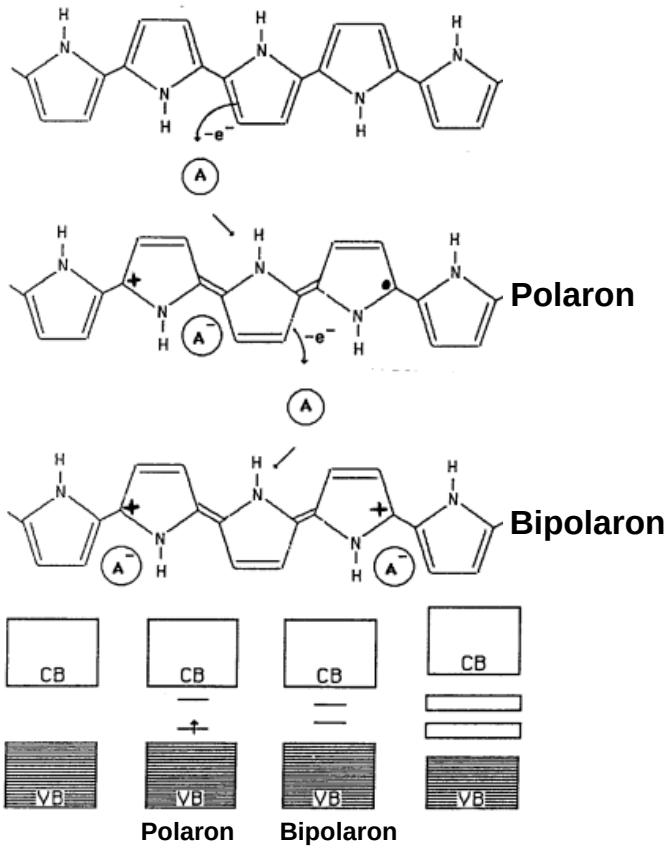

Figure 2. Electronic band model of PPy: Neutral, Polaron, and Bipolaron state. Reprinted with permission from reference [8].

1.1.1.2. Poly(3,4-ethylenedioxythiophene) (PEDOT)

PEDOT had been developed by the Bayer AG research laboratories in Germany for the 1980s.[11–13] The PEDOT has been considered as one of the most promising candidates for the paractical optoelectirnoc applications, due to its superior conductivity, electro-chemical properties, and air stability.[14–15] tandard oxidative or electrochemical polymerization methods were used for the synthesis of the PEDOT. Altohough it is insoluble polymer in the aqueous and organic solution, it showed unique characteristics, including high conductivity (*ca*. 300 S cm^{-1}), transparency in oxidized thin film, and remarkable stability in an oxidized state. To solve the solubility problem, a water-soluble polyelectrolyte, such as PSS, was used as the charge balancing dopant during polymerization.[16–18] The hybridization of PEDOT and PSS material exhibited a water-soluble CP, which formed good uniform film: conductivity (*ca.* 10 S cm^{-1}), high visible light transmittance, and good stability. The novel electrical properties of versatile functionalized PEDOT nanostructures have been reported.

1.1.1.3. Polyfuran (PF)

Nanoscale conducting polymers (NCPs) have many advantages, such as ease of fabrication, good biocompatibility, and high conductivity.[19–22] Among these materials, few examples of polyfuran (PF) have been reported. PF exhibited interesting properties compared with other CPs, especially PT and PPy, such as higher rigidity, better solubility, better packing, and higher fluorescence.[23–25] In addition, the computational studies suggest that PFs show a greater quinoid character and lower ionization energies than the corresponding PT, owing to the higher energy of their HOMO. These results are in agreement with experimental observations with respect to their extensive conjugation and good charge delocalization along the PF backbone. In spite of these outstanding properties, no study related to the control of PF nanoscale morphology and its functional group exists, owing to the limited availability of PF synthetic method and the poor solubility.

1.1.1.4. Polyselenophene (PSe)

Polythiophenes (PTs) are the most studied conducting polymers.[26–30] However, altohou the lots of papers published on PT and its derivates, few reports are known about its close analogue, PSe and its derivates. The outstanding properties of PTs propose that PSe can be a significant member of the CP family.[31–33] The possible advantages of PSe are anticipated, due to the unique properties of the Se atom and selenophene: (i) intermolecular Se-Se interactions, leading to a wide bandwith in organic conductors, enable to enforce inter-chain charge transfer. (ii) Selenophene monomer shows lower oxidation and reduction potentials than thiophene, resulting in lower oxidation and reduction potentials of PSe. (iii) The Se atom is more facily polarized than sulfur, which means that PSe can become more easily polarized than PTs. (iv) PSe can accommodate greater charge on doping than PS owing to the larger size of the Se atom compared with the S atom of PT. (v) PSe has a lower band gap than PT and, consequently, the absorption wavelgnth exhibits different trandency those of PT, leading to different optoelectronic performance compared those of PT. Nerverthless, PSe has attracted surprisingly sparse attention.

1.1.1.5. CP nanomaterials

A growing interst in nanostructured materials in the range of 1 to 100 nm has been shown because of their unique characteristics of nanomaterials, including electrical, mechanical, optical, and chemical performances.[34–37] The quantum-confinement effect occurred due to their discrete or quantized electronic levels on the nanomaterials. Over the last decades, various nanomaterials (carbon nanotubes (CNTs), quantum dots (QDs), catalysts/magnetic nanoparticles (NPs), and inorganic semiconductor nanocrystals (NCs)), have been actively investigated and published.[38–42] Yet, the preparation of CP nanomaterials has been unexploited relatively. In comparison with their large-scale counterparts, CP nanomaterials exhibit higher surface areans and smaller dimension, leading to superior chemical and physical properties.[43–45] These merits of CP nanomaterials have intrigued to chemists and physicist for decades. Interstingly, the electrical properties of CP nanomaterials, such as oxidation level, conjugation length, and doping level, depend highly on their shapes, including nanofibers (NFs), nanorods (NRs), nanotubes (NTs), or NPs. General methods, including soft and hard template, and template-free methods, have been used to synthesize and fabricate the shape of CP nanomaterials. Despite various shapes of CPs synthesized by using the template-assisted methods, several problems occurred to use as electrod

materials in energy and environmental applications: (i) There are lack of technologies to remove either hard or soft templates completely from the reaction medium. (ii) The electrical properties of CP could be reduced due to the remmant templates. (iii) In case of the template-free system, doping agents, the amounts of monomers, and oxidizing agents used may highly affect the formation of nanostructured CPs. The facts, which were the effects of the oxidizing agent/monomer ratior on the conductivity of CPs, were reported. However, optimizing synthetic condition for specifically controlled CP nanomaterials is still required. Thus, the novel synthetic method, for the high-quality CP nanomateirals with high conductivity and desirable morphologies, should be developed to use in practical applications.

1.1.1.5.1. 1D CP nanomaterials

One-dimensional (1D) nanomaterials, which show high charge carrier mobility along the long-axis, can be used for highly sensitive sensors.[46–48] Among various 1D nanomaterials, the remarkable physical and chemical characteristics of 1D CPs at the nanometer scale offer exceptional sensing performance in biosensor applications. These 1D CP nanomaterials boast several advantages, including facile functionalization and biocompatibility.[49–50] However, there has rarely been inverstigated to use these materials in the sensing appliactions.

1.1.1.5.1.1. Self-degradation method

The self-degrdation method for fabrication of CP NT has been reported in 2005 by Yang. et. al.[51] This method is facile, simple, and environmental friendly because synthetic method is under the aqueous solution condition. To fabricate the CP NTs by using self-degrdation method, firstly, the iron (Ⅲ) chloride and methyl orange (MO) were mixded in the aqueous solution and form temporary nano-template. After inject the CP monomer, the polymerization took place on the surface of the nano-template. Then, the nano-template was removed via exceed aqueous solution with vigorous stirring condition. Most of soft or hard template mathods required strong acid condition to remove the template, such as HF or HCl. In addition, the fabricated CP NTs have uniform size (approximately 70 nm) and large-scaled production (yield ~ 76 %).

1.1.2. Graphene

Graphene is a two-dimensional hexagonal honeycomb lattice of sp2-hybridized carbon with one-atom thick planar sheet.[52–53] Graphene has shown the possibility of using a next generation elcetronic material owing to its exceptional properties, such as high current density, thermal conductivity, ballistic transport, chemical inertness, optical transmittance and super hydrophobicity at nanometer scale, as shown in Figure 3.[54–56] Although graphene was only isolated for the first time in 2004, it has been extremely investigated during the last several years. The 2010 Nobel Prize in Physics was given to Andre Geim and Konstantin Novoselov due to the groundbreaking work on graphene. After that time, the rapid and fast uptake of interest in graphene is observed because of primarily to lots of outstanding properties that it has been found to possess. Intrinsic graphene has semie-metal or zero gap semiconductor properties, and offers a startlingly low absorption ratio of 2.3% of whift light, with an exceptionally high opacity for an atomic monolayer. Excellent high electron mobility at RT was reported throught the experimentally reported values in excess of 15,000 $cm^2 V^{-1} s^{-1}$.

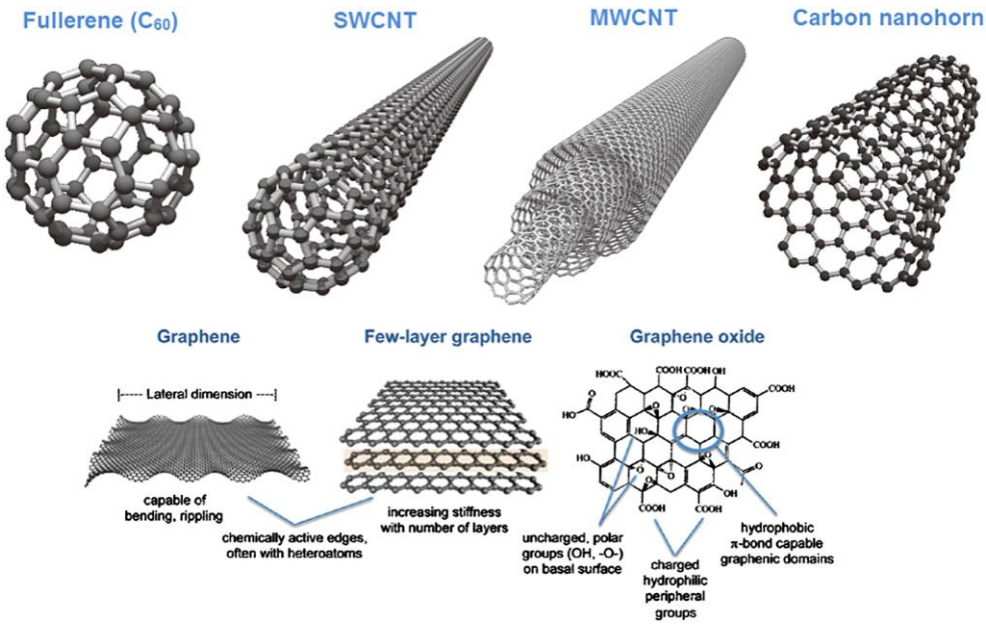

Figure 3. Structures of various important carbon nanomaterials: fullerene (C_{60}), single-walled carbon nanotube (SWCNT), multi-walled carbon nanotube (MWCNT), carbon nanohorn, graphene, few layer graphene and graphene oxide. Reprinted with permission from reference [52].

The graphene resistivity was reported 10^{-6} ohm–cm in the experimental value, which means that it was less than that of silver and the lowest resistivity substance known at RT.

Abnomal electrical performance of graphene have been deviced to use future electronics, including field emitter, ballistic transistors, components of integrated circuits, transparent conducting electrodes and sensors.[57–60] Graphene has not only a high electron or hole mobility, but also low Johnson noise. Electornic noise occurred by the thermal agitation of the charge carriers inside an electrical conductor at equilibrium, which generates regardless of any applied voltage. These characteristics allow to be used as the transducer in a field-effect transistor (FET). Graphene shows a superior sensor due to combination of outstanding electrical property and low noise. The 2D structure of graphene could efficiently detect adsorbed moleucles. Furthermore, the excellent electrical conductivity and optical transparency introduce the graphene to use the practical applications, including transparent conducting electrodes, touch-screens, liquid crystal displays, organic photovoltaic cells and organic light-emitting diodes (OLEDs).

1.1.3. Graphene/conducting polymer nanohybrid mateirals

To optimize the properties and performances of nanocomposites for using in the practical applications, a variety of graphene-based polymer nanohybrid materials have been developed, such as graphene–poly(methyl methacrylate) (PMMA) composites with improved flame-retardant property, graphene–epoxy composites with improved thermal conductivity, graphene–polypropylene composites with enhanced flexural properties and lower percolation threshold, graphene–polystyrene composites with increased viscosity and enhanced mechanical properties, graphene–poly(vinyl alcohol) composite with enhanced mechanical strength, graphene–thermoplastic polyurethane composite with increased optical/electric properties, graphene–nyloncompositeswithincreasedelectrical conductivity, graphene–poly(sodium 4-styrenesulfonate) (PSS) with improved dispersibility, and graphene–polyaniline (PANI) composites with increased capacitance.[61–65]

The advantages of graphene-CP nanohybrid materials offer platforms for versatile electronic device applications.[66–68] The graphene–CP nano-composites are simply divided into two categories: non-covalent and covalent nanocomposites. Water-soluble and organosoluble CPs, including PANI, PPy, PT and P3HT, were used to non-covalently modify graphene via secondary bonding interactions, such as π-π interaction or hydrogen interactions. On the

other hand, functional groups treated CPs ((e.g.–NH_2, –MeOH, etc.), including triphenylamine-based poly-azomethine (TPAPAM), P3HT and fluorene-, thiophene-, benzothiadiazole-based copolymers, were covalently attatched to surface of graphene to form nanohybrid materials.

1.1.3.1. Non-covalent graphene-CP nanohybrids

Micro- and nano-electronic devices based on the graphene-based nanohybrid materials request the preservation of the intrinsic electrical properties of graphene in the devices as well as demands the easy integration and homogeneous distribution of the graphene-based materials in various matrices. In this regard, the non-covalent functionalization of graphene with CPs, which is a non-destructive method occurring between the basal plane of graphene and CPs and modifies the graphene without significantly altering its chemical structure, is preferred as a facile way to obtain dispersive graphene–CP nano-composites for device applications.[69–70]

To prepare graphene nanohybrid materials, non-covalent interaction is frequently applied. Non-covalent interactions between organic molecules and graphene enable to easily attatch the organic species on graphene surfaces. Small molecules, including surfactants and polymers, can interact with graphene surfaces via secondary bonding interactions, such as π–π stacking, or electrostatic or hydrophobic interactions, supplying useful way to modify graphene surfaces for fabricating graphene nanocomposites.[71–72] Small molecules, including 1-pyrenebutyrate (PB^-), 3,4,9,10-peryl-enetetracarboxylic diimide bisbenzenesulfonic acid, sodium dodecylbenzene sulfonate, 1-pyrenecarboxylic acid, and dendronized perylene bisimides, can be

conveniently used to modify graphene. Highly water-soluble graphene was obtained by utilizing PB^- due to strong π-stacking intecations between graphene surfaces and pyrene moiety in the molecule, as shown in Figure 4.

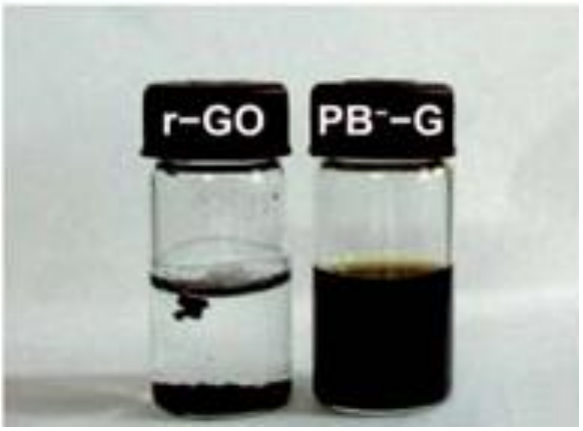

Figure 4. Photo image of rGO and graphene with PB^- materails. Reprinted with permission from reference [72].

Recently, graphene-CP nanohybrid mateirals have been actively investigated due to the synergitic effects, including enhanced conductivity, charge transport behavior, surface area, mechanical property, and chemical stability.[66–68] These mateirals could be utilized in various field appliactions, such as sensors and energy storage devices, as shown in Figure 5, 6, and 7.[66–70] In case of energy storage devices, graphene with CPs nanocomposites show fast electron/ion transport in electrodes, and electrochemical stability, which lead to improved supercapacitance or lithium-ion battery performances. Furthermore, the CPs exhibit psudocapacitor behavior in the supercapacitor system, which is oxidation or reduction operation on the CPs. On the other hand, carbon materials, including graphene and CNTs, show electric double layer capacitor (EDLC) behavior upon using in the supercpacitors. Thus, the graphene-CP nanohybrid materials display the combination EDLC and pesudocapacitor behaviors, leading to improved the supercapacitor performance. In another case, the strain sensor, the hexagonal honeycomb structure may be partially destroyed near the edges of the film under tensile stress, resulting in altering its electronic band structure and lead to a significant change in resistance, termed the piezo-resistive effect. Nowadays, reduced graphene oxide (RGO)/polyvinylfluoride (PVDF) nanohybrid materials show large Young's moduli and are optically transparent and mechanically flexible, leading to large

GF value.[73] Graphene-CP nanohybrid materials, in the biosensor appliaction, have exceptional charcateristics such as enhanced surface area and conductivity. Especially, increased surface area brings the high performance sensing behavior due to improved reactive binding sites between the anlyate and graphene-CP nanocomposites in biosensor applications.[74–79]

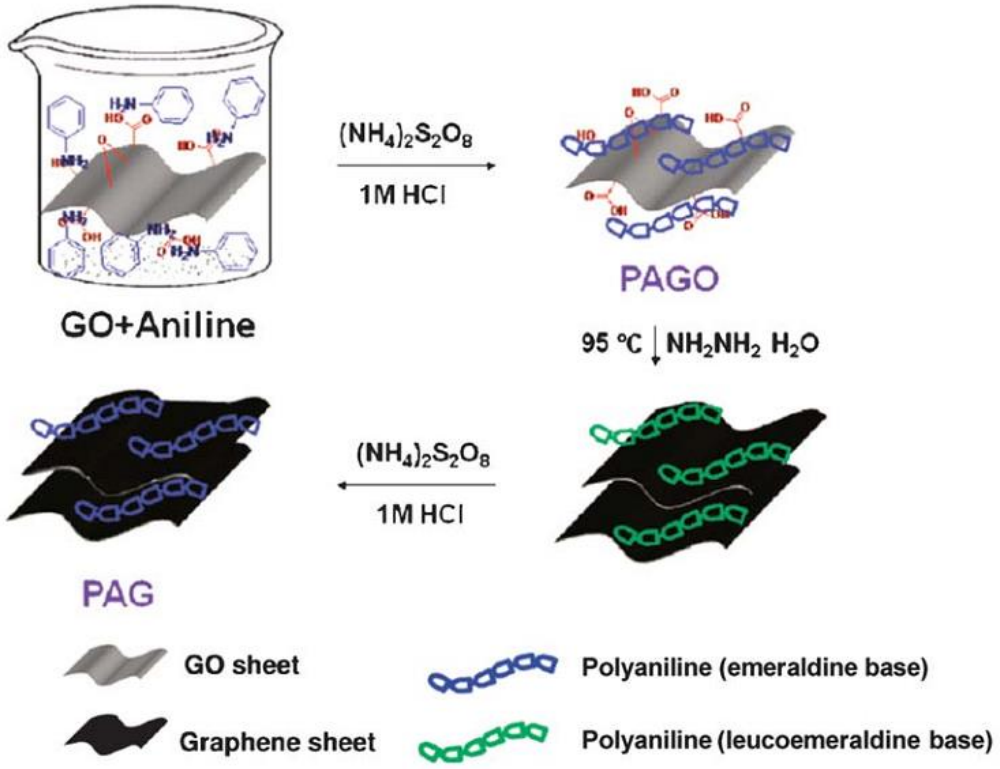

Figure 5. Illustration of the process for preparation of rGO–PANI composites. Reprinted with permission from reference [68].

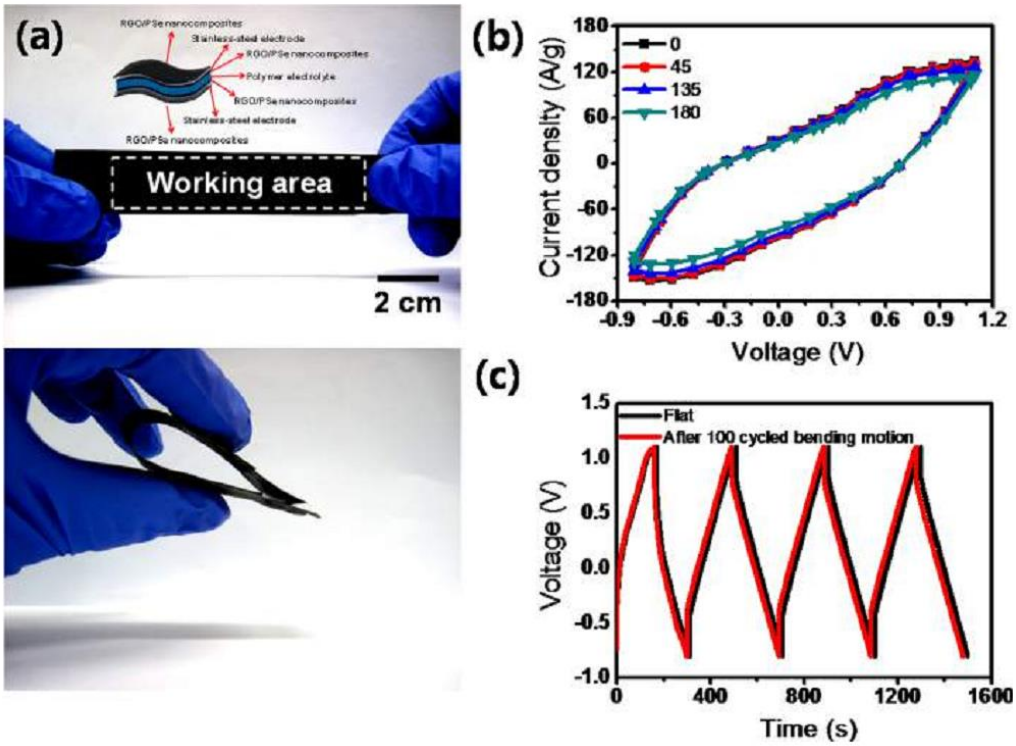

Figure 6. (a) Photograph of the all solid-state supercapacitor. (The inset is a schematic image of the solid-state supercapacitor.) (b) CV curves at 200mV s^{-1} with various bending angles and (c) galvanostatic charge−discharge curves at a current density of 4 A g^{-1} before (black) and after 100 bending cycles (red). Reprinted with permission from reference [81].

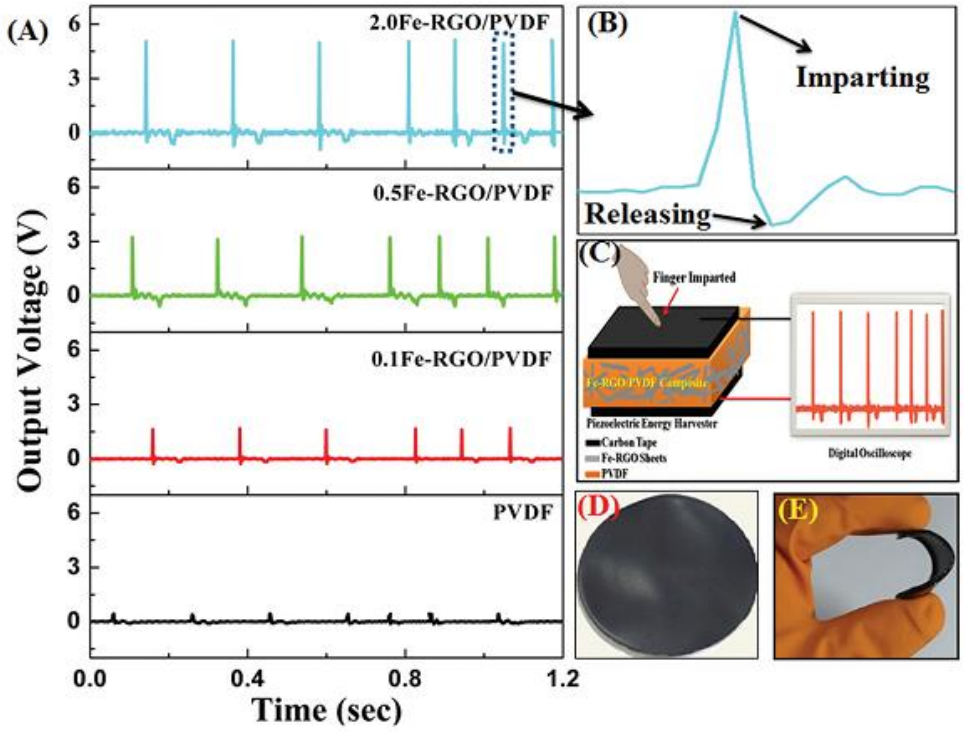

Figure 7. (A) Output voltage generation (human finger (B) touch and release response) from the ECE made with PVDF, 0.1Fe-RGO/PVDF, 0.5Fe-RGO/PVDF and 2.0Fe-RGO/PVDF nanocomposite films, and (C) schematic diagram for measuring the human finger response signal (voltage) for the Fe-RGO/PVDF film. Photograph of (D) the Fe-RGO/PVDF nanocomposite film and (E) a demonstration of the flexibility. Reprinted with permission from reference [82].

1.1.3.2. Covalent graphene-CP nanohybrids

Contrary to the non-covalent functionalization, covalent functionalization is another approach for the preparation of graphene–CP nanocomposites. In this method, CPs were covalently bindined to graphene via chemical reactions between the functional groups of CPs and those of GO or rGO. GO, which has lots of reactive oxygenated groups on its basal plane or edge, is the promising candidate for covalent grafting. For example, GO was covalently bindied onto TPAPAM containing the terminal $-NH_2$ group through the surface-bonded acyl chloride moieties (GO–COCl) for the rewritable memory device application.[83] This device exhibited nonvolatile rewritable memory effect and a typical bistable electrical switching, with an ON/OFF current ratio of over 10^3 at a turn-on voltage of ca. −1 V. Both the ON and OFF states were stable under a constant voltage stress, and survived up to 10^8 read cycles at a read voltage of −1.0 V. In another case, poly[{9,9-di(triphenylamine)fluorene}(9,9-dihexylfluorene)(4-aminophenylcarbazole)]) (PFCz) with NH_2-terminated side chains, was synthesized and also binded onto GO through the reaction with GO–COCl producing a soluble GO–PFCz nanohybrid material, as shown in Figure 8b.[84] The ON state of the GO–PFCz, in the memory device, is able even to withstand a constant voltage stress of −1 V for 3h. Except the memory device appliactions, GO–CP nanocomposites

were used in the photovoltaic devices. The GO sheets were covalently anchored with the MeOH-terminated P3HT chains through the esterification of carboxylic groups in GO.[85] The photovoltaic device based on the fabricated GO–P3HT nanohybrid material exhibited a 200% enhancement in the power conversion efficiency (0.61%) with respect to its P3HT/C60 counterpart under AM 1.5 illumination (100 mW cm^{-2}). In addition to GO, the surface of rGO can also be modified by CPs to form useful electronic materials. For instance, uorene-, thiophene-, and benzothiadazole-based copolymers were covalently anchored to the surface of rGO sheet and used in the optical-limiting device application.

1.1.4. Sensor application

To detect some characteristic environmental elements, sensor, a transducer device, is developed and composed of an active sensing material with a signal transducer. There are the roles of two important components in sensor system: (i) sensor transmits signal without any amplification from a selective compound, and (ii) from a change in a reaction. The sensor devices offer the thermal, electrical or optical output signals, which were able to be converted to digital signals for subsequent processing. Several types of sensor devices with source of target analyte were existed, including chemical-, bio-, and mechanical-sensor (e.q., pressure and strain sensor). The chemical sensor enables to offer information about the chemical component with a liquid or gas phase in the environment. The measureable physical signal, which ire related with the concentration of a certain analyte, is provided as the information. On the other hand, the biosensor detects biological component analytes, including protein, cells, and nucleic acid or biomimetic polymers. The mechanical sensor is a device that operates and respond to pressure or strain like forces. Recently, the electronic-skin (E-skin) device is operated based on the mechanical sensing mechanism.

Several critical elements for highly eefcetive sensor devices are required: (i) high sensitivity; ii) high selectivity to target analyte; iii) fast

response/recovery time; iv) cycle stability; and v) low working temperature. To satisfy these demands, sensor electrode based on the nanomaterial has been emerged as promising candidates due to its small size, including high surface to volume ratio and unique optical/electrical properties.

1.1.4.1. Chemical sensor

In the realm of chemical sensing device, resistive chemical sensors (i.e., chemiresistive sensor), which respond chemical information by means of two point contact electrical resistance changes, are the one of the most studied promising transduction mechanisms for conductive nanomaterials based systems.[86–91] This system is largely used in the practical field, owing to the fact that detecting the change of electrical resistance is one of the simplest methods to analyze requiring minimal supporting electronics for compact, deployable, self-contained systems. Among of the various chemiresistive sensing systems, interdigitated array (IDA) based chemiresistive sensors have several advantages to utilize the chemical sensing device. (See Figure 8) First, it shows high sensitivity and rapid response time than other sensing systems, due to fast siganal transfers from transducer materials to the electrode. Another merit is the simple and facile interpreted measurement with real-time monitoring chaing resistance of the signals during target analyte detection. Furthermore, the cycle stability is the one of the other strengths without any defect and destruction during repeated target chemical sensing.

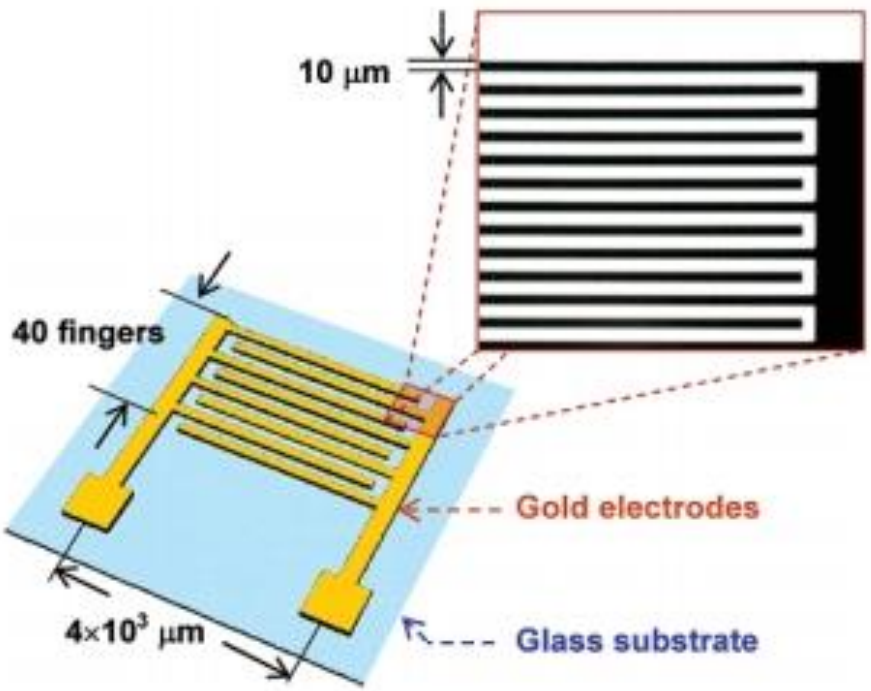

Figure 8. Illustration of IDA chemical sensing device. Reprinted with permission from reference [88].

1.1.4.1.1. Hazardous and toxic gases sensor

Environmentally harzardous and toxic gases, including hydrogen sulfide (H_2S), carbon monoxide (CO), and ammonia (NH_3), and volatile organic compounds (VOCs), such as acetone (CH_3COCH_3), ethanol (C_2H_5OH), and ethane (C_2H_6), have been detected in the exhaled breath of healthy subjects and patients with respiratory diseases.[92–95] In particular, NH_3 is a widely utilized gas with a colorless and unique pungent odor. In spite of its usefulness, when its concentration surpasses the 25 ppm, it is danger and hazardous to humans. Thus, effective and efficient methods with inexpensive systems are required to detect of hazardous gases like NH_3 for preventing adverse effects.

1.1.4.2. Liquid-ion gated FET-type biosensor

Biosensor, consistin of a biological sensing element including antibody, cell, receptor, and aptamers, detects bio-target analyte through binding with transducer (e.x., conductive nanomaterials).[96–102] To detect a target analyte, selectively molecular recognition occurs at the analyte-biological element anchored to transducers from a nonelectrical domain to an electrical signal. Then, a change in the electrical property at the sensing transducer is detected via the binding of the analyte.

FETs have attracted interest as primary candidates for fabricating state-of-the-art sensor platforms due to their ability to achieve high current amplification while maintaining a relatively high signal-to-noise (S/N) ratio.[103–105] Compared with other conventional films, CP nanomaterials have remarkable physical and chemical characteristics derived from anisotropic electronic properties, high surface area, and small dimensions, as shown in Figure 9.

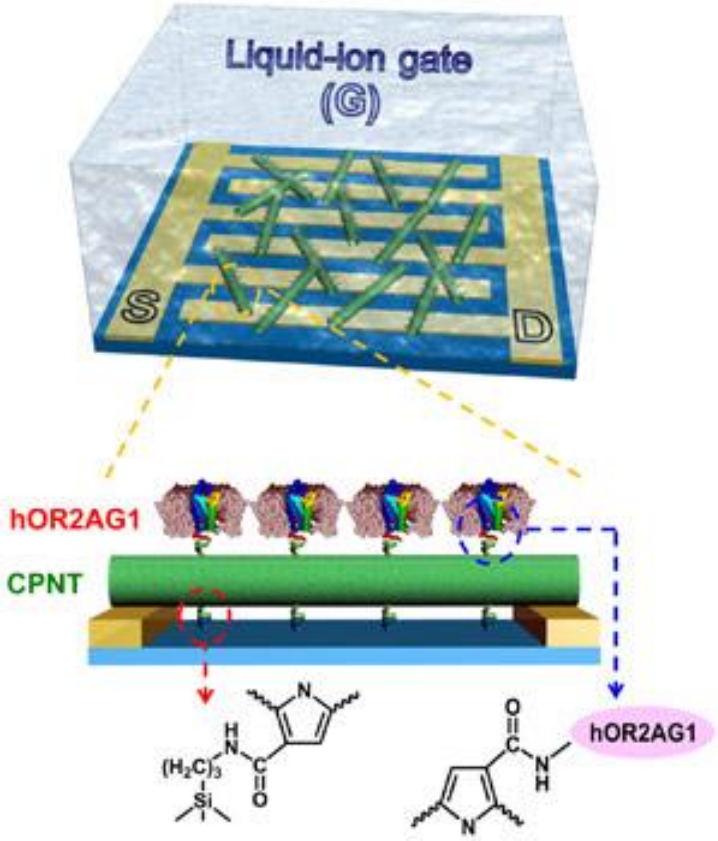

Figure 9. Illustration of liquid-ion gated FET sensing device. Reprinted with permission from reference [104].

1.1.4.2.1. H_2O_2 FET-type biosensor

Detecting hydrogen peroxide (H_2O_2) is an important challenge for applications including food science, healthcare, pharmaceutical science, and environmental monitoring.[107–110] H_2O_2, called reactive oxygen species, has been linked to several bodily disorders, including atherosclerosis, cancer, and Alzheimer's disease.[111–113] In contrast, H_2O_2 is also a component in the physiological signaling pathways of healthy cells and is essential for cell growth, immune system function, migration, and differentiation.[114–118] Thus, an accurate and sensitive means of detecting H_2O_2 is crucial for clinical diagnostics and patient monitoring. Several methods of detecting H_2O_2 have been proposed, such as various colorimetric, electrochemical, spectroscopic, and fluorescence-based methods.[119–122] Among these, electrochemical sensing of H_2O_2 has been most actively investigated due to its high sensitivity and specificity. Most electrochemical sensors, composed of enzymes or proteins, bind to H_2O_2. However, natural enzymes often suffer from limited stability, inefficiency, and sensitivity to environmental factors. Recently, metal nanomaterials, such as Ag, Au, Pt, and Pd NPs, have been studied as alternative electrochemical catalysts to construct non-enzymatic H_2O_2 sensors.[123–127] However, growing concerns with regard to rare resources, including noble metals, give rise to the development of low-cost, high-performance detection

systems for H_2O_2 in practical applications.

1.1.4.2.2. Glucose FET-type biosensor

Diabetes mellitus is considered to be one of the most serious diseases affecting human health in developed countries, with complications including increased risk of heart disease, kidney failure, and blindness.[128] The disease is caused when the body fails to regulate glucose levels. Therefore, accurate and sensitive glucose detection is important in the treatment and management of diabetes. Several detection methods have been proposed for glucose sensing, based on techniques including electrochemical, optical, and Raman spectroscopy.[129–132] Electrochemical sensing is particularly interesting due to the potential to create compact low-cost devices. However, such sensor devices require complicated electrode fabrication, surface modification, and/or synthesis of modifiers, including complexing agents. Thus, for using in practical application, the exploration and development of a simple, yet high performance glucose detection technology is extremely desirable.

1.1.4.2.3. Hg^{2+} FET-type biosensor

Mercury (Hg) has been used for decades as a chemical additive and energy source in industrial applications.[133] However, very low concentrations of Hg can be extremely toxic, both to human health and to the environment.[134–136] Hg has been linked to several fatal diseases, such as Minamata disease, pulmonary edema, cyanosis, and nephrotic syndrome.[137–140] Thus, an accurate and sensitive Hg detection method is important to the health care and environmental fields. Several methods have been developed for Hg sensing, including photoelectrochemical methods, colorimetric analysis, and oligonucleotide-based sensing.[141–146] These methods, however, have significant drawbacks, including slow response, high cost, complicated equipment requirements, and lack of high sensitivity and selectivity.[119–122] Recently, rapid and reliable Hg sensing performance has been reported for surface-functionalized electrochemical sensors.[147–149] However, these electrochemical sensors require complicated electrode fabrication, modification, and/or the synthesis of modifiers, such as complexing agents. Thus, the development of simple, high-performance Hg detection systems is desired.

1.1.4.3. Piezotronic sensor

Monitoring of physiological signals is an effective approach to the assessment of human health problems. This monitoring is currently limited to hospitals, as currently available devices, including infrared-based optical electronics and rigid multi-electrode pressure sensors, are not portable or wearable. Recently, flexible and stretchable artificial electronic skin (E-skin) has intensively studied due to its unique capability to detect subtle pressure changes, which may allow applications in wearable individual-centered health monitoring, sensitive tactile information acquisition, minimally invasive surgery, and prosthetics.[150–154] (See Figure 10) Over the last few years, flexible pressure/strain sensor devices based on nanostructured materials, such as SWNTs,[155] Si nanowires,[156] and vertical ZnO nanowire arrays,[157] have shown promising pressure-sensing performance in low-pressure regimes (<10 kPa).[123–126] In contrast to opaque, rigid metal/metal oxide nanowires, CPs have been demonstrated to be excellent candidates for flexible and wearable electronics, owing to their good biocompatibility, high conductivity and transparency, and physical robustness.[158–160] Despite their high pressure-sensing performance, such sensors are often mechanically unstable and have relatively small strain gauge factor (GF), which limits their ability to sense signals with small strain, such as pulse in the wrist. Free-standing

technology based on nanostructured CP is one approach to achieving mechanically stable and large GF sensor owing to enhancing contacting area and electrical performance, but significant challenges remain in vertical growth of nanostructured CPs with uniform morphology.

Graphene is a two-dimensional hexagonal honeycomb lattice of sp^2-hybridized carbon.[52–53] With tensile stress, the hexagonal honeycomb structure may be partially destroyed near the edges of the film, which can alter its electronic band structure and lead to a significant change in resistance, termed the piezo-resistive effect.[161–164] Recently, reduced graphene oxide (RGO)/PVDF nanocomposite materials, which have large Young's moduli and are optically transparent and mechanically flexible, have been found to have large GF value.[73] However, the aforementioned fabrication method requires multiple steps, time-consuming synthesis, and tightly restricted vacuum conditions, limiting its practical applicability. Thus, strain-sensing materials with a large GF that can be easily fabricated are desirable.

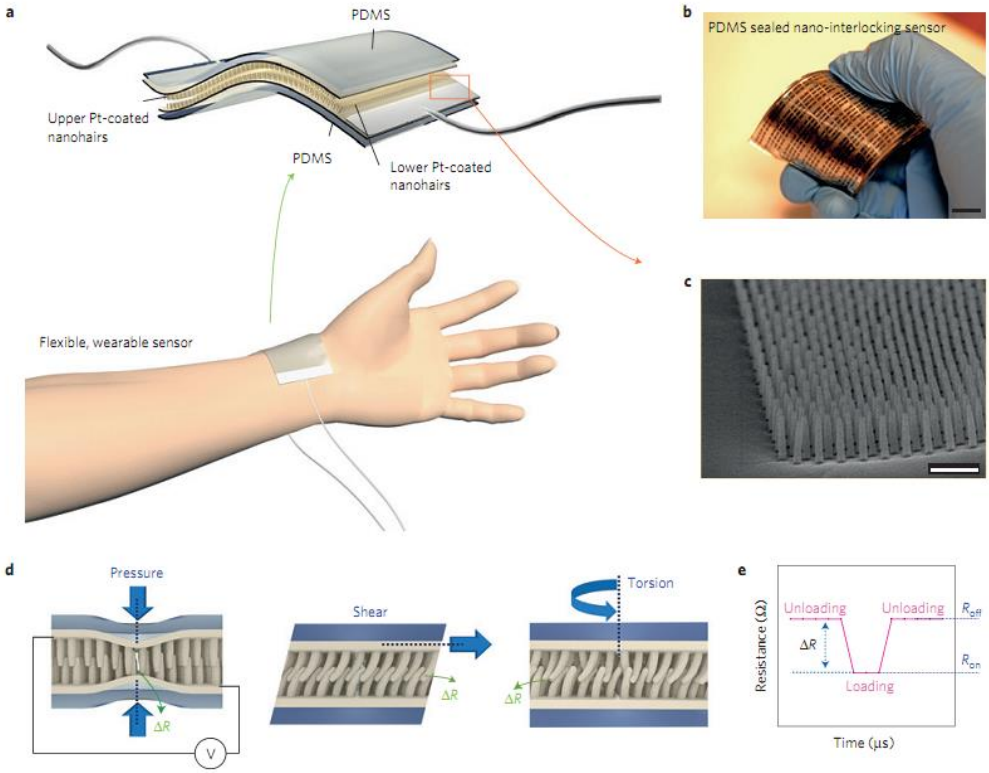

Figure 10. (a) Schematic of the assembly and operation of a flexible sensor layer sandwiched between thin PDMS supports (~500 μm thickness each). (b) Photograph showing the flexibility of the assembled sensor. Scale bar, 1 cm. (c) SEM image of a dense array of 50-nm radius nanohairs with AR = 10. Scale bar, 1 μm. (d) Schematic illustrations of the pressure, shear and torsion loads and their possible geometric distortions of the paired hairs. (e) Operation of a flexible sensor layer by means of recording of resistance change (Roff : unloading, Ron: loading). Reprinted with permission from reference [165].

1.2. Objectives and Outline of the Study

1.2.1. Objectives

In the preceding section, the importance of graphene/CP nanohybrid materials was introduced from the viewpoint of academic research and practical versatile sensing applications. The aim of this dissertation is to describe the fabrication of CP, graphene, and graphene/CP nanohbyrid materials by self-degradation, vapor deposition polymerization (VDP), in-situ polymerization methods. Furthermore, their applicable fields are also explored, including various sensors.

1.2.2. Outline

This dissertation involves the following subtopics:

I. Fabrication of polypyrrole nanotube embedded reduced graphene oxide transducer for field-effect transistor-type H_2O_2 biosensor
   1. Fabrication of RGO/PPy NT hybrid materials
   2. Electrical performance of RGO/PPy NT hybrid materials
   3. FET-type H_2O_2 biosensor based on RGO/PPy NT hybrid materials

II. Fabrication of carboxylated polypyrrole nanotube wrapped graphene sheet transducer for field-effect transistor-type glucose biosensor
   1. Fabrication of RGO/C–PPy NT hybrid materials
   2. Electrical performance of RGO/C–PPy NT hybrid materials
   3. FET-type glucose biosensor based on RGO/C–PPy NT hybrid materials

III. Fabrication of reduced graphene oxide-polyfuran nanohybrid for High-performance Hg^{2+} FET-type sensors
   1. Fabrication of RGO/PF NT hybrid materials
   2. Electrical performance of RGO/PF NT hybrid materials
   3. FET-type Hg^{2+} biosensor based on RGO/PF NT hybrid materials

IV. Fabrication of graphene/polyselenophene nanohybrid materials for highly sensitive and selective chemiresistive sensor
   1. Fabrication of RGO/PSe nanohybrid materials

2. Synthesis of RGO/PSe nanohybrid materials
3. Fabrication of chemiresistive sensor based on RGO/PSe nanohybrid materials
4. Chemiresistive sensing performance of the RGO/PSe nanohybrid film

V. Fabrication of graphene/free-standing nanofibrillar PEDOT/P(VDF-HFP) hybrid device for wearable and sensitive human motion detective piezo-resistive sensor

1. Fabrication of CVD graphene/free-standing nanofibrillar PEDOT/P(VDF-HFP) nanohbyrid devices
2. Sensing performance of E-skin device
3. Practical application of E-skin device

2. EXPERIMENTAL DETAILS

2.1. RGO/PPy NT hybrid materials

2.1.1. Fabrication of polypyrrole nanotube embedded reduced graphene oxide transducer for field-effect transistor-type H_2O_2 biosensor

2.1.1.1. Prepartation of PPy NTs

The preparation of PPy NTs was carried out using a self-degraded template method. $FeCl_3$ (0.243 g, 1.5 mmol) was added to a 5-mM methyl orange (MO) solution (sodium 4-[4′-(dimethylamino)phenyldiazo]phenylsulfonate in deionized water. After a flocculent precipitate appeared, the pyrrole monomer (105 μL, 1.5 mmol) was added, and the mixture was stirred at room temperature for 24 h. The resulting precipitate was purified by washing it with deionized water and methanol several times until the filtrate was colorless and had a neutral pH. The powdered PPy NTs (0.08 g, 79.5%) were then dried under vacuum at 60 ℃ for 24 h.

2.1.1.2. Prepratation of RGO/PPy NT hybrids

Graphene oxide (GO) was obtained from graphite powder using a modified Hummers and Offeman method.[166] GO was dispersed in water with a concentration of 0.06 mmol and then mixed with PPy NTs (also at a concentration of 0.06 mmol). The mixtures were ultrasonicated for 1 h. The resulting GO/PPy NT structures were exposed to 5 μL (35 wt %) of hydrazine solution for 1 h at 95 ℃, which reduced GO to RGO. The final product, an RGO/PPy NT composite (0.055 mmol, 91.7%), was obtained via filtration, purified using water, and dried in a vacuum oven at 25°C for hours.

2.1.1.3. Fabrication of RGO/PPy NT composite FET sensor

A microarray, consisting of 80 pairs of gold interdigitated microelectrodes, was patterned on a glass substrate using a 50-nm-thick Cr adhesion layer via a photolithographic process, resulting in electrodes with a gold layer thickness of 50 nm, a width of 10 μm, length of 4000 μm, and an interelectrode spacing of 10 μm. The microelectrode substrate was cleaned using sonication in ethanol. An aliquot of 0.1 mL of the ethanol solution containing 0.1 wt % RGO/PPy NT composites was dropped onto the interdigitated electrodes. The microelectrode substrate was finally dried under vacuum at room temperature for hours.

A solution chamber (volume 10 mL) was designed and employed for all solution-based measurements. The FET sensor substrate based on liquid-ion gate was fabricated with phosphate-buffered solution (PBS, pH 7.5). The current change of the sensor substrate was monitored at room temperature with a sourcemeter connected to a computer.

2.1.1.4. Characterization of RGO/PPy NT hybrids

The TEM images were taken with a JEOL JEM-2100 microscope. For TEM observation, the samples were diluted with ethanol and then the diluted solution was deposited on a copper grid coated with a carbon film. The FE-SEM images were obtained with a JEOL JSM-6700 F microscope. A specimen was coated with a thin layer of gold to eliminate charging effects. Raman spectra were recorded with a T64000 (Horiba Jobin Yvon). ATR-FTIR spectra were collected with a Thermo Scientific Nicolet 6700 FTIR spectrophotometer. X-ray diffraction (XRD) patterns were carried out with a New D8 Advance (Bruker). All electrical measurements were conducted with a Keithley 2612A sourcemeter, a probe station (MS TECH, model 4000) and a Wonatech WBCS 3000 potentiostat.

2.2. RGO/C–PPy NT hybrid materials

2.2.1. Fabrication of carboxylated polypyrrole nanotube wrapped graphene sheet transducer for field-effect transistor-type glucose biosensor

2.2.1.1 Preparation of C–PPy NTs

The C–PPy NTs were prepared using a self-degraded template method, whereby 0.243 g of 1.5-mM $FeCl_3$ solution was added to a 5-mM solution of sodium 4-[4-(dimethylamino)phenyldiazo] phenylsulfonate, $(CH_3)_2NC_6H_4$-N = $NC_6H_4SO_3Na$ in deionized water. After a flocculent precipitate appeared, 0.006 g of 0.05-mM P3CA and 0.1 g of 1.5-mM pyrrole monomer solution were added, and the mixture was stirred at room temperature for 24 h. The resulting precipitate was purified by washing it with deionized water and methanol several times until the filtrate was colorless and had a neutral pH. The powdered C–PPy NTs, weighing 0.08 g, and with 79.5 % purity, were then dried under vacuum at 60 ◦C for 24 hours.

2.2.1.2 Preparation of RGO/C–PPy NT hybrids

GO was obtained from graphite powder using a modified Hummers and Offeman method.[166] Graphene was obtained by reduction process of GO with 5 μL hydrazine (35 wt%) treatment at 95 ◦C for 1h. A 4-mg/mL suspension of graphene was dispersed in 5.1-mL of a 50:1 mixture of water and EtOH, and then mixed with 4 mg of the C–PPy NTs. The mixtures were ultrasonicated for 1 h, and the final product was a 6.3 mg of 78.8% purity graphene-C–PPy NT hybrid material, which was obtained via filtration, purified using water, and dried in a vacuum oven at 25 ◦C for 4 h.

2.2.1.3. Fabriaction of RGO/C–PPy NT composites FET sensor

A photolithographic process was used to pattern a microarray of 80 pairs of gold interdigitated microelectrodes on a glass substrate using a 50-nm-thick Cr adhesion layer. The resulting electrodes, formed on a 50-nm-thick gold layer, were 10-μm-wide and 4-mm-long, with an interelectrode spacing of 10 μm. The microelectrode substrate was cleaned using distilled water and ethanol. An aliquot of 0.1 mL of the ethanol solution containing 0.1-wt% RGO/C–PPy NT hybrid was dropped onto the interdigitated electrodes. A coupling reaction between enzyme and graphene-nanohybrid material was conducted by a modified previous our method. In brief, the coupling reaction was then carried out by exposing the substrate to a mixed solution of GOx and 10 μL of 1-wt% aqueous DMT-MM for 12 h to attach the GOx to the surface of the RGO/C–PPy NTs. The substrate was then rinsed with distilled water and dried under vacuum at room temperature for 12 h. A 10-mL solution chamber was employed for all solution-based measurements. The FET sensor substrate based on liquid-ion gate was fabricated with PBS, which had a pH of 7.5. The current was monitored at room temperature using a source meter.

2.2.1.4. Characterization of RGO/C–PPy NT hybrids

The TEM images were taken with a JEOL JEM-2100 microscope at the National Center for Inter-university Research Facilities (NCIRF) at Seoul National University. For TEM observation, the samples were diluted with in ethanol and then the diluted solution was deposited on a copper grid coated with a carbon film. The FE-SEM images were obtained with a JEOL JSM-6700F microscope. A specimen was coated with a thin layer of gold to eliminate charg-ing effects. Raman spectra were recorded with a T64000 (Horiba Jobin Yvon). ATR-FTIR spectra were collected with a Thermo Scientific Nicolet 6700 FTIR spectrophotometer. XRD patterns were carried out with a New D8 Advance (Bruker). All electrical measurements were conducted with a Keithley 2612A sourcemeter, a probe station (MS TECH, MODEL 4000) and a Wonatech WBCS 3000 potentiostat.

2.3. RGO/PF NT hybrid materials

2.3.1. Fabrication of reduced graphene oxide-polyfuran nanohybrid for High-performance Hg^{2+} FET-type sensors

2.3.1.1 Prepration of PF NTs

A self-degraded template method was carried out for the preparation of PF NTs. Firstly, $FeCl_3$ (0.243 g, 1.5 mmol) was added to a 5-mM MO solution in deionized water. After a flocculent precipitate appeared, the furan monomer (102 mg, 1.5 mmol) was added. The mixture was then stirred at room temperature for 24 hours. The resulting precipitate was purified by washing it with deionized water and methanol several times until the filtrate was colorless and had a neutral pH. Finally, the powdered PF NTs (80 mg, 78.4 %) were dried under vacuum at 60℃ for 24 hours.

2.3.1.2. Prepration of RGO/PF NT hybrids

GO was obtained from graphite powder using a modified Hummers and Offeman method.[166] GO (4 mg/mL) was dispersed in deionized water and then mixed with PF NTs (4 mg). The mixtures were ultrasonicated for 1 hour. The 5 μL (35 wt %) hydrazxine solution exposed to the resulting GO-PF NT structures for 1 hour at 95℃, leading to reduction process from GO to RGO. The final product, the RGO-PF NT composite (6.5 mg, 81.3 %), was obtained via purification by using water, filtration, and dried in a vacuum oven at 25℃ for hours.

2.3.1.3. Fabrication of RGO/PF NT composite FET sensor

A microarray (80 pairs of gold interdigitated microelectrodes) was patterned on a glass substrate using a 50-nm-thick Cr adhesion layer via a photolithographic process, resulting in electrodes with a gold layer thickness of 50 nm, a width of 10 μm, length of 4000 μm, and an interelectrode spacing of 10 μm. The microelectrode substrate was washed using sonication in ethanol. An aliquot of 0.1 mL of the ethanol solution containing 0.1 wt % RGO-PF NT composites was dropped onto the patterned electrodes. Then, the microelectrode substrate was dried under vacuum at room temperature for several hours. A solution chamber (volume 10 mL) was designed and employed for all liquid-based measurements. The FET sensor substrate based on liquid-ion gate was fabricated with PBS at pH 7.5.

2.3.1.4. Characterization of RGO/PF NT hybrids

The TEM images were obtained with a JEOL JEM-2100 microscope. For TEM observation, the samples were diluted with ethanol and then the diluted solution was deposited on a copper grid coated with a carbon film. The FE-SEM images were taken with a JEOL JSM-6700 F microscope. A specimen was coated with a thin layer of gold to eliminate charging effects. Raman spectra were recorded with a T64000 (Horiba Jobin Yvon). ATR-FTIR spectra were collected with a Thermo Scientific Nicolet 6700 FTIR spectrophotometer. XRD patterns were carried out with a New D8 Advance (Bruker). All electrical measurements were conducted with a Keithley 2612A sourcemeter, a probe station (MS TECH, MODEL 4000) and a Wonatech WBCS 3000 potentiostat.

2.4. RGO/PSe nanohybrid materials

2.4.1 Fabrication of graphene/polyselenophene nanohybrid materials for highly sensitive and selective chemiresistive sensor

2.4.1.1. Preparation of RGO/PSe nanohybrid materials

GO was obtained from graphite powder using a modification of the Hummers and Offeman method.[166] GO (4 mg/mL) was dispersed in 5 mL aqueous solution and then mixed with selenophene monomer (4 mg, 0.06 mmol) dissolved in EtOH (0.1 mL). The solution was sonicated for 1 min, and then iron chloride 1 mL (5 wt % in deionized water) was added to the mixture while stirring. After polymerization for 24 h, 2 mL of 35 wt% hydrazine solution was added dropwise to the GO/PSe nano-composites over 1 h at 95 ℃ to reduce GO to RGO. The final product, RGO/PSe nanocomposite (5.3 mg, 66%), was obtained after filtration, purification with excess water, and drying in a vacuum oven at 25 ℃.

2.4.1.2. Characterization of RGO/PSe nano hybrid materials

The TEM images were taken with a JEOL JEM-2100 microscope. For TEM observation, the samples were diluted with in ethanol and then the diluted solution was deposited on a copper grid coated with a carbon film. The FE-SEM images were obtained with a JEOL JSM-6700 F microscope. A specimen was coated with a thin layer of gold to eliminate charging effects. Raman spectra were recorded with a T64000 (Horiba Jobin Yvon). ATR-FTIR spectra were collected with a Thermo Scientific Nicolet 6700 FTIR spectrophotometer. XRD patterns were carried out with a New D8 Advance (Bruker). Significant data were extracted from the plot using the fitting software (ZMAN 2.3). All electrical measurements were conducted with a Keithley 2612A sourcemeter, a probe station (MS TECH, MODEL 4000) and a Wonatech WBCS 3000 potentiostat.

2.5. CVD graphene/PEDOT/P(VDF-HFP) nanohbyrid mateirals

2.5.1. Fabrication of graphene/free-standing nanofibrillar PEDOT/P(VDF-HFP) hybrid device for wearable and sensitive human motion detective piezo-resistive sensor

2.5.1.1. Prepatation of CVD graphene/free-standing PEDOT nanofiber/P(VDF-HFP) nanohbyrid materials

Single-layer graphene was prepared on Cu foil (9 x 6 cm) using chemical vapor deposition (CVD). The Cu foil was loaded into a thermal CVD reactor, and the temperature was increased to 1000℃ with 8 sccm of H_2 flowing at 90mTorr. The sample was maintained at 1000℃ for 30 min with a 20-sccm flow of CH4 and then cooled to room temperature with a 8-sccm flow of H_2. Using a wet transfer method, the single-layer graphene was transferred onto the PDMS substrate. The PDMS was prepared by mixing with degassed PDMS prepolymer (with a ratio of base to cross-linker of 10:1 by mass) in a petridish (125 x 125 x 20 mm^3), followed by curing at 60℃ for 2 h to produce 1-mm-thick PDMS substrates. The single-layer graphene was coated with PMMA (4000 rpm, 1min) and immersed in an etchant to remove the Cu foil. The graphene on PMMA was then rinsed several times with deionized (DI) water to remove etchant residues. Subsequently, the PMMA/graphene was transferred to a PDMS film. The PMMA was slowly removed by acetone. To synthesize

the free-standing PEDOT on the graphene surface, we used a technique described by Hammond and Kaner et al. To synthesize free-standing nanofibrillar PEDOT, iron (III) chloride solution 30mL in chlorobenzene solution at 5 wt% was sprayed onto the graphene surface, which acts like a seed template, nucleation sites, and oxidant for PEDOT polymerization. Then, 10 μL of the EDOT monomer in chlorobenzene solution (6 wt%) was placed into a vapor deposition polymerization (VDP) chamber and polymerized at 100℃ under vacuum conditions, resulting in vertical growth of PEDOT islands on the iron (III) chloride seeds. Anisotropic iron (III) chloride template was forms due to the accumulation of solids during evaporation of the solution. After the EDOT monomer injected into VDC, subsequently, vapor polymerization took place on the surface of the template, forming vertically aligned PEDOT islands. Following repeated rinsing with DI water and methanol, P(VDF-HFP) dissolved in chlorobenzene (6 wt%) was deposited using spin-coating at 3000 rpm for 60s. The P(VDF-HFP) was crystallized by annealing at 150℃ for 2 h. To form the devices, two sheets of the graphene/V-PEDOT/P(VDF-HFP) film were placed in a symmetrical double-layer configuration, and Ag paste was applied at the edges each layer to form electrical contacts.

2.5.1.2. Characterization of CVD graphene/PEDOT/P(VDF-HFP) nanohybrid materials

High-resolution transmission electron microscopy (HR-TEM) images were obtained using a JEOL JEM-3100 at the National Center for Inter-university Research Facilities (NCIRF) at Seoul National University. For TEM observation, the samples were diluted in ethanol and deposited onto a copper grid coated with a carbon film. FE-SEM images were obtained using a JEOL JSM-6700F. specimens were coated with a thin layer of gold to eliminate charging effects. Raman spectra were recorded using a Horiba Jobin Yvon T64000. Data were extracted from plots using the fitting software ZMAN 2.3. All electrical measurements were obtained using a Keithley 2612A source meter and MS TECH 4000 probe station.

3. RESULTS AND DISCUSSION

3.1. Fabrication of polypyrrole nanotube embedded reduced graphene oxide transducer for field-effect transistor-type H_2O_2 biosensor.

3.1.1. Fabrication of RGO/PPy NT hybrid materials

Figure 11 showed the fabrication of the RGO/PPy NT hybrid materials. SEM and TEM were used for characterizing the morphology of the RGO/PPy nanohybrid materials. The SEM and TEM images of the PPy NTs revealed that the diameter of the tubes was around 70 nm, as shown in Figure 12(a). The RGO sheet was observed using cross-sectional SEM image, which shows a structure that resembles paper with porous spaces. (See Figure 12(b)) Figure 12(c) and (d) display cross-sectional SEM and TEM images of the RGO/PPy NT hybrid material. The PPy NT structures were well organized on the large surface area of the graphene sheets. Note that the PPy NTs interact with the RGO sheets. These interactions are discussed in detail below. These results suggest that the RGO/PPy NT hybrid materials were stable due to the strong π–π interactions between the RGO layers and PPy NTs.

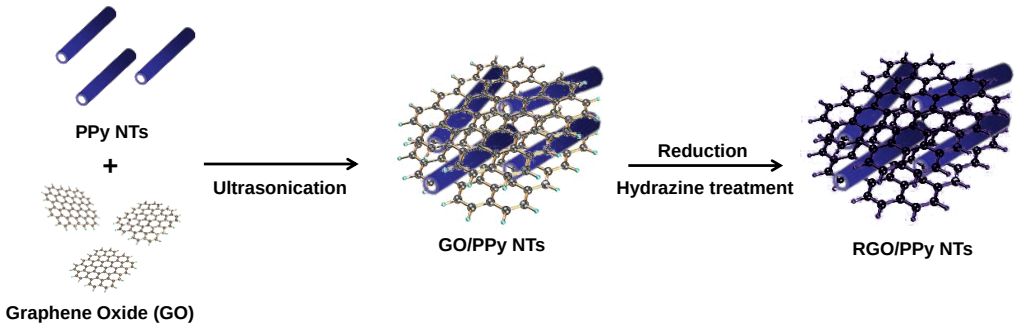

Figure 11**.** A schematic illustration of the synthesis of rGO/PPy NT hybrids.

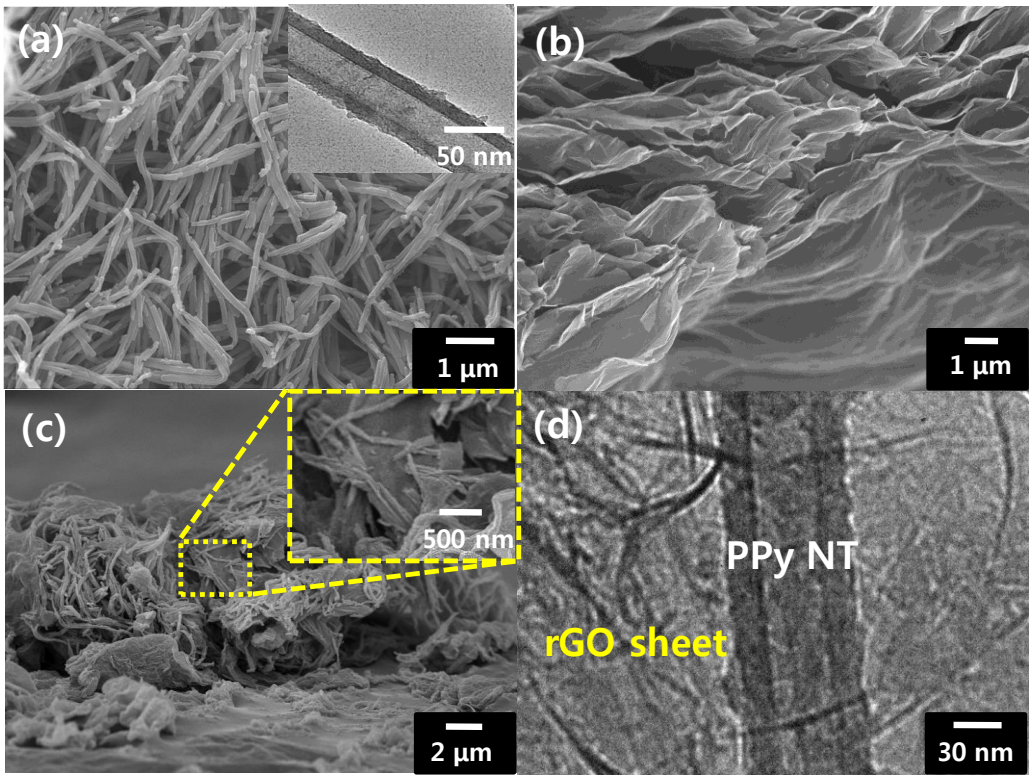

Figure 12**.** (a) SEM image shows PPy NTs. The inset shows a TEM image. Cross-sectional SEM images show (b) rGO and (c) rGO/PPy NTs. The inset indicates the magnification level. (d) A TEM image shows rGO/PPy NTs.

To investigate the structure of the RGO/PPy NT hybrid materials, RAMAN spectroscopy was carried, as shown in Figure 13. The Raman spectrum of GO exhibited D peaks at 1364 cm^{-1} and G peaks at 1610 cm^{-1}. The Raman spectrum of the RGO showed two prominent bands at 1343 cm^{-1} and 1592 cm^{-1}, which correspond to D and G bands. The Raman spectrum of PPy NTs displayed the C=C backbone stretching at ~ 1577 cm^{-1} and the ring stretching mode of PPy at 1361 cm^{-1}. The Raman spectrum of the RGO/PPy NT hybrid materials exhibited an enhanced intensity of the band around 1348 cm^{-1}, which indicates an interaction between PPy and the RGO sheets.

To further characterize the RGO/PPy NT hybrid mateirals, ATR- FTIR and XRD spectra were measured. (See Figure 14) GO showed characteristic absorption bands of oxide groups, including the C=O stretching peak at 1733 cm^{-1}, the vibration and deformation peaks of O-H groups at 3391 cm^{-1} and 1417 cm^{-1}, and the C-O (alkoyl) stretching peak at 1037 cm^{-1}. Most of the peaks related to oxygen-containing functional groups vanished in the FTIR spectra of RGO, which means that the reduction of GO was successful conducted. The characteristic bands of the RGO/PPy NT hybrid materials exhibited the pyrrole ring and graphene fundamental vibrations, which occur at 1561 cm^{-1} (C=C stretching), 1437 cm^{-1} (C-C stretching), 1282 cm^{-1} (C-N stretching), and 1038 cm^{-1} (C-H deformation). The peaks of the RGO/PPy NT

nanohybrids were shifted compared with those of the PPy NTs and RGO in isolation due to interactions between the RGO layers and PPy NTs.

The XRD diffractograms of GO contained a very sharp peak at 10.1° (d = 8.75 Å), which indicates that the structure of the original graphite was successfully oxidized to GO, as shown in Figure 15. A broad peak appeared at 25° (d = 3.56 Å), which implies that RGO formation was achieved by reduction of GO using hydrazine. The RGO/PPy NT hybrids displayed a broad peak at around 28° (d = 3.18 Å), which corresponds to the pyrrole intermolecular distance between the RGO/PPy NTs. We conclude that the PPy NTs and the RGO sheet formed a composite via π–π interactions.

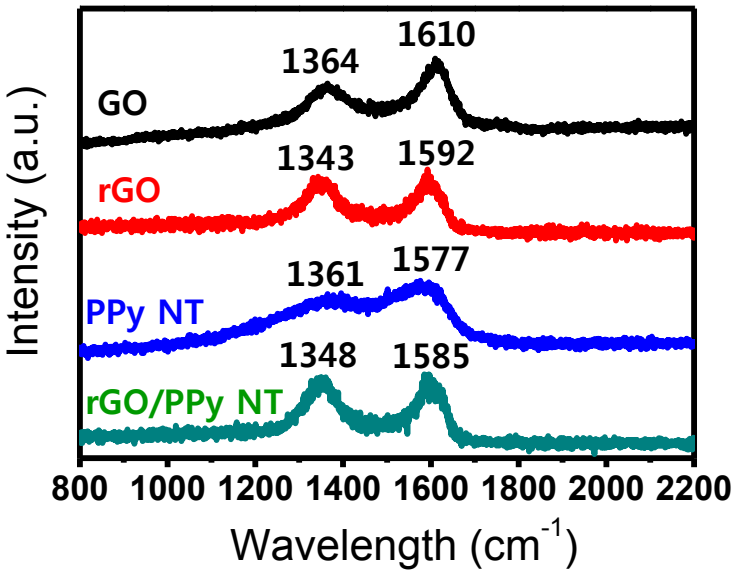

Figure 13**.** Raman spectra of GO, rGO, PPy, NT, and rGO/PPy NT hybrids.

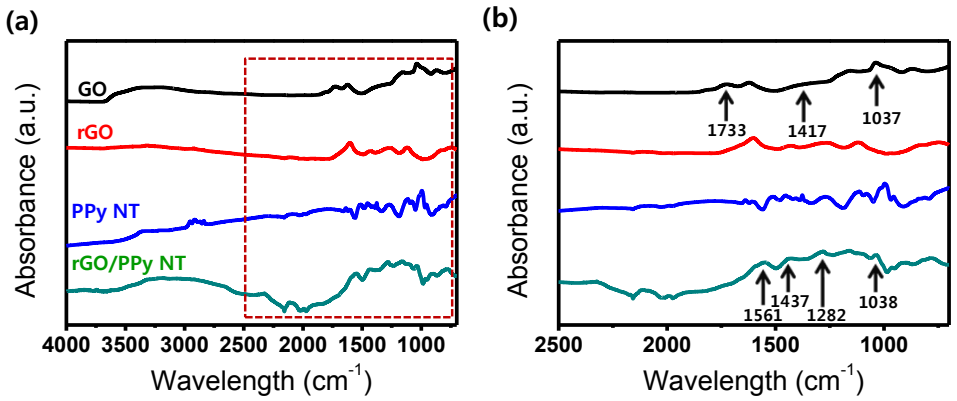

Figure 14. ATR-FTIR spectra of (a) GO, rGO, PPy, NT, and rGO/PPy NT hybrids. A magnified view of the marked area in (a) is shown in (b).

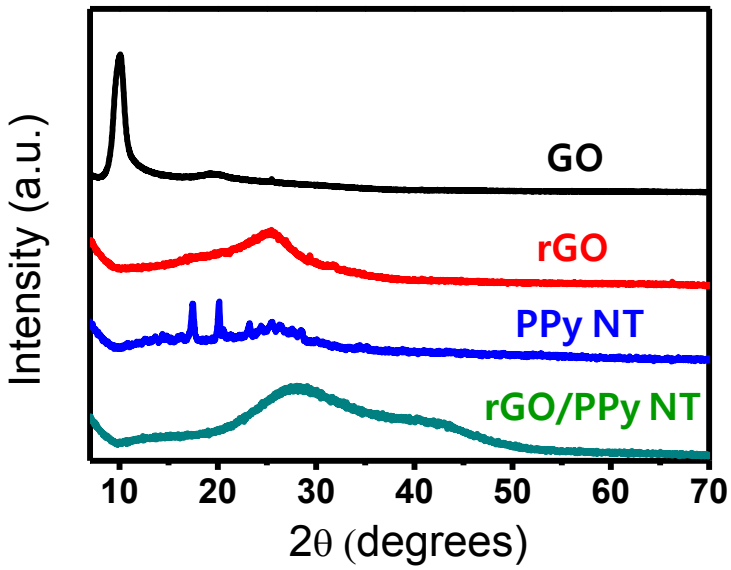

Figure 15. X-ray diffractions of GO, rGO, PPy NT, and rGO/PPy NT hybrids.

3.1.2. Electrical performance of RGO/PPy NT hybrid materials

To understand the electrical properties the RGO/PPy NT hybrid materials, current–voltage (*I*–*V*) curves were measured on the patterned electrode substrate. Linear *I*–*V* curves were observed over a range of –0.4 V to +0.4 V, which means that Ohmic contacts were formed between the nanohybrids and the gold electrodes, as shown in Figure 15(a). The conductivity of the RGO/PPy NT hybrids was higher than that of RGO and PPy NTs. This result is considered that the RGO/PPy NT hybrids showed effective electron transport between the PPy NTs and the RGO, resulting in a decrease in the resistance. Despite excellent electrical properties of the RGO sheet, the conductivity was highly anisotropic and interlayer electron transport was slow. However, the PPy NTs serve as conductive channels to connect the RGO layers, resulting in enhanced conductivity, as shown in Figure 16(a).

The electrical characteristics of the RGO/PPy NT conductive channels were characterized by measuring the source–drain current–voltage (I_{SD}–V_{SD}) characteristics of liquid-ion-gated transistors under various gate biases. Firstly, the devices based on the RGO/PPy NT hybrid materials were in phosphate-buffered saline (PBS) solution (pH 7.4). Then, V_g was varied in the range of –2.0 V to +0.4 V in steps of 0.2 V, with a gate voltage sweep rate of 0.2 Vs^{-1}, as shown in Figure 16(b). When a larger negative gate bais was applied, I_{SD}

increased (i.e., became more positive). This is a typical characteristic of *p*-channel transistors. Thus, the current in the device was controlled over the hole carrier density at the surface of RGO/PPy NT hybrid materials. Generally, the PPy materials showed the *p*-type semiconductor behavior.[78] Although unaltered graphene shows ambipolar properties in the semiconductor devices, the graphene samples used, in this work, displayed hole-transporting behavior due to the absorption of oxygen and/or water from air to yield RGO/PPy NT hybrids, resulting in enhancement of *p*-type systems. These result offered higher stability and improved sensing performance relative to that of the individual components alone.

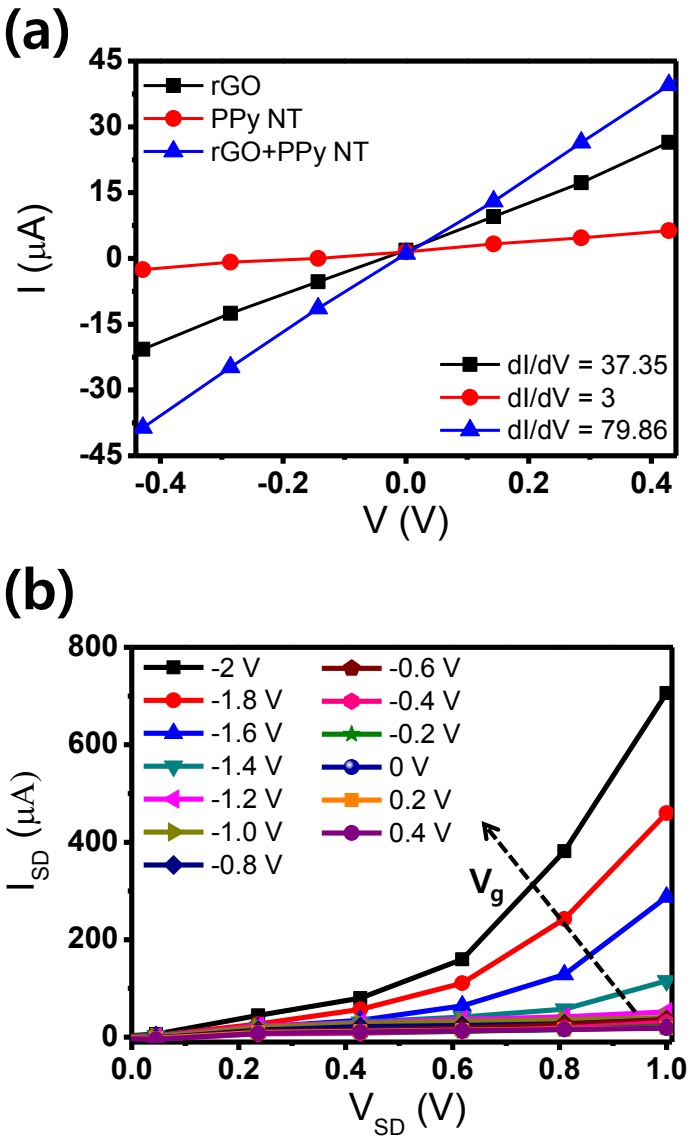

Figure 16. (a) Current−voltage (I−V) curves of GO, rGO, PPy NTs, and rGO/PPy NTs composites and (b) rGO/PPy NTs composites at V_g from –2.0 to 0.4 V in 0.2-V steps (V_{sd}: 0 to 1.0 V in 0.2-V steps).

3.1.3. FET-type H_2O_2 biosensor based on RGO/PPy NT hybrid materials

The fabricated liquid-ion-gated FETs were surrounded with PBS at pH 7.4 as the electrolyte. (See Figure 17(a)) Good contact between the RGO/PPy NT hybrid materials and the solution was offered by using a remote electrode in the surrounding electrolyte. The sensing performance of sensors can be enhanced using this strategy. The FET-type sensor, which is a *p*-channel FET (with V_g = 0.1 V), was used for the real-time response to H_2O_2 in varying concentrations. The modulations in I_{SD} were recorded in presponse to the various H_2O_2 concentrations in the solution, as shown in Figure 17(b). The normalized current, called the sensitivity, was determined by $\Delta I_{SD}/I_0 = (I_{SD}–I_0)/I_0$, where I_0 is the initial current and I_{SD} is the measured real-time current following stabilization after injecting the H_2O_2 into the liquid-ion-gated FET-type sensor device. The FET-type sensor based on the RGO/PPy NT hybrid materials showed an increase in I_{SD} in response to a gradual increase in the concentration of H_2O_2. This result is considered that the H_2O_2 analyte induces the accumulation of *p*-type charge carriers at the surface of the RGO/PPy NTs. (See below for a discussion of the sensor mechanism.) The RGO/PPy NT hybrid materials displayed highly sensitive responses to H_2O_2, with a detection limit of approximately 100 pM (signal-to-noise ratio (S/N) = 3.5). It is

generally considered a significant signal when S/N is greater than or equal to 3.0.[78–79] S/N (= 0.83) value is too low on the measurement for 10 pM, suggesting that it is not considered the signal as shown in Figure 18**.** Thus, 100 pM is regarded as a limitation of detection. The fabricated FET-type H_2O_2 sensor, in this work, enables much more rapid detection and 10 times higher sensitivity than oxidation-level-based methods in glassy carbon electrodes (GCEs), as shown in Table 1. The calibration curve was shown in Figure 17(c). When the H_2O_2 concentration increases, stronger signals were recorded. In all measurements, the FET-type sensors exhibited rapid response times of less than 1 s and showed linear tendency to normalized current changes. Furthermore, the FET-type sensors showed good reproducibility and storage stability. After ten repeated experiments, the response of the H_2O_2 sensor displayed similar result, which means that it had good reproducibility. Storage stability was evaluated in air. The FET-type sensor detected 1 nM of H_2O_2, after one month of storage (See Figure 17(d)), with no variation in the response normalized current relative to that of freshly prepared sensors. Tese results were considerd that FET-type H_2O_2 sensor based on the RGO/PPy NT hybrid mateirals had excellent air and storage stability.

To clearly confirm the mechanism of H_2O_2 sensing behavior, not only the real-time response of the FET-type sensor based on PPy NTs, but also sensors

based on RGO materials were measured (both at V_g = 0.1 V). The sensor device based on PPy NTs had limit of detection to H_2O_2 at a concentration of 1 μM. (See Figure 17(a)) The sensing device based on an RGO layer was sensitive to H_2O_2 at a concentration of 1 mM. This result is deduced that H_2O_2 enables to alter the electrical signal more effectively in PPy NTs than in RGO. The applied gate bias of V_g = 0.1 V was less than the oxidation potential of H_2O_2. Thus, the change of I_{SD} did not occur due to electrochemical oxidation of H_2O_2. Therefore, H_2O_2 could alter the charge carrier density more efficient in the PPy backbone compared with that in the graphene backbone, indicating that a positive charge was formed by reacting with PPy. It has been reported that *p*-doping effects result from the addition of H_2O_2 molecules as opposed to the direct transfer of electrons via oxidative reactions between the graphene and PPy backbone. The reasons for the improved performance of the sensor based on the RGO/PPy NT hybrids are owing to the following effects. First, an efficient response to H_2O_2 occurred due to the enhanced surface area and strong interactions between the RGO sheet and PPy NTs. Second, the enhanced *p*-type semiconductor behavior improved signal transduction.

To investigate the specificity of the response to H_2O_2, real-time monitoring of I_{SD} in various solutions containing compounds found in biological fluids, including UA, AA, and glucose solutions was evaluated, as shown in Figure

17(e). After injecting 1-mM UA, 1-mM AA, 1-mM glucose, and 0.05-mM H_2O_2, the real-time responses were recorded in response to analytes. A remarkable increase in the normalized current was observed when H_2O_2 was injected, even at much lower concentrations than the other compounds in the analyte. (See Figure 17(f)) When UA and AA were exposure into the sensors, the little change of the signals was observed in the charge density on the surface of the RGO/PPy NTs relative to the changes recorded upon exposure to H_2O_2. Glucose could not bind to the graphene-PPy nanohybrid materials because of the lack of an appropriate binding site. These results clearly demonstrate specificity towards H_2O_2.

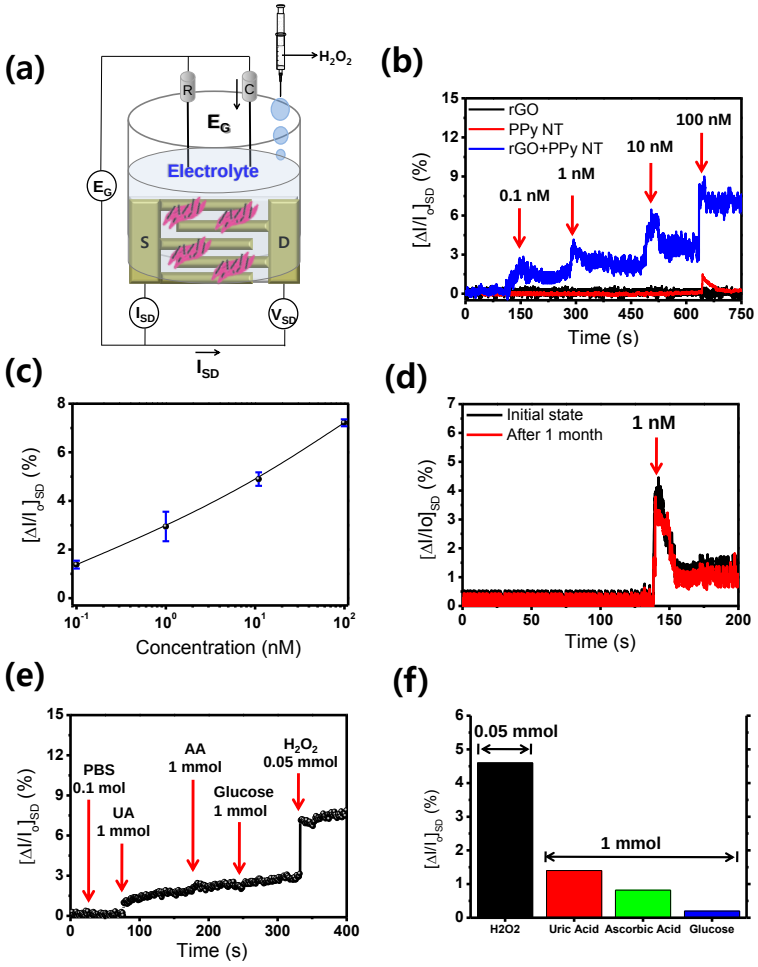

Figure 17. (a) Schematic diagram shows a liquid-ion-gated FET-type sensor. (Ag/AgCl reference electrode, R; platinum counter electrode, C; source and drain electrodes, S and D) (b) Real-time responses and (c) a calibration curve for H_2O_2 based on rGO, PPy NTs, and rGO/PPy NTs composites were measured at V_{sd} = 10 mV (V_g = 0.1 V) with H_2O_2 concentrations of 0.1 nM to 100 nM. Storage stability biosensor performance is shown in (d). Real-time responses to PBS, UA, AA, glucose, and H_2O_2 are shown in (e). (f) A histogram details the sensing performance to UA, AA, glucose, and H_2O_2.

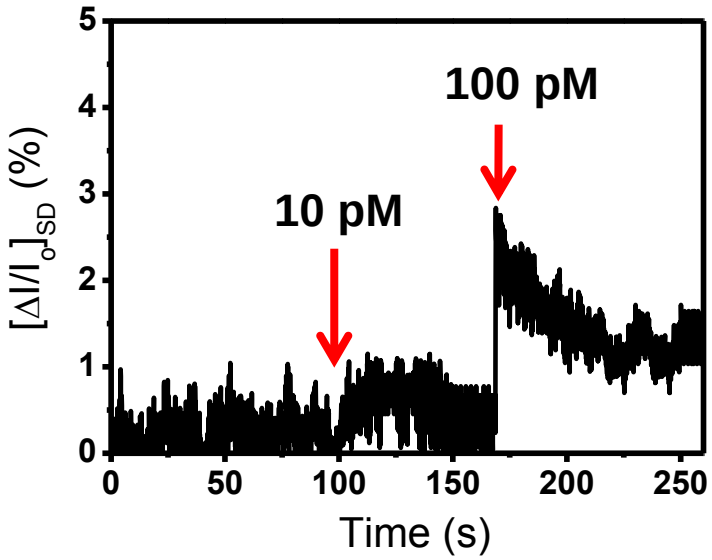

Figure 18. Real-time responses for H_2O_2 based on rGO/PPy NTs composites were measrured at V_{sd} = 10 mV (V_g = 0.1 V) with H_2O_2 concentration of 10 pM to 100 pM.

Table 1. Comparison of the performance of various H_2O_2 sensors.

Biosensor configuration	Detection limit (μM)	Reference
AgNP/SnO_2/GCE	5	[167]
AgNP/Graphene/GCE	28	[168]
AgNP/CNT/GCE	0.5	[169]
AgNP/ZnO/GCE	0.42	[170]
AgNP/DNA/GCE	1.7	[171]
AgNP/MWCNT/Au electrode	0.5	[172]
MnO_2/GO/GCE	0.8	[173]
Ni/Al-LDHs Films	0.009	[174]
Co/Al-LDHs Films	0.05	[174]
Pt/PPy Hollow microsphere	1	[175]
Pt/Graphene/GCE	0.5	[176]
Fe_3O_4/rGO/GCE	0.006	[177]
PPy NWs/Cu/Au electrode	2.3	[178]
Hb/CeO_2/MWNTs	0.65	[179]
PPy NT/rGO FET-type sensor	0.0001	This work

NP = Nanoparticle, NW = Nanowire, rGO = Reduced graphene oxide, GCE = Glassy carbon electrode, MWCNT = Multi-wall carbon nanotube, Hb = Hemoglobin, LDH = Layered double hydroxides.

3.2. Fabrication of carboxylated polypyrrole nanotube wrapped graphene sheet transducer for field-effect transistor-type glucose biosensor

3.2.1. Fabrication of RGO/C−PPy NT hybrid materials

Figure 19 described the fabrication of RGO/C–PPy NT hybrid materials. SEM and TEM images of the C–PPy NTs were shown in Figure 20(a). The diameter of the C–PPy NTs was observed in the range of 70-80 nm. To characterize the graphene sheets, cross-sectional SEM was carried out. (See Figure 20(b)) It showed paper-like structure with porous regions. Figures 20(c) and 1(d) display cross-sectional SEM and TEM images of the RGO/C-PPy NT hybrid materials. The structure of the C-PPy NTs was well organized and coupled on the surface of the graphene sheets. This proposes that the RGO/C−PPy NT composites were stable due to the strong π–π interactions between the graphene layers and C−PPy NTs.

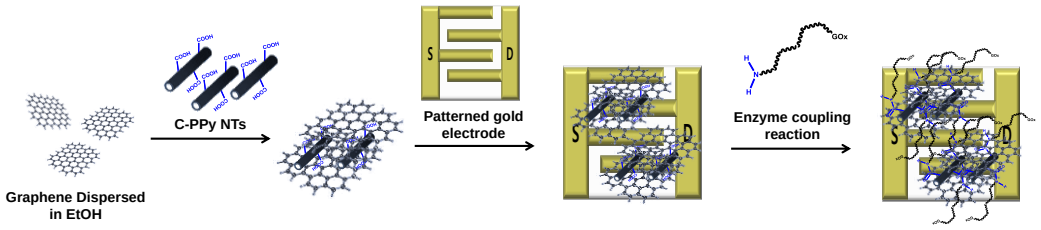

Figure 19. Schematic illustration of the fabrication of rGO/C-PPy NT hybrid glucose sensing device.

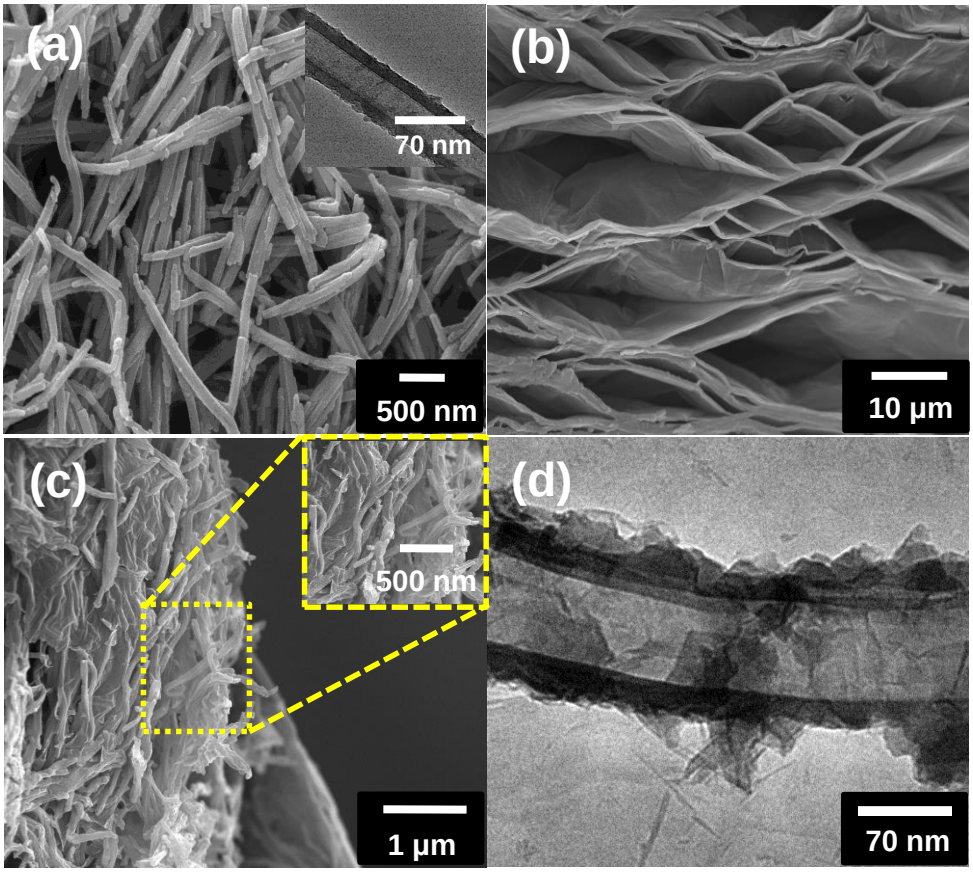

Figure 20. (a) SEM image of the C-PPy NTs. The inset shows a TEM image. (b) Cross-sectional SEM images of the rGO layers and (c) the rGO/C-PPy NTs. (d) TEM image of rGO/C-PPy NTs.

To confirm the chemical characterization of the C−PPy NTs, RGO, and RGO/C−PPy NTs, ATR-FTIR spectroscopy was carried out, as shown in Figure 21 and 22. The spectrum from the C−PPy NTs showed a carboylic acid stretching peak at 1733 cm^{-1}, a pyrrole ring stretching peak at 1554 and 1475 cm^{-1}, and a C−N stretching peak at 1294 cm^{-1}.[77] The characteristic bands of the RGO/C−PPy NT hybrid materials showed peaks owing to pyrrole ring and graphene fundamental vibrations, which occurred at 1551 cm^{-1} (C=C stretching), 1467 cm^{-1} (C−C stretching), 1303 cm^{-1} (C−N stretching), and 1038 cm^{-1} (C−H deformation). The characteristic bands of the RGO/C−PPy NT hybrids were shifted compared with those of the C−PPy NTs and graphene in isolation, due to the interactions between the RGO layers and PPy NTs.

The XRD patterns of GO showed a very sharp peak at 10.1° (d = 8.75 Å), as shown in Figure 23(a). This indicates that the structure of the original graphite was preserved, and that the material was successfully oxidized to form GO. A broad peak at around 25° (d = 3.56 Å) was observed for the RGO sheets, which means that RGO formation was successfully fabricated by reduction of the GO using hydrazine. The RGO/C−PPy NT hybrids showed a broad peak at around 24° (d = 3.7 Å), corresponding to the pyrrole intermolecular distance between the RGO/C−PPy NTs. Thus, C−PPy NTs and graphene sheets have been completely interacted.

To gain further insight into the structure of the RGO/C−PPy NT hybrids, Raman spectroscopy was carried out, as shown in Figure 23(b). The D peaks (~1364 cm^{-1}) and G peaks (~1610 cm^{-1}) in GO were clearly visible. In contrast, the Raman spectrum of the RGO showed two prominent bands at 1343 cm^{-1} and 1592 cm^{-1}, corresponding to the D and G bands. The ratio of the D band peak to the G band peak, I_D/I_G, increased slightly compared with that of GO, suggesting that the reduction process induced defects or edges in the RGO sheets. The Raman spectrum of the C−PPy NTs showed peaks corresponding to C=C backbone stretching at ~ 1569 cm^{-1} and to the ring stretching mode of C−PPy at 1345 cm^{-1}. Interestingly, the Raman spectrum of the RGO/C−PPy NT composites exhibited an increased intensity of the band around 1340 cm^{-1}, which implies that an interaction between C−PPy and the graphene sheets occurred.

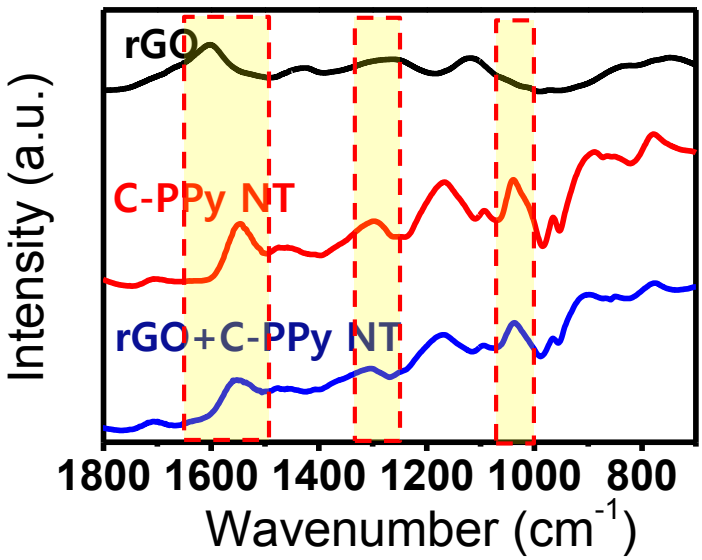

Figure 21. ATR-FT-IR spectra of rGO, C-PPy NT, and rGO/C-PPy NT hybrids.

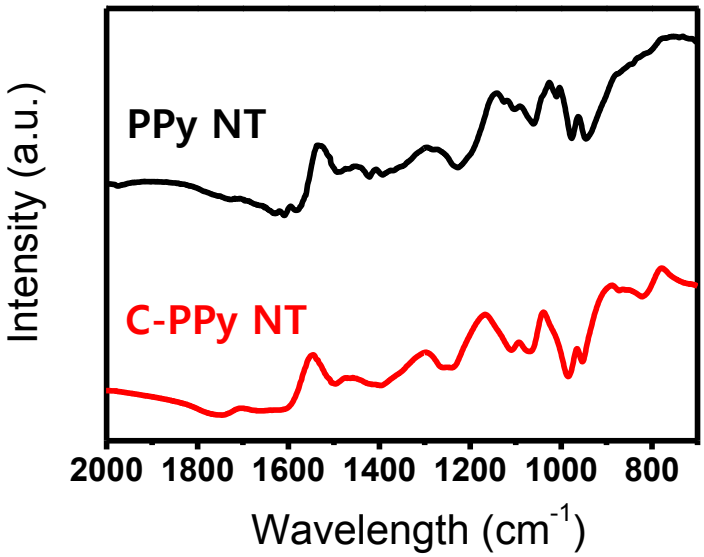

Figure 22. ATR-FT-IR spectra of PPy NT and C-PPy NT.

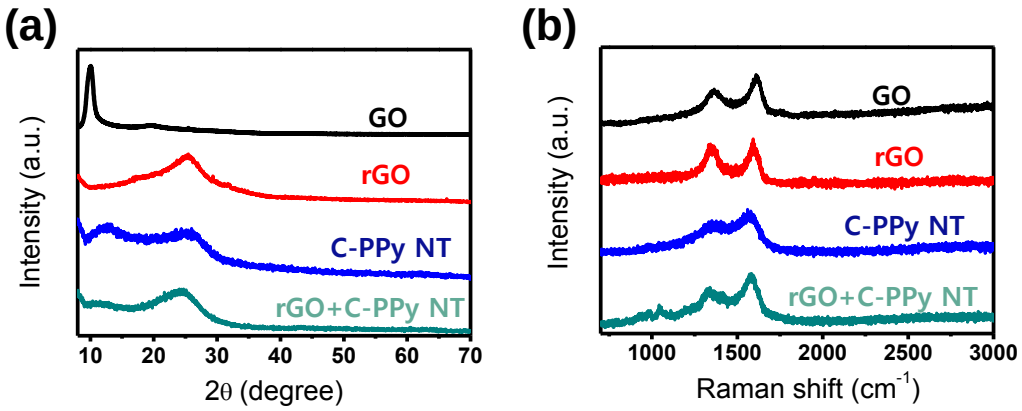

Figure 23. (a) X-ray diffraction patterns and (b) Raman spectra of GO, rGO, C-PPy NT, and rGO/C-PPy NTs.

3.2.2. Electrical performance of RGO/C–PPy NT hybrid materials

To investigate the electrical performance of the samples on the gold electrode substrate, current–voltage (*I–V*) curves were measured, as shown in Figure 24. Linear *I–V* curves were recorded over a range of –0.4 V to +0.4 V, which means that Ohmic contacts were formed between the samples and the gold elcetrodes. The electrical conductivity of the RGO/C−PPy NT hybrids was higher than that of the graphene or C−PPy NTs in isolation. This result indicates that the RGO/C−PPy NT hybrids facilitated efficient electrical transport between the C−PPy NTs and the graphene, decreasing the resistance. In general, the graphene sheet exhibited outstanding electrical properties. However, the conductivity was highly anisotropic and the interlayer electron transport was slow. The RGO/C−PPy NTs showed improved conductivity, due to the C−PPy NTs acting as conductive channels to connect the graphene layers.

The electrical properties of the RGO/C−PPy NTs conductive channels were characterized by liquid-ion-gated transistors with PBS solution (pH 7.4), which can efficiently offer effective gate control. (See Figure 25(a)). The output curves of the RGO/C−PPy NTs at room temperature with various gate biases were shown in Figure 25(b). The source-drain current (I_{SD}) increased when the gate voltage (V_G) became more negative. This is a typical characteristic of *p*-channel transistors and, suggesting the current in the device was owing to hole

transport and that the modulation of I_{SD} resulted from gate control over the hole carrier density at the surface of RGO/C−PPy NT hybrids. In the previouse report, the PPy materials showed *p*-type semiconductor behavior. Although unaltered garphene shows ambipolar properties in electrical devices, the graphene samples used here displayed *p*-type behavior, due to the absorption of oxygen and/or water from air to yield RGO/C−PPy NT composites. Therefore, these results enhanced stability and improved sensing performance relative to that of the individual components alone.

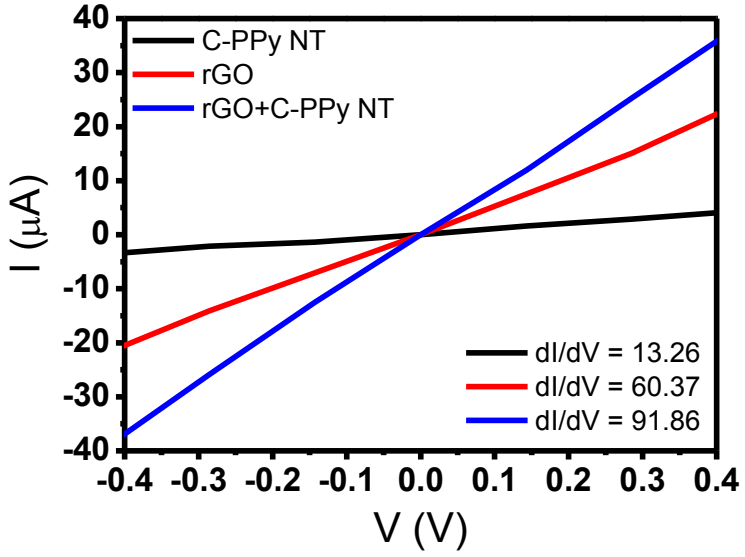

Figure 24. Current−voltage (*I*−*V*) curves of C-PPy NTs, rGO, and rGO/C-PPy NT hybrids.

3.2.3. FET-type glucose biosensor based on RGO/C–PPy NT hybrid materials

To fabricate FET-type glucose biosensor, the GOx, which was used as the glucose capture probe, was anchored on the RGO/C−PPy NTs via a chemical coupling reaction. Using the FET-type sensor with V_G = – 0.1 V, the real-time response to glucose in varying concentrations was characterized, as shown in Figure 25(c). The modulation of I_{SD} was recored in response to the variation of the glucose concentration in the solution. The normalized change in the current, i.e., $\Delta I_{SD}/I_0 = (I_{SD}–I_0)/I_0$, where I_0 is the initial current and I_{SD} is the measured current following stabilization after changing the glucose concentration., was used to determine the sensitivity. The sensor showed an increase in I_{SD} in response to a gradual increase in the concentration of glucose, indicating that the accumulation of *p*-type charge carriers at the surface of the RGO/C−PPy NT hybrids occurred. The GOx catalyzes the oxidation of glucose according to the following reaction: ß-D-glucose + O_2 + H_2O → d-glucono-1,5-lactone + H_2O_2. To clarify the mechanism of the FET-type glucose sensor, a sensing test has been carried out with various concentrations of H_2O_2, as shown in Figure 26. A similar trend to the response to glucose was observed in the sensing behavior. Thus, H_2O_2 induces indirect *p*-type doping effects, which result from the direct transfer of electrons via oxidative reactions between the graphene

and C−PPy backbone.

The FET-type biosensor, based on the RGO/C−PPy NT hybrids, exhibited very sensitive responses to glucose, with a detection limit of approximately 1 nM (S/N = 3.22). When S/N ≥ 3.0, this signal is generally considered as an useful signal. With a glucose concentration of 100 pM, S/N = 0.89 was found, which is not considered to be a significant signal.[76] (See Figure 27) Thus, the limitation of detection is determined at 1 nM. This result is 2–3 orders of magnitude more sensitive than previously reported glucose sensors. In contrast, the FET-type biosensor based on C−PPy NTs with GOx enzymes showed a detection limit of about 100 mM (with S/N = 3.08). The sensing device based on the C−PPy NTs without GOx enzymes could not display any variation in I_{SD} following a change in the glucose concentration. This result clearly shows that the GOx is essential for glucose detection.

The reasons for the enhanced performance of the sensor based on the RGO/C−PPy NT hybrids are as follows: first, an enhanced response to glucose occurred because of the increased surface area, which allowed more binding sites to become available, and second, the enhanced *p*-type semiconductor behavior led to improved signal transduction. Figure 25(d) shows the calibration curve. When the glucose concentration increased, stronger signals were detected. In all measurements, the FET sensors had response times of less

than 1 s. The reproducibility and storage stability of the hybrid FET sensors were also evaluated. The response of the glucose sensor did not change appreciably after 50 repeated experiments, indicating good reproducibility, as shown in Figure 28(a). The storage stability was assessed in air. After one month of storage, the FET sensor detected 1 nM of glucose, as shown in Figure 28(b), with no change in the response relative to that of a freshly prepared sensor. This result is considered that the highly coupling interaction between C−PPy NTs and enzyme via covalent bond induces physically and chemically stable environment in the liquid and/or air.

The specificity of the response to glucose was evaluated by real-time monitoring of I_{SD} in various solutions containing compounds found in biological fluids, including uric acid (UA), and ascorbic acid (AA), as shown in Figure 25(e). The real-time responses were detected in response to injecting 0.1-M PBS, 100-μM UA, 100-μM AA, and 1-μM glucose solutions. A remarkable increase in the current occurred when glucose was injected, even at far lower concentrations than the other compounds in the analyte. Exposure of the sensors to UA and AA did not significantly change the charge density on the surface of the RGO/C−PPy NTs relative to the changes observed upon exposure to glucose. These results clearly demonstrate specificity towards glucose.

To evaluate the application of the biosensor for the determination of the concentration of glucose in real samples, solutions were prepared. (1.0 mL real sample was added into 4.0 mL 0.1 M PBS solution) The fabricated biosensing device, in this work, showed high agreement with measured commercial glucose detector, as shown in Table 2. This result showed the biosensing device had a great potential for practical application.

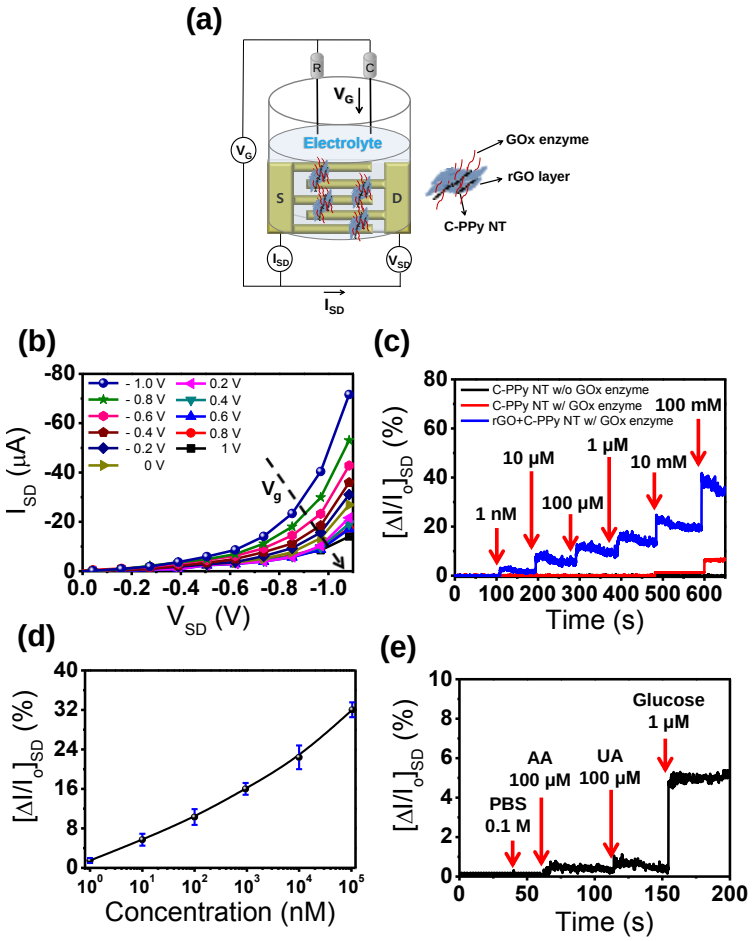

Figure 25. (a) A schematic diagram showing the liquid-ion-gated FET-type sensor, with a Ag/AgCl reference electrode, labeled R, platinum counter electrode, labeled C, and source and drain electrodes, labeled S and D. (b) The source–drain current of the biosensors as a function of V_{SD} at various values of V_G in the range from –1.0 to +1.0 V. (c) The real-time responses and (d) a calibration curve for glucose biosensor with and without the GOx enzyme, which were measured at V_{SD} = 10 mV and V_G = – 0.1 V, with glucose concentrations of 1 nM to 100 mM. (e) The real-time response to PBS, AA, UA, and glucose solutions.

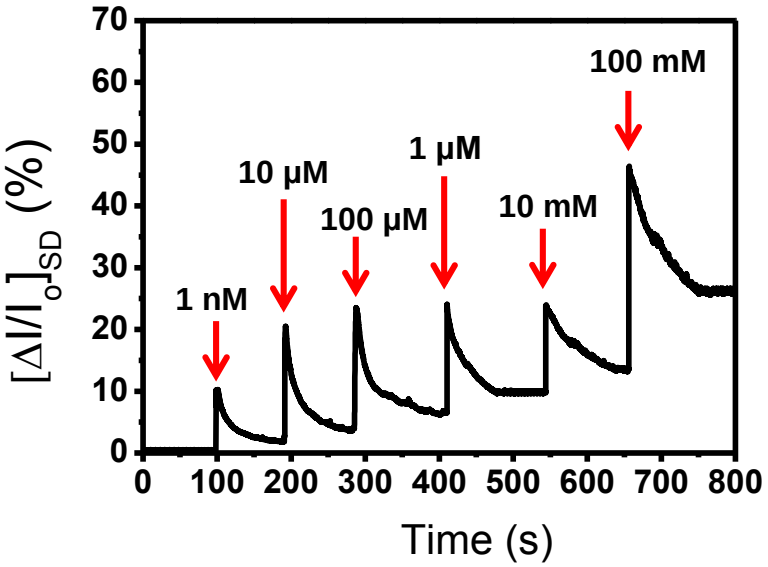

Figure 26. Real-time responses to exposure to H_2O_2 based on rGO/C-PPy NTs with GOD aptamer measured at V_{SD} = 10 mV and V_G = – 0.1 V, with H_2O_2 concentrations in the range 1–100 mM.

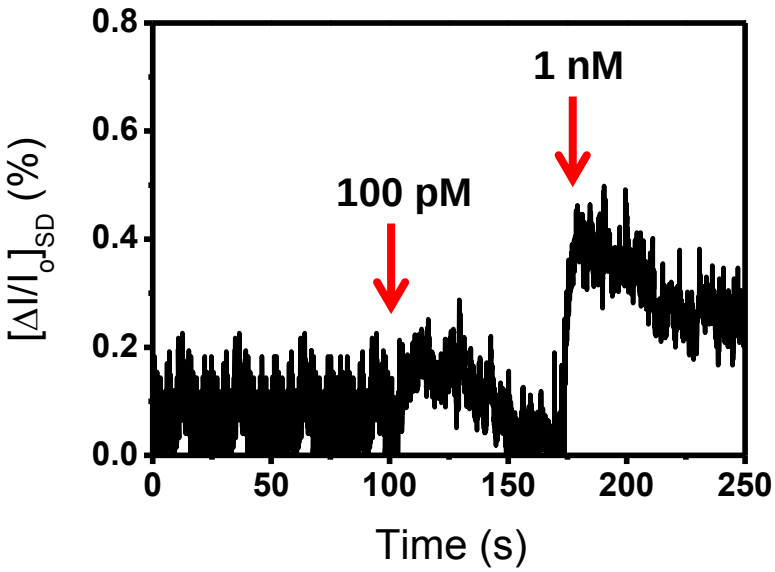

Figure 27. The real-time responses towards glucose of the rGO/C-PPy NTs measured at V_{SD} = 10 mV and V_G = – 0.1 V, with glucose concentrations of 100 pM and 1 nM.

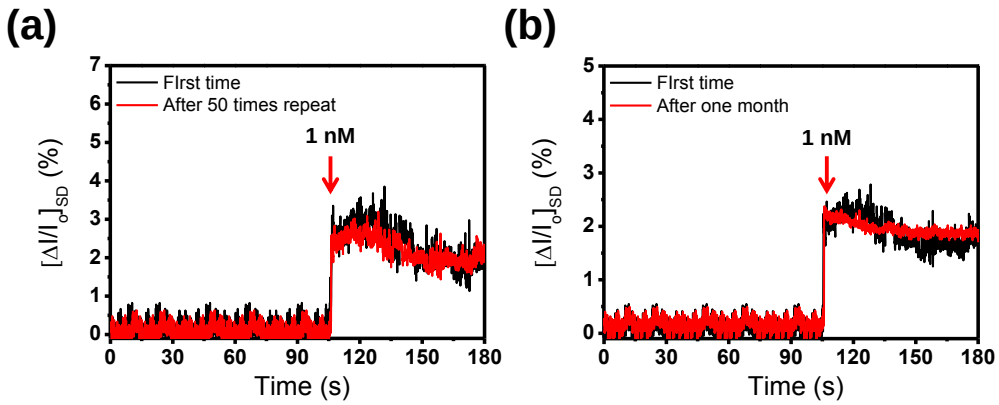

Figure 28. The real-time response of the rGO/C-PPy NTs hybrid FET-based biosensor (a) after 50 repetitions, and (b) after one month. Both datasets were measured with at V_{SD} = 10 mV and V_G = – 0.1 V, and with a glucose concentration of 1 nM.

Table 2**.** Determination of glucose concentration in real samples using the biosensors.

Real sample	Biosensor (mM)	Home blood glucose meter (mM)	Relative error
Human serum	10.92	10.6	2.93 %
Bovine serum	5.76	5.6	2.78 %
Horse serum	9.76	9.44	3.27 %

3.3. Fabrication of reduced graphene oxide-polyfuran nanohybrid for High-performance Hg^{2+} FET-type sensors

3.3.1. Fabrication of RGO/PF NT hybrid materials

A schematic diagram of the synthesis of graphene–PF NT hybrids was shown in Figure 29. First, self-degradation method was used to synthesize PF NTs. Then, PF NTs were anchored to the GO surface through π–π intermolecular interactions. Reduction process by using hydrazine was then conducted, and the prepared RGO–PF NTs were prufied several times with distilled water. Finally, the product was obtained by centrifugal precipitation and dried in a vacuum oven at 25℃. SEM and TEM were used to characterize the morphology of the RGO–PF NT hybrids. The SEM and TEM images of the PF NTs displays that the iameter of the tubes was approximately 70 nm, as shown in Figure 30(a). A cross-sectional SEM image of the RGO sheet was observed, which was a structure resemebling paper with porous spaces. (See Figure 30(b)) Figure 30(c) and (d) exhibit cross-sectional SEM and TEM images of the RGO–PF NT hybrid materials. The PF NTs were well coupled on the large surface area of the graphene sheets. The structure of the PF NTs was highly organized and compacted with the RGO sheets. These results were deduced that the RGO–PF NT hybrids were stable, and the stability was due to the strong π–π interactions between the RGO layers and PF NTs.

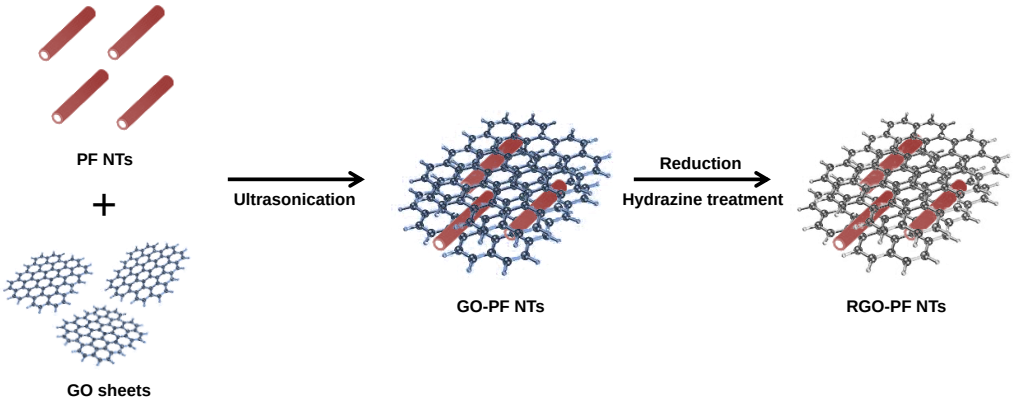

Figure 29. The schematic illustration of the synthesis of rGO-PF NT hybrids.

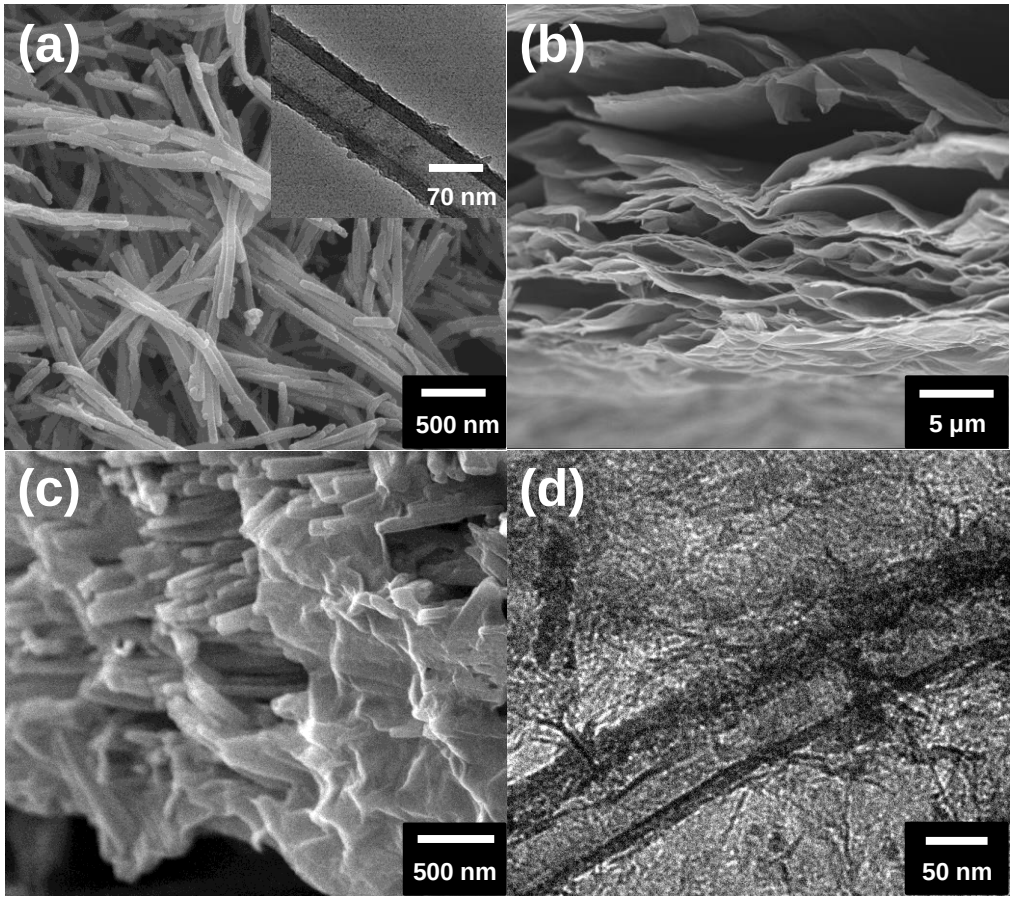

Figure 30. (a) SEM image of PF NTs; the inset is a TEM image. Cross-sectional SEM images of (b) rGO layers and (c) rGO-PF NTs. (d) TEM image of rGO/PF NTs.

To gain insight into the structure of the graphene–PF NT composites, Raman spectroscopy was carried out, and the resulting spectra are shown in Figure 31(a). The Raman spectrum of GO contained D peaks at 1364 cm^{-1} and G peaks at 1610 cm^{-1}. The Raman spectrum of the RGO exhibited two prominent bands at 1343 cm^{-1} and 1592 cm^{-1}, which correspond to D and G bands. The ratio of the D band to G band (I_d/I_G) was minimally greater than that of GO, suggesting that the reduction process induced defects or edge areas in the RGO sheets. The Raman spectrum of PF NTs contained a C=C backbone stretching peak at ~ 1590 cm^{-1} and a PF ring stretching peak at 1410 cm^{-1}. The Raman spectrum of the RGO–PF NT hybrids exhibited increased intensity of the band around 1350 cm^{-1}, indicating an interaction between PF and the RGO sheets.

The structure of the RGO–PF NTs was further studied using XRD and ATR-FTIR spectroscopy, as shown in Figure 31(b) and (c). The XRD diffractograms of GO contained a very sharp peak at 10.1° (d = 8.75 Å), which indicated that the structure of the original graphite was successfully oxidized to form GO. A broad peak appeared at 24.8° (d = 3.59 Å), which implied that RGO formation was achieved by hydrazine reduction of GO. The graphene–PF NT hybrids contained a broad peak at approximately 25.3° (d = 3.52 Å), which corresponded to the furan intermolecular distance between the RGO–PF NTs. This result suggested that the PF NTs and the RGO sheet formed a composite

via π–π interactions.

GO exhibited characteristic oxide absorption bands, including the C=O stretching peak at 1733 cm^{-1}, the vibrational and deformation peaks of O-H groups at 3391 cm^{-1} and 1417 cm^{-1}, and the C-O (alkoyl) stretching peak at 1037 cm^{-1} (see Figure 31(c). Most of the peaks related to oxygen-containing functional groups vanished in the FTIR spectrum of RGO, thus indicating that the reduction of GO was successful. The spectrum of the RGO–PF NT composite material contained characteristic furan ring and graphene fundamental vibrations: 1598 cm^{-1} (C=C stretching); 1512 and 1498 cm^{-1} (C-C stretching); 1026 and 1001 cm^{-1} (C-O-C plane deformation); and 1149, 1096, and 1052 cm^{-1} (C-H bending and stretching).[23–25] The peaks in the spectrum of the RGO–PF NT composites were shifted compared with those of the separate PF NTs and RGO spectra due to interactions between the RGO layers and PF NTs.

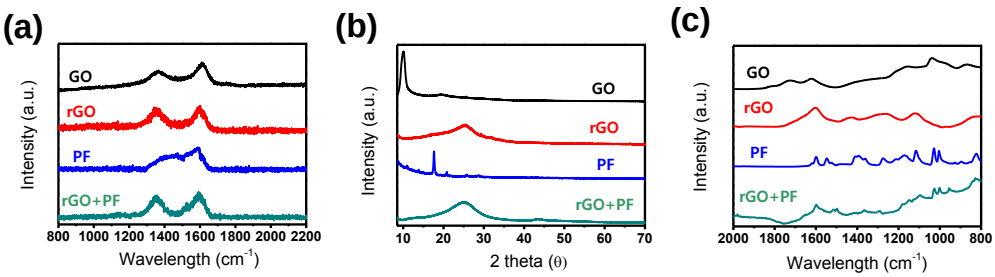

Figure 31. (a) Raman, (b) X-ray diffraction patterns, and (c) ATR-FT-IR spectra of GO, rGO, PF, and rGO+PF NT hybrids.

3.3.2. Electrical performance of RGO/PF NT hybrid materials

Measuring current–voltage (*I–V*) curves was used to characterize the electrical properties of the RGO, PF NTs, and RGO–PF NT hybrid materials on the patterned electrode substrate. Figure 32(a) shows linear *I–V* curves over a range of –0.6 V to +0.6 V, which means that Ohmic contacts were formed between samples and the gold electrodes. The conductivity of the RGO–PF NT hybrid was higher than that of RGO and PF NTs. This result proposed that RGO–PF NT hybrids exhibited effective electron transport between the PF NTs and the RGO, resulting in a decrease in the resistance. Despite excellent electrical properties of RGO sheet, the conductivity was highly anisotropic, and interlayer electron transport was slow. However, the PF NTs acted as conductive channels to connect the RGO layers, resulting in enhanced conductivity. To study the electrical characteristics of the RGO–PF NT conductive channels, we measured the source–drain current–voltage (I_{SD}–V_{SD}) characteristics of liquid-ion-gated transistors under various gate biases. For these measurements, V_g was varied from –1.0 V to +0.6 V in steps of 0.2 V, with a gate voltage sweep rate of 0.2 Vs^{-1}; the devices were in a phosphate-buffered saline (PBS) solution (pH 7.4), as shown in Figure 32(b). I_{SD} increased when a larger negative gate bias was applied, which is typical of *p*-channel transistors. Thus, the current in the device was attributable to hole transport and

that the modulation of I_{SD} resulted from control over the hole carrier density at the surface of the RGO–PF NT composites. PF NTs exhibited *p*-type semiconductor behavior (see Figure 33). Although unaltered graphene exhibits ambipolar properties in electrical devices, the graphene samples used herein exhibited hole-transporting behavior due to the absorption of oxygen and/or water from air to yield RGO–PF NT composites that behaved as enhanced *p*-type systems.[79] This behavior, in turn, results in higher stability and improved sensing performance relative to that of the individual components alone.

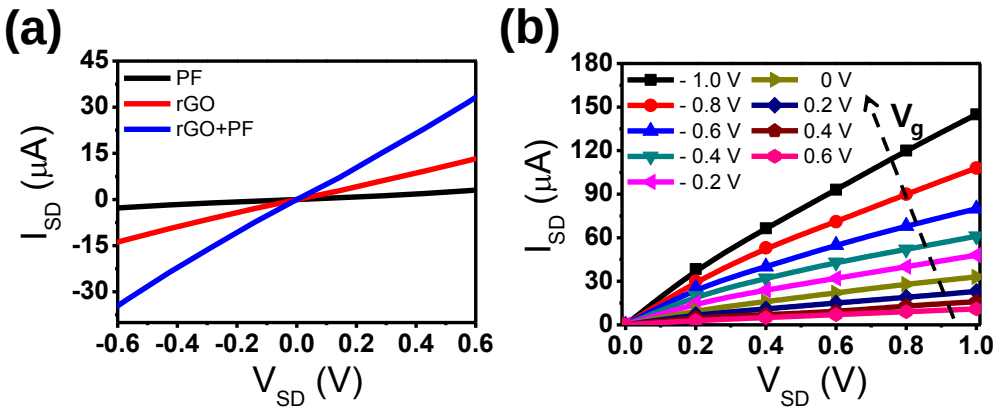

Figure 32. (a) Current−voltage (I−V) curves of PF NTs, rGO, and rGO-PF NT hybrids and (b) rGO-PF NT composites at V_g from –1.0 to +0.6 V in 0.2-V steps (Vsd: 0 to 1.0 V in 0.2-V steps).

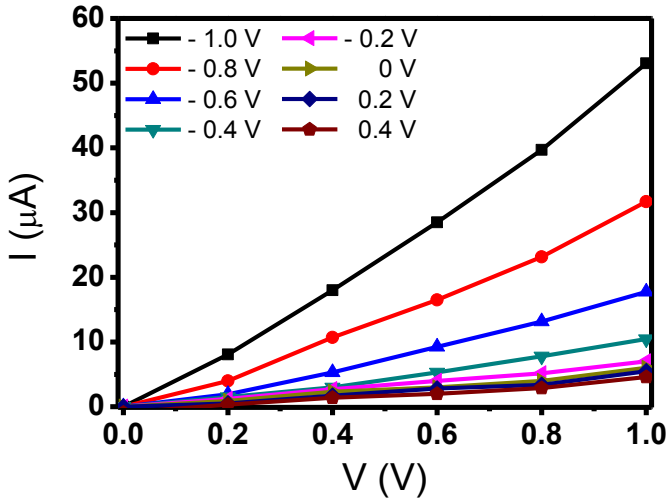

Figure 33. PF NTs at V_g from −1.0 to 0.4 V in 0.2-V steps (Vsd: 0 to 1.0 V in 0.2-V steps).

3.3.3. FET-type Hg^{2+} biosensor based on RGO/PF NT hybrid materials

Liquid-ion-gated FETs were fabricated and immersed in PBS electrolyte at pH 7.4, as shown in Figure 34(a). A remote electrode in the surrounding electrolyte provided good contact between the RGO–PF NT composites and the solution. This strategy enhanced the sensitivity via signal amplification. Using the FET-type sensor as a *p*-channel FET (with V_g = – 0.1 V), the real-time response to Hg^{2+} at various concentrations was observed. The lone-pair electrons on the oxygen atom of furan bind to the Hg^{2+}. As shown in Figure 34(b), the changes in I_{SD} were measured in response to variations in the Hg^{2+} concentration in the solution. The sensitivity was determined from the normalized change in the current $\Delta I_{SD}/I_0 = (I_{SD}–I_0)/I_0$, where I_0 is the initial current and I_{SD} is the measured real-time current following stabilization after adding the Hg^{2+} ion. The I_{SD} of the sensor increased in response to a gradual increase in the concentration of Hg^{2+}, which occurred due to the accumulation of *p*-type charge carriers at the surface of the RGO–PF NT hybrids. Moreover, the real-time responses of the FET-type Hg sensor were rapid (on a time scale of less than 1 s), and instantaneous signal changes were observed over a wide range of Hg^{2+} ion concentrations (10 pM to 100 nM).

The RGO–PF NT composites exhibited very sensitive responses to Hg,

with a detection limit of approximately 10 pM [signal-to-noise (S/N) ratio = 3.12]. Typically, S/N ratios of ≥ 3.0 are considered sufficiently high to indicate a significant signal. As shown in Figure 35, the S/N ratio at the 1 pM level was only 0.89 and thus too low to obtain a reliable signal measurement.[79] Thus, 10 pM is determined to be the detection limit in this system. On the other hand, the FET-type sensor based on PF NTs exhibited a detection limit of about 100 nM (S/N = 3.28). No change in the current after adding the Hg^{2+} was observed for the sensing device based on RGO material alone, thereby indicating that the PF functional groups are critical to sensing performance. Enhanced performance in the sensor based on the RGO–PF NT composites was attributed to the following: (i) an efficient response to Hg^{2+} occurred due to the enhanced surface area and conductivity on the RGO–PF NT hybrid materials, and (ii) the enhanced *p*-type semiconductor behavior improved signal transduction. Figure 4c shows the calibration curve; stronger signals were detected when the Hg^{2+} concentration increased. In all measurements, the FET sensors had rapid response times of less than 1 s and exhibited linear responses to current changes.

The selectivity of the RGO–PF NTs toward Hg^{2+} was evaluated using real-time monitoring of I_{SD} in the presence of various interfering metal ions (e. g., Zn^{2+}, Ce^{2+}, Na^{+}, Ni^{2+}, Pb^{2+}, Cu^{2+}, Co^{2+}, and Li^{+}), as shown in Figure 36. A

remarkable increase in the current was observed when Hg^{2+} ions were injected, even at far lower concentrations (two orders of magnitude) than the other compounds in the analyte (see Figure 34(d)). Exposure to other metal ions did not significantly alter the charge density on the surface of the RGO–PF NTs relative to the changes observed upon exposure to Hg^{2+}, because RGO–PF NTs have a greater binding affinity for Hg^{2+} than for the other metal ions.

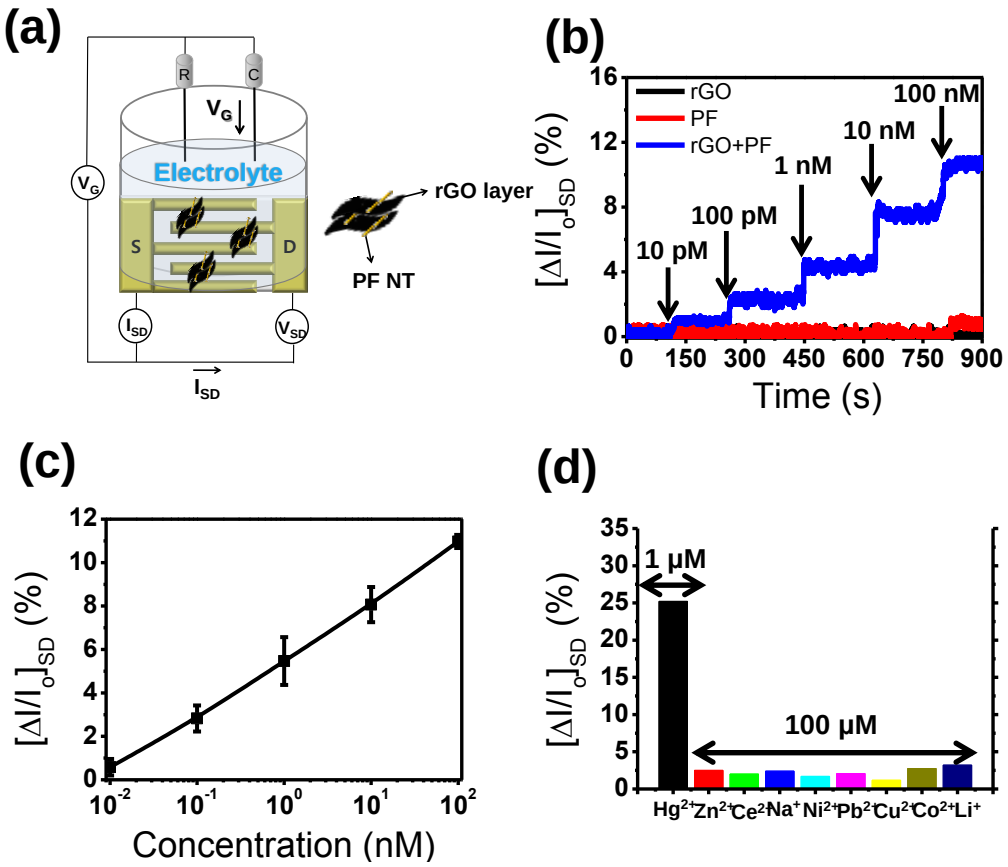

Figure 34. (a) A liquid-ion-gated FET-type sensor based on rGO-PF NTs. (Ag/AgCl reference electrode, R; platinum counter electrode, C; source and drain electrodes, S and D) (b) Real-time responses and (c) a calibration curve for Hg^{2+} based on rGO, PF NTs; rGO-PF NT composites were measured at Vsd = 10 mV (V_g = – 0.1 V) with Hg^{2+} concentrations of 10 pM to 100 nM. (d) A histogram of the sensitivity of the rGO-PF NT composites to Hg^{2+}, Zn^{2+}, Ce^{2+}, Na^{+}, Ni^{2+}, Pb^{2+}, Cu^{2+}, Co^{2+}, Li^{+}.

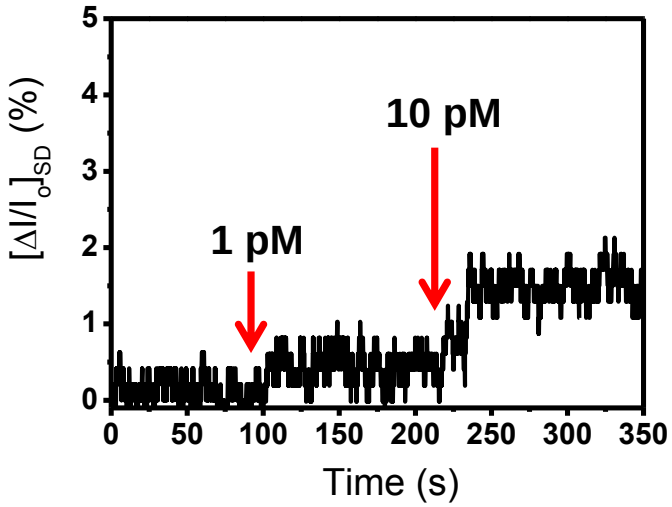

Figure 35. Real-time responses for Hg^{2+} sensor based on rGO-PF NT composites measured at V_{sd} = 10 mV (V_g = - 0.1 V) with a Hg^{2+} concentration of 1 pM to 10 pM.

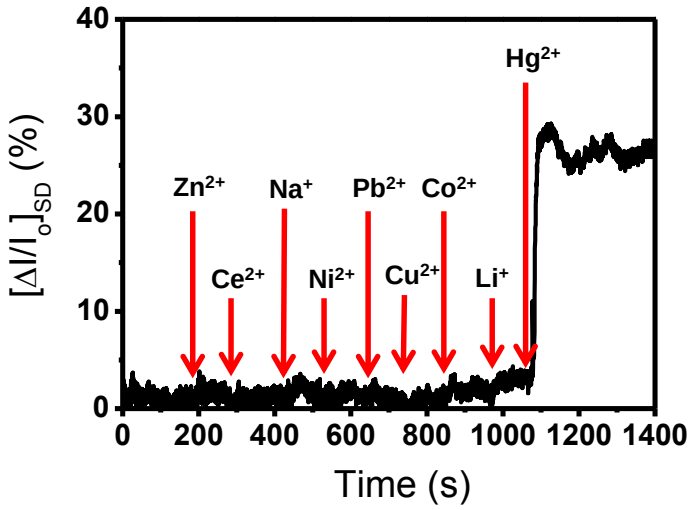

Figure 36. Real-time responses to Zn^{2+}, Ce^{2+}, Na^{+}, Ni^{2+}, Pb^{2+}, Cu^{2+}, Co^{2+}, Li^{+}, and Hg^{2+} measured at V_{SD}= 10 mV (V_g = - 0.1 V).

Table 3. Comparison of the mercury sensing performance of various sensor type devices.

Electrode materials	Sensor type	Sensitivity (μM)	Reference
CNT	Vapor	1	[180]
Ni/Au NHs	Vapor	0.1	[181]
PPy/Pd NHs	Vapor	1	[182]
CNT/Au NPs	Vapor	0.002	[183]
rGO/PF NHs	LE FET	0.000001	In this work

CNT = Carbon nanotube, NP = Nanoparticle, LE FET = Liquid electrolyte field effect transistor, NH = Nanohybrid

3.4. Fabrication of graphene/polyselenophene nanohybrid materials for highly sensitive and selective chemiresistive sensor

3.4.1. Fabrication of RGO/PSe nanohybrid materials

The morphology of the RGO/PSe nanohybrid material was characterized using FE-SEM and TEM. The FE-SEM images of RGO and RGO/PSe nanocomposites are shown in Figure 36(b) and (c). A rougher surface on the RGO/PSe nanocomposits than on the RGO sheets was observed, indicating that the PSe was coated onto the RGO layer. The morphology of the as-synthesized materials was confirmed using TEM. (See the insets of Figure 37(b) and (c).) The PSe was highly coupled to the graphene sheets, enabling the original morphology of the graphene sheets to be maintained. Scanning transmission electron microscopy (STEM) was conducted to obtain additional structural information about the graphene–PSe nanohybrid material. (See Figure 37(d)) Elemental analysis (Figure 36(e) and (f)) indicated uniform distribution of C and Se. (The greater intensity of the elemental C signal compared with that of Se was attributed to the fact that the TEM sample grid was C based.)

For greater insight into the structure of the RGO/PSe nanocomposites, Raman spectroscopy was carried out, as shown in Figure 38(a). The Raman spectrum of GO exhibited D peaks at 1364 cm^{-1}, and G peaks at 1610 cm^{-1}. On the other hand, the Raman spectrum of the RGO showed two prominent bands,

at 1356 cm^{-1} and 1602 cm^{-1}, corresponding to the D and G bands, respectively. These results clearly indicated perfect reduction of GO to RGO. The Raman spectrum of PSe exhibited C=C backbone stretching at ~1609 cm^{-1} and a ring stretching mode at 1372 cm^{-1}. The Raman spectrum of the RGO/PSe nanocomposites exhibited increased band intensity around 1357 cm^{-1}, indicating an interaction between PSe and the RGO sheets.

XRD patterns and ATR-FTIR were also conducted for structural analysis of graphene–PSe nanocomposites, as shown in Figure 38(b) and (c). The XRD pattern of GO exhibited a very sharp peak at 10.1° (d = 8.75 Å), indicating that the original graphite was successfully oxidized to form GO. A broad peak appeared at 24.8° (d = 3.59 Å), suggesting that RGO formation was achieved by reduction of GO using hydrazine. The RGO/PSe nanohybrids exhibited a broad peak at around 25.0° (d = 3.56), which corresponded to the PSe intermolecular distance in the RGO/PSe nanocomposites. This result is deduced that the PSe was successfully coated on the RGO layer via strong intermolecular π–π interactions.

ATR-FTIR spectra of the GO displayed characteristic absorption bands for oxide groups, including a C=O stretching peak at 1733 cm^{-1}, vibration and deformation peaks associated with O–H groups at 3391 cm^{-1} and 1417 cm^{-1}, respectively, and a C–O (alkoyl) stretching peak at 1037 cm^{-1} as shown in

Figure 38(c). Most of the peaks related to oxygen-containing functional groups were not evident in the FTIR spectra of RGO, indicating that the reduction of GO was successful. The spectra of the RGO/PSe nanohybrids exhibited characteristic bands for a selenophene ring and graphene fundamental vibrations, which occurred at 1624 cm^{-1} (C=C stretching), 1557 cm^{-1} (C–C stretching), 1196 cm^{-1} (C–Se stretching), and 1012 cm^{-1} (C–H deformation). [81] The RGO/PSe nanocomposite peaks were shifted compared with those of isolated PSe and RGO due to interactions between the RGO layers and PSe. Overall, the spectra indicated that the PSe materials were successfully coated onto the surface of the RGO layer.

The surface of RGO/PSe nanohybrids was further characterized by X-ray photoelectron spectroscopy (XPS), as shown in Figure 39. The XPS survey scan spectrum exhibited the principal C 1s, O 1s, Se 3d, and Cl 2p core levels, without any evidence of impurities. The O 1s peak was attributed to physisorbed oxygen on the RGO/PSe nanonetworks, even after reduction GO. Cl atoms doped the RGO/PSe nanocomposites during oxidation polymerization of the selenophene monomer, as confirmed by the Cl 2p XPS profiles. Therefore, the RGO/PSe nanohybrid material was successfully synthesized and characterized.

To quantify the amount of PSe in the rGO/PSe nanohybrid materials,

thermogravimetric analysis (TGA) analysis was carried out under air flow. Figure 40 shows the TGA curve of the rGO-PSe nanocomposites with thos of PSe and rGO when heated from 20 to 800 ℃ at a rate of 20 ℃/min under air flow. The PSe showed a 90.72 % weight loss at temperatures between 82 and 800 ℃ due to the evaporation of adsorbed water and decomposition of oligomers and the main backbone of PSe. There is around 8.9 wt% oxidant remaining. While the graphene powder displayed 12.6 % weight loss throughout the temperature range used for this experiment, the rGO-PSe nanohybrids exhibited a 32.79 % weight loss from 100 to 800 ℃, corresponding to the burning of PSe. Thus, it can be calculated that the weight percentage of PSe in this nanohybrids is 20.19 wt%.

To further evaluate the increased electrochemical properties, we conducted Brunauer−Emmett−Teller (BET) surface area measurements. (See Figure 41) Nitrogen isotherm adsorption measurement on the as-prepared PSe, rGO, and rGO/PSe nanocomposites revealed that graphene−PSe nanohybrids had a BET surface area of 95.06 $m^2 g^{-1}$, which was higher than that observed for pure PSe (19.57 $m^2 g^{-1}$) and rGO (63.5 $m^2 g^{-1}$). These results suggested that the rGO sheet served as a conductive channel, leading to enhanced conductivity (See Figure 42) and enlarged surface area.

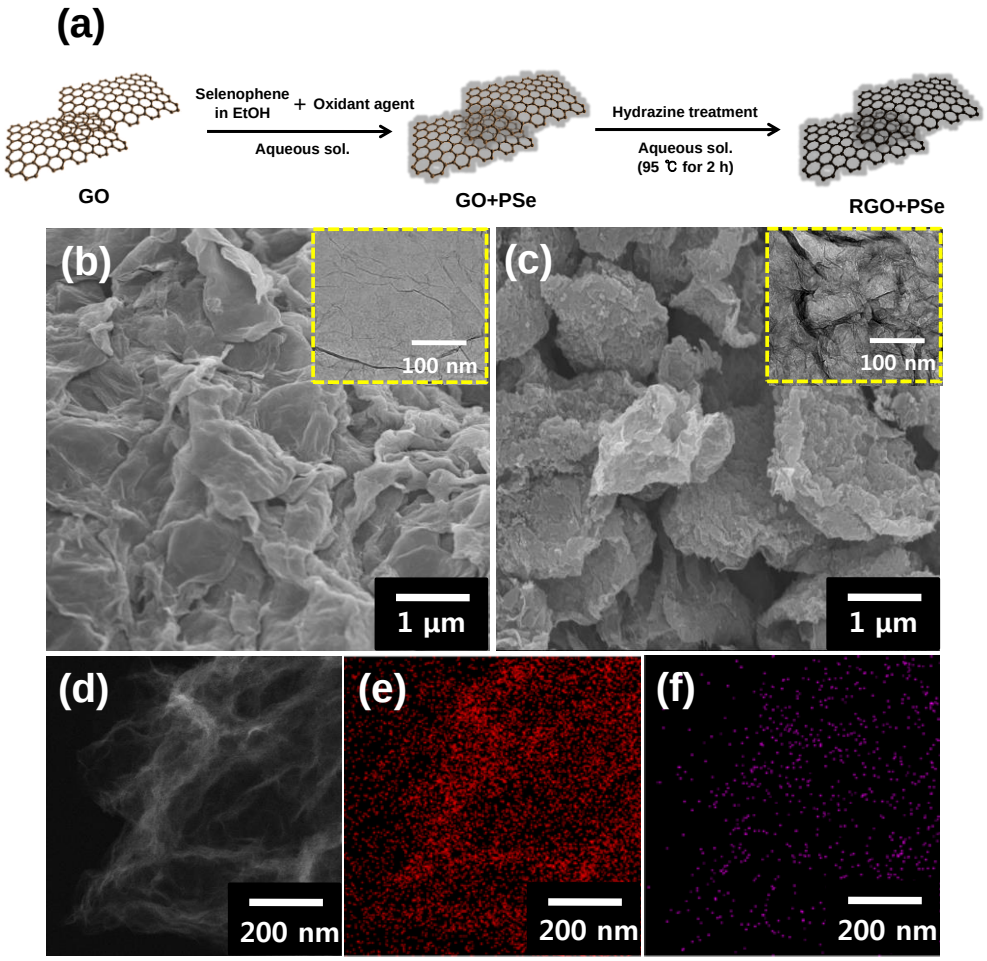

Figure 37. (a) Schematic illustration of the preparation of graphene–PSe nanocomposites. FE-SEM images of (b) rGO and (c) rGO/PSe nanocomposites. (Insets are the TEM images of rGO and rGO/PSe nanohybrid materials.) (d) Typical STEM image of graphene–PSe nanohybrids. Corresponding elemental mapping images of (e) C and (f) Se.

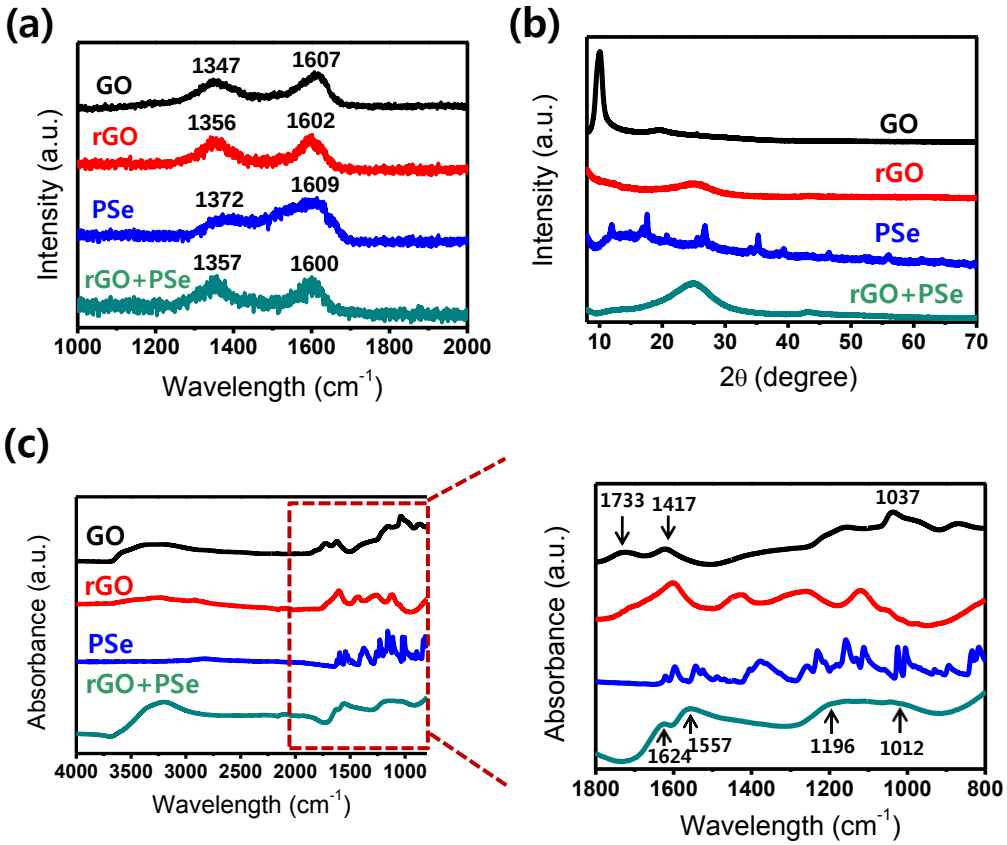

Figure 38. (a) Raman spectroscopy, (b) XRD patterns, and (c) ATR-FTIR spectra of GO, rGO, PSe, and rGO/PSe nanohybrids.

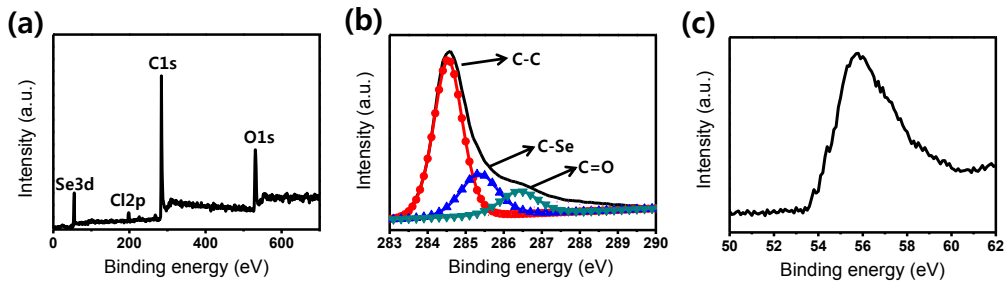

Figure 39. (a) Overall, (b) C 1s, and (c) Se 3d XPS profiles of rGO/PSe nanohybrids.

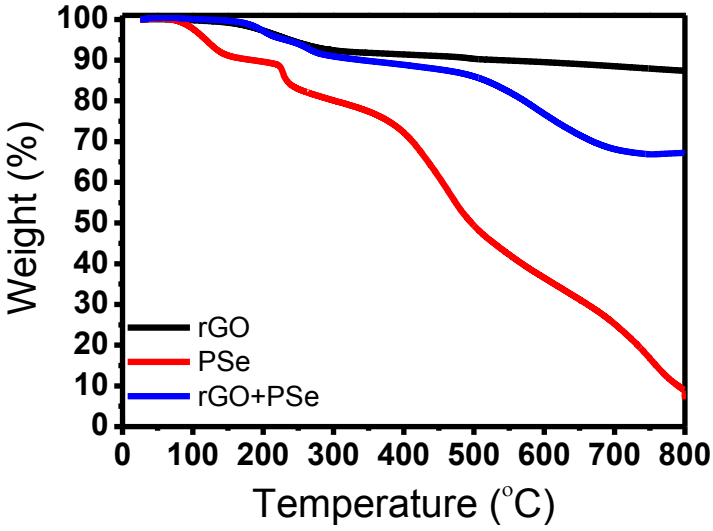

Figure 40. TGA curves of rGO, PSe, and rGO-PSe nanohybrid materials.

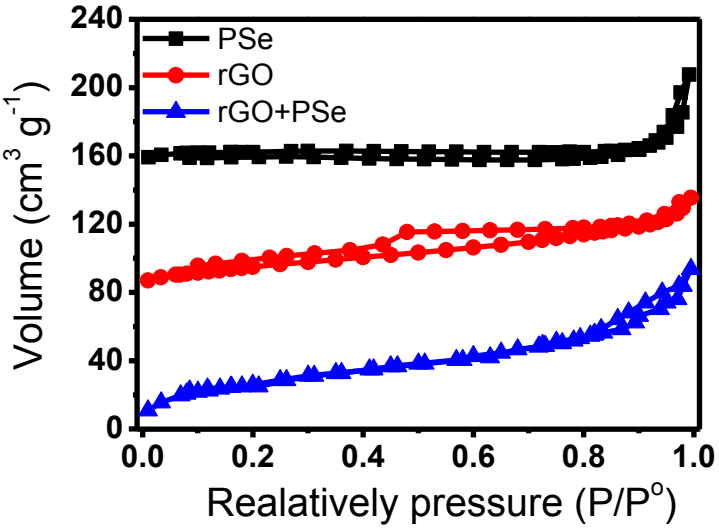

Figure 41. N_2 adsorption/desorption isotherms of PSe, rGO, and rGO/PSe nanohybrids.

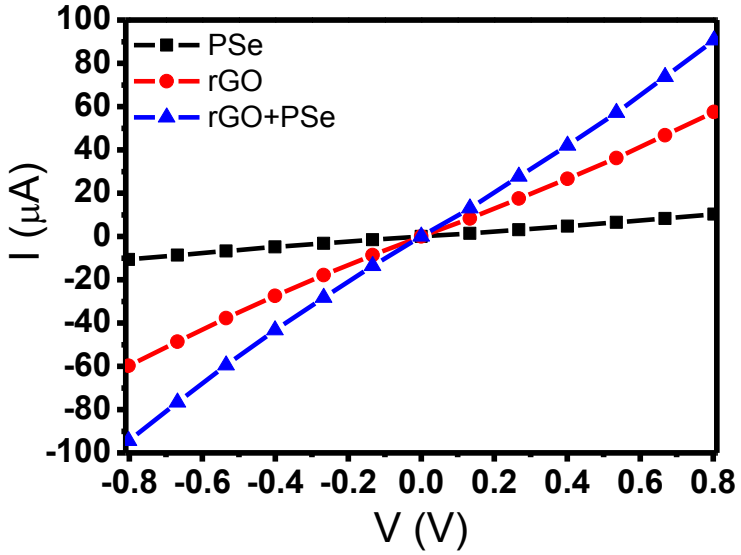

Figure 42. Current−voltage ($I-V$) curves of PSe, RGO, and RGO−PSe nanohybrid materials.

3.4.2. Fabrication of chemiresistive sensor based on RGO/PSe nanohybrid materials

RGO/PSe nanohbrid inks in chlroform solution were prepared and introduced on to the PET film by using screen printing method, as shown in Figure 43(a). Consecutively, building source and drain electrodes (PT, 100 nm) were pattered on the RGO/Pse film through shadow mask sputtering method. The optical microscopy images of RGO/PSe nanohybrid films were observed before and after Pt coated process, as shown in Figure 43(b) and (c). The resistance changes on the as-prepared electrode based on the RGO/PSe nanohybrid was measured via a source-meter connected to a computer. The chemiresistive sensor based on the RGO/PSe nanohybrid was placed in a vacuum chamber with a vapor inlet/outlet pressure of 100 Torr. Various concentrations of NH_3 (0.01–10 ppm), MeOH (1–100 ppm), and other organic gases were injected into the chamber using a mass flow controller (MFC, KNH Instruments). The real-time responses from the RGO/PSe nanohbyrid were systematically appraised by normalized resistance changes ($\triangle R/R_0$). The normalized resistance change ($\triangle R/R_0$) of the RGO/PSe based sensor was monitored in real-time during exposure to various gases at a constant applied current (10^{-6} A) until saturation was reached. $\triangle R/R_0$ of the RGO/PSe nanohybrid is given by the following equation:

$\Delta R/R_0 = (R - R_0)/R_0$ (1)

where R_0 is the initial resistance and R is themeasured real-time resistance, respectively.

After the RGO/PSe nanohybrids were exposed to various concentrations of NH_3 or MeOH gas for several minutes, the gas vapor was then replaced by compressed air to remove any molecules attached to the nanomaterials. This process was repeated several times. Vapor/air was supplied at various concentrate ranging from 2 to 8 slm and 1 to 5 sccm, as controlled by the MFC.

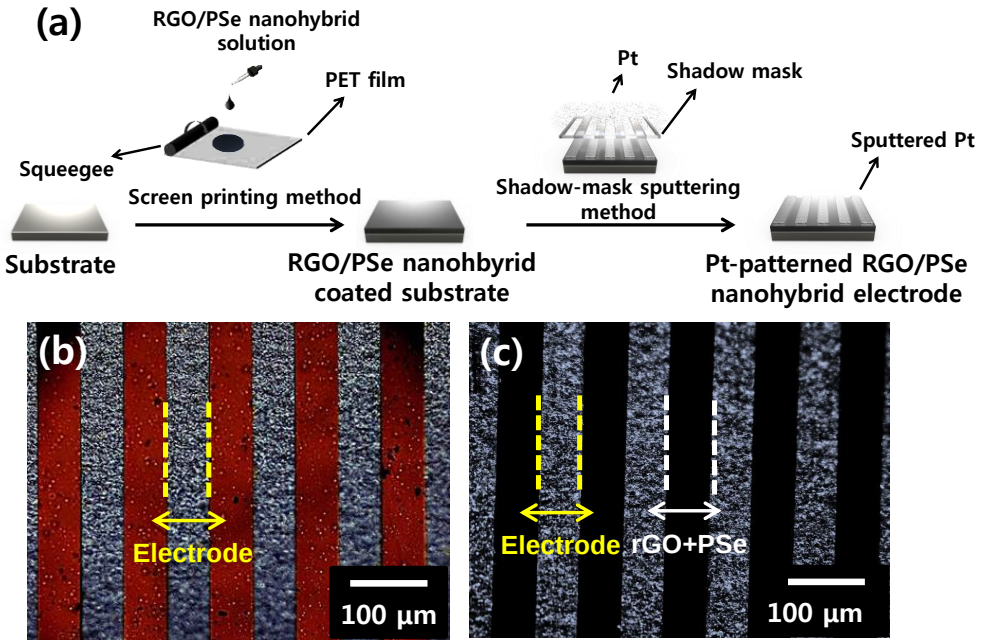

Figure 43. (a) Schematic illustration of RGO/PSe nanohybrid chemiresistive electrode. Optical microscopic images of fabricated electrode (b) before and (c) after RGO/PSe nanohybrid material coataing process.

3.4.3. Chemiresistive sensing performance of the RGO/PSe nanohybrid film

To investigate the sensing performance of the RGO/PSe nanohybrids, their electrical response (resistance changes) was recorded in real-time during exposure to various gases. When the chemiresistive sensor based on the RGO/PSe nanohybrid was exposed to various gases at room temperature, excellent sensitivity and rapid response/recovery times were observed. Figure 44(a) exhibits the response upon exposure to NH_3 and MeOH vapor as a function of analyte concentration. In particular, the sensing performance of devices based on the graphene nanohybird materials depends on the charge carrier density. The responses upon exposed gas molecules enable to change the charge carrier density in the RGO/PSe nanohbyrid structure. The electrical responses of the RGO/PSe nanohybrid sensor were different behavior for the two gases tested. The resistance increased after exposure to NH_3 and decreased after exposure to MeOH. This result proposes that the introduction of electron-donating molecules (NH_3) into the RGO/PSe nanohybrid backbone (p-type transducer) decreased the charge carrier density (hole density) via a redox reaction, resulting in the enhanced resistance of the transducer. In contrast, the electron-acceptor MeOH created new holes in the RGO/PSe nanohbyrid structure, leading to the opposite result. The limitation detection level (LDL) of

the RGO/PSe nanohybrid gas sensor was 0.01 and 1 ppm for NH_3 and MeOH, respectively. The LDL of both gases was within specifications offered by the Occupational Safety and Health Administration (NH_3: 25 ppm; MeOH: 200 ppm). The enhanced surface area of the RGO/PSe nanohybrids enabled not only fast diffusion of the analyte gas molecules for rapid response times, but also improved sensitivity compared with pure PSe nanomaterial, owing to the synergetic effects of RGO/PSe nanohybirds, leading to the increased the interaction between the target analyte and the nanohybrid material. To test the reproducibility and reversibility of the sensing performance, the electrical response of the chemiresistive sensor based on the RGO/PSe nanohybrid was monitored upon periodic exposure to 10 ppm of NH_3 and 100 ppm of MeOH at room temperature, as shown in Figure 44(b). The PSe nanomaterial displayed similar responses for both NH_3 and MeOH compared with the RGO/PSe nanohybrid material. Moreover, this gas sensor had excellent cycle stability (Figure 44(c)). Figure 44(d) exhibits the calibration curve of the sensor as a function of NH_3 and MeOH gas concentrations. The normalized resistance change was nearly zero at 0 ppm. At low concentrations (<1 ppm), the chemiresistive sensor displayed a nonlinear change in sensitivity. On the other hand, linear behavior was monitored over the concentration ranges of 0.01–0.1 ppm for NH_3 and 1–100 ppm for MeOH. Therefore, RGO/PSe nanohybrids can

be efficiently used for detecting NH_3 and MeOH gases of various concentrations. In addition, Figure 45 shows the sensitivity of RGO/PSe nanohybrids to several representative VOCs and toxic gases at 10 ppm. RGO/PSe nanohybrids showed remarkable signal changes in the presence of all of the selected gases evaluated except for hexane. Among all gases tested, the sensitivity and selectivity were greatest for NH_3. In addition, the LDL of NH_3 was 10–10^3 times higher than that of other gases.

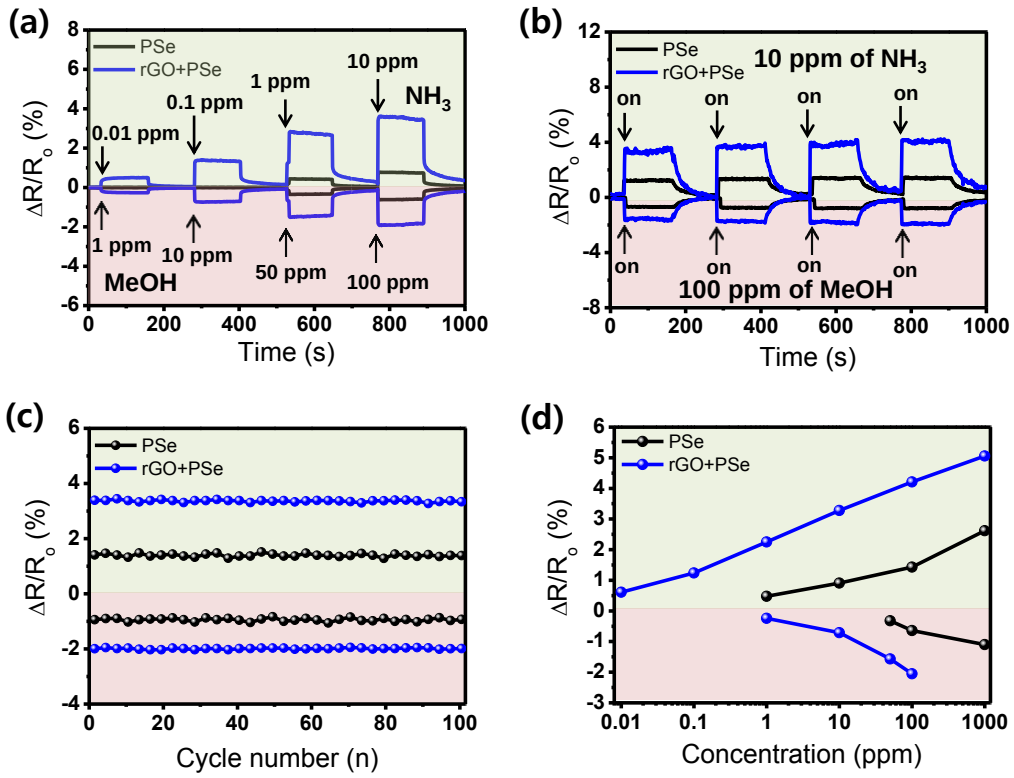

Figure 44. (a) Real-time responses of PSe and RGO/PSe nanohybrid materials upon sequential exposure to NH_3 (0.01 to 10 ppm) and MeOH (1 to 100 ppm). (b) Real-time responses of PSe and RGO/PSe nanohybrid materials on periodic exposure to 10 ppm of NH_3 and 100 ppm of MeOH. (c) Normalized resistance changes of PSe and RGO/PSe nanohybrids with periodic exposure to 10 ppm of NH_3 and 100 ppm of MeOH gases for 100 cycles. (d) Calibration curve of PSe and RGO/PSe nanohybrids as a function of NH_3 and MeOH concentration.

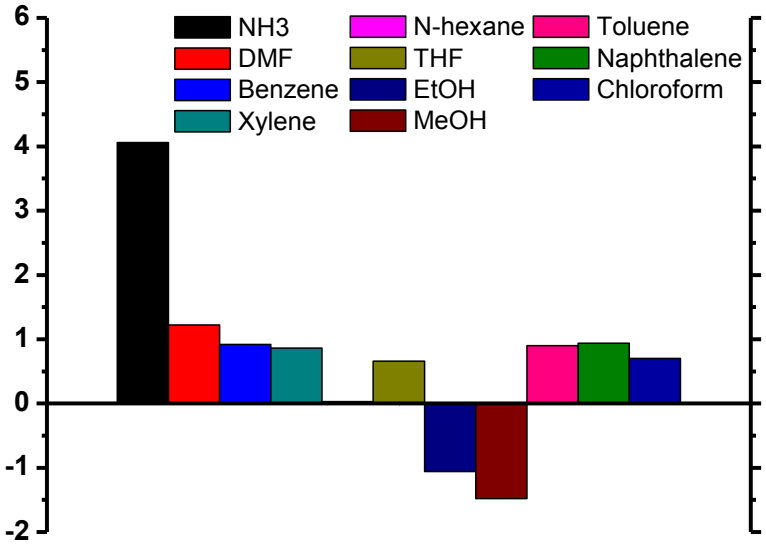

Figure 45. Sensing performance histrogram of RGO/PSe nanohybrid mateirals to 11 analytes: each analyte concentration was fixed at around 10 ppm.

3.5. Fabrication of graphene/free-standing nanofibrillar PEDOT/P(VDF-HFP) hybrid device for wearable and sensitive human motion detective piezo-resistive sensor

3.5.1. Fabrication of CVD graphene/free-standing nanofibrillar PEDOT/P(VDF-HFP) nanohbyrid devices

A schematic diagram of the fabrication process of the graphene/P(VDF-HFP)/V-PEDOT nanohybrid E-skin device was described, as shown in Figure 46. Single-layered graphene was synthesized on a copper foil substrate using CVD method. Then, a PMMA solution was poured and spin-coated (4000 rpm, 60 s) on the graphene film. Subsequently, the copper was removed by wet chemical etching process. A wet transfer method was used to transfer graphene on a flexible PDMS substrate. The PMMA was then removed using actone solution. The reason why PDMS was used is that this substrate has good flexibility, optical transparency, strength, and low weight.

To clearly understand the property of the graphene, atomic force microscopy (AFM) and HR-TEM were used. AFM showed the thickness of graphene to be 0.4 nm (Figure 47(a)) and HR-TEM proposed that it consisted of a single layer (Figure 47(b)). Figure 47(c) showed ultraviolet/visible (UV-Vis) spectra of a graphene film with dimensions in the range 400-800 nm. The optical transmittance measured following transfer of the graphene to the

flexible PDMS substrate, and was found to be 96.6% at 550 nm. The sheet resistance of the graphene was approximately 1 kΩ sq^{-1}. These results clearly indicate that CVD provides a monolayer of graphene.

The VDP process was conducted to vertically grow PEDOT nanofiber on the graphene surface. The resulting densely grown vertically aligned PEDOT islands on the graphene film were observed by FE-SEM, as shown in Figure 48(a) and (b). To clearly observe the formation of vertically growing PEDOT nanofibrillar deposition, SEM images according to vapor deposition reaction times were observed, as shown in Figure 49. Firstly, iron nanoparticles were formed on the surface of graphene. The iron/PEDOT nanofibers were clearly observed with increasing reaction time. After rinsing process was conducted several times, the optimized PEDOT islands were approximately 70 nm in diameter and 10 μm in length. Then, P(VDF-HFP) was deposited onto the V-PEDOT/graphene film by spin-coating at 3000 rpm for 60 s. To crystallize the P(VDF-HFP), the film was annealed at 150℃ for 2 h. The vertically aligned structure was preserved upon P(VDF-HFP) coating (See Figure 48(c)), suggesting that the structure was highly stable.

The properties of the graphene/V-PEDOT/P(VDF-HFP) nanohybrid film were compared to those of its component materials by Raman spectroscopy, as shown in Figure 50. The Raman spectrum of graphene exhibited G peak (at

~1600 cm^{-1}) and a 2D peak (at ~2700 cm^{-1}). This spectrum further confirms fabrication of single-layer graphene, as the 2D peak is sharper and more pronounced than the G peak. The Raman spectrum of PEDOT exhibited C=C backbone stretching peaks at 1541 cm^{-1} and 1573 cm^{-1}, symmetric C=C (–O) stretching at 1429 cm^{-1}, C–C stretching deformation at 1357 cm^{-1}, and a oxyethylene ring deformation feature at 988 cm^{-1}. The Raman spectrum of the P(VDF-HFP) exhibited peaks at 837 cm^{-1} and 910 cm^{-1}, indicating symmetric C–F_2 stretching of the crystalline beta phase.[184] The Raman spectrum of the graphene/V-PEDOT/P(VDF-HFP) nanohybrid film exhibited features of graphene and PEDOT, as well as P(VDF-HFP) fundamental vibrations, which were shifted compared with those of these materials in isolation due to interactions between them.

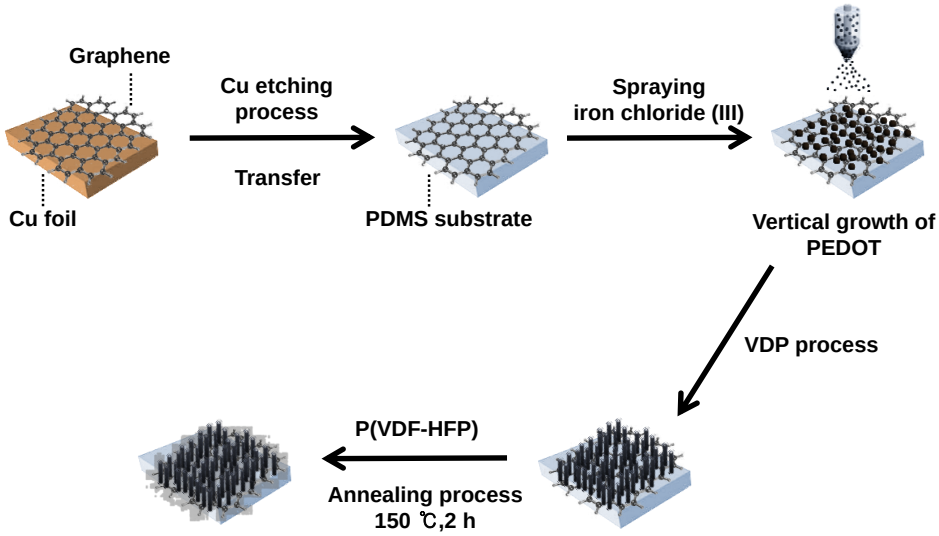

Figure 46. Schematic diagram showing the fabrication process of E-skin based on graphene/V-PEDOT/P(VDF-HFP) nanohybrid device.

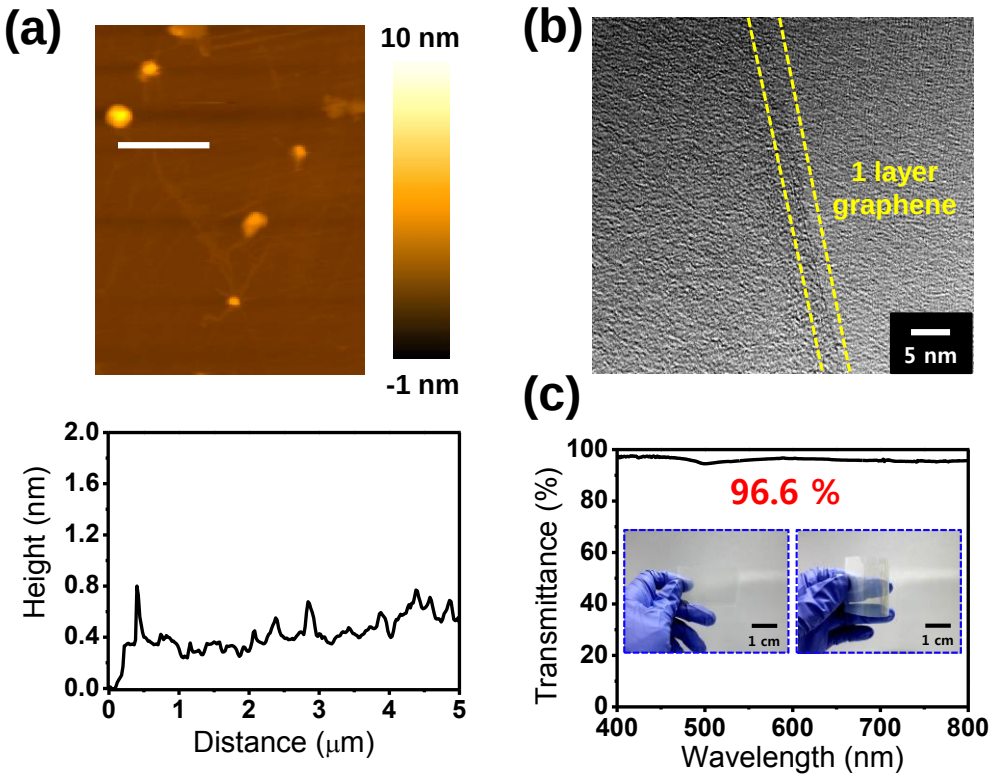

Figure 47. (a) AFM and (b) HR-TEM images of the single-layer graphene. (c) UV-Vis spectra of the graphene transferred onto the PDMS film. The inset shows a photograph of the flexible and transparent graphene film.

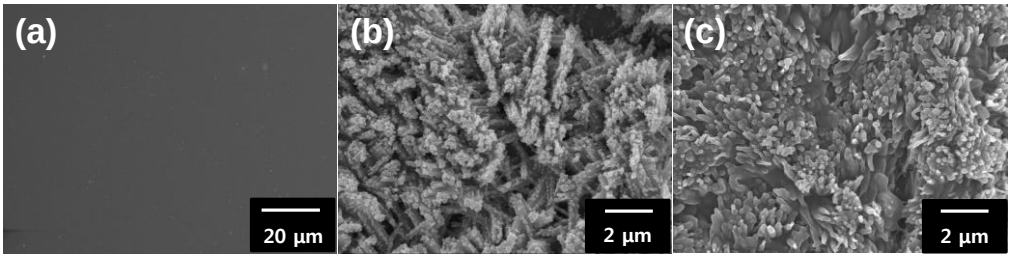

Figure 48. SEM image of the (a) graphene, (b) the vertically grown PEDOT (via VDP) nanofibers on the graphene, and (c) the fabricated P(VDF-HFP)/PEDOT/graphene films.

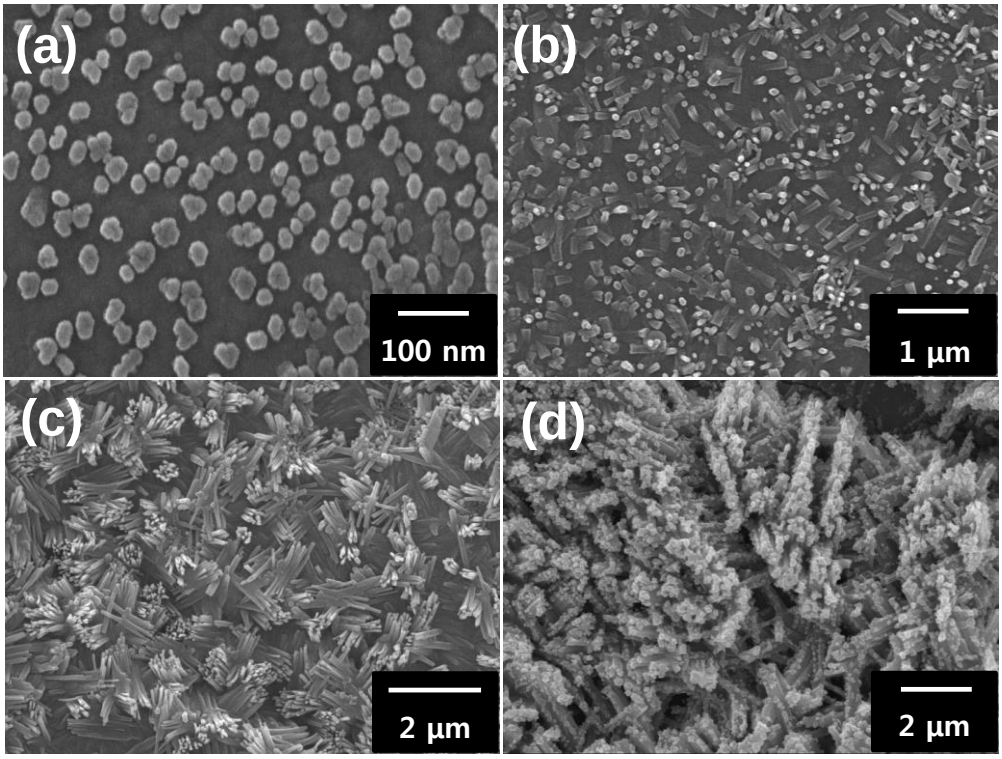

Figure 49. SEM images of V-PEDOT according to VDP reaction time (a) 0, (b) 15, (c) 30 min, and (d) 1h.

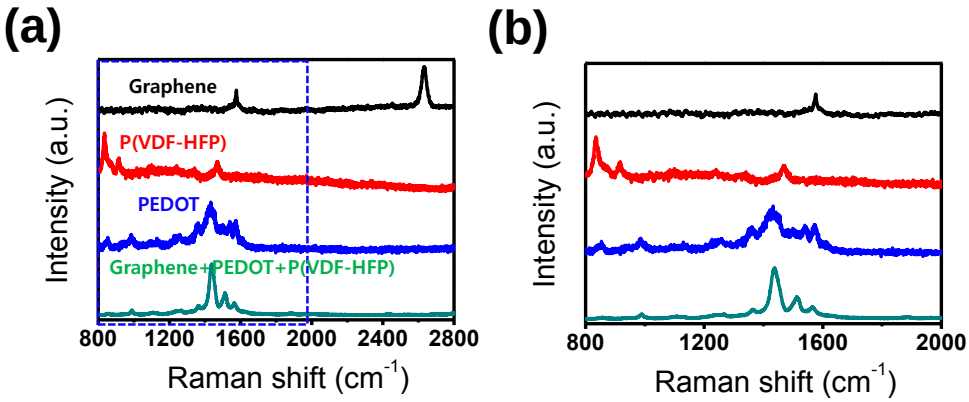

Figure 50. Raman spectra of graphene, P(VDF-HFP), PEDOT, and graphene/PEDOT/P(VDF-HFP) nanohybrid materials.

3.5.2. Sensing performance of E-skin device

The E-skin was constructed from two layers of graphene/V-PEDOT/P(VDF-HFP) films placed face to face, and Ag paste was placed at the edges of both films to form source and drain electrodes, as shown in Figure 51(a). The device's pressure response was first tested in real time by finger pressing. Then, response to pressure of varying force was tested. During these experiments, a thin glass slide (75×25 mm) was placed over the E-skin device to improve its stability. Signal (change in resistance) increased as the applied pressure increased from 5 to 30 Pa (See Figure 51(b)). The device's sensitivity was determined from the change in the resistance $\Delta R/R_0 = (R–R_0)/R_0$, where R_0 is the initial resistance and R is the measured real-time resistance following stabilization after application of pressure. The reason of change in E-skin resistance is a piezo-resistive effect, which may result from disturbances in conducting pathways, state changes in the nanohybrid material, or variation in tunneling effects between neighboring materials and the deformed graphene flakes. The detection limit of the fabricated novel E-skin was very low (0.5 Pa), indicating that it is almost 10-fold more sensitive than previous devices, as shown in Table 4. Interestingly, the piezo-resistivity of the graphene/V-PEDOT/P(VDF-HFP) nanohybrid device was larger than that of pure graphene or the graphene/P(VDF-HFP) device (See Figure 51(c)). To understand this

result, GF values of pure graphene, graphene/V-PEDOT, graphene/P(VDF-HFP), and graphene/V-PEDOT/P(VDF-HFP) nanohybrid devices were calculated, as shown in Figure 52. The GF was calculated according to:

$$GF = \frac{(R - R_o)}{R_o \times \varepsilon} \quad (1),$$

where R is resistance under mechanical strain, R_o is resistance without strain, and ε is mechanical strain.

With 0.2% tensile mechanical strain, the GF of each material was: pure graphene, 10,; graphene/V-PEDOT, 23; graphene/P(VDF-HFP), 34; and graphene/V-PEDOT/P(VDF-HFP), 67. With 2% tensile strain, the GF values were: pure graphene, 55; graphene/V-PEDOT, 83; graphene/P(VDF-HFP), 138; and graphene/V-PEDOT/P(VDF-HFP), 320. Interestingly, the GF of the graphene/V-PEDOT/P(VDF-HFP) nanohybrid device was up to sixfold greater than that of the simpler devices, suggesting that synergetic effects of the nanohybrid materials; i.e., enhanced piezo-resistive effect and contact area result in a large GF.

To test the electrical properties of the samples, current-voltage (*I-V*) curves were measured by using probe station (See Figure 53). In addition, the sheet resistance values of the samples were recoreded, as shown in Table 5. Firstly, the samples were fabricated on the gold patterned electrode substrate as the same method. Linear *I-V* curves were observed over a range of -0.6 V to +0.6

V. The conductivity of the graphene/V-PEDOT nanohybrid material was greater than that of the pure graphene, suggesting effective charge transport between the graphene and PEDOT. However, the graphene/V-PEDOT/P(VDF-HFP) nanohybrid device exhibited the smallest conductivity, which is attributed to the insulating properties of the P(VDF-HFP). Although the graphene/V-PEDOT/P(VDF-HFP) nanohybrid device showed reduced conductivity compared with graphene/V-PEDOT device, the high mechanical property of the P(VDF-HFP) maintains vertically grown PEDOT under strain stimulus, which leading to more durable, flexible, and stretchable character with large GF value.

Therefore, the graphene/V-PEDOT/P(VDF-HFP) nanohybrid E-skin device's highly sensitive strain-sensing behavior may be explained by the following factors: (i) the nano-scale vertically grown PEDOT provides increased contact surface area between the layers, (ii) the P(VDF-HFP) material reduces the number of conducting pathways, both of which lead to a larger strain-induced resistance change, and hence a larger GF, and (iii) high mechanical property of P(VDF-HFP) fixes free-standing PEDOT, responding more stable and sensible toward the pressure stimulus.

To investigate the pressure sensor's stability, its change in resistance was measured upon cyclic applied pressure of 30 Pa for more than 1,000 cycles at a

cycle length of 2 s (Figure 54). No defects or deterioration in performance were observed. This result indicates the E-skin device showed excellent stability and durability.

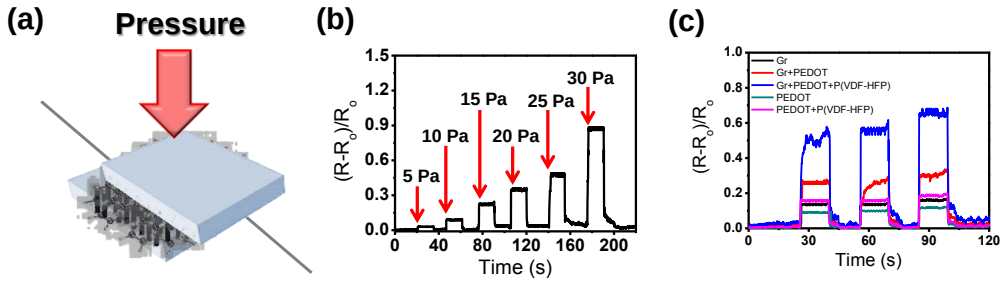

Figure 51. (a) Schematic diagram of the E-skin device. (b) Sensitivities to pressure with various stimuli. (c) Real-time change in resistance of the electronic skin devices as a function of the graphene, graphene/P(VDF-HFP), graphene/V-PEDOT/P(VDF-HFP), V-PEDOT, and V-PEDOT/P(VDF-HFP) material.

Table 4. Comparison between the detection limit performances of our flexible strain sensor and those of strain sensors based on other materials.

Material	GF	Ref
3D ZnO NW	3.5 kPa	185
Ag NPs	1 kPa	186
OFET	1 kPa	187
PT-coated polymer NFs	5 Pa	188
FE FET	2 Pa	189
ITO/PET film	3 Pa	190
Graphene/V-PEDOT/P(VDF-HFP) NC	0.5 Pa	This work

NW = Nanowire, NP = Nanoparticle, OFET = Oragnic Field-effect transistor, FE = Ferroelectret, NF = Nanofibre, NR = Nanoribbon, NC = Nanocomposite

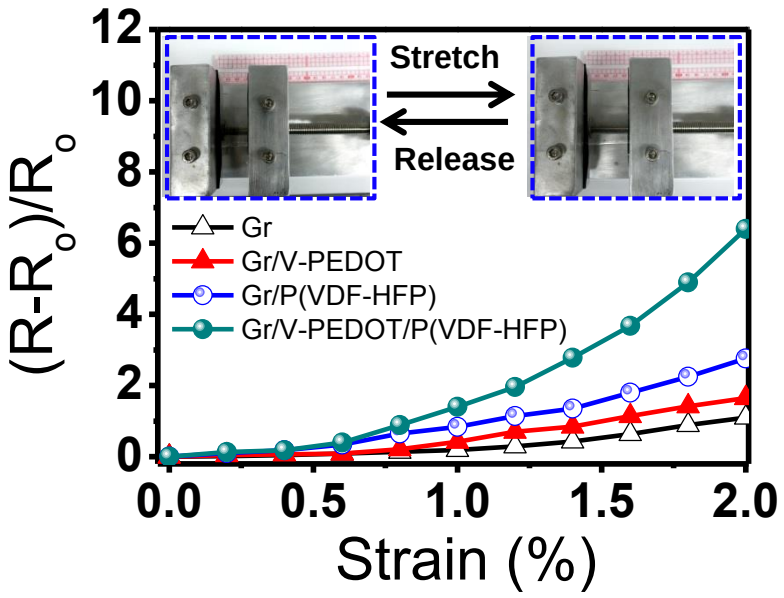

Figure 52. Resistance as a function of strain for graphene, graphene/V-PEDOT, graphene/P(VDF-HFP), and graphene/V-PEDOT/P(VDF-HFP) nanohybrid film.

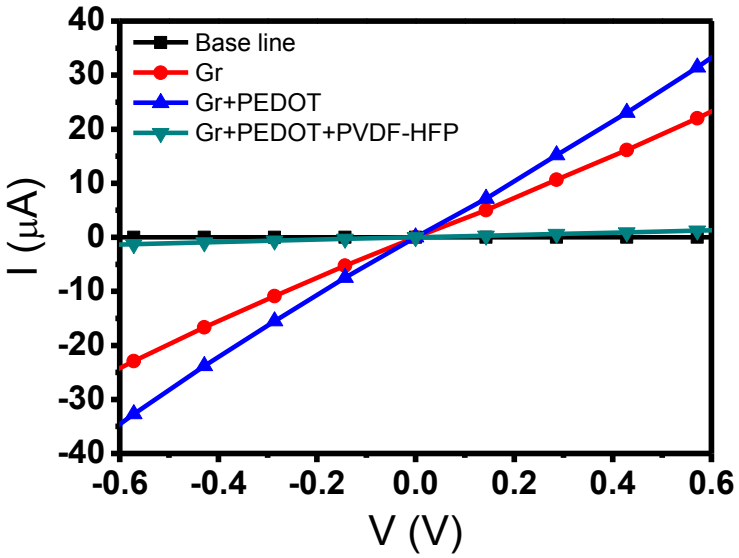

Figure 53. Current–voltage (*I*-*V*) curves of graphene, graphene/PEDOT, and graphene/PEDOT/P(VDF-HFP) nanohybrids.

Table 5. Comparison of the sheet resistance values based on graphene, graphene/V-PEDOT, and graphene/V-PEDOT/P(VDF-HFP) nanohybrids.

Samples	Resistance (kΩ)
Graphene	1.1
Graphene/V-PEDOT	0.43
Graphene/V-PEDOT/P(VDF-HFP)	4.5×10^2

Table 6. Comparison between the GF value of our E-skin device and those of strain sensors based on other materials

Material	GF	Ref
Single VO_2 NB	100	191
ZnO NW/PS film	116	192
ZnO – Paper NC	21.12	193
Graphene/PVDF NC	12.1	73
Polymer/CNT NC	117	195
Graphene/V-PEDOT/P(VDF-HFP) NC	320	This work

NB = Nanobeam, GF = Gauge factor, NW = Nanowire, PS = Polystyrene, NC = Nanocomposite, CNT = Carbon nanotube

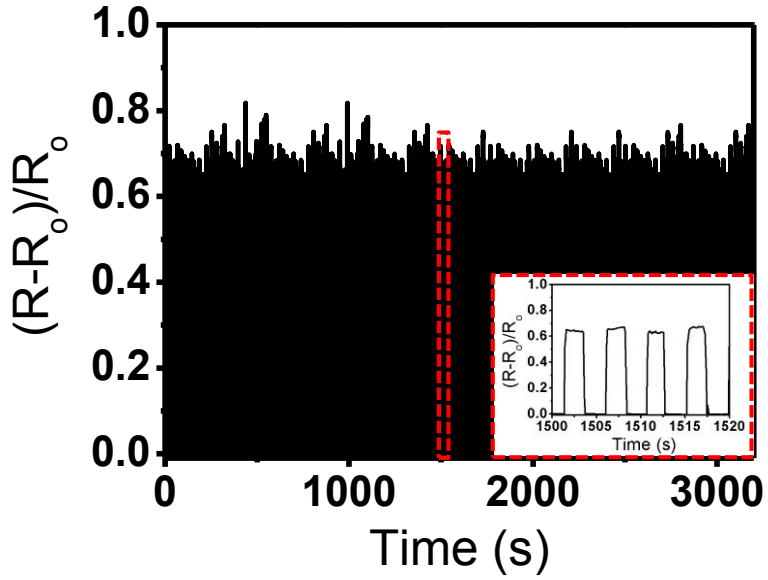

Figure 54. Real-time change in the resistance of the E-skin over more than 1000 loading cycles, with a cycle length of 2 s and an applied pressure of 30 Pa. The inset shows a magnified image in the red rectangular region.

3.5.3. Practical application of E-skin device

The GF value of graphene/V-PEDOT/P(VDF-HFP) nanohybrid E-skin device is much higher than that of other reported materials, as shown in Table 7. This extremely large GF value suggests that the device could detect very small strains associated with subtle motions, such as wrist pulse. Figure 55(a) exhibited the resistance change as a function of time in the wearable E-skin device during an *in situ* tensile test as the hand moved from an out-stretched to a clenched-fist position. The E-skin could provide an interesting and effective method for detecting human motion owing to ultra-sensitive and fast respond of the devices.

In modern medical practice, wrist pulse is an important indicator of arterial blood pressure and heart rate, providing useful information for non-invasive medical diagnosis. The E-skin fabricated, in this work, may be useful to measure wrist pulse in real time, as its rapid response (<1 s) gives sufficient resolution to measure pulse. Resistance change of the device as a function of time was observed when placed over the artery in the wrist reveals a pulse frequency of 75 bpm, as well as regular and repeatable pulse shapes (Figure 55(b)). This demonstrates potential biomedical applications.

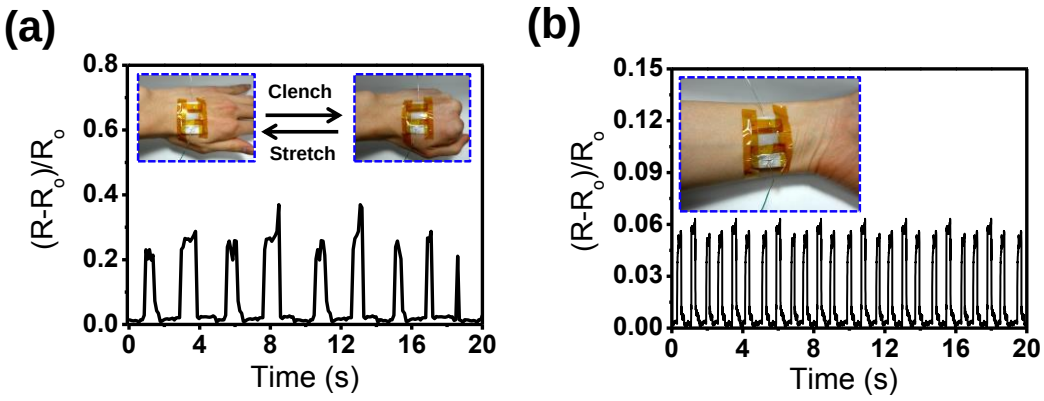

Figure 55. (a) Resistance as a function of time during motion of the hand from an outstretched to a clenched-fist position. (b) Resistance as a function of time while measuring the pulse in the wrist.

4. CONCLUSIONS

1. High sensitivity and specificity towards H_2O_2 using a liquid-ion-gated FET sensor based on RGO/PPy nanohybrid materials were demonstrated. Raman and ATR-FTIR spectroscopy were used for characterizing of the nanohybrid materials. The nanohybrid materials exhibited Ohmic contacts on the source and drain electrodes, which means the good contacts were formed between the materials and electordes. The FET devices based on the nanohybrid mateirals showed *p*-channel behavior, with excellent electrical conductivity. The fabricated FET devices exhibited *p*-channel behavior, with good electrical conductivity, and Ohmic contacts were formed with the source and drain electrodes. The fabricated FET devices were used in the biosensing applications, leading to a rapid response to changes in H_2O_2 concentration with a detection limit of 100 pM. These results are more attractive than those in previous reports for H_2O_2 biosensors. This FET-type biosensor displayed high reproducibility and stability in air condition. Furthermore, ultra-high sensitivity towards H_2O_2 was observed by testing the response of the biosensors in various biological fulids, such as UA, AA, and glucose. From the perspective of sensor performance, these FET-type biosensors based on RGO/PPy NTs may be utilized in environmental and food applications as alternative detecting methods of H_2O_2.

2. A liquid-ion-gated FET sensor based on RGO/C−PPy NT hybrid materials demonstrated high sensitivity and specificity with a rapid response time towards glucose. RAMAN, ATR-FTIR spectroscopy, and XRD were used for characterizing of the synthesized RGO/C−PPy NT hybrid materials. The synthesized nanohybrid mateirals showed synergetic effects of graphene and C−PPy NTs, such as enhanced conductivity and surface area. The FET devices based on the RGO/C−PPy NT hybrid materials display *p*-type semiconducting behavior. The fabricated FET-type biosensor showed a rapid response to electrical changes in glucose concentration with a detection limit of 1 nM (signal-to-noise = 3.22). These results are more attractive and 2–3 orders more sensible than those of previous reports of electrochemical biosensors for glucose detection. The fabricated biosensor had excellent reproducibility and stability in the air or liquid phases. In addition, high specificity towards glucose was demonstrated by testing the response of the biosensor in biological fluids containing UA and AA. These FET-type biosensors based on RGO/C-PPy NTs may be potential utilized as medical diagnosis, diabetes management, bioprocess monitoring, the beverage industry and environmental fields.

3. Liquid-ion-gated FET-type sensor based on the RGO–PF NTs was demonstrated for highly sensitive and selective Hg^{2+} detection. Interestingly, the synthesized RGO–PF NT hybrid materials bound specifically to Hg^{2+} ions

in the various metal ion mixed solution. The fabricated FET-type biosensor showed a rapid response (< 1 s) to electrical changes in Hg^{2+} concentration with a detection limit of 1 pM (signal-to-noise = 3.12). The fabricated biosensor showed excellent reproducibility and stability in the air/liquid phases. Furthermore, high specificity towards Hg^{2+} was demonstrated in real-time experiments in versatile metal ion solution. These FET-type sensors based on RGO–PF NTs could be potentially useful methods for the detection of Hg.

4. A new class of graphene–PSe nanohybrid materials were successfully synthesized and characterized for use as high-performance chemiresistive sensor application. The graphene–PSe nanohybrid materials were synthesized via a simple and facile *in situ* method. The synthesized nanohybrid materials showed the unique properties of both graphene and conducting polymers, such as high conductivity, excellent mechanical properties, and high surface area, which enhanced charge transport behavior and surface area, resulting in increasing the intereaction with the target analyte. These results were regarded as synergitic effects between the graphene and PSe materials. To the best of our knowledge, this is the first demonstration using in the chemiresistive sensing application based on graphene−PSe nanohybrid materials. The synthesized RGO/PSe nanohybrid materials were highly sensitive to various hazardous gases, especially NH_3 gas. The RGO/PSe nanohybrid gas sensor exhibited 10–

100 times greater sensing ability to various gases than that of pristine PSe sensor. In particular, RGO/PSe nanohybrid materials showed 0.01 ppm for NH_3 as limit of detection, which was higher than that observed for other chemical sensor decvice systems. Therefore, this research demonstrated an efficient method to fabricate graphene−PSe nanohybrid materials for use in high performance chemical sensors.

5. A new class of ultra-sensitive E-skin device using a graphene/V−PEDOT/P(VDF−HFP) nanohybrid material was successfully fabricated and developed. CVD method was used for fabrication of single-layer graphene, and nanofibrillar PEDOT was vertically grown on the graphene via vapor polymerization method. The uniform and well-aligned PEDOT nanofibers were clearly monitored by using experimental tool, such as FE-SEM. After deposition of P(VDF−HFP) material on the PEDOT nanofiber structure, the morphology of the PEDOT maintained, which means that the nanohbyrid materials was physically and chemically stable. This E-skin device based on graphene/V−PEDOT/P(VDF−HFP) nanohybrid materials showed werable and flexible properties, detecting strain or stretch with high sensitivity with fast response time, and good stability and durability. The E-skin had very large GF values: 320 at 2% tensile strain and 67 at 0.2% tensile strain, leading to the pressure detection limit was 0.5 Pa. These results are far more sensible and

higher value than those of other previous reports. Furthermore, monitoring human physiological signals, such as real-time monitoring wrist pulse, was demonstrated, suggesting utility for individual-centered health monitoring.

In summary, graphene/CP nanohybrid materials have been fabricated using in-situ polymerization and reduction from GO methods. These approaches were simple, facile, and possible to synthesize the uniform sheets based on the graphene/CP nanocomposites. Graphene/CP nanohybrid materials showed synergitic effects, including enhanced surface area, conductivity, and rapid charge carrier (electron or hole) transporting behavior, leading to high performance sensing performances. This strategy, using graphene/CP nanohybrid materials in the sensor application, may offer new opportunities of theoretical studies, as well as figure out the parameters determining performance of sensing devices. Thus, these findings were used not only general sensing devices, inlcuidng chemical/biological sensors, but also E-skin, such as pressure or strain sensors. Furthermore, this strategy, using graphene/CP nanohybrid materials in the sensor application, may offer new opportunities of theoretical studies, as well as figure out the parameters determining performance of sensing devices. Therefore, the graphene/CP nanohybrid materials have been successfully synthesized and utilized as various signal transducers in sensor platforms, suggesting that these materials could be potentially useful in many new types of applications related to electronic/optoelectronic devices, such as actuators, catalytic supports, energy storage/conversion, and drug delivery systems.

References

[1] M. R. Abidian, D. H. Kim, D. C. Martin, Advanced Materials 2006, 18, 405.

[2] R. Gangopadhyay, A. De, Chemistry of Materials 2000, 12, 608.

[3] M. Gratzel, Nature 2001, 414, 338.

[4] L. Groenendaal, F. Jonas, D. Freitag, H. Pielartzik, J. R. Reynolds, Advanced Materials 2000, 12, 481.

[5] A. Malinauskas, Polymer 2001, 42, 3957.

[6] N. Nuraje, K. Su, N.-l. Yang, H. Matsui, ACS Nano 2008, 2, 502.

[7] M. R. Arcila-Velez, M. E. Roberts, Chemistry of Materials 2014, 26, 1601.

[8] W. He, G. Li, S. Zhang, Y. Wei, J. Wang, Q. Li, X. Zhang, ACS Nano 2015, 9, 4244.

[9] A. T. Lawal, S. B. Adeloju, Biosensors and Bioelectronics 2013, 40, 377.

[10] H. C. Kang, K. E. Geckeler, Polymer 2000, 41, 6931.

[11] S. Kirchmeyer, K. Reuter, Journal of Materials Chemistry 2005, 15, 2077.

[12] B. Wei, J. Liu, L. Ouyang, C.-C. Kuo, D. C. Martin, ACS Applied Materials & Interfaces 2015, 7, 15388.

[13] H. Hlaing, X. Lu, C.-Y. Nam, B. M. Ocko, Small 2012, 8, 3443.

[14] F. C. Krebs, S. A. Gevorgyan, J. Alstrup, Journal of Materials Chemistry 2009, 19, 5442.

[15] S. Kirchmeyer, K. Reuter, Journal of Materials Chemistry 2005, 15, 2077.

[16] H. Hlaing, X. Lu, C.-Y. Nam, B. M. Ocko, Small 2012, 8, 3443.

[17] J. Ouyang, C. W. Chu, F. C. Chen, Q. Xu, Y. Yang, Advanced Functional Materials 2005, 15, 203.

[18] M. Vosgueritchian, D. J. Lipomi, Z. Bao, Advanced Functional Materials 2012, 22, 421.

[19] C. Li, H. Bai, G. Shi, Chemical Society Reviews 2009, 38, 2397.

[20] S. Nambiar, J. T. W. Yeow, Biosensors and Bioelectronics 2011, 26, 1825.

[21] J. Sekine, S.-C. Luo, S. Wang, B. Zhu, H.-R. Tseng, H.-h. Yu, Advanced Materials 2011, 23, 4788.

[22] R. J. Tseng, J. Huang, J. Ouyang, R. B. Kaner, Yang, Nano Letters 2005, 5, 1077.

[23] C. C. Ferron, M. C. R. Delgado, O. Gidron, S. Sharma, D. Sheberla, Y. Sheynin, M. Bendikov, J. T. L. Navarrete, V. Hernandez, Chemical Communications 2012, 48, 6732.

[24] O. Gidron, A. Dadvand, E. Wei-Hsin Sun, I. Chung, L. J. W. Shimon, M. Bendikov, D. F. Perepichka, Journal of Materials Chemistry C 2013, 1, 4358.

[25] O. Gidron, Y. Diskin-Posner, M. Bendikov, Journal of the American Chemical Society 2010, 132, 2148.

[26] A. Facchetti, M.-H. Yoon, C. L. Stern, H. E. Katz, T. J. Marks, Angewandte Chemie International Edition 2003, 42, 3900.

[27] R. Joseph Kline, M. D. McGehee, M. F. Toney, Nat Mater 2006, 5, 222.

[28] D. H. Kim, Y. D. Park, Y. Jang, H. Yang, Y. H. Kim, J. I. Han, D. G. Moon, S. Park, T. Chang, C. Chang, M. Joo, C. Y. Ryu, K. Cho, Advanced Functional Materials 2005, 15, 77.

[29] R. J. Kline, M. D. McGehee, E. N. Kadnikova, J. Liu, J. M. J. Fréchet, Advanced Materials 2003, 15, 1519.

[30] B. S. Ong, Y. Wu, P. Liu, S. Gardner, Journal of the American Chemical Society 2004, 126, 3378.

[31] A. Patra, M. Bendikov, Journal of Materials Chemistry 2010, 20, 422.

[32] M. Li, A. Patra, Y. Sheynin, M. Bendikov, Advanced Materials 2009, 21, 1707.

[33] B. Kim, H. Shin, T. Park, H. Lim, E. Kim, Advanced Materials 2013, 25, 5483.

[34] D. Astruc, F. Lu, J. R. Aranzaes, Angewandte Chemie International

Edition 2005, 44, 7852.

[35] C. Burda, X. Chen, R. Narayanan, M. A. El-Sayed, Chemical Reviews 2005, 105, 1025.

[36] B. D. Gates, Q. Xu, M. Stewart, D. Ryan, C. G. Willson, G. M. Whitesides, Chemical Reviews 2005, 105, 1171.

[37] N. L. Rosi, C. A. Mirkin, Chemical Reviews 2005, 105, 1547.

[38] R. H. Baughman, A. A. Zakhidov, W. A. de Heer, Science 2002, 297, 787.

[39] B. L. Cushing, V. L. Kolesnichenko, C. J. O'Connor, Chemical Reviews 2004, 104, 3893.

[40] W. W. Yu, L. Qu, W. Guo, X. Peng, Chemistry of Materials 2003, 15, 2854.

[41] X. Michalet, F. F. Pinaud, L. A. Bentolila, J. M. Tsay, S. Doose, J. J. Li, G. Sundaresan, A. M. Wu, S. S. Gambhir, S. Weiss, Science 2005, 307, 538.

[42] S. M. Bachilo, M. S. Strano, C. Kittrell, R. H. Hauge, R. E. Smalley, R. B. Weisman, Science 2002, 298, 2361.

[43] C. Dhand, M. Das, M. Datta, B. D. Malhotra, Biosensors and Bioelectronics 2011, 26, 2811.

[44] R. J. Tseng, J. Huang, J. Ouyang, R. B. Kaner, Yang, Nano Letters 2005, 5, 1077.

[45] Y. Wang, H. D. Tran, L. Liao, X. Duan, R. B. Kaner, Journal of the American Chemical Society 2010, 132, 10365.

[46] J. I. Lee, S. H. Cho, S.-M. Park, J. K. Kim, J. K. Kim, J.-W. Yu, Y. C. Kim, T. P. Russell, Nano Letters 2008, 8, 2315.

[47] M. Schierhorn, S. W. Boettcher, S. Kraemer, G. D. Stucky, M. Moskovits, Nano Letters 2009, 9, 3262.

[48] R. A. Potyrailo, Angewandte Chemie International Edition 2006, 45, 702.

[49] O. S. Kwon, S. J. Park, J. Jang, Biomaterials 2010, 31, 4740.

[50] H. D. Tran, D. Li, R. B. Kaner, Advanced Materials 2009, 21, 1487.

[51] X. Yang, Z. Zhu, T. Dai, Y. Lu, Macromolecular Rapid Communications 2005, 26, 1736.

[52] Y. Mao, W. L. Wang, D. Wei, E. Kaxiras, J. G. Sodroski, ACS Nano 2011, 5, 1395.

[53] J. C. Meyer, A. K. Geim, M. I. Katsnelson, K. S. Novoselov, T. J. Booth, S. Roth, Nature 2007, 446, 60.

[54] A. A. Balandin, S. Ghosh, W. Bao, I. Calizo, D. Teweldebrhan, F. Miao, C. N. Lau, Nano Letters 2008, 8, 902.

[55] K. S. Kim, Y. Zhao, H. Jang, S. Y. Lee, J. M. Kim, K. S. Kim, J.-H. Ahn, P. Kim, J.-Y. Choi, B. H. Hong, Nature 2009, 457, 706.

[56] Y. Zhang, Y.-W. Tan, H. L. Stormer, P. Kim, Nature 2005, 438, 201.

[57] S. Gilje, S. Han, M. Wang, K. L. Wang, R. B. Kaner, Nano Letters 2007, 7, 3394.

[58] S. Bae, H. Kim, Y. Lee, X. Xu, J.-S. Park, Y. Zheng, J. Balakrishnan, T. Lei, H. Ri Kim, Y. I. Song, Y.-J. Kim, K. S. Kim, B. Ozyilmaz, J.-H. Ahn, B. H. Hong, S. Iijima, Nat Nano 2010, 5, 574.

[59] Y. Zhu, S. Murali, W. Cai, X. Li, J. W. Suk, J. R. Potts, R. S. Ruoff, Advanced Materials 2010, 22, 3906.

[60] F. Xia, T. Mueller, Y.-m. Lin, A. Valdes-Garcia, P. Avouris, Nat Nano 2009, 4, 839.

[61] RamanathanT, A. A. Abdala, StankovichS, D. A. Dikin, M. Herrera Alonso, R. D. Piner, D. H. Adamson, H. C. Schniepp, ChenX, R. S. Ruoff, S. T. Nguyen, I. A. Aksay, R. K. Prud'Homme, L. C. Brinson, Nat Nano 2008, 3, 327.

[62] Z.-S. Wu, W. Ren, L. Wen, L. Gao, J. Zhao, Z. Chen, G. Zhou, F. Li, H.-M. Cheng, ACS Nano 2010, 4, 3187.

[63] H. Zhang, X. Lv, Y. Li, Y. Wang, J. Li, ACS Nano 2010, 4, 380.

[64] W. Chen, S. Li, C. Chen, L. Yan, Advanced Materials 2011, 23, 5679.

[65] J. R. Potts, D. R. Dreyer, C. W. Bielawski, R. S. Ruoff, Polymer 2011, 52, 5.

[66] L. Al-Mashat, K. Shin, K. Kalantar-zadeh, J. D. Plessis, S. H. Han, R. W. Kojima, R. B. Kaner, D. Li, X. Gou, S. J. Ippolito, W. Wlodarski, The Journal of Physical Chemistry C 2010, 114, 16168.

[67] Q. Wu, Y. Xu, Z. Yao, A. Liu, G. Shi, ACS Nano 2010, 4, 1963.

[68] K. Zhang, L. L. Zhang, X. S. Zhao, J. Wu, Chemistry of Materials 2010, 22, 1392.

[69] H. Chang, H. Wu, Energy & Environmental Science 2013, 6, 3483.

[70] Q. Su, S. Pang, V. Alijani, C. Li, X. Feng, K. Müllen, Advanced Materials 2009, 21, 3191.

[71] X. An, T. Simmons, R. Shah, C. Wolfe, K. M. Lewis, M. Washington, S. K. Nayak, S. Talapatra, S. Kar, Nano Letters 2010, 10, 4295.

[72] N. V. Kozhemyakina, J. M. Englert, G. Yang, E. Spiecker, C. D. Schmidt, F. Hauke, A. Hirsch, Advanced Materials 2010, 22, 5483.

[73] V. Eswaraiah, K. Balasubramaniam, S. Ramaprabhu, Nanoscale 2012, 4, 1258.

[74] X. Chen, X. Jia, J. Han, J. Ma, Z. Ma, Biosensors and Bioelectronics 2013, 50, 356.

[75] Y. Fan, J.-H. Liu, C.-P. Yang, M. Yu, P. Liu, Sensors and Actuators B: Chemical 2011, 157, 669.

[76] S. Liu, X. Xing, J. Yu, W. Lian, J. Li, M. Cui, J. Huang, Biosensors and

Bioelectronics 2012, 36, 186.

[77] J. W. Park, C. Lee, J. Jang, Sensors and Actuators B: Chemical 2015, 208, 532.

[78] J. W. Park, S. J. Park, O. S. Kwon, C. Lee, J. Jang, Analytical Chemistry 2014, 86, 1822.

[79] J. W. Park, S. J. Park, O. S. Kwon, C. Lee, J. Jang, Analyst 2014, 139, 3852.

[80] N. Ruecha, R. Rangkupan, N. Rodthongkum, O. Chailapakul, Biosensors and Bioelectronics 2014, 52, 13.

[81] J. W. Park, S. J. Park, O. S. Kwon, C. Lee, J. Jang, J. Jang, J. W. Park, S. J. Park, C. Lee, O. S. Kwon, Chemistry of Materials 2014, 26, 2354.

[82] S. K. Karan, D. Mandal, B. B. Khatua, Nanoscale 2015, 7, 10655.

[83] A. Midya, V. Mamidala, J.-X. Yang, P. K. L. Ang, Z.-K. Chen, W. Ji, K. P. Loh, Small 2010, 6, 2292.

[84] D. Yu, Y. Yang, M. Durstock, J.-B. Baek, L. Dai, ACS Nano 2010, 4, 5633.

[85] X.-D. Zhuang, Y. Chen, G. Liu, P.-P. Li, C.-X. Zhu, E.-T. Kang, K.-G. Noeh, B. Zhang, J.-H. Zhu, Y.-X. Li, Advanced Materials 2010, 22, 1731.

[86] Y. Cui, Q. Wei, H. Park, C. M. Lieber, Science 2001, 293, 1289.

[87] H. Liu, J. Kameoka, D. A. Czaplewski, H. G. Craighead, Nano Letters

2004, 4, 671.

[88] Y. Liu, X. Dong, P. Chen, Chemical Society Reviews 2012, 41, 2283.

[89] R. Martínez-Máñez, F. Sancenón, Chemical Reviews 2003, 103, 4419.

[90] D. T. McQuade, A. E. Pullen, T. M. Swager, Chemical Reviews 2000, 100, 2537.

[91] F. Schedin, A. K. Geim, S. V. Morozov, E. W. Hill, P. Blake, M. I. Katsnelson, K. S. Novoselov, Nat Mater 2007, 6, 652.

[92] N. Pinna, G. Neri, M. Antonietti, M. Niederberger, Angewandte Chemie International Edition 2004, 43, 4345.

[93] F. Schedin, A. K. Geim, S. V. Morozov, E. W. Hill, P. Blake, M. I. Katsnelson, K. S. Novoselov, Nat Mater 2007, 6, 652.

[94] Q. Wan, Q. H. Li, Y. J. Chen, T. H. Wang, X. L. He, J. P. Li, C. L. Lin, Applied Physics Letters 2004, 84, 3654.

[95] J. Xu, Q. Pan, Y. a. Shun, Z. Tian, Sensors and Actuators B: Chemical 2000, 66, 277.

[96] B. R. Azamian, J. J. Davis, K. S. Coleman, C. B. Bagshaw, M. L. H. Green, Journal of the American Chemical Society 2002, 124, 12664.

[97] K. Besteman, J.-O. Lee, F. G. M. Wiertz, H. A. Heering, C. Dekker, Nano Letters 2003, 3, 727.

[98] A. Bianco, K. Kostarelos, C. D. Partidos, M. Prato, Chemical Communications 2005, 571.

[99] S. M. Borisov, O. S. Wolfbeis, Chemical Reviews 2008, 108, 423.

[100] T. Kuila, S. Bose, P. Khanra, A. K. Mishra, N. H. Kim, J. H. Lee, Biosensors and Bioelectronics 2011, 26, 4637.

[101] V. S.-Y. Lin, K. Motesharei, K.-P. S. Dancil, M. J. Sailor, M. R. Ghadiri, Science 1997, 278, 840.

[102] M. Zhou, Y. Zhai, S. Dong, Analytical Chemistry 2009, 81, 5603.

[103] X. P. A. Gao, G. Zheng, C. M. Lieber, Nano Letters 2010, 10, 547.

[104] Y. Ohno, K. Maehashi, K. Matsumoto, Journal of the American Chemical Society 2010, 132, 18012.

[105] Z. Kuang, S. N. Kim, W. J. Crookes-Goodson, B. L. Farmer, R. R. Naik, ACS Nano 2010, 4, 452.

[106] H. Yoon, S. H. Lee, O. S. Kwon, H. S. Song, E. H. Oh, T. H. Park, J. Jang, Angewandte Chemie International Edition 2009, 48, 2755.

[107] D. Vione, V. Maurino, C. Minero, D. Borghesi, M. Lucchiari, E. Pelizzetti, Environmental Science & Technology 2003, 37, 4635.

[108] R. K. Gilpin, L. A. Pachla, Analytical Chemistry 2005, 77, 3755.

[109] J. Jia, B. Wang, A. Wu, G. Cheng, Z. Li, S. Dong, Analytical Chemistry 2002, 74, 2217.

[110] X. Shu, Y. Chen, H. Yuan, S. Gao, D. Xiao, Analytical Chemistry 2007, 79, 3695.

[111] J. Foreman, V. Demidchik, J. H. F. Bothwell, P. Mylona, H. Miedema, M. A. Torres, P. Linstead, S. Costa, C. Brownlee, J. D. G. Jones, J. M. Davies, L. Dolan, Nature 2003, 422, 442.

[112] J. D. Lambeth, Nat Rev Immunol 2004, 4, 181.

[113] P. Niethammer, C. Grabher, A. T. Look, T. J. Mitchison, Nature 2009, 459, 996.

[114] H. Sauer, G. Rahimi, J. Hescheler, M. Wartenberg, FEBS Letters 2000, 476, 218.

[115] C. Amatore, S. Arbault, D. Bruce, P. de Oliveira, M. Erard, M. Vuillaume, Chemistry – A European Journal 2001, 7, 4171.

[116] H. Ohshima, M. Tatemichi, T. Sawa, Archives of Biochemistry and Biophysics 2003, 417, 3.

[117] W. Maruyama, P. Dostert, K. Matsubara, M. Naoi, Free Radical Biology and Medicine 1995, 19, 67.

[118] K. Wang, Q. Liu, X.-Y. Wu, Q.-M. Guan, H.-N. Li, Talanta 2010, 82, 372.

[119] K. Sunil, B. Narayana, Bull Environ Contam Toxicol 2008, 81, 422.

[120] S. Xu, B. Peng, X. Han, Biosensors and Bioelectronics 2007, 22, 1807.

[121] Y. Wang, X. Chen, J.-J. Zhu, Electrochemistry Communications 2009, 11, 323.

[122] J. Bai, X. Jiang, Analytical Chemistry 2013, 85, 8095.

[123] A. K. M. Kafi, A. Ahmadalinezhad, J. Wang, D. F. Thomas, A. Chen, Biosensors and Bioelectronics 2010, 25, 2458.

[124] X. Sun, S. Guo, Y. Liu, S. Sun, Nano Letters 2012, 12, 4859.

[125] Y. Wang, X. Yang, J. Bai, X. Jiang, G. Fan, Biosensors and Bioelectronics 2013, 43, 180.

[126] C. Xu, X. Wang, J. Zhu, The Journal of Physical Chemistry C 2008, 112, 19841.

[127] J. Wang, Chemical Reviews 2007, 108, 814.

[128] R. Ballerstadt, A. Kholodnykh, C. Evans, A. Boretsky, M. Motamedi, A. Gowda, R. McNichols, Analytical Chemistry 2007, 79, 6965.

[129] N. C. Shah, O. Lyandres, J. T. Walsh, M. R. Glucksberg, R. P. Van Duyne, Analytical Chemistry 2007, 79, 6927.

[130] C. Shan, H. Yang, J. Song, D. Han, A. Ivaska, L. Niu, Analytical Chemistry 2009, 81, 2378.

[131] S. Hrapovic, Y. Liu, K. B. Male, J. H. T. Luong, Analytical Chemistry 2003, 76, 1083.

[132] J. A. Fernández, J. R. Aboal, A. Carballeira, Science of The Total

Environment 2000, 256, 151.

[133] J. K. Nicholson, M. D. Kendall, D. Osborn, Nature 1983, 304, 633.

[134] G.-B. Jiang, J.-B. Shi, X.-B. Feng, Environmental Science & Technology 2006, 40, 3672.

[135] C. Deng, D. Zhangb, X. Pan, F. Chang, S. Wang, Journal of Photochemistry and Photobiology B: Biology 2013, 127, 1.

[136] T. W. Clarkson, L. Magos, G. J. Myers, New England Journal of Medicine 2003, 349, 1731.

[137] S. Ekino, M. Susa, T. Ninomiya, K. Imamura, T. Kitamura, Journal of the Neurological Sciences 2007, 262, 131.

[138] D. A. Geier, M. R. Geier, Journal of Toxicology and Environmental Health, Part A 2007, 70, 837.

[139] M. Korbas, S. R. Blechinger, P. H. Krone, I. J. Pickering, G. N. George, Proceedings of the National Academy of Sciences 2008, 105, 12108.

[140] H. G. Sudibya, Q. He, H. Zhang, P. Chen, ACS Nano 2011, 5, 1990.

[141] T. H. Kim, J. Lee, S. Hong, The Journal of Physical Chemistry C 2009, 113, 19393.

[142] T. P. McNicholas, K. Zhao, C. Yang, S. C. Hernandez, A. Mulchandani, N. V. Myung, M. A. Deshusses, The Journal of Physical Chemistry C 2011, 115, 13927.

[143] L. Zhang, T. Li, B. Li, J. Li, E. Wang, Chemical Communications 2010, 46, 1476.

[144] S. V. Wegner, A. Okesli, P. Chen, C. He, Journal of the American Chemical Society 2007, 129, 3474.

[145] N. Dave, M. Y. Chan, P.-J. J. Huang, B. D. Smith, J. Liu, Journal of the American Chemical Society 2010, 132, 12668.

[146] T. Qian, S. Wu, J. Shen, Chemical Communications 2013, 49, 4610.

[147] T. Qian, C. Yu, S. Wu, J. Shen, Journal of Materials Chemistry A 2013, 1, 6539.

[148] Z.-Q. Zhao, X. Chen, Q. Yang, J.-H. Liu, X.-J. Huang, Chemical Communications 2012, 48, 2180.

[149] M. L. Hammock, A. Chortos, B. C. K. Tee, J. B. H. Tok, Z. Bao, Advanced Materials 2013, 25, 5997.

[150] D.-H. Kim, N. Lu, R. Ma, Y.-S. Kim, R.-H. Kim, S. Wang, J. Wu, S. M. Won, H. Tao, A. Islam, K. J. Yu, T.-i. Kim, R. Chowdhury, M. Ying, L. Xu, M. Li, H.-J. Chung, H. Keum, M. McCormick, P. Liu, Y.-W. Zhang, F. G. Omenetto, Y. Huang, T. Coleman, J. A. Rogers, Science 2011, 333, 838.

[151] J. Park, Y. Lee, J. Hong, M. Ha, Y.-D. Jung, H. Lim, S. Y. Kim, H. Ko, ACS Nano 2014, 8, 4689.

[152] A. N. Sokolov, B. C. K. Tee, C. J. Bettinger, J. B. H. Tok, Z. Bao,

Accounts of Chemical Research 2011, 45, 361.

[153] B. C. K. Tee, C. Wang, R. Allen, Z. Bao, Nat Nano 2012, 7, 825.

[154] X. Wang, Y. Gu, Z. Xiong, Z. Cui, T. Zhang, Advanced Materials 2014, 26, 1336.

[155] M. Madsen, K. Takei, R. Kapadia, H. Fang, H. Ko, T. Takahashi, A. C. Ford, M. H. Lee, A. Javey, Advanced Materials 2011, 23, 3115.

[156] J. Zhou, Y. Gu, P. Fei, W. Mai, Y. Gao, R. Yang, G. Bao, Z. L. Wang, Nano Letters 2008, 8, 3035.

[157] D. J. Lipomi, J. A. Lee, M. Vosgueritchian, B. C. K. Tee, J. A. Bolander, Z. Bao, Chemistry of Materials 2011, 24, 373.

[158] O. S. Kwon, S. J. Park, J.-Y. Hong, A. R. Han, J. S. Lee, J. S. Lee, J. H. Oh, J. Jang, ACS Nano 2012, 6, 1486.

[159] N. Hu, Y. Karube, M. Arai, T. Watanabe, C. Yan, Y. Li, Y. Liu, H. Fukunaga, Carbon 2010, 48, 680.

[160] A. D. Smith, F. Niklaus, A. Paussa, S. Vaziri, A. C. Fischer, M. Sterner, F. Forsberg, A. Delin, D. Esseni, P. Palestri, M. Ö stling, M. C. Lemme, Nano Letters 2013, 13, 3237.

[161] C. Yan, J. Wang, W. Kang, M. Cui, X. Wang, C. Y. Foo, K. J. Chee, P. S. Lee, Advanced Materials 2014, 26, 2022.

[162] H.-B. Yao, J. Ge, C.-F. Wang, X. Wang, W. Hu, Z.-J. Zheng, Y. Ni, S.-

H. Yu, Advanced Materials 2013, 25, 6692.

[163] W. Cai, Y. Huang, D. Wang, C. Liu, Y. Zhang, Journal of Applied Polymer Science 2014, 131, 39778.

[164] H. Gullapalli, V. S. M. Vemuru, A. Kumar, A. Botello-Mendez, R. Vajtai, M. Terrones, S. Nagarajaiah, P. M. Ajayan, Small 2010, 6, 1641.

[165] C. Pang, G.-Y. Lee, T.-i. Kim, S. M. Kim, H. N. Kim, S.-H. Ahn, K.-Y. Suh, Nat Mater 2012, 11, 795.

[166] W. S. Hummers, R. E. Offeman, Journal of the American Chemical Society 1958, 80, 1339.

[167] Y.-E. Miao, S. He, Y. Zhong, Z. Yang, W. W. Tjiu, T. Liu, Electrochimica Acta 2013, 99, 117.

[168] S. Liu, J. Tian, L. Wang, H. Li, Y. Zhang, X. Sun, Macromolecules 2010, 43, 10078.

[169] W. Zhao, H. Wang, X. Qin, X. Wang, Z. Zhao, Z. Miao, L. Chen, M. Shan, Y. Fang, Q. Chen, Talanta 2009, 80, 1029.

[170] Q. Wang, J. Zheng, Microchim Acta 2010, 169, 361.

[171] K. Cui, Y. Song, Y. Yao, Z. Huang, L. Wang, Electrochemistry Communications 2008, 10, 663.

[172] W. Zhao, H. Wang, X. Qin, X. Wang, Z. Zhao, Z. Miao, L. Chen, M. Shan, Y. Fang, Q. Chen, Talanta 2009, 80, 1029.

[173] L. Li, Z. Du, S. Liu, Q. Hao, Y. Wang, Q. Li, T. Wang, Talanta 2010, 82, 1637.

[174] Z. Yin, J. Wu, Z. Yang, Biosensors and Bioelectronics 2011, 26, 1970.

[175] Y. Li, Y. Chang, M. Jin, Y. Liu, G. Han, Journal of Applied Polymer Science 2012, 126, 1316.

[176] F. Xu, Y. Sun, Y. Zhang, Y. Shi, Z. Wen, Z. Li, Electrochemistry Communications 2011, 13, 1131.

[177] H. Teymourian, A. Salimi, S. Khezrian, Biosensors and Bioelectronics 2013, 49, 1.

[178] T. Zhang, R. Yuan, Y. Chai, W. Li, S. Ling, Sensors 2008, 8, 5141.

[179] X. Zhang, B. Qi, S. Zhang, Analytical Letters 2008, 41, 3100.

[180] A. Safavi, N. Maleki, M. M. Doroodmand, J. Hazard. Mater. 2010, 173, 622.

[181] Y. M. Sabri, S. J. Ippolito, A. J. Atanacio, V. Bansal, S. K. Bhargava, J. *J. Mater. Chem.*, **2012**, *22*, 21395.

[182] Y. M. Sabri, R. Kojima, S. J. Ippolito, W. Wlodarski, K. Kalantaradeh, R. B. Kaner, S. K. Bhargava, *Sens. Actuators B*, **2011**, *160*, 616.

[183] T. P. McNicholas, K. Zhao, C. Yang, S. C. Hernandez, A. Mulchandani, N. V. Myung and M. A. Deshusses, *J. Phys. Chem. C*, 2011, **115**, 13927.

[184] J. W. Park, J. Jang, Carbon 2015, 87, 275.

[185] W. Wu, X. Wen, Z. L. Wang, Science 2013, 340, 952.

[186] J. Lee, S. Kim, J. Lee, D. Yang, B. C. Park, S. Ryu, I. Park, Nanoscale 2014.

[187] J. Kim, T. Nga Ng, W. Soo Kim, Applied Physics Letters 2012, 101.

[188] C. Pang, G.-Y. Lee, T.-i. Kim, S. M. Kim, H. N. Kim, S.-H. Ahn, K.-Y. Suh, Nat Mater 2012, 11, 795.

[189] I. Graz, M. Kaltenbrunner, C. Keplinger, R. Schwödiauer, S. Bauer, S. P. Lacour, S. Wagner, Applied Physics Letters 2006, 89.

[190] S. C. B. Mannsfeld, B. C. K. Tee, R. M. Stoltenberg, C. V. H. H. Chen, S. Barman, B. V. O. Muir, A. N. Sokolov, C. Reese, Z. Bao, Nat Mater 2010, 9, 859.

[191] B. Hu, Y. Ding, W. Chen, D. Kulkarni, Y. Shen, V. V. Tsukruk, Z. L. Wang, Advanced Materials 2010, 22, 5134.

[192] H. Gullapalli, V. S. M. Vemuru, A. Kumar, A. Botello-Mendez, R. Vajtai, M. Terrones, S. Nagarajaiah, P. M. Ajayan, Small 2010, 6, 1641.

[193] X. Xiao, L. Yuan, J. Zhong, T. Ding, Y. Liu, Z. Cai, Y. Rong, H. Han, J. Zhou, Z. L. Wang, Advanced Materials 2011, 23, 5440.

[194] N. Hu, Y. Karube, M. Arai, T. Watanabe, C. Yan, Y. Li, Y. Liu, H. Fukunaga, Carbon 2010, 48, 680.

국문초록

그래핀/전도성 고분자 나노하이브리드 물질들은 향상된 표면적, 전하 운반체 이동속도, 열/전기적 전도율, 그리고 화학적/기계적 안정성 등과 같은 그들의 시너지 효과들 때문에 많은 관심을 받고 있다. 전자장치에 사용하기 위한 그래핀/전도성 고분자 나노하이브리드 물질들을 제조하기 위해서, 공유 그리고 비공유 합성법들이 소개되어 왔다. 비공유 합성법과는 달리, 공유 합성법은 그래핀과 전도성고분자 표면에 작용기를 먼저 도입시켜야 하기 때문에 시간소유와 까다로운 조건들을 요구하게 된다. 반면에, 비공유 합성법은 π–π 결합과 같은 이차적인 결합을 통해 그래핀/전도성 고분자 나노하이브리드 물지들을 쉽게 제조할 수가 있다. 비공유 합성법 중에 하나인 제자리 합성법은 균일한 나노하이브리드 물질을 얻을 수 있기 때문에 매우 유망하고 효과적인 제조법이다. 게다가, 그래핀/전도성 고분자 나노하이브리드 물질들의 형태와 모양을 전구체 물질들을 (그래핀 또는 전도성 고분자) 선택적으로 변형시킴에 따라 제어할 수 있다.

본 연구에서는, 다양한 그래핀/전도성 고분자 나노하이브리드 물질들을 제자리 합성법에 의해서 소개되었다. 합성된 나노하이브리드 물질들은 훌륭한 전기적/화학적 특성들을 보여주어, 센서응용분야에 활용할 수 있게 한다. 그래핀/전도성 고분자 나노하이브리드 물질들의 시너지효과들은 센서디바이스에서 전달체로 활용될 때, 굉장히 빠른 응답/복원 속도를

제공한다. 또, 그래핀/전도성 고분자 나노하이브리드물질들의 넓은 표면적은 향상된 목표 물질들과 상호작용을 제공하여, 고감도 센서 성능을 보여주게 된다.

주요어: 그래핀, 전도성 고분자, 나노하이브리드 물질, 전계-효과 트랜지스터, 센서 응용

학번: 2013-30778

工學博士學位論文

Fabrication of Graphene/Conducting Polymer Nanohybrid Materials and Their Sensor Applications

그래핀/전도성 고분자 나노하이브리드 물질의 제조 및 센서로의 응용

2016 年 2 月

서울大學校 大學院

化學生物工學部

朴 秦 煜

Fabrication of Graphene/Conducting Polymer Nanohybrid Materials and Their Sensor Applications

그래핀/전도성 고분자 나노하이브리드 물질의 제조 및 센서로의 응용

指導敎授: 張 正 植

이 論文을 工學博士 學位論文으로 提出함

2015 年 11 月

서울大學校 大學院

化學生物工學部

朴 秦 煜

朴 秦 煜의 工學博士 學位論文을 認准함

2015 年 11 月

委 員 長 _____ (인)

副委員長 _____ (인)

委 員 _____ (인)

委 員 _____ (인)

委 員 _____ (인)

Fabrication of Graphene/Conducting Polymer Nanohybrid Materials and Their Sensor Applications

by

Jin Wook Park

Submitted to the Graduate School of Seoul National University

in Partial Fulfillment of the Requirements

for the Degree of Doctor of Philosophy

February, 2016

Thesis Adviser: Jyongsik Jang

ABSTRACT

Graphene/conducting polymer (CP) nanohybrid materials have attracted considerable attention, due to their synergetic effects, including enhanced surface area, charge carrier mobility, thermal/electrical conductivity, and chemical/mechanical stability. To synthesize the graphene/CP nanohybrid materials for using in electronic device applications, covalent and non-covalent synthetic methods have been introduced. Contrary to non-covalent method, covalent functionalization requires time-consuming and harsh conditions, because it needs firstly to introduce functional group on the surface of graphene and CPs. On the other hand, non-covalent functionalization offers facile way to obtain graphene/CP nanohbyrid materials through secondary bonding interactions, such as π–π interactions. In-situ synthetic method, as one of the non-covalent synthetic method, is very promising and powerful tool to design graphene/CP nanohybrids owing to getting uniform nanohbyrid materials. Furthermore, the morphology and shape of the graphene/CP nanohybrids can be controlled by selectively designing the morphology of starting materials (graphene or CP materials).

In this study, various graphene/CP nanohbyrid materials are introduced by using in-situ synthetic method. The synthesized nanohybrid materials exhibit excellent electrical/chemical properties, enabling to be applied in sensor applications. Synergetic effects of graphene/CP nanohbyrid mateirals provide rapid response/recovery time, when using as a transducer in the sensing device. Furthermore, the enlarged surface area from graphene/CP nanohybrids can provide the improved interactions with target analytes, leading to the ultrasensitive sensing performance.

KEYWORDS: Graphene; conducting polymers (CP); nanohybrid materials; Field-effect transistor (FET); sensor applications

STUDENT NUMBER: 2013–30778

List of Abbreviations

CP : conducting polymer

PPy : polypyrrole

PANI : polyaniline

PT : polythiophene

PEDOT : poly(3,4-ethylenedioxylthiophene)

PF : polyfuran

PSe : polyselenophene

PPV : poly(para-phenylene vinylene)

RT : room temperature

NCP : nanoscaled conducting polymer

CNTs : carbon nanotubes

QDs : quantum dots

NPs : nanoparticles

NCs : nanocrystals

NFs : nanofibers

NRs : nanorods

NTs : nanotubes

1D : one-dimensional

SWCNT : single-walled carbon nanotbue

FET : filed-effect transistor

OLED : organic light emitting diode

PSS : poly(sodium 4-styrenesulfonate)

TPAPAM : triphenylamine-based poly-azomethine

PB^- : 1-pyrenebutyrate

EDLC : electric double layer capacitor

GO : graphene oxide

RGO : reduced graphene oxide

CPPy : carboxylated polypyrrole

DMT-MM : 4-(4,6-Dimethoxy-1,3,5-triazin-2-yl)-4-methyl-morpholinium chloride

EDOT : 3,4-ethylenedioxythiophene

PVDF : polyvinylfluoride

IDA : interdigitated array

S/N : signal-to-noise

GF : gauge factor

MO : methyl orange

PBS : phosphate-buffered solution

XRD : X-ray diffraction

FE-SEM : field emission-scanning electron microscope

TEM : transmission electron microscope

HRTEM: high resolution transmission electron microscope

ATR-FTIR : Attenuated total reflection-fourier transform infrared spectroscopy

AFM : Atomic Force Microscope

XPS : X−ray photoelectron spectra

TGA : Thermogravimetric analysis

CVD : chemical vapor deposition

GCE : glassy carbon electrode

List of Figures

Figure 1. Typical conducting polymer structures (undoped form).

Figure 2. Electronic band model of PPy: Neutral, Polaron, and Bipolaron state.

Figure 3. Structures of various important carbon nanomaterials: fullerene (C_{60}), single-walled carbon nanotube (SWCNT), multi-walled carbon nanotube (MWCNT), carbon nanohorn, graphene, few layer graphene and graphene oxide.

Figure 4. Photo image of rGO and graphene with PB^- materails.

Figure 5. Illustration of the process for preparation of rGO–PANI composites.

Figure 6. (a) Photograph of the all solid-state supercapacitor. (The inset is a schematic image of the solid-state supercapacitor.) (b) CV curves at 200mV s^{-1} with various bending angles and (c) galvanostatic charge−discharge curves at a current density of 4 A g^{-1} before (black) and after 100 bending cycles (red).

Figure 7. (A) Output voltage generation (human finger (B) touch and release response) from the ECE made with PVDF, 0.1Fe-RGO/PVDF,

0.5Fe-RGO/PVDF and 2.0Fe-RGO/PVDF nanocomposite films, and (C) schematic diagram for measuring the human finger response signal (voltage) for the Fe-RGO/PVDF film. Photograph of (D) the Fe-RGO/PVDF nanocomposite film and (E) a demonstration of the flexibility.

Figure 8. Illustration of IDA chemical sensing device.

Figure 9. Illustration of liquid-ion gated FET sensing device.

Figure 10. (a) Schematic of the assembly and operation of a flexible sensor layer sandwiched between thin PDMS supports (~500 μm thickness each). (b) Photograph showing the flexibility of the assembled sensor. Scale bar, 1 cm. (c) SEM image of a dense array of 50-nm radius nanohairs with AR = 10. Scale bar, 1 μm. (d) Schematic illustrations of the pressure, shear and torsion loads and their possible geometric distortions of the paired hairs. (e) Operation of a flexible sensor layer by means of recording of resistance change (Roff : unloading, Ron: loading).

Figure 11. A schematic illustration of the synthesis of rGO/PPy NT hybrids.

Figure 12. (a) SEM image shows PPy NTs. The inset shows a TEM image. Cross-sectional SEM images show (b) rGO and (c) rGO/PPy NTs. The inset indicates the magnification level. (d) A TEM image shows rGO/PPy NTs.

Figure 13. Raman spectra of GO, rGO, PPy, NT, and rGO/PPy NT composites.

Figure 14. ATR-FTIR spectra of (a) GO, rGO, PPy, NT, and rGO/PPy NT hybrids. A magnified view of the marked area in (a) is shown in (b).

Figure 15. X-ray diffractions of GO, rGO, PPy NT, and rGO/PPy NT hybrids.

Figure 16. (a) Current−voltage (I−V) curves of GO, rGO, PPy NTs, and rGO/PPy NTs composites and (b) rGO/PPy NTs composites at V_g from –2.0 to 0.4 V in 0.2-V steps (V_{sd}: 0 to 1.0 V in 0.2-V steps).

Figure 17. (a) Schematic diagram shows a liquid-ion-gated FET-type sensor. (Ag/AgCl reference electrode, R; platinum counter electrode, C; source and drain electrodes, S and D) (b) Real-time responses and (c) a calibration curve for H_2O_2 based on rGO, PPy NTs, and rGO/PPy NTs composites were measured at V_{sd} = 10 mV (V_g = 0.1

V) with H_2O_2 concentrations of 0.1 nM to 100 nM. Storage stability biosensor performance is shown in (d). Real-time responses to PBS, UA, AA, glucose, and H_2O_2 are shown in (e). (f) A histogram details the sensing performance to UA, AA, glucose, and H_2O_2.

Figure 18. Real-time responses for H_2O_2 based on rGO/PPy NTs composites were measrured at V_{sd} = 10 mV (V_g = 0.1 V) with H_2O_2 concentration of 10 pM to 100 pM.

Figure 19. Schematic illustration of the fabrication of rGO/C-PPy NT hybrid glucose sensing device.

Figure 20. (a) SEM image of the C-PPy NTs. The inset shows a TEM image. (b) Cross-sectional SEM images of the rGO layers and (c) the rGO/C-PPy NTs. (d) TEM image of rGO/C-PPy NTs.

Figure 21. ATR-FT-IR spectra of rGO, C-PPy NT, and rGO/C-PPy NT hybrids.

Figure 22. ATR-FT-IR spectra of PPy NT and C-PPy NT.

Figure 23. (a) X-ray diffraction patterns and (b) Raman spectra of GO, rGO, C-PPy NT, and rGO/C-PPy NTs.

Figure 24. Current−voltage ($I-V$) curves of C-PPy NTs, rGO, and rGO/C-PPy NT hybrids.

Figure 25. (a) A schematic diagram showing the liquid-ion-gated FET-type sensor, with a Ag/AgCl reference electrode, labeled R, platinum counter electrode, labeled C, and source and drain electrodes, labeled S and D. (b) The source–drain current of the biosensors as a function of V_{SD} at various values of V_G in the range from –1.0 to +1.0 V. (c) The real-time responses and (d) a calibration curve for glucose biosensor with and without the GOx enzyme, which were measured at V_{SD} = 10 mV and V_G = – 0.1 V, with glucose concentrations of 1 nM to 100 mM. (e) The real-time response to PBS, AA, UA, and glucose solutions.

Figure 26. Real-time responses to exposure to H_2O_2 based on rGO/C-PPy NTs with GOD aptamer measured at V_{SD} = 10 mV and V_G = – 0.1 V, with H_2O_2 concentrations in the range 1–100 mM.

Figure 27. The real-time responses towards glucose of the rGO/C-PPy NTs measured at V_{SD} = 10 mV and V_G = – 0.1 V, with glucose

concentrations of 100 pM and 1 nM.

Figure 28. The real-time response of the rGO/C-PPy NTs hybrid FET-based biosensor (a) after 50 repetitions, and (b) after one month. Both datasets were measured with at V_{SD} = 10 mV and V_G = – 0.1 V, and with a glucose concentration of 1 nM.

Figure 29. The schematic illustration of the synthesis of rGO-PF NT hybrids.

Figure 30. (a) SEM image of PF NTs; the inset is a TEM image. Cross-sectional SEM images of (b) rGO layers and (c) rGO-PF NTs. (d) TEM image of rGO/PF NTs.

Figure 31. (a) Raman, (b) X-ray diffraction patterns, and (c) ATR-FT-IR spectra of GO, rGO, PF, and rGO+PF NT hybrids.

Figure 32. (a) Current−voltage (I−V) curves of PF NTs, rGO, and rGO-PF NT hybrids and (b) rGO-PF NT composites at V_g from –1.0 to +0.6 V in 0.2-V steps (Vsd: 0 to 1.0 V in 0.2-V steps).

Figure 33. PF NTs at V_g from −1.0 to 0.4 V in 0.2-V steps (Vsd: 0 to 1.0 V in 0.2-V steps).

Figure 34. (a) A liquid-ion-gated FET-type sensor based on rGO-PF NTs.

(Ag/AgCl reference electrode, R; platinum counter electrode, C; source and drain electrodes, S and D) (b) Real-time responses and (c) a calibration curve for Hg^{2+} based on rGO, PF NTs; rGO-PF NT composites were measured at Vsd = 10 mV (V_g = – 0.1 V) with Hg^{2+} concentrations of 10 pM to 100 nM. (d) A histogram of the sensitivity of the rGO-PF NT composites to Hg^{2+}, Zn^{2+}, Ce^{2+}, Na^{+}, Ni^{2+}, Pb^{2+}, Cu^{2+}, Co^{2+}, Li^{+}.

Figure 35. Real-time responses for Hg^{2+} sensor based on rGO-PF NT composites measured at V_{sd} = 10 mV (V_g = - 0.1 V) with a Hg^{2+} concentration of 1 pM to 10 pM.

Figure 36. Real-time responses to Zn^{2+}, Ce^{2+}, Na^{+}, Ni^{2+}, Pb^{2+}, Cu^{2+}, Co^{2+}, Li^{+}, and Hg^{2+} measured at V_{SD}= 10 mV (V_g = - 0.1 V).

Figure 37. (a) Schematic illustration of the preparation of graphene–PSe nanocomposites FE-SEM images of (b) rGO and (c) rGO/PSe nanocomposites. (Insets are the TEM images of rGO and rGO/PSe nanohybrid materials.) (d) Typical STEM image of graphene–PSe nanohybrids. Corresponding elemental mapping images of (e) C

and (f) Se.

Figure 38. (a) Raman spectroscopy, (b) XRD patterns, and (c) ATR-FTIR spectra of GO, rGO, PSe, and rGO/PSe nanohybrids.

Figure 39. (a) Overall, (b) C 1s, and (c) Se 3d XPS profiles of rGO/PSe nanohybrids.

Figure 40. TGA curves of rGO, PSe, and rGO-PSe nanohybrid materials.

Figure 41. N_2 adsorption/desorption isotherms of PSe, rGO, and rGO/PSe nanohybrids.

Figure 42. Current−voltage ($I-V$) curves of PSe, RGO, and RGO-PSe nanohybrid materials.

Figure 43. (a) schematic illustration of RGO/PSe nanohybrid chemiresistive electrode. Optical microscopic images of fabricated electrode (b) before and (c) after RGO/PSe nanohybrid material coataing process.

Figure 44. (a) Real-time responses of PSe and RGO/PSe nanohybrid materials upon sequential exposure to NH_3 (0.01 to 10 ppm) and MeOH (1 to 100 ppm). (b) Real-time responses of PSe and RGO/PSe nanohybrid materials on periodic exposure to 10 ppm of

NH_3 and 100 ppm of MeOH. (c) Normalized resistance changes of PSe and RGO/PSe nanohybrids with periodic exposure to 10 ppm of NH_3 and 100 ppm of MeOH gases for 100 cycles. (d) Calibration curve of PSe and RGO/PSe nanohybrids as a function of NH_3 and MeOH concentration.

Figure 45. Sensing performance histrogram of RGO/PSe nanohybrid mateirals to 11 analytes: each analyte concentration was fixed at around 10 ppm.

Figure 46. Schematic diagram showing the fabrication process of E-skin based on graphene/V-PEDOT/P(VDF-HFP) nanohybrid device.

Figure 47. (a) AFM and (b) HR-TEM images of the single-layer graphene. (c) UV-Vis spectra of the graphene transferred onto the PDMS film. The inset shows a photograph of the flexible and transparent graphene film.

Figure 48. SEM image of the (a) graphene, (b) the vertically grown PEDOT (via VDP) nanofibers on the graphene, and (c) the fabricated P(VDF-HFP)/PEDOT/graphene films.

Figure 49. SEM images of V-PEDOT according to VDP reaction time (a) 0, (b) 15, (c) 30 min, and (d) 1h.

Figure 50. Raman spectra of graphene, P(VDF-HFP), PEDOT, and graphene/PEDOT/P(VDF-HFP) nanohybrid materials.

Figure 51. (a) Schematic diagram of the E-skin device. (b) Sensitivities to pressure with various stimuli. (c) Real-time change in resistance of the electronic skin devices as a function of the graphene, graphene/P(VDF-HFP), graphene/V-PEDOT/P(VDF-HFP), V-PEDOT, and V-PEDOT/P(VDF-HFP) material.

Figure 52. Resistance as a function of strain for graphene, graphene/V-PEDOT, graphene/P(VDF-HFP), and graphene/V-PEDOT/P(VDF-HFP) nanohybrid film.

Figure 53. Current–voltage (*I-V*) curves of graphene, graphene/PEDOT, and graphene/PEDOT/P(VDF-HFP) nanohybrids.

Figure 54. Real-time change in the resistance of the E-skin over more than 1000 loading cycles, with a cycle length of 2 s and an applied pressure of 30 Pa. The inset shows a magnified image in the red

rectangular region.

Figure 55. (a) Resistance as a function of time during motion of the hand from an outstretched to a clenched-fist position. (b) Resistance as a function of time while measuring the pulse in the wrist.

List of Tables

Table 1. Comparison of the performance of various H_2O_2 sensors.

Table 2. Determination of glucose concentration in real samples using the biosensors.

Table 3. Comparison of the mercury sensing performance of various sensor type devices.

Table 4. Comparison between the detection limit performances of our flexible strain sensor and those of strain sensors based on other materials.

Table 5. Comparison of the sheet resistance values based on graphene, graphene/V-PEDOT, and graphene/V-PEDOT/P(VDF-HFP) nanohybrids..

Table of Contents

Abstract ..... **i**

List of Abbreviations ..... **iii**

List of Figures ..... **vi**

List of Tables ..... **xvii**

Table of Contents ..... **xviii**

1. INTRODUCTION **1**

1.1. Background **1**

1.1.1. Conducting polymers 1

1.1.1.1. Polypyrrole (PPy) 3

1.1.1.2. Poly(3,4,- ethylenedioxythiophene) (PEDOT) 6

1.1.1.3. Polyfuran (PF) 7

1.1.1.4. Polyselenophene (PSe) 8

1.1.1.5. CP nanomaterials 9

1.1.1.5.1 1D CP nanomaterials 11

1.1.1.5.1.1 Self-degradation method 12

1.1.2. Graphene 13

1.1.3. Graphene/conducting polymer nanohybrid mateirals 16

1.1.3.1. Non-covalent graphene-CP nanohybrids 18

1.1.3.2. Covalent graphene-CP nanohybrids 26

1.1.4. Sensor application 28
1.1.4.1. Chemical sensor 30
1.1.4.1.1. Hazardous and toxic gases sensor 31
1.1.4.2. Liquid-ion gated FET-type biosensor 33
1.1.4.2.1. H_2O_2 FET-type biosensor 35
1.1.4.2.2. Glucose FET-type biosensor 37
1.1.4.2.3. Hg^{2+} FET-type biosensor 38
1.1.4.3. Piezotronic sensor 39

1.2. Objectives and Outlines 42
1.2.1. Objectives 42
1.2.2. Outlines 43

2. EXPERIMENTAL DETAILS 45

2.1. RGO/PPy NT hybrid materials 45
2.1.1. Fabrication of polypyrrole nanotube embedded reduced graphene oxide transducer for field-effect transistor-type H_2O_2 biosensor 45
2.1.1.1. Prepartation of PPy NTs 45
2.1.1.2. Prepratation of RGO/PPy NT hybrids 46
2.1.1.3. Fabrication of RGO/PPy NT composite FET sensor 47
2.1.1.4. Characterization of RGO/PPy NT hybrids 48

2.2. RGO/C–PPy NT hybrid materials 49
2.2.1. Fabrication of carboxylated polypyrrole nanotube wrapped graphene sheet transducer for field-effect

transistor-type glucose biosensor 49
2.2.1.1. Preparation of C–PPy NTs 49
2.2.1.2. Preparation of RGO/C–PPy NT hybrids 50
2.2.1.3. Fabrication of RGO/C–PPy NT composites FET sensor 51
2.2.1.4. Characterization of RGO/C–PPy NT hybrids 52

2.3. RGO/PF NT hybrid materials 53
2.3.1. Fabrication of reduced graphene oxide-polyfuran nanohybrid for High-performance Hg^{2+} FET-type sensors 53
2.3.1.1. Prepration of PF NTs 53
2.3.1.2. Prepration of RGO/PF NT hybrids 54
2.3.1.3. Fabrication of RGO/PF NT composite FET sensor 55
2.3.1.4. Characterization of RGO/PF NT hybrids 56

2.4. RGO/PSe nanohybrid materials 57
2.4.1. Fabrication of graphene/polyselenophene nanohybrid materials for highly sensitive and selective chemiresistive sensor 57
2.4.1.1. Preparation of RGO/PSe nanohybrid materials 57
2.4.1.2. Characterization of RGO/PSe nano hybrid materials 58

2.5. CVD graphene/PEDOT/P(VDF-HFP) nanohbyrid mateirals 59
2.5.1. Prepatation of CVD graphene/free-standing PEDOT nanofiber/P(VDF-HFP) nanohbyrid materials 59
2.5.1.1. Prepatation of CVD graphene/free-standing PEDOT

nanofiber/P(VDF-HFP) nanohbyrid materials 59
2.5.1.2. Characterization of CVD graphene/PEDOT/P(VDF-HFP) nanohybrid materials 61

3. RESULTS AND DISCUSSION 62

3.1. Fabrication of polypyrrole nanotube embedded reduced graphene oxide transducer for field-effect transistor-type H_2O_2 biosensor. 62

3.1.1. Fabrication of RGO/PPy NT hybrid materials 62
3.1.2. Electrical performance of RGO/PPy NT hybrid materials 70
3.1.3. FET-type H_2O_2 biosensor based on RGO/PPy NT hybrid materials 73

3.2. Fabrication of carboxylated polypyrrole nanotube wrapped graphene sheet transducer for field-effect transistor-type glucose biosensor 80

3.2.1. Fabrication of RGO/C–PPy NT hybrid materials 80
3.2.2. Electrical performance of RGO/C–PPy NT hybrid materials 88
3.2.3. FET-type glucose biosensor based on RGO/C–PPy NT hybrid material 91

3.3. Fabrication of reduced graphene oxide-polyfuran nanohybrid for High-performance Hg^{2+} FET-type sensors 100

3.3.1. Fabrication of RGO/PF NT hybrid materials 100

3.3.2. Electrical performance of RGO/PF NT hybrid materials 106
3.3.3. FET-type Hg^{2+} biosensor based on RGO/PF NT hybrid materials 110

3.4. Fabrication of graphene/polyselenophene nanohybrid materials for highly sensitive and selective chemiresistive sensor 117
3.4.1. Fabrication of RGO/PSe nanohybrid materials 117
3.4.2. Fabrication of chemiresistive sensor based on RGO/PSe nanohybrid materials 127
3.4.3. Chemiresistive sensing performance of the RGO/PSe nanohybrid film 130

3.5. Fabrication of graphene/free-standing nanofibrillar PEDOT/P(VDF-HFP) hybrid device for wearable and sensitive human motion detective piezo-resistive sensor 135
3.5.1. Fabrication of CVD graphene/free-standing nanofibrillar PEDOT/P(VDF-HFP) nanohbyrid devices 135
3.5.2. Sensing performance of E-skin device 143
3.5.3. Practical application of E-skin device 147

4. CONCLUSIONS 156

REFERENCES 162

국문초록 180

1. INTRODUCTION

1.1. Background

1.1.1. Conducting polymers

During several decades, π-conjugated conducting polymers (CPs) have actively investigated due to their unique and outstanding properties.[1−6] Since the discovery of polyacetylene in 1977, various kinds of CPs have been continuously studied, such as polypyrrole (PPy), polyaniline (PANI), polythiophene (PT), poly(3,4-ethylenedioxylthiophene) (PEDOT), polyfuran (PF), polyselenophene (PSe), and poly(para-phenylene vinylene) (PPV). CPs have polyconjugated system, consisting of alternating single (σ bond) and doulble (π bond) bonds, and these π-conjugated cahins regard as determining the mechanical and optoelectrical properties of conducting polymers. In general, the conjugated length, the intra-/inter-chain interaction, and the extent of disorder are the crucial parameters for the physical properties of CPs.

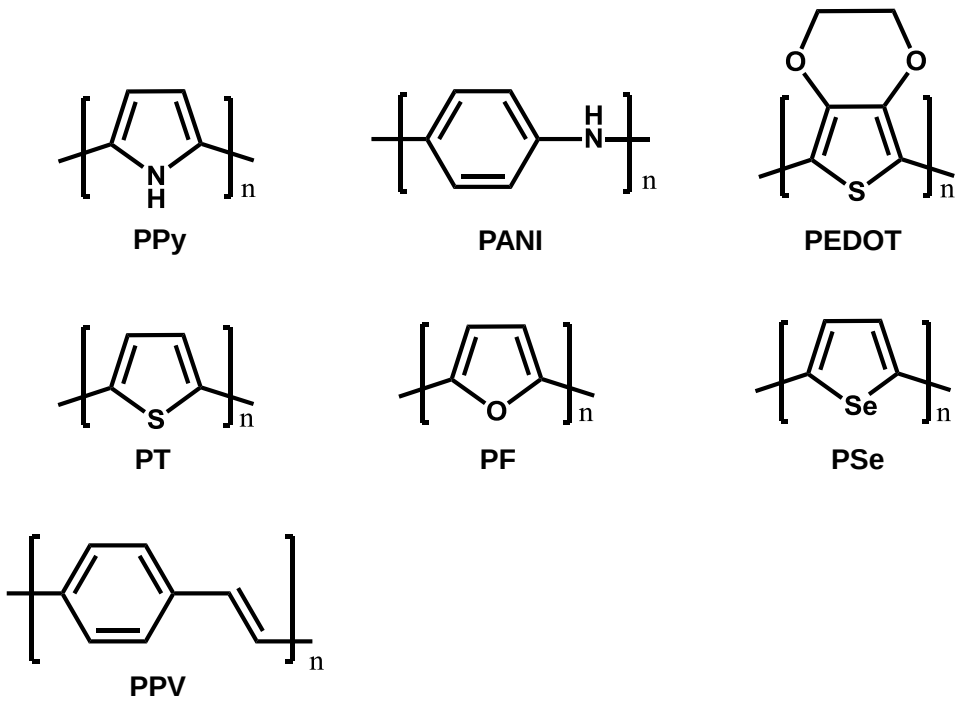

Figure 1. Typical conducting polymer structures (undoped form).

1.1.1.1. Polypyrrole (PPy)

Among of the CPs, polypyrrole (PPy), which was firstly synthesized in 1912, is the one of the most frequently used in practical applications, owing to excellent conductivity, biocompatibility, and good long-tem stability.[7–10] The structure and ability of charge transport of CPs are the key factors to determin the electrical conductivity. Charge transport relies on the charge carrier, which carries electric charges in electrical conductors. Charge carriers ared dividied two types: i) electron and ii) hole transport. This is determined by the spin number of the charge carriers. However, the charge carrier in PPy is spinless and has a positive sign, indicating that PPy does not have unpaired electron. To describe the electornic phenomena in PPy, new existence of the charge carrier finally indentified, called biploaron. The oxidation level of the PPy chains resolves the concentration of charge carrier in PPy. In neutral phase, the PPy has benzoniod-like structure, as shown in Figure 2. PPy, in neutral state, acts as an insulator because the bandgap is too wide for electrons in valence band to jump to conduction band at room temperature (RT) without any irritation. When oxidation reaction occurs in PPy structure, one electorn is removed from a neutral segment of PPy chain. To stabilize the state, electronic and structure rearrangement happen on the polymer backbone, resulting in formation of polaron. Two localized

electronic levels in the band gap was caused by the presence of the polaron on the chain. When another electron is extracted from the same segment of PPy chain, bipolaron (doubly charged state) was formed. A bipolaron, which is a pair of delocalized positive charges, extens over about four pyrrole rings (conjugation length). This conjugtation length depends on oxidation state, which means that the energy obtained by the distortion into bipolaron state is larger than the Coulomb repulsion between the two positive charges. However, the lower energy of bipolaron state is empty, indicating that the species has a spin of zero. A bipolaron enable to jump along the PPy chain through the reaarangemnt of double and single bonds in the PPy backbone structure. Thus, the PPy, in oxidized state, can transfer charge.

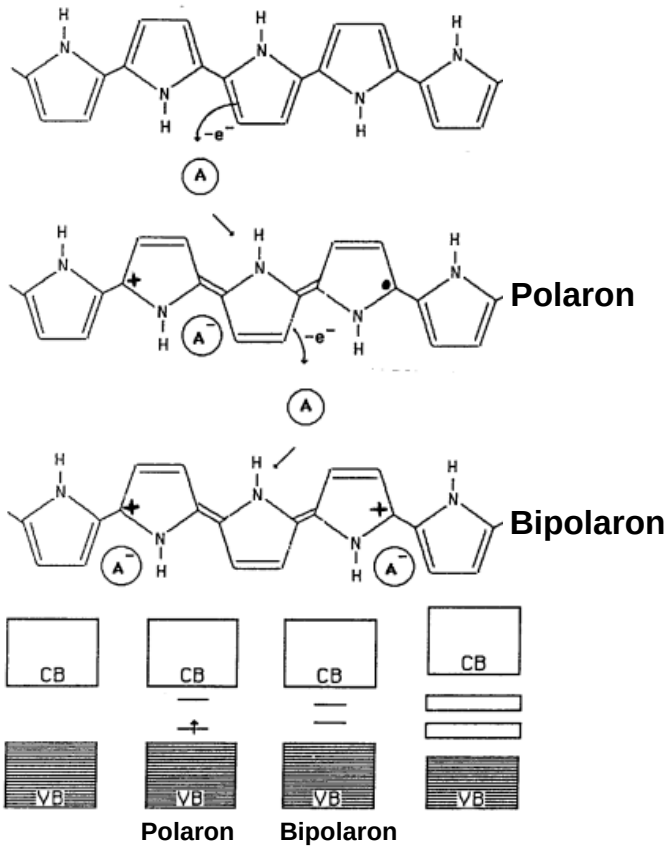

Figure 2. Electronic band model of PPy: Neutral, Polaron, and Bipolaron state. Reprinted with permission from reference [8].

1.1.1.2. Poly(3,4-ethylenedioxythiophene) (PEDOT)

PEDOT had been developed by the Bayer AG research laboratories in Germany for the 1980s.[11–13] The PEDOT has been considered as one of the most promising candidates for the paractical optoelectirnoc applications, due to its superior conductivity, electro-chemical properties, and air stability.[14–15] tandard oxidative or electrochemical polymerization methods were used for the synthesis of the PEDOT. Altohough it is insoluble polymer in the aqueous and organic solution, it showed unique characteristics, including high conductivity (*ca*. 300 S cm^{-1}), transparency in oxidized thin film, and remarkable stability in an oxidized state. To solve the solubility problem, a water-soluble polyelectrolyte, such as PSS, was used as the charge balancing dopant during polymerization.[16–18] The hybridization of PEDOT and PSS material exhibited a water-soluble CP, which formed good uniform film: conductivity (*ca.* 10 S cm^{-1}), high visible light transmittance, and good stability. The novel electrical properties of versatile functionalized PEDOT nanostructures have been reported.

1.1.1.3. Polyfuran (PF)

Nanoscale conducting polymers (NCPs) have many advantages, such as ease of fabrication, good biocompatibility, and high conductivity.[19–22] Among these materials, few examples of polyfuran (PF) have been reported. PF exhibited interesting properties compared with other CPs, especially PT and PPy, such as higher rigidity, better solubility, better packing, and higher fluorescence.[23–25] In addition, the computational studies suggest that PFs show a greater quinoid character and lower ionization energies than the corresponding PT, owing to the higher energy of their HOMO. These results are in agreement with experimental observations with respect to their extensive conjugation and good charge delocalization along the PF backbone. In spite of these outstanding properties, no study related to the control of PF nanoscale morphology and its functional group exists, owing to the limited availability of PF synthetic method and the poor solubility.

1.1.1.4. Polyselenophene (PSe)

Polythiophenes (PTs) are the most studied conducting polymers.[26–30] However, altohou the lots of papers published on PT and its derivates, few reports are known about its close analogue, PSe and its derivates. The outstanding properties of PTs propose that PSe can be a significant member of the CP family.[31–33] The possible advantages of PSe are anticipated, due to the unique properties of the Se atom and selenophene: (i) intermolecular Se-Se interactions, leading to a wide bandwith in organic conductors, enable to enforce inter-chain charge transfer. (ii) Selenophene monomer shows lower oxidation and reduction potentials than thiophene, resulting in lower oxidation and reduction potentials of PSe. (iii) The Se atom is more facily polarized than sulfur, which means that PSe can become more easily polarized than PTs. (iv) PSe can accommodate greater charge on doping than PS owing to the larger size of the Se atom compared with the S atom of PT. (v) PSe has a lower band gap than PT and, consequently, the absorption wavelgnth exhibits different trandency those of PT, leading to different optoelectronic performance compared those of PT. Nerverthless, PSe has attracted surprisingly sparse attention.

1.1.1.5. CP nanomaterials

A growing interst in nanostructured materials in the range of 1 to 100 nm has been shown because of their unique characteristics of nanomaterials, including electrical, mechanical, optical, and chemical performances.[34–37] The quantum-confinement effect occurred due to their discrete or quantized electronic levels on the nanomaterials. Over the last decades, various nanomaterials (carbon nanotubes (CNTs), quantum dots (QDs), catalysts/magnetic nanoparticles (NPs), and inorganic semiconductor nanocrystals (NCs)), have been actively investigated and published.[38–42] Yet, the preparation of CP nanomaterials has been unexploited relatively. In comparison with their large-scale counterparts, CP nanomaterials exhibit higher surface areans and smaller dimension, leading to superior chemical and physical properties.[43–45] These merits of CP nanomaterials have intrigued to chemists and physicist for decades. Interstingly, the electrical properties of CP nanomaterials, such as oxidation level, conjugation length, and doping level, depend highly on their shapes, including nanofibers (NFs), nanorods (NRs), nanotubes (NTs), or NPs. General methods, including soft and hard template, and template-free methods, have been used to synthesize and fabricate the shape of CP nanomaterials. Despite various shapes of CPs synthesized by using the template-assisted methods, several problems occurred to use as electrod

materials in energy and environmental applications: (i) There are lack of technologies to remove either hard or soft templates completely from the reaction medium. (ii) The electrical properties of CP could be reduced due to the remmant templates. (iii) In case of the template-free system, doping agents, the amounts of monomers, and oxidizing agents used may highly affect the formation of nanostructured CPs. The facts, which were the effects of the oxidizing agent/monomer ratior on the conductivity of CPs, were reported. However, optimizing synthetic condition for specifically controlled CP nanomaterials is still required. Thus, the novel synthetic method, for the high-quality CP nanomateirals with high conductivity and desirable morphologies, should be developed to use in practical applications.

1.1.1.5.1. 1D CP nanomaterials

One-dimensional (1D) nanomaterials, which show high charge carrier mobility along the long-axis, can be used for highly sensitive sensors.[46–48] Among various 1D nanomaterials, the remarkable physical and chemical characteristics of 1D CPs at the nanometer scale offer exceptional sensing performance in biosensor applications. These 1D CP nanomaterials boast several advantages, including facile functionalization and biocompatibility.[49–50] However, there has rarely been inverstigated to use these materials in the sensing appliactions.

1.1.1.5.1.1. Self-degradation method

The self-degrdation method for fabrication of CP NT has been reported in 2005 by Yang. et. al.[51] This method is facile, simple, and environmental friendly because synthetic method is under the aqueous solution condition. To fabricate the CP NTs by using self-degrdation method, firstly, the iron (Ⅲ) chloride and methyl orange (MO) were mixded in the aqueous solution and form temporary nano-template. After inject the CP monomer, the polymerization took place on the surface of the nano-template. Then, the nano-template was removed via exceed aqueous solution with vigorous stirring condition. Most of soft or hard template mathods required strong acid condition to remove the template, such as HF or HCl. In addition, the fabricated CP NTs have uniform size (approximately 70 nm) and large-scaled production (yield ~ 76 %).

1.1.2. Graphene

Graphene is a two-dimensional hexagonal honeycomb lattice of sp2-hybridized carbon with one-atom thick planar sheet.[52–53] Graphene has shown the possibility of using a next generation elcetronic material owing to its exceptional properties, such as high current density, thermal conductivity, ballistic transport, chemical inertness, optical transmittance and super hydrophobicity at nanometer scale, as shown in Figure 3.[54–56] Although graphene was only isolated for the first time in 2004, it has been extremely investigated during the last several years. The 2010 Nobel Prize in Physics was given to Andre Geim and Konstantin Novoselov due to the groundbreaking work on graphene. After that time, the rapid and fast uptake of interest in graphene is observed because of primarily to lots of outstanding properties that it has been found to possess. Intrinsic graphene has semie-metal or zero gap semiconductor properties, and offers a startlingly low absorption ratio of 2.3% of whift light, with an exceptionally high opacity for an atomic monolayer. Excellent high electron mobility at RT was reported throught the experimentally reported values in excess of 15,000 $cm^2 V^{-1} s^{-1}$.

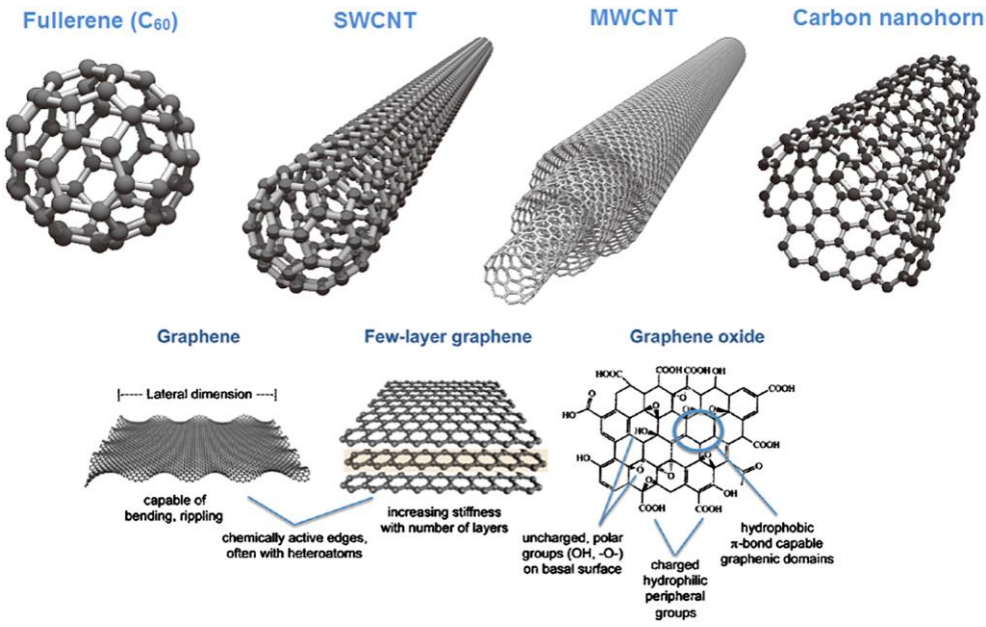

Figure 3. Structures of various important carbon nanomaterials: fullerene (C_{60}), single-walled carbon nanotube (SWCNT), multi-walled carbon nanotube (MWCNT), carbon nanohorn, graphene, few layer graphene and graphene oxide. Reprinted with permission from reference [52].

The graphene resistivity was reported 10^{-6} ohm–cm in the experimental value, which means that it was less than that of silver and the lowest resistivity substance known at RT.

Abnomal electrical performance of graphene have been deviced to use future electronics, including field emitter, ballistic transistors, components of integrated circuits, transparent conducting electrodes and sensors.[57–60] Graphene has not only a high electron or hole mobility, but also low Johnson noise. Electornic noise occurred by the thermal agitation of the charge carriers inside an electrical conductor at equilibrium, which generates regardless of any applied voltage. These characteristics allow to be used as the transducer in a field-effect transistor (FET). Graphene shows a superior sensor due to combination of outstanding electrical property and low noise. The 2D structure of graphene could efficiently detect adsorbed moleucles. Furthermore, the excellent electrical conductivity and optical transparency introduce the graphene to use the practical applications, including transparent conducting electrodes, touch-screens, liquid crystal displays, organic photovoltaic cells and organic light-emitting diodes (OLEDs).

1.1.3. Graphene/conducting polymer nanohybrid mateirals

To optimize the properties and performances of nanocomposites for using in the practical applications, a variety of graphene-based polymer nanohybrid materials have been developed, such as graphene–poly(methyl methacrylate) (PMMA) composites with improved flame-retardant property, graphene–epoxy composites with improved thermal conductivity, graphene–polypropylene composites with enhanced flexural properties and lower percolation threshold, graphene–polystyrene composites with increased viscosity and enhanced mechanical properties, graphene–poly(vinyl alcohol) composite with enhanced mechanical strength, graphene–thermoplastic polyurethane composite with increased optical/electric properties, graphene–nyloncompositeswithincreasedelectrical conductivity, graphene–poly(sodium 4-styrenesulfonate) (PSS) with improved dispersibility, and graphene–polyaniline (PANI) composites with increased capacitance.[61–65]

The advantages of graphene-CP nanohybrid materials offer platforms for versatile electronic device applications.[66–68] The graphene–CP nano-composites are simply divided into two categories: non-covalent and covalent nanocomposites. Water-soluble and organosoluble CPs, including PANI, PPy, PT and P3HT, were used to non-covalently modify graphene via secondary bonding interactions, such as π-π interaction or hydrogen interactions. On the

other hand, functional groups treated CPs ((e.g.–NH_2, –MeOH, etc.), including triphenylamine-based poly-azomethine (TPAPAM), P3HT and fluorene-, thiophene-, benzothiadiazole-based copolymers, were covalently attatched to surface of graphene to form nanohybrid materials.

1.1.3.1. Non-covalent graphene-CP nanohybrids

Micro- and nano-electronic devices based on the graphene-based nanohybrid materials request the preservation of the intrinsic electrical properties of graphene in the devices as well as demands the easy integration and homogeneous distribution of the graphene-based materials in various matrices. In this regard, the non-covalent functionalization of graphene with CPs, which is a non-destructive method occurring between the basal plane of graphene and CPs and modifies the graphene without significantly altering its chemical structure, is preferred as a facile way to obtain dispersive graphene–CP nano-composites for device applications.[69–70]

To prepare graphene nanohybrid materials, non-covalent interaction is frequently applied. Non-covalent interactions between organic molecules and graphene enable to easily attatch the organic species on graphene surfaces. Small molecules, including surfactants and polymers, can interact with graphene surfaces via secondary bonding interactions, such as π–π stacking, or electrostatic or hydrophobic interactions, supplying useful way to modify graphene surfaces for fabricating graphene nanocomposites.[71–72] Small molecules, including 1-pyrenebutyrate (PB^-), 3,4,9,10-peryl-enetetracarboxylic diimide bisbenzenesulfonic acid, sodium dodecylbenzene sulfonate, 1-pyrenecarboxylic acid, and dendronized perylene bisimides, can be

conveniently used to modify graphene. Highly water-soluble graphene was obtained by utilizing PB^- due to strong π-stacking intecations between graphene surfaces and pyrene moiety in the molecule, as shown in Figure 4.

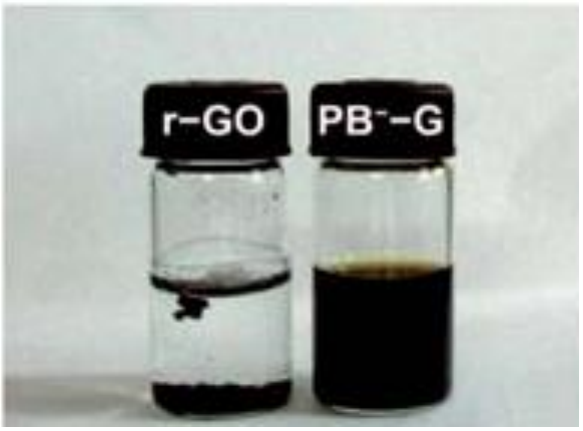

Figure 4. Photo image of rGO and graphene with PB^- materails. Reprinted with permission from reference [72].

Recently, graphene-CP nanohybrid mateirals have been actively investigated due to the synergitic effects, including enhanced conductivity, charge transport behavior, surface area, mechanical property, and chemical stability.[66–68] These mateirals could be utilized in various field appliactions, such as sensors and energy storage devices, as shown in Figure 5, 6, and 7.[66–70] In case of energy storage devices, graphene with CPs nanocomposites show fast electron/ion transport in electrodes, and electrochemical stability, which lead to improved supercapacitance or lithium-ion battery performances. Furthermore, the CPs exhibit psudocapacitor behavior in the supercapacitor system, which is oxidation or reduction operation on the CPs. On the other hand, carbon materials, including graphene and CNTs, show electric double layer capacitor (EDLC) behavior upon using in the supercpacitors. Thus, the graphene-CP nanohybrid materials display the combination EDLC and pesudocapacitor behaviors, leading to improved the supercapacitor performance. In another case, the strain sensor, the hexagonal honeycomb structure may be partially destroyed near the edges of the film under tensile stress, resulting in altering its electronic band structure and lead to a significant change in resistance, termed the piezo-resistive effect. Nowadays, reduced graphene oxide (RGO)/polyvinylfluoride (PVDF) nanohybrid materials show large Young's moduli and are optically transparent and mechanically flexible, leading to large

GF value.[73] Graphene-CP nanohybrid materials, in the biosensor appliaction, have exceptional charcateristics such as enhanced surface area and conductivity. Especially, increased surface area brings the high performance sensing behavior due to improved reactive binding sites between the anlyate and graphene-CP nanocomposites in biosensor applications.[74–79]

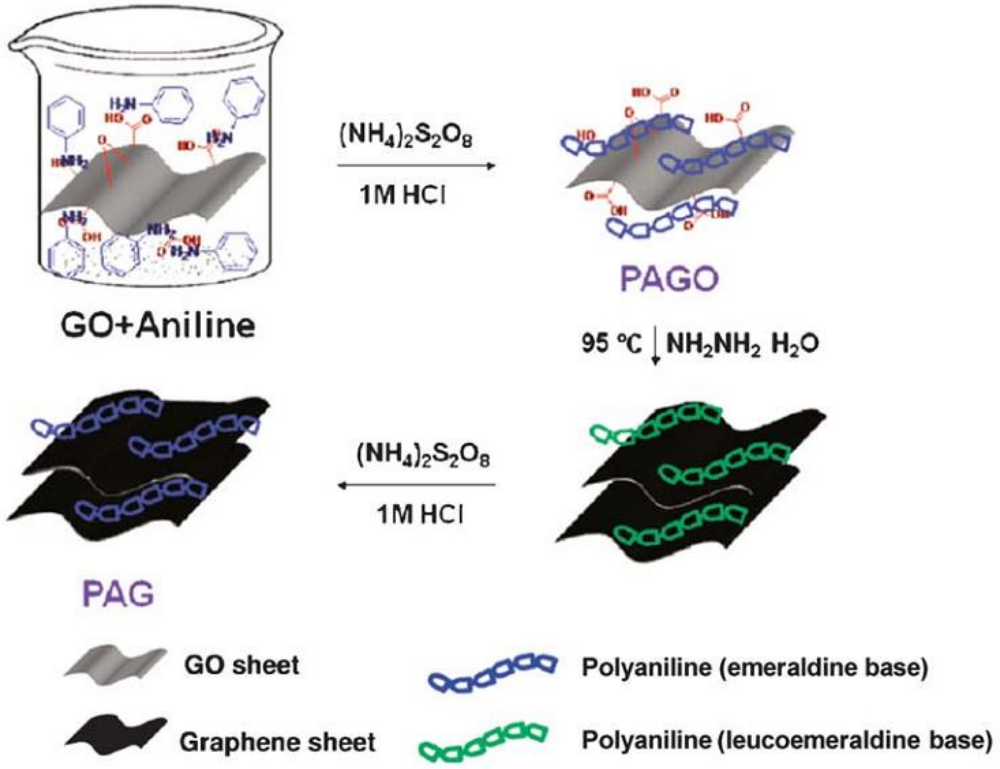

Figure 5. Illustration of the process for preparation of rGO–PANI composites. Reprinted with permission from reference [68].

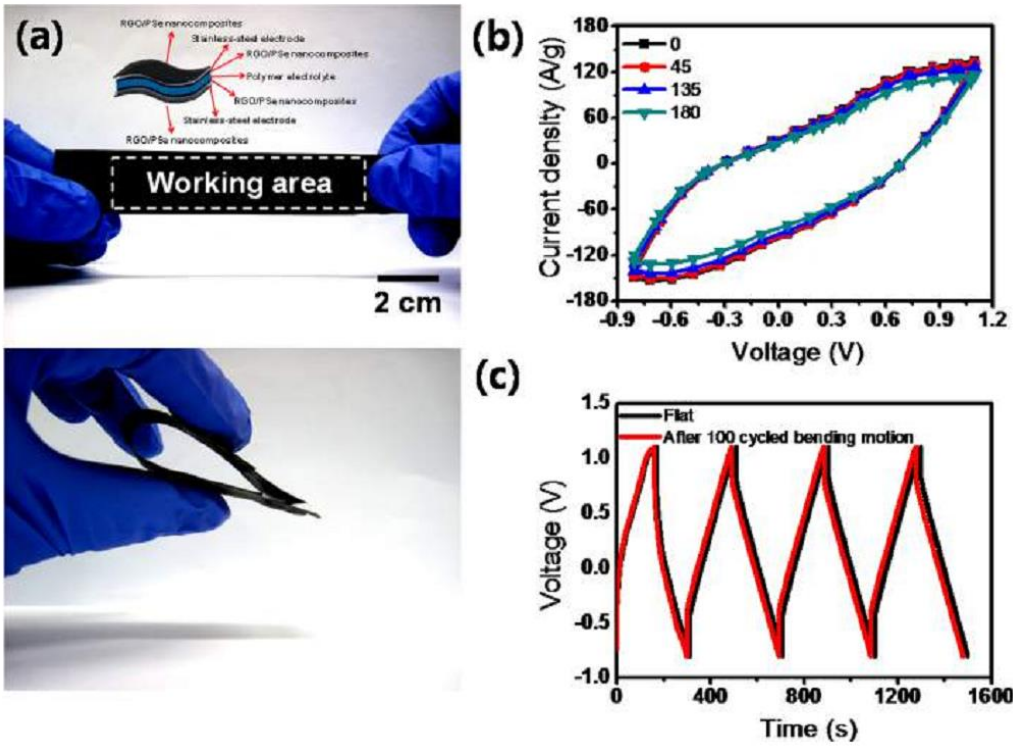

Figure 6. (a) Photograph of the all solid-state supercapacitor. (The inset is a schematic image of the solid-state supercapacitor.) (b) CV curves at 200mV s^{-1} with various bending angles and (c) galvanostatic charge−discharge curves at a current density of 4 A g^{-1} before (black) and after 100 bending cycles (red). Reprinted with permission from reference [81].

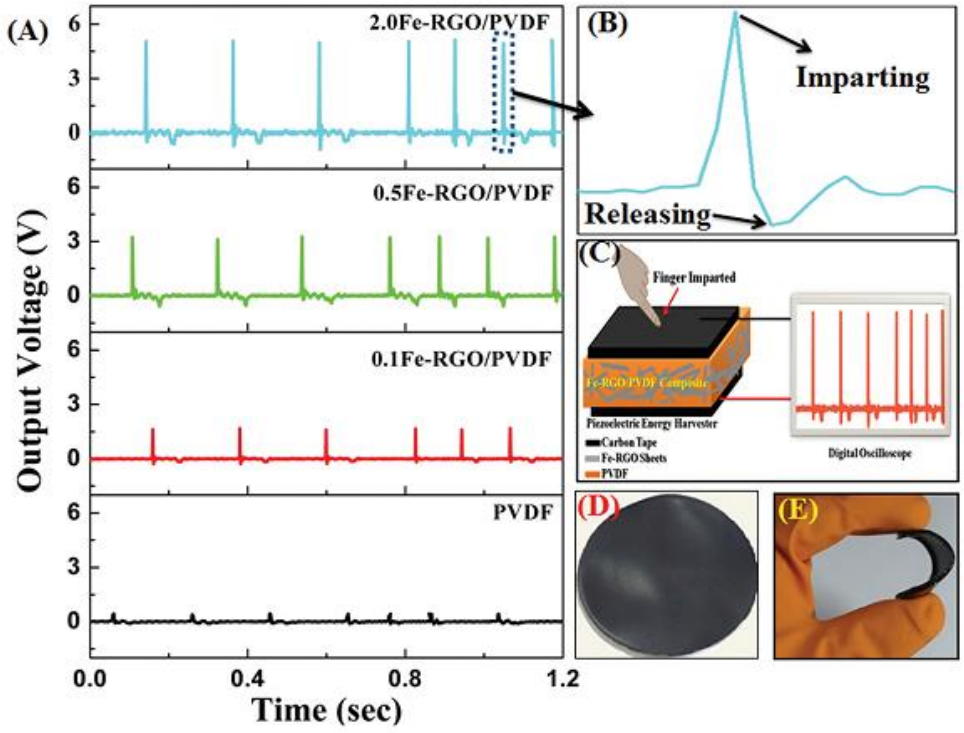

Figure 7. (A) Output voltage generation (human finger (B) touch and release response) from the ECE made with PVDF, 0.1Fe-RGO/PVDF, 0.5Fe-RGO/PVDF and 2.0Fe-RGO/PVDF nanocomposite films, and (C) schematic diagram for measuring the human finger response signal (voltage) for the Fe-RGO/PVDF film. Photograph of (D) the Fe-RGO/PVDF nanocomposite film and (E) a demonstration of the flexibility. Reprinted with permission from reference [82].

1.1.3.2. Covalent graphene-CP nanohybrids

Contrary to the non-covalent functionalization, covalent functionalization is another approach for the preparation of graphene–CP nanocomposites. In this method, CPs were covalently bindined to graphene via chemical reactions between the functional groups of CPs and those of GO or rGO. GO, which has lots of reactive oxygenated groups on its basal plane or edge, is the promising candidate for covalent grafting. For example, GO was covalently bindied onto TPAPAM containing the terminal $-NH_2$ group through the surface-bonded acyl chloride moieties (GO–COCl) for the rewritable memory device application.[83] This device exhibited nonvolatile rewritable memory effect and a typical bistable electrical switching, with an ON/OFF current ratio of over 10^3 at a turn-on voltage of ca. −1 V. Both the ON and OFF states were stable under a constant voltage stress, and survived up to 10^8 read cycles at a read voltage of −1.0 V. In another case, poly[{9,9-di(triphenylamine)fluorene}(9,9-dihexylfluorene)(4-aminophenylcarbazole)]) (PFCz) with NH_2-terminated side chains, was synthesized and also binded onto GO through the reaction with GO–COCl producing a soluble GO–PFCz nanohybrid material, as shown in Figure 8b.[84] The ON state of the GO–PFCz, in the memory device, is able even to withstand a constant voltage stress of −1 V for 3h. Except the memory device appliactions, GO–CP nanocomposites

were used in the photovoltaic devices. The GO sheets were covalently anchored with the MeOH-terminated P3HT chains through the esterification of carboxylic groups in GO.[85] The photovoltaic device based on the fabricated GO–P3HT nanohybrid material exhibited a 200% enhancement in the power conversion efficiency (0.61%) with respect to its P3HT/C60 counterpart under AM 1.5 illumination (100 mW cm^{-2}). In addition to GO, the surface of rGO can also be modified by CPs to form useful electronic materials. For instance, uorene-, thiophene-, and benzothiadazole-based copolymers were covalently anchored to the surface of rGO sheet and used in the optical-limiting device application.

1.1.4. Sensor application

To detect some characteristic environmental elements, sensor, a transducer device, is developed and composed of an active sensing material with a signal transducer. There are the roles of two important components in sensor system: (i) sensor transmits signal without any amplification from a selective compound, and (ii) from a change in a reaction. The sensor devices offer the thermal, electrical or optical output signals, which were able to be converted to digital signals for subsequent processing. Several types of sensor devices with source of target analyte were existed, including chemical-, bio-, and mechanical-sensor (e.q., pressure and strain sensor). The chemical sensor enables to offer information about the chemical component with a liquid or gas phase in the environment. The measureable physical signal, which ire related with the concentration of a certain analyte, is provided as the information. On the other hand, the biosensor detects biological component analytes, including protein, cells, and nucleic acid or biomimetic polymers. The mechanical sensor is a device that operates and respond to pressure or strain like forces. Recently, the electronic-skin (E-skin) device is operated based on the mechanical sensing mechanism.

Several critical elements for highly eefcetive sensor devices are required: (i) high sensitivity; ii) high selectivity to target analyte; iii) fast

response/recovery time; iv) cycle stability; and v) low working temperature. To satisfy these demands, sensor electrode based on the nanomaterial has been emerged as promising candidates due to its small size, including high surface to volume ratio and unique optical/electrical properties.

1.1.4.1. Chemical sensor

In the realm of chemical sensing device, resistive chemical sensors (i.e., chemiresistive sensor), which respond chemical information by means of two point contact electrical resistance changes, are the one of the most studied promising transduction mechanisms for conductive nanomaterials based systems.[86–91] This system is largely used in the practical field, owing to the fact that detecting the change of electrical resistance is one of the simplest methods to analyze requiring minimal supporting electronics for compact, deployable, self-contained systems. Among of the various chemiresistive sensing systems, interdigitated array (IDA) based chemiresistive sensors have several advantages to utilize the chemical sensing device. (See Figure 8) First, it shows high sensitivity and rapid response time than other sensing systems, due to fast siganal transfers from transducer materials to the electrode. Another merit is the simple and facile interpreted measurement with real-time monitoring chaing resistance of the signals during target analyte detection. Furthermore, the cycle stability is the one of the other strengths without any defect and destruction during repeated target chemical sensing.

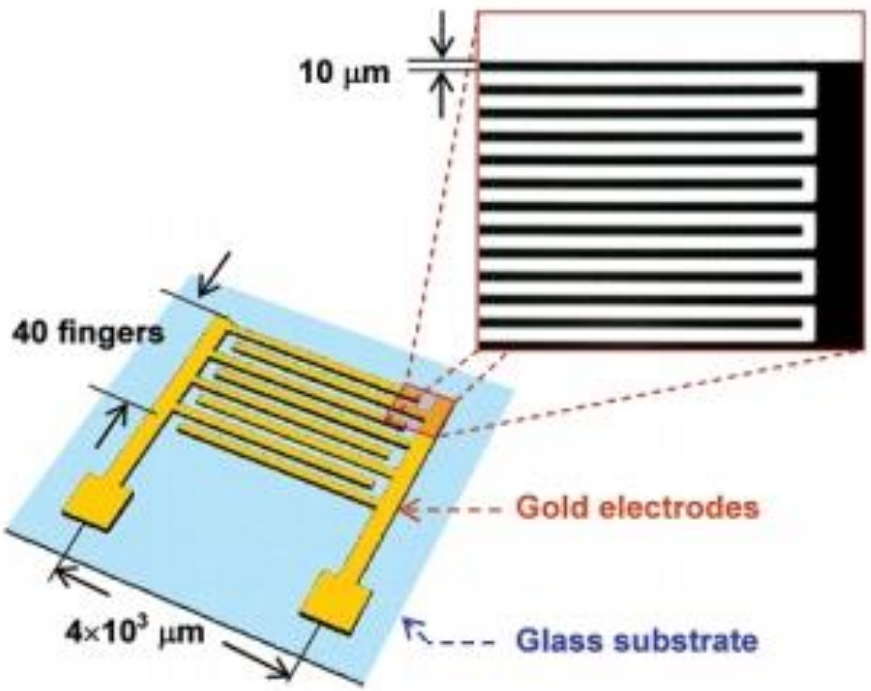

Figure 8. Illustration of IDA chemical sensing device. Reprinted with permission from reference [88].

1.1.4.1.1. Hazardous and toxic gases sensor

Environmentally harzardous and toxic gases, including hydrogen sulfide (H_2S), carbon monoxide (CO), and ammonia (NH_3), and volatile organic compounds (VOCs), such as acetone (CH_3COCH_3), ethanol (C_2H_5OH), and ethane (C_2H_6), have been detected in the exhaled breath of healthy subjects and patients with respiratory diseases.[92–95] In particular, NH_3 is a widely utilized gas with a colorless and unique pungent odor. In spite of its usefulness, when its concentration surpasses the 25 ppm, it is danger and hazardous to humans. Thus, effective and efficient methods with inexpensive systems are required to detect of hazardous gases like NH_3 for preventing adverse effects.

1.1.4.2. Liquid-ion gated FET-type biosensor

Biosensor, consistin of a biological sensing element including antibody, cell, receptor, and aptamers, detects bio-target analyte through binding with transducer (e.x., conductive nanomaterials).[96–102] To detect a target analyte, selectively molecular recognition occurs at the analyte-biological element anchored to transducers from a nonelectrical domain to an electrical signal. Then, a change in the electrical property at the sensing transducer is detected via the binding of the analyte.

FETs have attracted interest as primary candidates for fabricating state-of-the-art sensor platforms due to their ability to achieve high current amplification while maintaining a relatively high signal-to-noise (S/N) ratio.[103–105] Compared with other conventional films, CP nanomaterials have remarkable physical and chemical characteristics derived from anisotropic electronic properties, high surface area, and small dimensions, as shown in Figure 9.

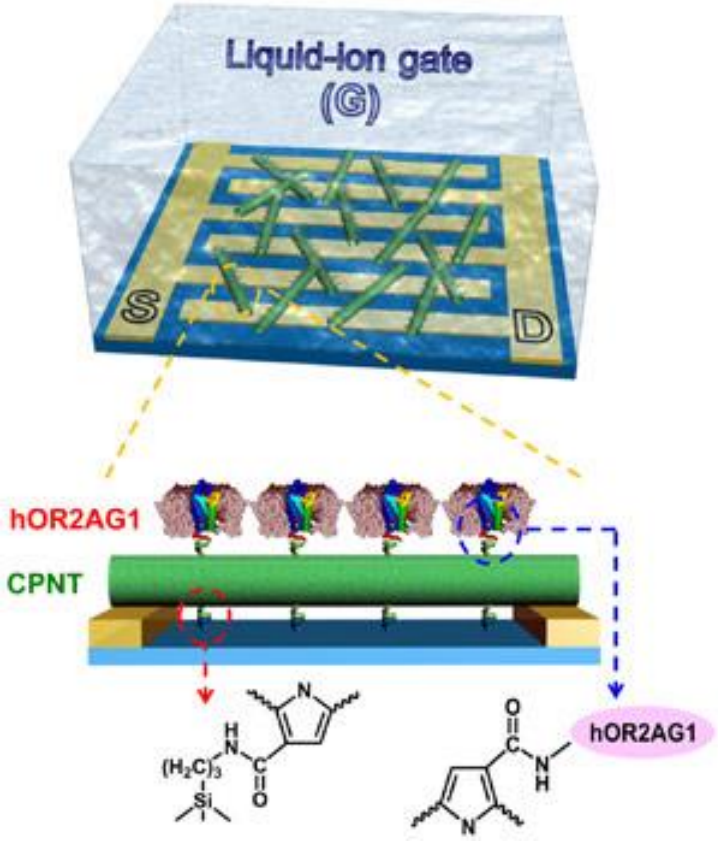

Figure 9. Illustration of liquid-ion gated FET sensing device. Reprinted with permission from reference [104].

1.1.4.2.1. H_2O_2 FET-type biosensor

Detecting hydrogen peroxide (H_2O_2) is an important challenge for applications including food science, healthcare, pharmaceutical science, and environmental monitoring.[107–110] H_2O_2, called reactive oxygen species, has been linked to several bodily disorders, including atherosclerosis, cancer, and Alzheimer's disease.[111–113] In contrast, H_2O_2 is also a component in the physiological signaling pathways of healthy cells and is essential for cell growth, immune system function, migration, and differentiation.[114–118] Thus, an accurate and sensitive means of detecting H_2O_2 is crucial for clinical diagnostics and patient monitoring. Several methods of detecting H_2O_2 have been proposed, such as various colorimetric, electrochemical, spectroscopic, and fluorescence-based methods.[119–122] Among these, electrochemical sensing of H_2O_2 has been most actively investigated due to its high sensitivity and specificity. Most electrochemical sensors, composed of enzymes or proteins, bind to H_2O_2. However, natural enzymes often suffer from limited stability, inefficiency, and sensitivity to environmental factors. Recently, metal nanomaterials, such as Ag, Au, Pt, and Pd NPs, have been studied as alternative electrochemical catalysts to construct non-enzymatic H_2O_2 sensors.[123–127] However, growing concerns with regard to rare resources, including noble metals, give rise to the development of low-cost, high-performance detection

systems for H_2O_2 in practical applications.

1.1.4.2.2. Glucose FET-type biosensor

Diabetes mellitus is considered to be one of the most serious diseases affecting human health in developed countries, with complications including increased risk of heart disease, kidney failure, and blindness.[128] The disease is caused when the body fails to regulate glucose levels. Therefore, accurate and sensitive glucose detection is important in the treatment and management of diabetes. Several detection methods have been proposed for glucose sensing, based on techniques including electrochemical, optical, and Raman spectroscopy.[129–132] Electrochemical sensing is particularly interesting due to the potential to create compact low-cost devices. However, such sensor devices require complicated electrode fabrication, surface modification, and/or synthesis of modifiers, including complexing agents. Thus, for using in practical application, the exploration and development of a simple, yet high performance glucose detection technology is extremely desirable.

1.1.4.2.3. Hg^{2+} FET-type biosensor

Mercury (Hg) has been used for decades as a chemical additive and energy source in industrial applications.[133] However, very low concentrations of Hg can be extremely toxic, both to human health and to the environment.[134–136] Hg has been linked to several fatal diseases, such as Minamata disease, pulmonary edema, cyanosis, and nephrotic syndrome.[137–140] Thus, an accurate and sensitive Hg detection method is important to the health care and environmental fields. Several methods have been developed for Hg sensing, including photoelectrochemical methods, colorimetric analysis, and oligonucleotide-based sensing.[141–146] These methods, however, have significant drawbacks, including slow response, high cost, complicated equipment requirements, and lack of high sensitivity and selectivity.[119–122] Recently, rapid and reliable Hg sensing performance has been reported for surface-functionalized electrochemical sensors.[147–149] However, these electrochemical sensors require complicated electrode fabrication, modification, and/or the synthesis of modifiers, such as complexing agents. Thus, the development of simple, high-performance Hg detection systems is desired.

1.1.4.3. Piezotronic sensor

Monitoring of physiological signals is an effective approach to the assessment of human health problems. This monitoring is currently limited to hospitals, as currently available devices, including infrared-based optical electronics and rigid multi-electrode pressure sensors, are not portable or wearable. Recently, flexible and stretchable artificial electronic skin (E-skin) has intensively studied due to its unique capability to detect subtle pressure changes, which may allow applications in wearable individual-centered health monitoring, sensitive tactile information acquisition, minimally invasive surgery, and prosthetics.[150–154] (See Figure 10) Over the last few years, flexible pressure/strain sensor devices based on nanostructured materials, such as SWNTs,[155] Si nanowires,[156] and vertical ZnO nanowire arrays,[157] have shown promising pressure-sensing performance in low-pressure regimes (<10 kPa).[123–126] In contrast to opaque, rigid metal/metal oxide nanowires, CPs have been demonstrated to be excellent candidates for flexible and wearable electronics, owing to their good biocompatibility, high conductivity and transparency, and physical robustness.[158–160] Despite their high pressure-sensing performance, such sensors are often mechanically unstable and have relatively small strain gauge factor (GF), which limits their ability to sense signals with small strain, such as pulse in the wrist. Free-standing

technology based on nanostructured CP is one approach to achieving mechanically stable and large GF sensor owing to enhancing contacting area and electrical performance, but significant challenges remain in vertical growth of nanostructured CPs with uniform morphology.

Graphene is a two-dimensional hexagonal honeycomb lattice of sp^2-hybridized carbon.[52–53] With tensile stress, the hexagonal honeycomb structure may be partially destroyed near the edges of the film, which can alter its electronic band structure and lead to a significant change in resistance, termed the piezo-resistive effect.[161–164] Recently, reduced graphene oxide (RGO)/PVDF nanocomposite materials, which have large Young's moduli and are optically transparent and mechanically flexible, have been found to have large GF value.[73] However, the aforementioned fabrication method requires multiple steps, time-consuming synthesis, and tightly restricted vacuum conditions, limiting its practical applicability. Thus, strain-sensing materials with a large GF that can be easily fabricated are desirable.

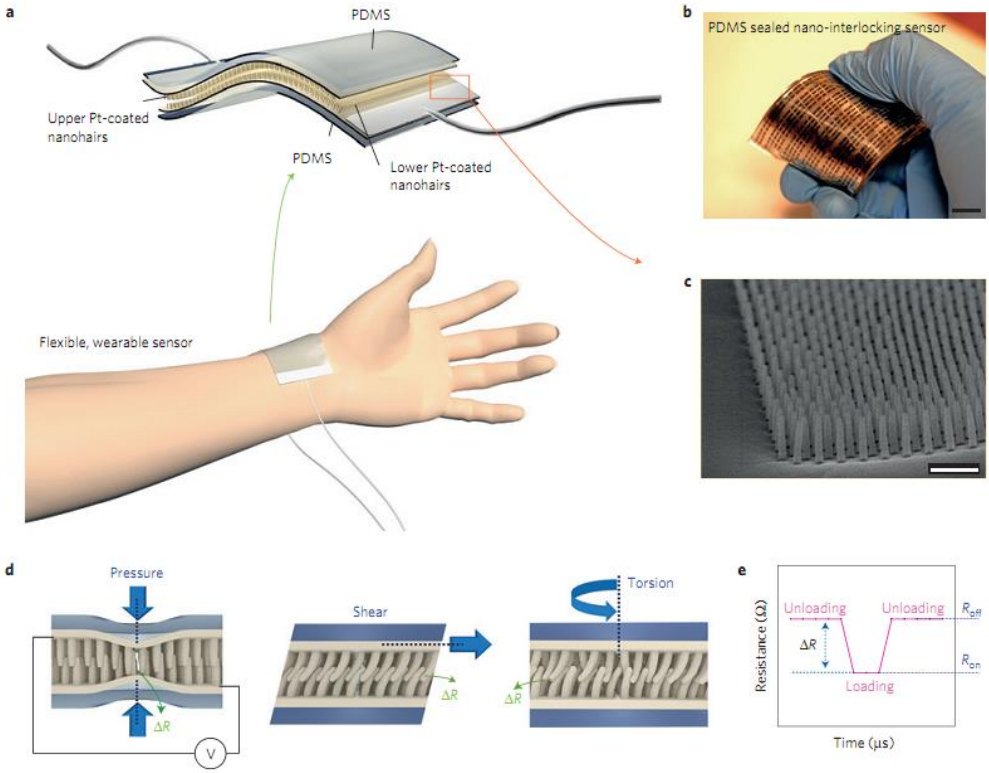

Figure 10. (a) Schematic of the assembly and operation of a flexible sensor layer sandwiched between thin PDMS supports (~500 μm thickness each). (b) Photograph showing the flexibility of the assembled sensor. Scale bar, 1 cm. (c) SEM image of a dense array of 50-nm radius nanohairs with AR = 10. Scale bar, 1 μm. (d) Schematic illustrations of the pressure, shear and torsion loads and their possible geometric distortions of the paired hairs. (e) Operation of a flexible sensor layer by means of recording of resistance change (Roff : unloading, Ron: loading). Reprinted with permission from reference [165].

1.2. Objectives and Outline of the Study

1.2.1. Objectives

In the preceding section, the importance of graphene/CP nanohybrid materials was introduced from the viewpoint of academic research and practical versatile sensing applications. The aim of this dissertation is to describe the fabrication of CP, graphene, and graphene/CP nanohbyrid materials by self-degradation, vapor deposition polymerization (VDP), in-situ polymerization methods. Furthermore, their applicable fields are also explored, including various sensors.

1.2.2. Outline

This dissertation involves the following subtopics:

I. Fabrication of polypyrrole nanotube embedded reduced graphene oxide transducer for field-effect transistor-type H_2O_2 biosensor
   1. Fabrication of RGO/PPy NT hybrid materials
   2. Electrical performance of RGO/PPy NT hybrid materials
   3. FET-type H_2O_2 biosensor based on RGO/PPy NT hybrid materials

II. Fabrication of carboxylated polypyrrole nanotube wrapped graphene sheet transducer for field-effect transistor-type glucose biosensor
   1. Fabrication of RGO/C–PPy NT hybrid materials
   2. Electrical performance of RGO/C–PPy NT hybrid materials
   3. FET-type glucose biosensor based on RGO/C–PPy NT hybrid materials

III. Fabrication of reduced graphene oxide-polyfuran nanohybrid for High-performance Hg^{2+} FET-type sensors
   1. Fabrication of RGO/PF NT hybrid materials
   2. Electrical performance of RGO/PF NT hybrid materials
   3. FET-type Hg^{2+} biosensor based on RGO/PF NT hybrid materials

IV. Fabrication of graphene/polyselenophene nanohybrid materials for highly sensitive and selective chemiresistive sensor
   1. Fabrication of RGO/PSe nanohybrid materials

2. Synthesis of RGO/PSe nanohybrid materials
3. Fabrication of chemiresistive sensor based on RGO/PSe nanohybrid materials
4. Chemiresistive sensing performance of the RGO/PSe nanohybrid film

V. Fabrication of graphene/free-standing nanofibrillar PEDOT/P(VDF-HFP) hybrid device for wearable and sensitive human motion detective piezo-resistive sensor

1. Fabrication of CVD graphene/free-standing nanofibrillar PEDOT/P(VDF-HFP) nanohbyrid devices
2. Sensing performance of E-skin device
3. Practical application of E-skin device

2. EXPERIMENTAL DETAILS

2.1. RGO/PPy NT hybrid materials

2.1.1. Fabrication of polypyrrole nanotube embedded reduced graphene oxide transducer for field-effect transistor-type H_2O_2 biosensor

2.1.1.1. Prepartation of PPy NTs

The preparation of PPy NTs was carried out using a self-degraded template method. $FeCl_3$ (0.243 g, 1.5 mmol) was added to a 5-mM methyl orange (MO) solution (sodium 4-[4′-(dimethylamino)phenyldiazo]phenylsulfonate in deionized water. After a flocculent precipitate appeared, the pyrrole monomer (105 μL, 1.5 mmol) was added, and the mixture was stirred at room temperature for 24 h. The resulting precipitate was purified by washing it with deionized water and methanol several times until the filtrate was colorless and had a neutral pH. The powdered PPy NTs (0.08 g, 79.5%) were then dried under vacuum at 60 ℃ for 24 h.

2.1.1.2. Prepratation of RGO/PPy NT hybrids

Graphene oxide (GO) was obtained from graphite powder using a modified Hummers and Offeman method.[166] GO was dispersed in water with a concentration of 0.06 mmol and then mixed with PPy NTs (also at a concentration of 0.06 mmol). The mixtures were ultrasonicated for 1 h. The resulting GO/PPy NT structures were exposed to 5 μL (35 wt %) of hydrazine solution for 1 h at 95 ℃, which reduced GO to RGO. The final product, an RGO/PPy NT composite (0.055 mmol, 91.7%), was obtained via filtration, purified using water, and dried in a vacuum oven at 25°C for hours.

2.1.1.3. Fabrication of RGO/PPy NT composite FET sensor

A microarray, consisting of 80 pairs of gold interdigitated microelectrodes, was patterned on a glass substrate using a 50-nm-thick Cr adhesion layer via a photolithographic process, resulting in electrodes with a gold layer thickness of 50 nm, a width of 10 μm, length of 4000 μm, and an interelectrode spacing of 10 μm. The microelectrode substrate was cleaned using sonication in ethanol. An aliquot of 0.1 mL of the ethanol solution containing 0.1 wt % RGO/PPy NT composites was dropped onto the interdigitated electrodes. The microelectrode substrate was finally dried under vacuum at room temperature for hours.

A solution chamber (volume 10 mL) was designed and employed for all solution-based measurements. The FET sensor substrate based on liquid-ion gate was fabricated with phosphate-buffered solution (PBS, pH 7.5). The current change of the sensor substrate was monitored at room temperature with a sourcemeter connected to a computer.

2.1.1.4. Characterization of RGO/PPy NT hybrids

The TEM images were taken with a JEOL JEM-2100 microscope. For TEM observation, the samples were diluted with ethanol and then the diluted solution was deposited on a copper grid coated with a carbon film. The FE-SEM images were obtained with a JEOL JSM-6700 F microscope. A specimen was coated with a thin layer of gold to eliminate charging effects. Raman spectra were recorded with a T64000 (Horiba Jobin Yvon). ATR-FTIR spectra were collected with a Thermo Scientific Nicolet 6700 FTIR spectrophotometer. X-ray diffraction (XRD) patterns were carried out with a New D8 Advance (Bruker). All electrical measurements were conducted with a Keithley 2612A sourcemeter, a probe station (MS TECH, model 4000) and a Wonatech WBCS 3000 potentiostat.

2.2. RGO/C–PPy NT hybrid materials

2.2.1. Fabrication of carboxylated polypyrrole nanotube wrapped graphene sheet transducer for field-effect transistor-type glucose biosensor

2.2.1.1 Preparation of C–PPy NTs

The C–PPy NTs were prepared using a self-degraded template method, whereby 0.243 g of 1.5-mM $FeCl_3$ solution was added to a 5-mM solution of sodium 4-[4-(dimethylamino)phenyldiazo] phenylsulfonate, $(CH_3)_2NC_6H_4$-N = $NC_6H_4SO_3Na$ in deionized water. After a flocculent precipitate appeared, 0.006 g of 0.05-mM P3CA and 0.1 g of 1.5-mM pyrrole monomer solution were added, and the mixture was stirred at room temperature for 24 h. The resulting precipitate was purified by washing it with deionized water and methanol several times until the filtrate was colorless and had a neutral pH. The powdered C–PPy NTs, weighing 0.08 g, and with 79.5 % purity, were then dried under vacuum at 60 ◦C for 24 hours.

2.2.1.2 Preparation of RGO/C–PPy NT hybrids

GO was obtained from graphite powder using a modified Hummers and Offeman method.[166] Graphene was obtained by reduction process of GO with 5 μL hydrazine (35 wt%) treatment at 95 ◦C for 1h. A 4-mg/mL suspension of graphene was dispersed in 5.1-mL of a 50:1 mixture of water and EtOH, and then mixed with 4 mg of the C–PPy NTs. The mixtures were ultrasonicated for 1 h, and the final product was a 6.3 mg of 78.8% purity graphene-C–PPy NT hybrid material, which was obtained via filtration, purified using water, and dried in a vacuum oven at 25 ◦C for 4 h.

2.2.1.3. Fabriaction of RGO/C–PPy NT composites FET sensor

A photolithographic process was used to pattern a microarray of 80 pairs of gold interdigitated microelectrodes on a glass substrate using a 50-nm-thick Cr adhesion layer. The resulting electrodes, formed on a 50-nm-thick gold layer, were 10-μm-wide and 4-mm-long, with an interelectrode spacing of 10 μm. The microelectrode substrate was cleaned using distilled water and ethanol. An aliquot of 0.1 mL of the ethanol solution containing 0.1-wt% RGO/C–PPy NT hybrid was dropped onto the interdigitated electrodes. A coupling reaction between enzyme and graphene-nanohybrid material was conducted by a modified previous our method. In brief, the coupling reaction was then carried out by exposing the substrate to a mixed solution of GOx and 10 μL of 1-wt% aqueous DMT-MM for 12 h to attach the GOx to the surface of the RGO/C–PPy NTs. The substrate was then rinsed with distilled water and dried under vacuum at room temperature for 12 h. A 10-mL solution chamber was employed for all solution-based measurements. The FET sensor substrate based on liquid-ion gate was fabricated with PBS, which had a pH of 7.5. The current was monitored at room temperature using a source meter.

2.2.1.4. Characterization of RGO/C–PPy NT hybrids

The TEM images were taken with a JEOL JEM-2100 microscope at the National Center for Inter-university Research Facilities (NCIRF) at Seoul National University. For TEM observation, the samples were diluted with in ethanol and then the diluted solution was deposited on a copper grid coated with a carbon film. The FE-SEM images were obtained with a JEOL JSM-6700F microscope. A specimen was coated with a thin layer of gold to eliminate charg-ing effects. Raman spectra were recorded with a T64000 (Horiba Jobin Yvon). ATR-FTIR spectra were collected with a Thermo Scientific Nicolet 6700 FTIR spectrophotometer. XRD patterns were carried out with a New D8 Advance (Bruker). All electrical measurements were conducted with a Keithley 2612A sourcemeter, a probe station (MS TECH, MODEL 4000) and a Wonatech WBCS 3000 potentiostat.

2.3. RGO/PF NT hybrid materials

2.3.1. Fabrication of reduced graphene oxide-polyfuran nanohybrid for High-performance Hg^{2+} FET-type sensors

2.3.1.1 Prepration of PF NTs

A self-degraded template method was carried out for the preparation of PF NTs. Firstly, $FeCl_3$ (0.243 g, 1.5 mmol) was added to a 5-mM MO solution in deionized water. After a flocculent precipitate appeared, the furan monomer (102 mg, 1.5 mmol) was added. The mixture was then stirred at room temperature for 24 hours. The resulting precipitate was purified by washing it with deionized water and methanol several times until the filtrate was colorless and had a neutral pH. Finally, the powdered PF NTs (80 mg, 78.4 %) were dried under vacuum at 60℃ for 24 hours.

2.3.1.2. Prepration of RGO/PF NT hybrids

GO was obtained from graphite powder using a modified Hummers and Offeman method.[166] GO (4 mg/mL) was dispersed in deionized water and then mixed with PF NTs (4 mg). The mixtures were ultrasonicated for 1 hour. The 5 μL (35 wt %) hydrazxine solution exposed to the resulting GO-PF NT structures for 1 hour at 95℃, leading to reduction process from GO to RGO. The final product, the RGO-PF NT composite (6.5 mg, 81.3 %), was obtained via purification by using water, filtration, and dried in a vacuum oven at 25℃ for hours.

2.3.1.3. Fabrication of RGO/PF NT composite FET sensor

A microarray (80 pairs of gold interdigitated microelectrodes) was patterned on a glass substrate using a 50-nm-thick Cr adhesion layer via a photolithographic process, resulting in electrodes with a gold layer thickness of 50 nm, a width of 10 μm, length of 4000 μm, and an interelectrode spacing of 10 μm. The microelectrode substrate was washed using sonication in ethanol. An aliquot of 0.1 mL of the ethanol solution containing 0.1 wt % RGO-PF NT composites was dropped onto the patterned electrodes. Then, the microelectrode substrate was dried under vacuum at room temperature for several hours. A solution chamber (volume 10 mL) was designed and employed for all liquid-based measurements. The FET sensor substrate based on liquid-ion gate was fabricated with PBS at pH 7.5.

2.3.1.4. Characterization of RGO/PF NT hybrids

The TEM images were obtained with a JEOL JEM-2100 microscope. For TEM observation, the samples were diluted with ethanol and then the diluted solution was deposited on a copper grid coated with a carbon film. The FE-SEM images were taken with a JEOL JSM-6700 F microscope. A specimen was coated with a thin layer of gold to eliminate charging effects. Raman spectra were recorded with a T64000 (Horiba Jobin Yvon). ATR-FTIR spectra were collected with a Thermo Scientific Nicolet 6700 FTIR spectrophotometer. XRD patterns were carried out with a New D8 Advance (Bruker). All electrical measurements were conducted with a Keithley 2612A sourcemeter, a probe station (MS TECH, MODEL 4000) and a Wonatech WBCS 3000 potentiostat.

2.4. RGO/PSe nanohybrid materials

2.4.1 Fabrication of graphene/polyselenophene nanohybrid materials for highly sensitive and selective chemiresistive sensor

2.4.1.1. Preparation of RGO/PSe nanohybrid materials

GO was obtained from graphite powder using a modification of the Hummers and Offeman method.[166] GO (4 mg/mL) was dispersed in 5 mL aqueous solution and then mixed with selenophene monomer (4 mg, 0.06 mmol) dissolved in EtOH (0.1 mL). The solution was sonicated for 1 min, and then iron chloride 1 mL (5 wt % in deionized water) was added to the mixture while stirring. After polymerization for 24 h, 2 mL of 35 wt% hydrazine solution was added dropwise to the GO/PSe nano-composites over 1 h at 95 ℃ to reduce GO to RGO. The final product, RGO/PSe nanocomposite (5.3 mg, 66%), was obtained after filtration, purification with excess water, and drying in a vacuum oven at 25 ℃.

2.4.1.2. Characterization of RGO/PSe nano hybrid materials

The TEM images were taken with a JEOL JEM-2100 microscope. For TEM observation, the samples were diluted with in ethanol and then the diluted solution was deposited on a copper grid coated with a carbon film. The FE-SEM images were obtained with a JEOL JSM-6700 F microscope. A specimen was coated with a thin layer of gold to eliminate charging effects. Raman spectra were recorded with a T64000 (Horiba Jobin Yvon). ATR-FTIR spectra were collected with a Thermo Scientific Nicolet 6700 FTIR spectrophotometer. XRD patterns were carried out with a New D8 Advance (Bruker). Significant data were extracted from the plot using the fitting software (ZMAN 2.3). All electrical measurements were conducted with a Keithley 2612A sourcemeter, a probe station (MS TECH, MODEL 4000) and a Wonatech WBCS 3000 potentiostat.

2.5. CVD graphene/PEDOT/P(VDF-HFP) nanohbyrid mateirals

2.5.1. Fabrication of graphene/free-standing nanofibrillar PEDOT/P(VDF-HFP) hybrid device for wearable and sensitive human motion detective piezo-resistive sensor

2.5.1.1. Prepatation of CVD graphene/free-standing PEDOT nanofiber/P(VDF-HFP) nanohbyrid materials

Single-layer graphene was prepared on Cu foil (9 x 6 cm) using chemical vapor deposition (CVD). The Cu foil was loaded into a thermal CVD reactor, and the temperature was increased to 1000℃ with 8 sccm of H_2 flowing at 90mTorr. The sample was maintained at 1000℃ for 30 min with a 20-sccm flow of CH4 and then cooled to room temperature with a 8-sccm flow of H_2. Using a wet transfer method, the single-layer graphene was transferred onto the PDMS substrate. The PDMS was prepared by mixing with degassed PDMS prepolymer (with a ratio of base to cross-linker of 10:1 by mass) in a petridish (125 x 125 x 20 mm^3), followed by curing at 60℃ for 2 h to produce 1-mm-thick PDMS substrates. The single-layer graphene was coated with PMMA (4000 rpm, 1min) and immersed in an etchant to remove the Cu foil. The graphene on PMMA was then rinsed several times with deionized (DI) water to remove etchant residues. Subsequently, the PMMA/graphene was transferred to a PDMS film. The PMMA was slowly removed by acetone. To synthesize

the free-standing PEDOT on the graphene surface, we used a technique described by Hammond and Kaner et al. To synthesize free-standing nanofibrillar PEDOT, iron (III) chloride solution 30mL in chlorobenzene solution at 5 wt% was sprayed onto the graphene surface, which acts like a seed template, nucleation sites, and oxidant for PEDOT polymerization. Then, 10 μL of the EDOT monomer in chlorobenzene solution (6 wt%) was placed into a vapor deposition polymerization (VDP) chamber and polymerized at 100℃ under vacuum conditions, resulting in vertical growth of PEDOT islands on the iron (III) chloride seeds. Anisotropic iron (III) chloride template was forms due to the accumulation of solids during evaporation of the solution. After the EDOT monomer injected into VDC, subsequently, vapor polymerization took place on the surface of the template, forming vertically aligned PEDOT islands. Following repeated rinsing with DI water and methanol, P(VDF-HFP) dissolved in chlorobenzene (6 wt%) was deposited using spin-coating at 3000 rpm for 60s. The P(VDF-HFP) was crystallized by annealing at 150℃ for 2 h. To form the devices, two sheets of the graphene/V-PEDOT/P(VDF-HFP) film were placed in a symmetrical double-layer configuration, and Ag paste was applied at the edges each layer to form electrical contacts.

2.5.1.2. Characterization of CVD graphene/PEDOT/P(VDF-HFP) nanohybrid materials

High-resolution transmission electron microscopy (HR-TEM) images were obtained using a JEOL JEM-3100 at the National Center for Inter-university Research Facilities (NCIRF) at Seoul National University. For TEM observation, the samples were diluted in ethanol and deposited onto a copper grid coated with a carbon film. FE-SEM images were obtained using a JEOL JSM-6700F. specimens were coated with a thin layer of gold to eliminate charging effects. Raman spectra were recorded using a Horiba Jobin Yvon T64000. Data were extracted from plots using the fitting software ZMAN 2.3. All electrical measurements were obtained using a Keithley 2612A source meter and MS TECH 4000 probe station.

3. RESULTS AND DISCUSSION

3.1. Fabrication of polypyrrole nanotube embedded reduced graphene oxide transducer for field-effect transistor-type H_2O_2 biosensor.

3.1.1. Fabrication of RGO/PPy NT hybrid materials

Figure 11 showed the fabrication of the RGO/PPy NT hybrid materials. SEM and TEM were used for characterizing the morphology of the RGO/PPy nanohybrid materials. The SEM and TEM images of the PPy NTs revealed that the diameter of the tubes was around 70 nm, as shown in Figure 12(a). The RGO sheet was observed using cross-sectional SEM image, which shows a structure that resembles paper with porous spaces. (See Figure 12(b)) Figure 12(c) and (d) display cross-sectional SEM and TEM images of the RGO/PPy NT hybrid material. The PPy NT structures were well organized on the large surface area of the graphene sheets. Note that the PPy NTs interact with the RGO sheets. These interactions are discussed in detail below. These results suggest that the RGO/PPy NT hybrid materials were stable due to the strong π–π interactions between the RGO layers and PPy NTs.

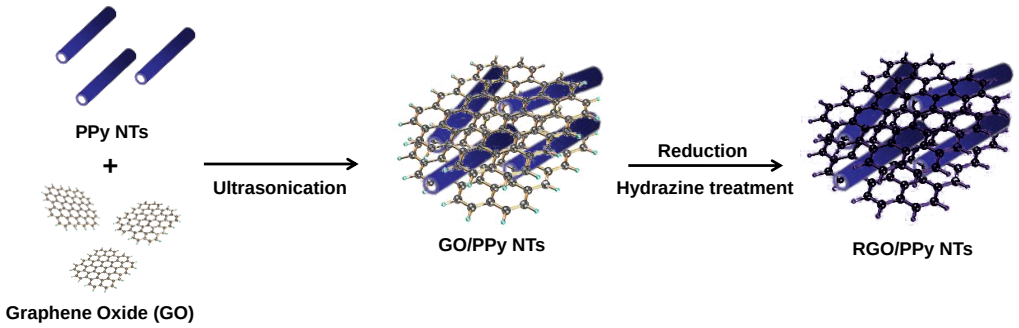

Figure 11**.** A schematic illustration of the synthesis of rGO/PPy NT hybrids.

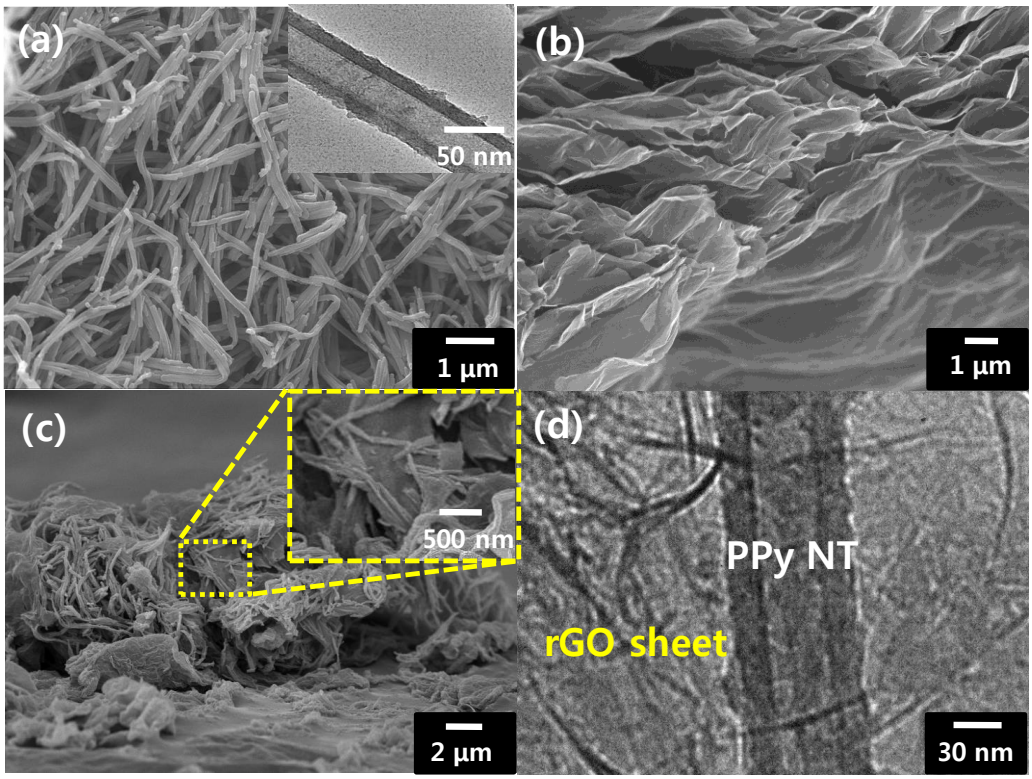

Figure 12**.** (a) SEM image shows PPy NTs. The inset shows a TEM image. Cross-sectional SEM images show (b) rGO and (c) rGO/PPy NTs. The inset indicates the magnification level. (d) A TEM image shows rGO/PPy NTs.

To investigate the structure of the RGO/PPy NT hybrid materials, RAMAN spectroscopy was carried, as shown in Figure 13. The Raman spectrum of GO exhibited D peaks at 1364 cm^{-1} and G peaks at 1610 cm^{-1}. The Raman spectrum of the RGO showed two prominent bands at 1343 cm^{-1} and 1592 cm^{-1}, which correspond to D and G bands. The Raman spectrum of PPy NTs displayed the C=C backbone stretching at ~ 1577 cm^{-1} and the ring stretching mode of PPy at 1361 cm^{-1}. The Raman spectrum of the RGO/PPy NT hybrid materials exhibited an enhanced intensity of the band around 1348 cm^{-1}, which indicates an interaction between PPy and the RGO sheets.

To further characterize the RGO/PPy NT hybrid mateirals, ATR- FTIR and XRD spectra were measured. (See Figure 14) GO showed characteristic absorption bands of oxide groups, including the C=O stretching peak at 1733 cm^{-1}, the vibration and deformation peaks of O-H groups at 3391 cm^{-1} and 1417 cm^{-1}, and the C-O (alkoyl) stretching peak at 1037 cm^{-1}. Most of the peaks related to oxygen-containing functional groups vanished in the FTIR spectra of RGO, which means that the reduction of GO was successful conducted. The characteristic bands of the RGO/PPy NT hybrid materials exhibited the pyrrole ring and graphene fundamental vibrations, which occur at 1561 cm^{-1} (C=C stretching), 1437 cm^{-1} (C-C stretching), 1282 cm^{-1} (C-N stretching), and 1038 cm^{-1} (C-H deformation). The peaks of the RGO/PPy NT

nanohybrids were shifted compared with those of the PPy NTs and RGO in isolation due to interactions between the RGO layers and PPy NTs.

The XRD diffractograms of GO contained a very sharp peak at 10.1° (d = 8.75 Å), which indicates that the structure of the original graphite was successfully oxidized to GO, as shown in Figure 15. A broad peak appeared at 25° (d = 3.56 Å), which implies that RGO formation was achieved by reduction of GO using hydrazine. The RGO/PPy NT hybrids displayed a broad peak at around 28° (d = 3.18 Å), which corresponds to the pyrrole intermolecular distance between the RGO/PPy NTs. We conclude that the PPy NTs and the RGO sheet formed a composite via π–π interactions.

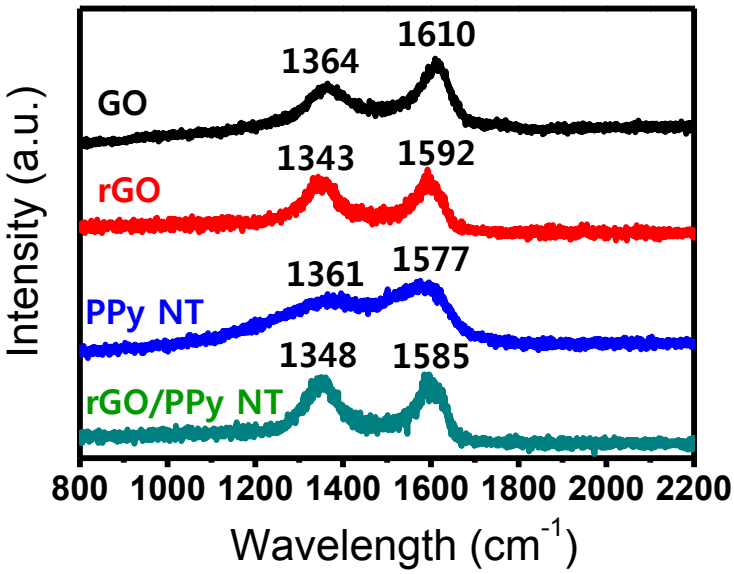

Figure 13**.** Raman spectra of GO, rGO, PPy, NT, and rGO/PPy NT hybrids.

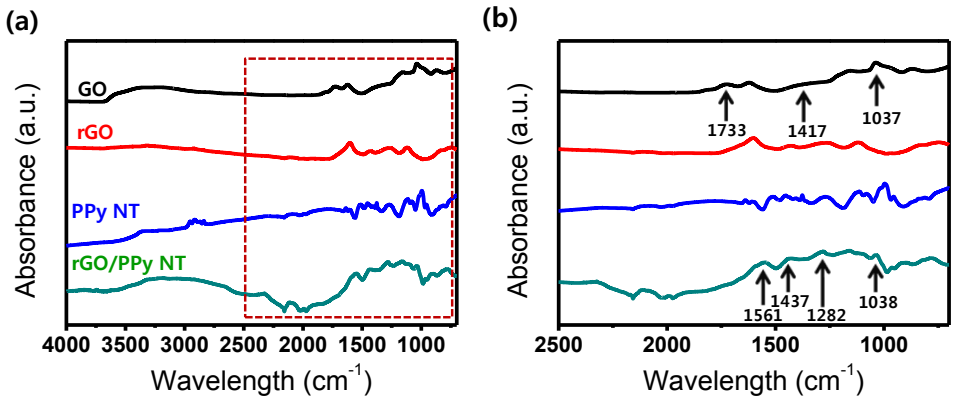

Figure 14. ATR-FTIR spectra of (a) GO, rGO, PPy, NT, and rGO/PPy NT hybrids. A magnified view of the marked area in (a) is shown in (b).

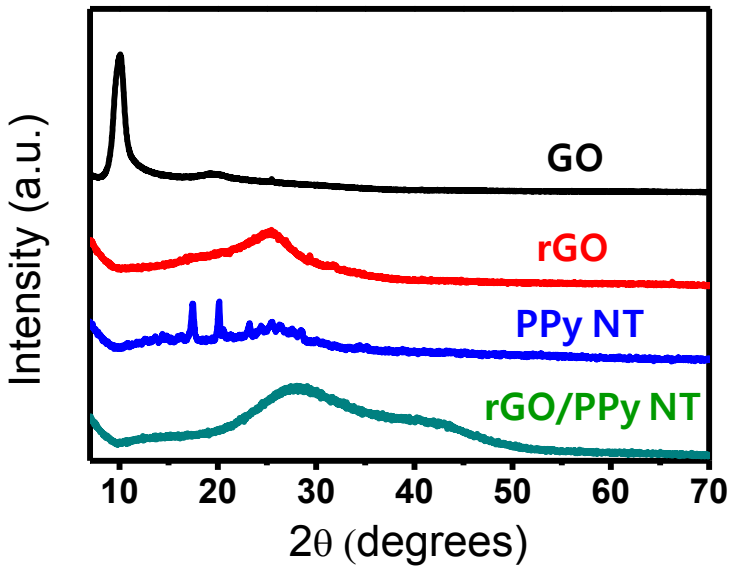

Figure 15. X-ray diffractions of GO, rGO, PPy NT, and rGO/PPy NT hybrids.

3.1.2. Electrical performance of RGO/PPy NT hybrid materials

To understand the electrical properties the RGO/PPy NT hybrid materials, current–voltage (*I*–*V*) curves were measured on the patterned electrode substrate. Linear *I*–*V* curves were observed over a range of –0.4 V to +0.4 V, which means that Ohmic contacts were formed between the nanohybrids and the gold electrodes, as shown in Figure 15(a). The conductivity of the RGO/PPy NT hybrids was higher than that of RGO and PPy NTs. This result is considered that the RGO/PPy NT hybrids showed effective electron transport between the PPy NTs and the RGO, resulting in a decrease in the resistance. Despite excellent electrical properties of the RGO sheet, the conductivity was highly anisotropic and interlayer electron transport was slow. However, the PPy NTs serve as conductive channels to connect the RGO layers, resulting in enhanced conductivity, as shown in Figure 16(a).

The electrical characteristics of the RGO/PPy NT conductive channels were characterized by measuring the source–drain current–voltage (I_{SD}–V_{SD}) characteristics of liquid-ion-gated transistors under various gate biases. Firstly, the devices based on the RGO/PPy NT hybrid materials were in phosphate-buffered saline (PBS) solution (pH 7.4). Then, V_g was varied in the range of –2.0 V to +0.4 V in steps of 0.2 V, with a gate voltage sweep rate of 0.2 Vs^{-1}, as shown in Figure 16(b). When a larger negative gate bais was applied, I_{SD}

increased (i.e., became more positive). This is a typical characteristic of *p*-channel transistors. Thus, the current in the device was controlled over the hole carrier density at the surface of RGO/PPy NT hybrid materials. Generally, the PPy materials showed the *p*-type semiconductor behavior.[78] Although unaltered graphene shows ambipolar properties in the semiconductor devices, the graphene samples used, in this work, displayed hole-transporting behavior due to the absorption of oxygen and/or water from air to yield RGO/PPy NT hybrids, resulting in enhancement of *p*-type systems. These result offered higher stability and improved sensing performance relative to that of the individual components alone.

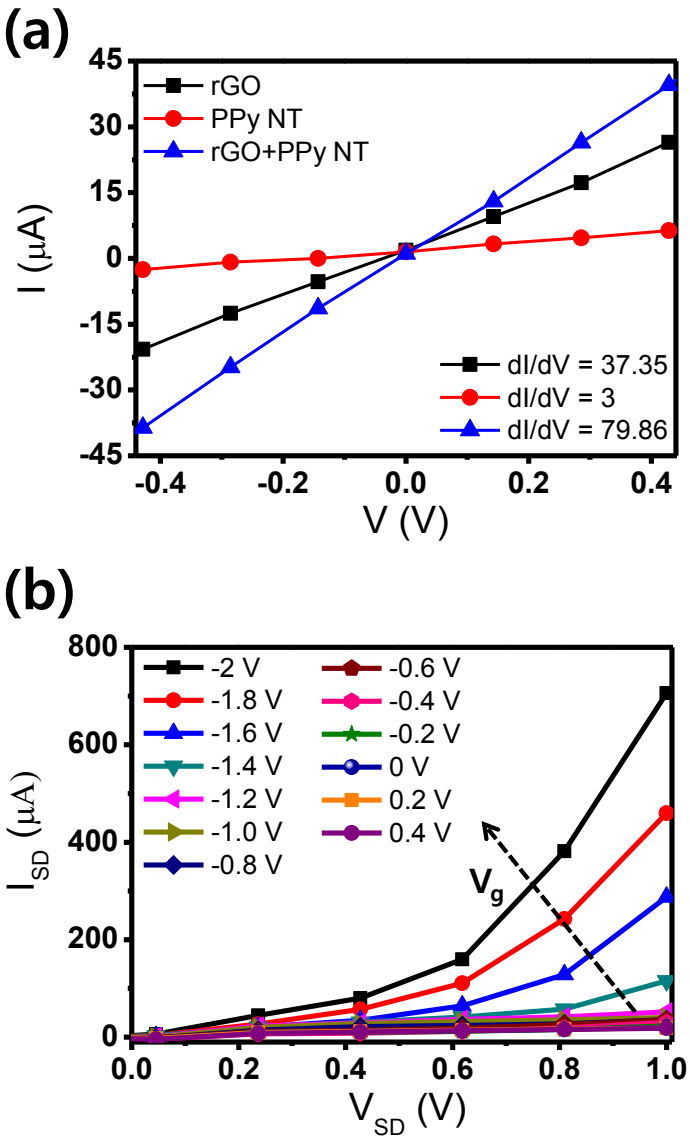

Figure 16. (a) Current−voltage (I−V) curves of GO, rGO, PPy NTs, and rGO/PPy NTs composites and (b) rGO/PPy NTs composites at V_g from –2.0 to 0.4 V in 0.2-V steps (V_{sd}: 0 to 1.0 V in 0.2-V steps).

3.1.3. FET-type H_2O_2 biosensor based on RGO/PPy NT hybrid materials

The fabricated liquid-ion-gated FETs were surrounded with PBS at pH 7.4 as the electrolyte. (See Figure 17(a)) Good contact between the RGO/PPy NT hybrid materials and the solution was offered by using a remote electrode in the surrounding electrolyte. The sensing performance of sensors can be enhanced using this strategy. The FET-type sensor, which is a *p*-channel FET (with V_g = 0.1 V), was used for the real-time response to H_2O_2 in varying concentrations. The modulations in I_{SD} were recorded in presponse to the various H_2O_2 concentrations in the solution, as shown in Figure 17(b). The normalized current, called the sensitivity, was determined by $\Delta I_{SD}/I_0 = (I_{SD}–I_0)/I_0$, where I_0 is the initial current and I_{SD} is the measured real-time current following stabilization after injecting the H_2O_2 into the liquid-ion-gated FET-type sensor device. The FET-type sensor based on the RGO/PPy NT hybrid materials showed an increase in I_{SD} in response to a gradual increase in the concentration of H_2O_2. This result is considered that the H_2O_2 analyte induces the accumulation of *p*-type charge carriers at the surface of the RGO/PPy NTs. (See below for a discussion of the sensor mechanism.) The RGO/PPy NT hybrid materials displayed highly sensitive responses to H_2O_2, with a detection limit of approximately 100 pM (signal-to-noise ratio (S/N) = 3.5). It is

generally considered a significant signal when S/N is greater than or equal to 3.0.[78–79] S/N (= 0.83) value is too low on the measurement for 10 pM, suggesting that it is not considered the signal as shown in Figure 18**.** Thus, 100 pM is regarded as a limitation of detection. The fabricated FET-type H_2O_2 sensor, in this work, enables much more rapid detection and 10 times higher sensitivity than oxidation-level-based methods in glassy carbon electrodes (GCEs), as shown in Table 1. The calibration curve was shown in Figure 17(c). When the H_2O_2 concentration increases, stronger signals were recorded. In all measurements, the FET-type sensors exhibited rapid response times of less than 1 s and showed linear tendency to normalized current changes. Furthermore, the FET-type sensors showed good reproducibility and storage stability. After ten repeated experiments, the response of the H_2O_2 sensor displayed similar result, which means that it had good reproducibility. Storage stability was evaluated in air. The FET-type sensor detected 1 nM of H_2O_2, after one month of storage (See Figure 17(d)), with no variation in the response normalized current relative to that of freshly prepared sensors. Tese results were considerd that FET-type H_2O_2 sensor based on the RGO/PPy NT hybrid mateirals had excellent air and storage stability.

To clearly confirm the mechanism of H_2O_2 sensing behavior, not only the real-time response of the FET-type sensor based on PPy NTs, but also sensors

based on RGO materials were measured (both at V_g = 0.1 V). The sensor device based on PPy NTs had limit of detection to H_2O_2 at a concentration of 1 μM. (See Figure 17(a)) The sensing device based on an RGO layer was sensitive to H_2O_2 at a concentration of 1 mM. This result is deduced that H_2O_2 enables to alter the electrical signal more effectively in PPy NTs than in RGO. The applied gate bias of V_g = 0.1 V was less than the oxidation potential of H_2O_2. Thus, the change of I_{SD} did not occur due to electrochemical oxidation of H_2O_2. Therefore, H_2O_2 could alter the charge carrier density more efficient in the PPy backbone compared with that in the graphene backbone, indicating that a positive charge was formed by reacting with PPy. It has been reported that *p*-doping effects result from the addition of H_2O_2 molecules as opposed to the direct transfer of electrons via oxidative reactions between the graphene and PPy backbone. The reasons for the improved performance of the sensor based on the RGO/PPy NT hybrids are owing to the following effects. First, an efficient response to H_2O_2 occurred due to the enhanced surface area and strong interactions between the RGO sheet and PPy NTs. Second, the enhanced *p*-type semiconductor behavior improved signal transduction.

To investigate the specificity of the response to H_2O_2, real-time monitoring of I_{SD} in various solutions containing compounds found in biological fluids, including UA, AA, and glucose solutions was evaluated, as shown in Figure

17(e). After injecting 1-mM UA, 1-mM AA, 1-mM glucose, and 0.05-mM H_2O_2, the real-time responses were recorded in response to analytes. A remarkable increase in the normalized current was observed when H_2O_2 was injected, even at much lower concentrations than the other compounds in the analyte. (See Figure 17(f)) When UA and AA were exposure into the sensors, the little change of the signals was observed in the charge density on the surface of the RGO/PPy NTs relative to the changes recorded upon exposure to H_2O_2. Glucose could not bind to the graphene-PPy nanohybrid materials because of the lack of an appropriate binding site. These results clearly demonstrate specificity towards H_2O_2.

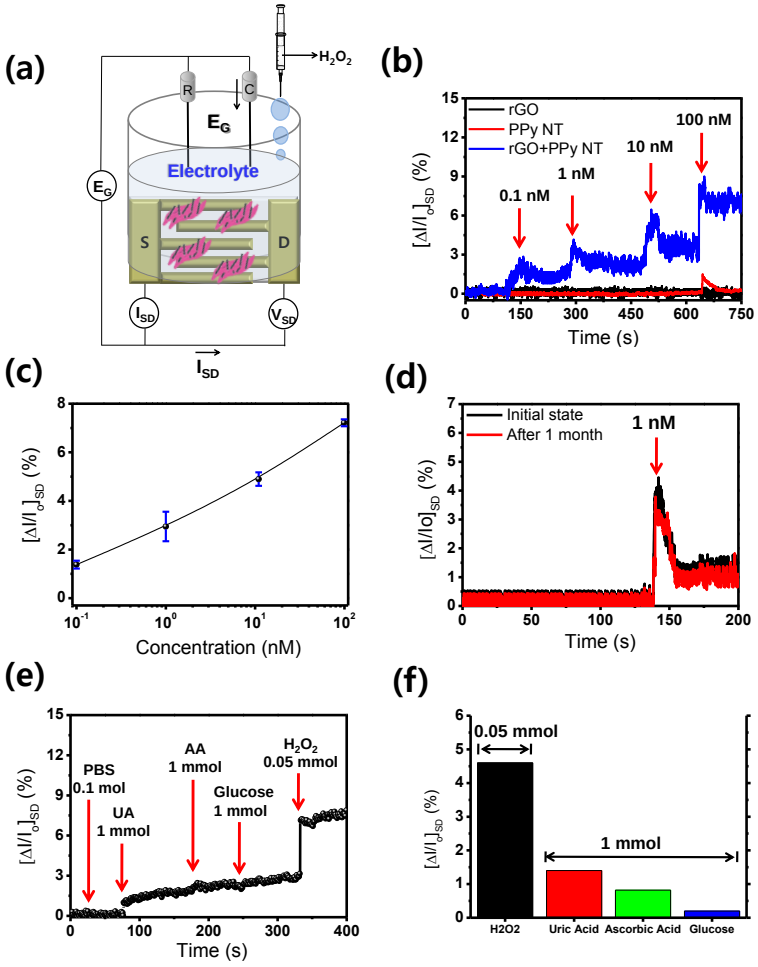

Figure 17. (a) Schematic diagram shows a liquid-ion-gated FET-type sensor. (Ag/AgCl reference electrode, R; platinum counter electrode, C; source and drain electrodes, S and D) (b) Real-time responses and (c) a calibration curve for H_2O_2 based on rGO, PPy NTs, and rGO/PPy NTs composites were measured at V_{sd} = 10 mV (V_g = 0.1 V) with H_2O_2 concentrations of 0.1 nM to 100 nM. Storage stability biosensor performance is shown in (d). Real-time responses to PBS, UA, AA, glucose, and H_2O_2 are shown in (e). (f) A histogram details the sensing performance to UA, AA, glucose, and H_2O_2.

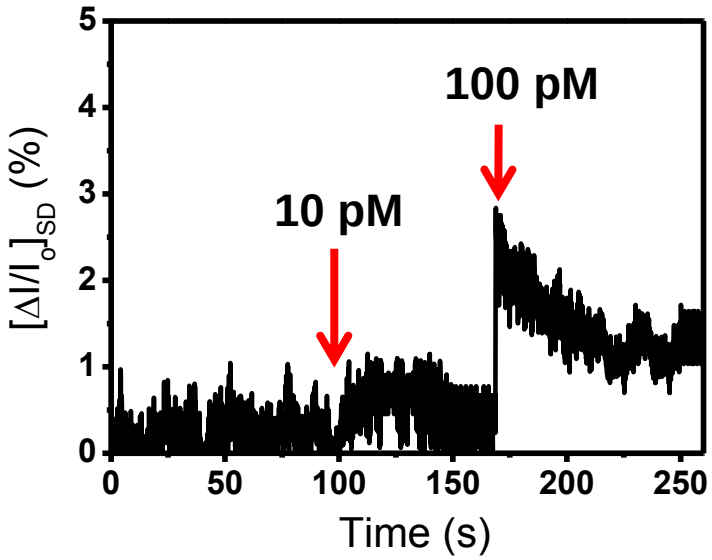

Figure 18. Real-time responses for H_2O_2 based on rGO/PPy NTs composites were measrured at V_{sd} = 10 mV (V_g = 0.1 V) with H_2O_2 concentration of 10 pM to 100 pM.

Table 1. Comparison of the performance of various H_2O_2 sensors.

Biosensor configuration	Detection limit (μM)	Reference
AgNP/SnO_2/GCE	5	[167]
AgNP/Graphene/GCE	28	[168]
AgNP/CNT/GCE	0.5	[169]
AgNP/ZnO/GCE	0.42	[170]
AgNP/DNA/GCE	1.7	[171]
AgNP/MWCNT/Au electrode	0.5	[172]
MnO_2/GO/GCE	0.8	[173]
Ni/Al-LDHs Films	0.009	[174]
Co/Al-LDHs Films	0.05	[174]
Pt/PPy Hollow microsphere	1	[175]
Pt/Graphene/GCE	0.5	[176]
Fe_3O_4/rGO/GCE	0.006	[177]
PPy NWs/Cu/Au electrode	2.3	[178]
Hb/CeO_2/MWNTs	0.65	[179]
PPy NT/rGO FET-type sensor	0.0001	This work

NP = Nanoparticle, NW = Nanowire, rGO = Reduced graphene oxide, GCE = Glassy carbon electrode, MWCNT = Multi-wall carbon nanotube, Hb = Hemoglobin, LDH = Layered double hydroxides.

3.2. Fabrication of carboxylated polypyrrole nanotube wrapped graphene sheet transducer for field-effect transistor-type glucose biosensor

3.2.1. Fabrication of RGO/C−PPy NT hybrid materials

Figure 19 described the fabrication of RGO/C–PPy NT hybrid materials. SEM and TEM images of the C–PPy NTs were shown in Figure 20(a). The diameter of the C–PPy NTs was observed in the range of 70-80 nm. To characterize the graphene sheets, cross-sectional SEM was carried out. (See Figure 20(b)) It showed paper-like structure with porous regions. Figures 20(c) and 1(d) display cross-sectional SEM and TEM images of the RGO/C-PPy NT hybrid materials. The structure of the C-PPy NTs was well organized and coupled on the surface of the graphene sheets. This proposes that the RGO/C−PPy NT composites were stable due to the strong π–π interactions between the graphene layers and C−PPy NTs.

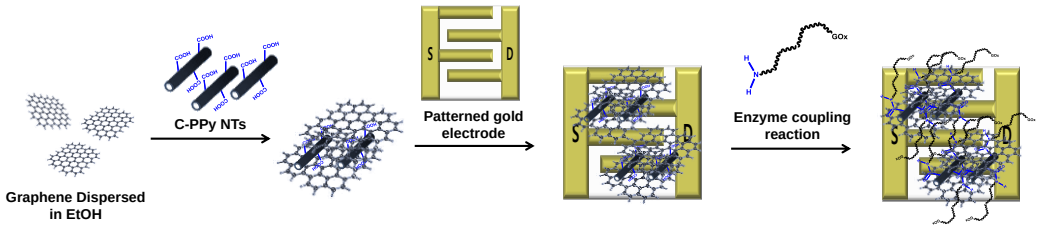

Figure 19. Schematic illustration of the fabrication of rGO/C-PPy NT hybrid glucose sensing device.

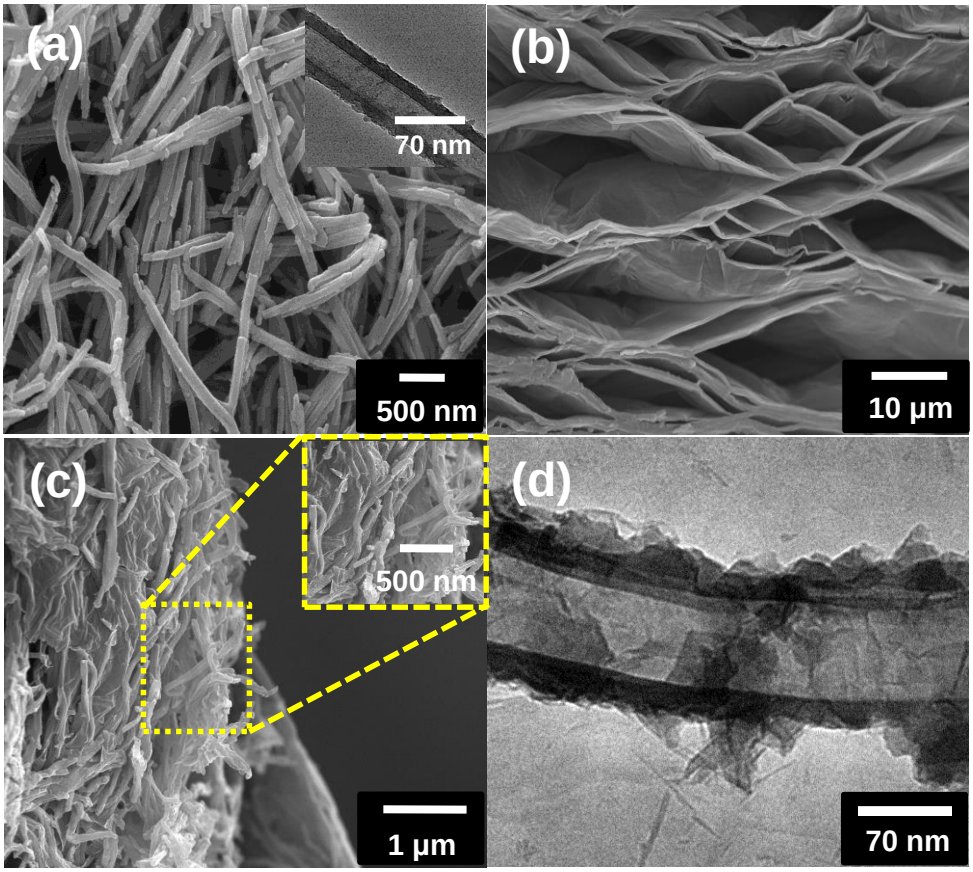

Figure 20. (a) SEM image of the C-PPy NTs. The inset shows a TEM image. (b) Cross-sectional SEM images of the rGO layers and (c) the rGO/C-PPy NTs. (d) TEM image of rGO/C-PPy NTs.

To confirm the chemical characterization of the C−PPy NTs, RGO, and RGO/C−PPy NTs, ATR-FTIR spectroscopy was carried out, as shown in Figure 21 and 22. The spectrum from the C−PPy NTs showed a carboylic acid stretching peak at 1733 cm^{-1}, a pyrrole ring stretching peak at 1554 and 1475 cm^{-1}, and a C−N stretching peak at 1294 cm^{-1}.[77] The characteristic bands of the RGO/C−PPy NT hybrid materials showed peaks owing to pyrrole ring and graphene fundamental vibrations, which occurred at 1551 cm^{-1} (C=C stretching), 1467 cm^{-1} (C−C stretching), 1303 cm^{-1} (C−N stretching), and 1038 cm^{-1} (C−H deformation). The characteristic bands of the RGO/C−PPy NT hybrids were shifted compared with those of the C−PPy NTs and graphene in isolation, due to the interactions between the RGO layers and PPy NTs.

The XRD patterns of GO showed a very sharp peak at 10.1° (d = 8.75 Å), as shown in Figure 23(a). This indicates that the structure of the original graphite was preserved, and that the material was successfully oxidized to form GO. A broad peak at around 25° (d = 3.56 Å) was observed for the RGO sheets, which means that RGO formation was successfully fabricated by reduction of the GO using hydrazine. The RGO/C−PPy NT hybrids showed a broad peak at around 24° (d = 3.7 Å), corresponding to the pyrrole intermolecular distance between the RGO/C−PPy NTs. Thus, C−PPy NTs and graphene sheets have been completely interacted.

To gain further insight into the structure of the RGO/C−PPy NT hybrids, Raman spectroscopy was carried out, as shown in Figure 23(b). The D peaks (~1364 cm^{-1}) and G peaks (~1610 cm^{-1}) in GO were clearly visible. In contrast, the Raman spectrum of the RGO showed two prominent bands at 1343 cm^{-1} and 1592 cm^{-1}, corresponding to the D and G bands. The ratio of the D band peak to the G band peak, I_D/I_G, increased slightly compared with that of GO, suggesting that the reduction process induced defects or edges in the RGO sheets. The Raman spectrum of the C−PPy NTs showed peaks corresponding to C=C backbone stretching at ~ 1569 cm^{-1} and to the ring stretching mode of C−PPy at 1345 cm^{-1}. Interestingly, the Raman spectrum of the RGO/C−PPy NT composites exhibited an increased intensity of the band around 1340 cm^{-1}, which implies that an interaction between C−PPy and the graphene sheets occurred.

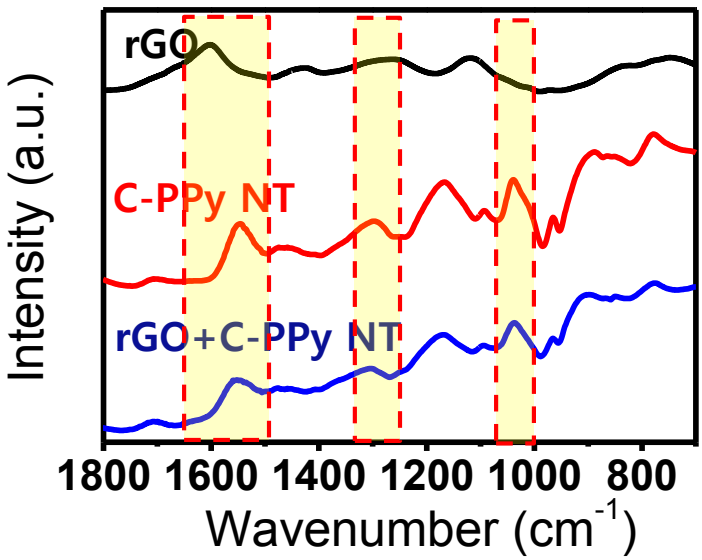

Figure 21. ATR-FT-IR spectra of rGO, C-PPy NT, and rGO/C-PPy NT hybrids.

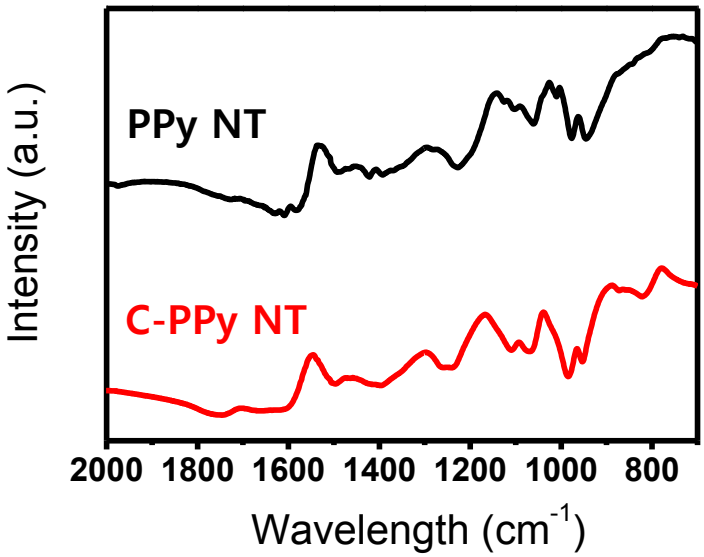

Figure 22. ATR-FT-IR spectra of PPy NT and C-PPy NT.

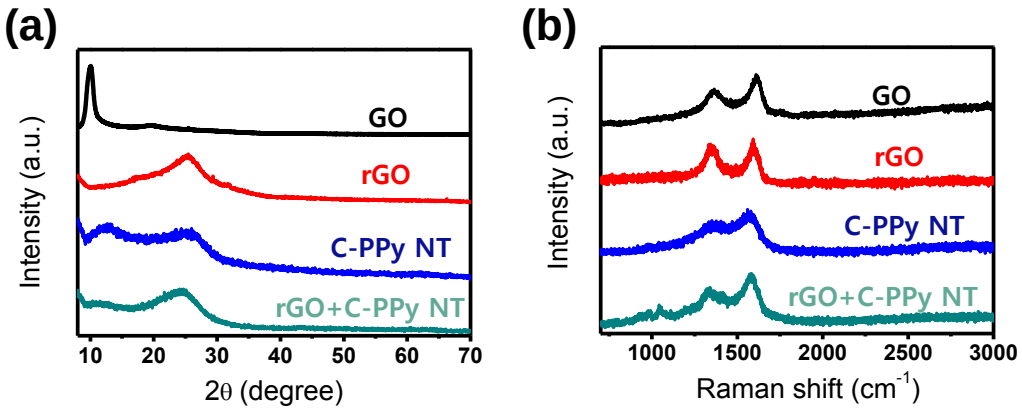

Figure 23. (a) X-ray diffraction patterns and (b) Raman spectra of GO, rGO, C-PPy NT, and rGO/C-PPy NTs.

3.2.2. Electrical performance of RGO/C–PPy NT hybrid materials

To investigate the electrical performance of the samples on the gold electrode substrate, current–voltage (*I–V*) curves were measured, as shown in Figure 24. Linear *I–V* curves were recorded over a range of –0.4 V to +0.4 V, which means that Ohmic contacts were formed between the samples and the gold elcetrodes. The electrical conductivity of the RGO/C−PPy NT hybrids was higher than that of the graphene or C−PPy NTs in isolation. This result indicates that the RGO/C−PPy NT hybrids facilitated efficient electrical transport between the C−PPy NTs and the graphene, decreasing the resistance. In general, the graphene sheet exhibited outstanding electrical properties. However, the conductivity was highly anisotropic and the interlayer electron transport was slow. The RGO/C−PPy NTs showed improved conductivity, due to the C−PPy NTs acting as conductive channels to connect the graphene layers.

The electrical properties of the RGO/C−PPy NTs conductive channels were characterized by liquid-ion-gated transistors with PBS solution (pH 7.4), which can efficiently offer effective gate control. (See Figure 25(a)). The output curves of the RGO/C−PPy NTs at room temperature with various gate biases were shown in Figure 25(b). The source-drain current (I_{SD}) increased when the gate voltage (V_G) became more negative. This is a typical characteristic of *p*-channel transistors and, suggesting the current in the device was owing to hole

transport and that the modulation of I_{SD} resulted from gate control over the hole carrier density at the surface of RGO/C−PPy NT hybrids. In the previouse report, the PPy materials showed *p*-type semiconductor behavior. Although unaltered garphene shows ambipolar properties in electrical devices, the graphene samples used here displayed *p*-type behavior, due to the absorption of oxygen and/or water from air to yield RGO/C−PPy NT composites. Therefore, these results enhanced stability and improved sensing performance relative to that of the individual components alone.

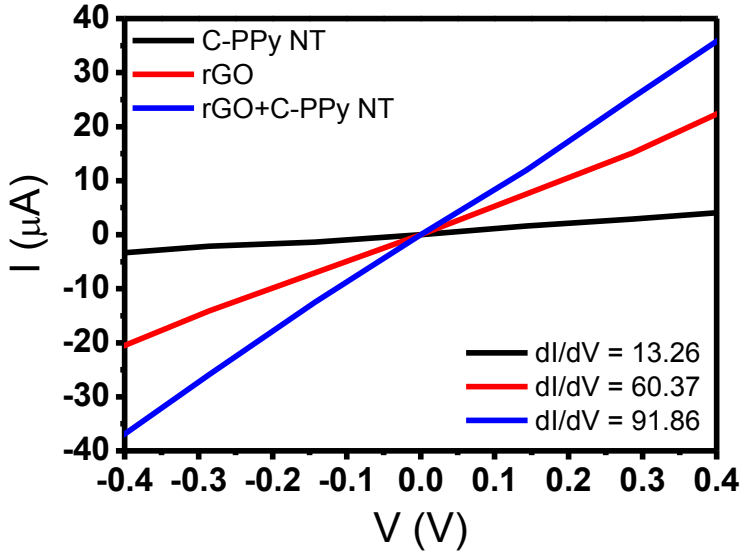

Figure 24. Current−voltage (*I*−*V*) curves of C-PPy NTs, rGO, and rGO/C-PPy NT hybrids.

3.2.3. FET-type glucose biosensor based on RGO/C–PPy NT hybrid materials

To fabricate FET-type glucose biosensor, the GOx, which was used as the glucose capture probe, was anchored on the RGO/C−PPy NTs via a chemical coupling reaction. Using the FET-type sensor with V_G = – 0.1 V, the real-time response to glucose in varying concentrations was characterized, as shown in Figure 25(c). The modulation of I_{SD} was recored in response to the variation of the glucose concentration in the solution. The normalized change in the current, i.e., $\Delta I_{SD}/I_0 = (I_{SD}–I_0)/I_0$, where I_0 is the initial current and I_{SD} is the measured current following stabilization after changing the glucose concentration., was used to determine the sensitivity. The sensor showed an increase in I_{SD} in response to a gradual increase in the concentration of glucose, indicating that the accumulation of *p*-type charge carriers at the surface of the RGO/C−PPy NT hybrids occurred. The GOx catalyzes the oxidation of glucose according to the following reaction: ß-D-glucose + O_2 + H_2O → d-glucono-1,5-lactone + H_2O_2. To clarify the mechanism of the FET-type glucose sensor, a sensing test has been carried out with various concentrations of H_2O_2, as shown in Figure 26. A similar trend to the response to glucose was observed in the sensing behavior. Thus, H_2O_2 induces indirect *p*-type doping effects, which result from the direct transfer of electrons via oxidative reactions between the graphene

and C−PPy backbone.

The FET-type biosensor, based on the RGO/C−PPy NT hybrids, exhibited very sensitive responses to glucose, with a detection limit of approximately 1 nM (S/N = 3.22). When S/N ≥ 3.0, this signal is generally considered as an useful signal. With a glucose concentration of 100 pM, S/N = 0.89 was found, which is not considered to be a significant signal.[76] (See Figure 27) Thus, the limitation of detection is determined at 1 nM. This result is 2–3 orders of magnitude more sensitive than previously reported glucose sensors. In contrast, the FET-type biosensor based on C−PPy NTs with GOx enzymes showed a detection limit of about 100 mM (with S/N = 3.08). The sensing device based on the C−PPy NTs without GOx enzymes could not display any variation in I_{SD} following a change in the glucose concentration. This result clearly shows that the GOx is essential for glucose detection.

The reasons for the enhanced performance of the sensor based on the RGO/C−PPy NT hybrids are as follows: first, an enhanced response to glucose occurred because of the increased surface area, which allowed more binding sites to become available, and second, the enhanced *p*-type semiconductor behavior led to improved signal transduction. Figure 25(d) shows the calibration curve. When the glucose concentration increased, stronger signals were detected. In all measurements, the FET sensors had response times of less

than 1 s. The reproducibility and storage stability of the hybrid FET sensors were also evaluated. The response of the glucose sensor did not change appreciably after 50 repeated experiments, indicating good reproducibility, as shown in Figure 28(a). The storage stability was assessed in air. After one month of storage, the FET sensor detected 1 nM of glucose, as shown in Figure 28(b), with no change in the response relative to that of a freshly prepared sensor. This result is considered that the highly coupling interaction between C−PPy NTs and enzyme via covalent bond induces physically and chemically stable environment in the liquid and/or air.

The specificity of the response to glucose was evaluated by real-time monitoring of I_{SD} in various solutions containing compounds found in biological fluids, including uric acid (UA), and ascorbic acid (AA), as shown in Figure 25(e). The real-time responses were detected in response to injecting 0.1-M PBS, 100-μM UA, 100-μM AA, and 1-μM glucose solutions. A remarkable increase in the current occurred when glucose was injected, even at far lower concentrations than the other compounds in the analyte. Exposure of the sensors to UA and AA did not significantly change the charge density on the surface of the RGO/C−PPy NTs relative to the changes observed upon exposure to glucose. These results clearly demonstrate specificity towards glucose.

To evaluate the application of the biosensor for the determination of the concentration of glucose in real samples, solutions were prepared. (1.0 mL real sample was added into 4.0 mL 0.1 M PBS solution) The fabricated biosensing device, in this work, showed high agreement with measured commercial glucose detector, as shown in Table 2. This result showed the biosensing device had a great potential for practical application.

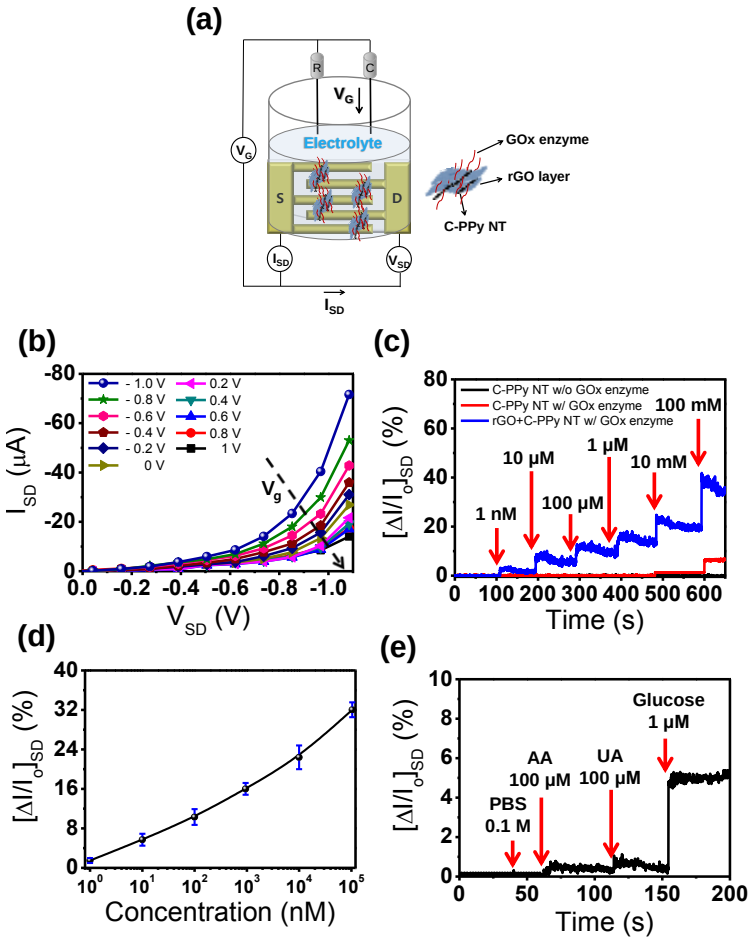

Figure 25. (a) A schematic diagram showing the liquid-ion-gated FET-type sensor, with a Ag/AgCl reference electrode, labeled R, platinum counter electrode, labeled C, and source and drain electrodes, labeled S and D. (b) The source–drain current of the biosensors as a function of V_{SD} at various values of V_G in the range from –1.0 to +1.0 V. (c) The real-time responses and (d) a calibration curve for glucose biosensor with and without the GOx enzyme, which were measured at V_{SD} = 10 mV and V_G = – 0.1 V, with glucose concentrations of 1 nM to 100 mM. (e) The real-time response to PBS, AA, UA, and glucose solutions.

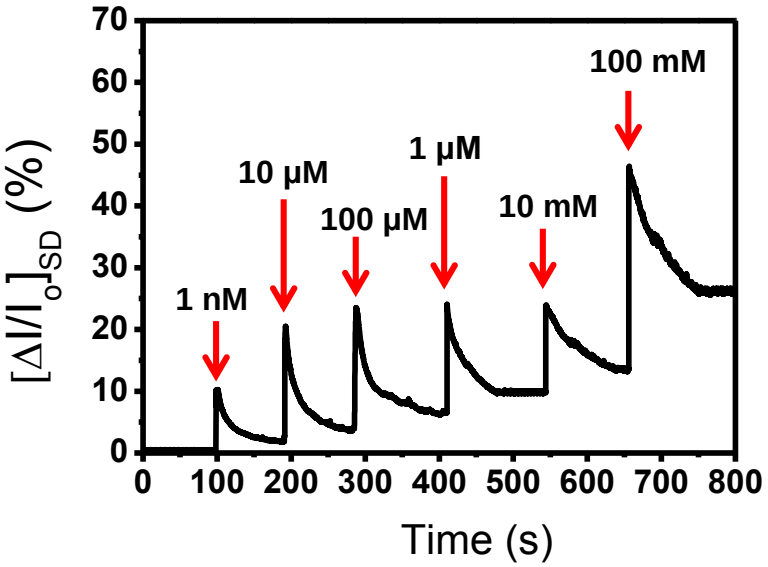

Figure 26. Real-time responses to exposure to H_2O_2 based on rGO/C-PPy NTs with GOD aptamer measured at V_{SD} = 10 mV and V_G = – 0.1 V, with H_2O_2 concentrations in the range 1–100 mM.

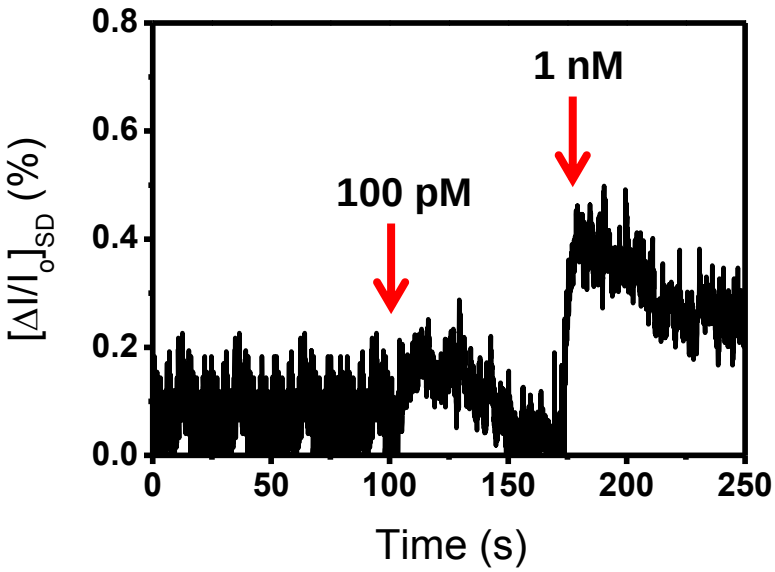

Figure 27. The real-time responses towards glucose of the rGO/C-PPy NTs measured at V_{SD} = 10 mV and V_G = – 0.1 V, with glucose concentrations of 100 pM and 1 nM.

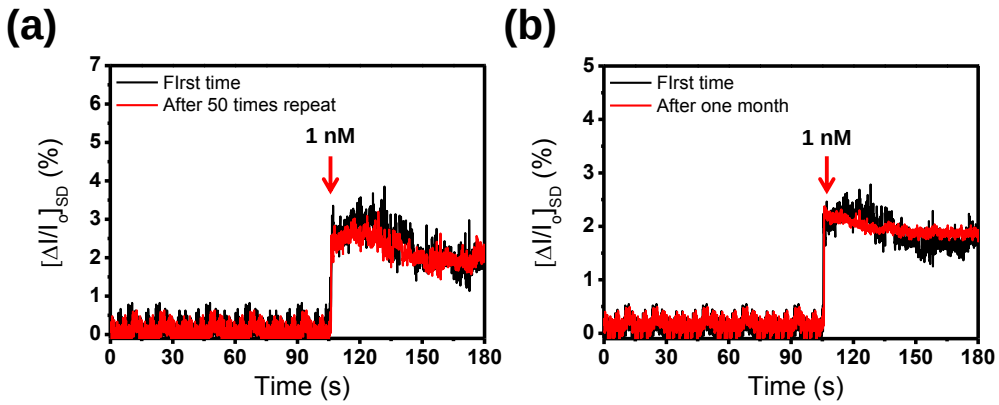

Figure 28. The real-time response of the rGO/C-PPy NTs hybrid FET-based biosensor (a) after 50 repetitions, and (b) after one month. Both datasets were measured with at V_{SD} = 10 mV and V_G = – 0.1 V, and with a glucose concentration of 1 nM.

Table 2**.** Determination of glucose concentration in real samples using the biosensors.

Real sample	Biosensor (mM)	Home blood glucose meter (mM)	Relative error
Human serum	10.92	10.6	2.93 %
Bovine serum	5.76	5.6	2.78 %
Horse serum	9.76	9.44	3.27 %

3.3. Fabrication of reduced graphene oxide-polyfuran nanohybrid for High-performance Hg^{2+} FET-type sensors

3.3.1. Fabrication of RGO/PF NT hybrid materials

A schematic diagram of the synthesis of graphene–PF NT hybrids was shown in Figure 29. First, self-degradation method was used to synthesize PF NTs. Then, PF NTs were anchored to the GO surface through π–π intermolecular interactions. Reduction process by using hydrazine was then conducted, and the prepared RGO–PF NTs were prufied several times with distilled water. Finally, the product was obtained by centrifugal precipitation and dried in a vacuum oven at 25℃. SEM and TEM were used to characterize the morphology of the RGO–PF NT hybrids. The SEM and TEM images of the PF NTs displays that the iameter of the tubes was approximately 70 nm, as shown in Figure 30(a). A cross-sectional SEM image of the RGO sheet was observed, which was a structure resemebling paper with porous spaces. (See Figure 30(b)) Figure 30(c) and (d) exhibit cross-sectional SEM and TEM images of the RGO–PF NT hybrid materials. The PF NTs were well coupled on the large surface area of the graphene sheets. The structure of the PF NTs was highly organized and compacted with the RGO sheets. These results were deduced that the RGO–PF NT hybrids were stable, and the stability was due to the strong π–π interactions between the RGO layers and PF NTs.

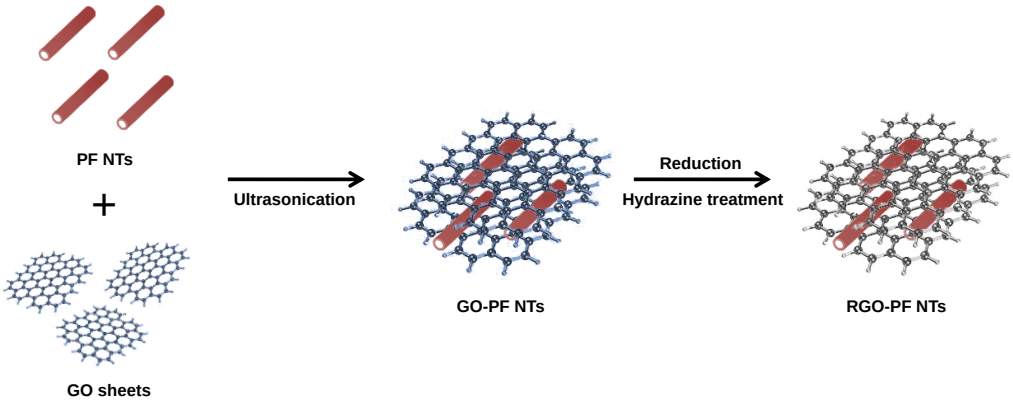

Figure 29. The schematic illustration of the synthesis of rGO-PF NT hybrids.

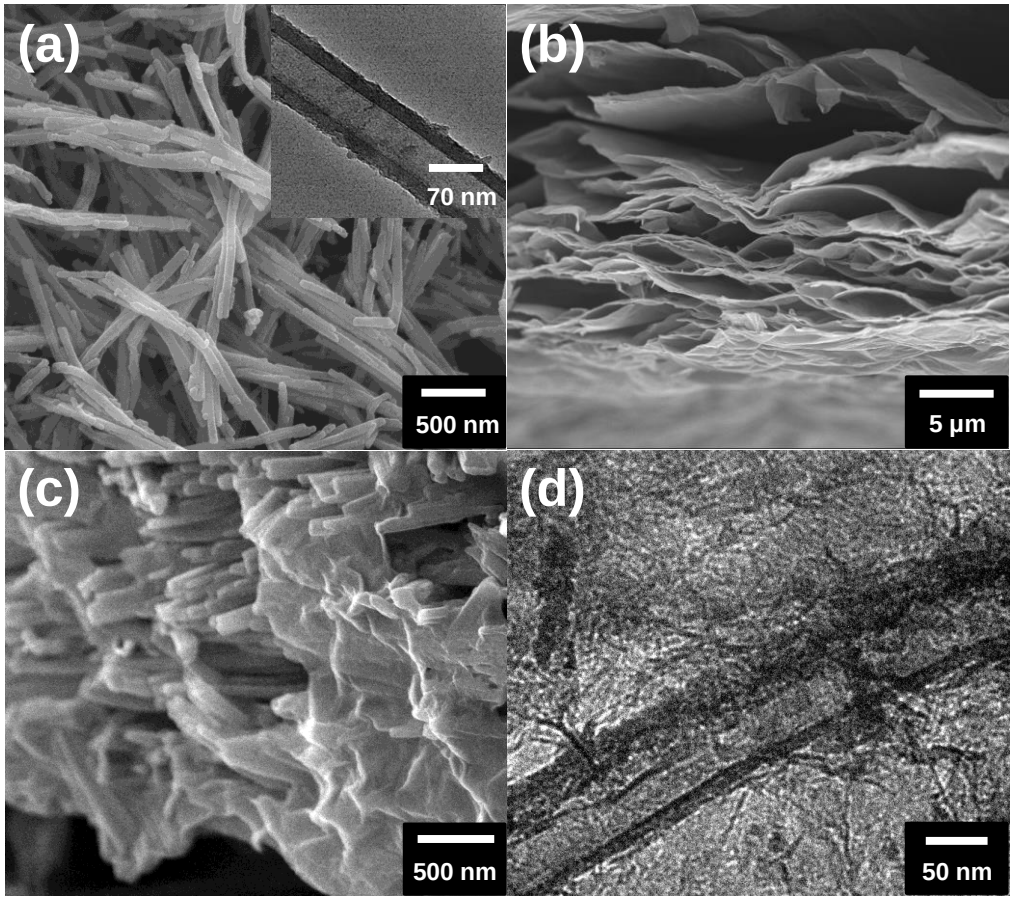

Figure 30. (a) SEM image of PF NTs; the inset is a TEM image. Cross-sectional SEM images of (b) rGO layers and (c) rGO-PF NTs. (d) TEM image of rGO/PF NTs.

To gain insight into the structure of the graphene–PF NT composites, Raman spectroscopy was carried out, and the resulting spectra are shown in Figure 31(a). The Raman spectrum of GO contained D peaks at 1364 cm^{-1} and G peaks at 1610 cm^{-1}. The Raman spectrum of the RGO exhibited two prominent bands at 1343 cm^{-1} and 1592 cm^{-1}, which correspond to D and G bands. The ratio of the D band to G band (I_d/I_G) was minimally greater than that of GO, suggesting that the reduction process induced defects or edge areas in the RGO sheets. The Raman spectrum of PF NTs contained a C=C backbone stretching peak at ~ 1590 cm^{-1} and a PF ring stretching peak at 1410 cm^{-1}. The Raman spectrum of the RGO–PF NT hybrids exhibited increased intensity of the band around 1350 cm^{-1}, indicating an interaction between PF and the RGO sheets.

The structure of the RGO–PF NTs was further studied using XRD and ATR-FTIR spectroscopy, as shown in Figure 31(b) and (c). The XRD diffractograms of GO contained a very sharp peak at 10.1° (d = 8.75 Å), which indicated that the structure of the original graphite was successfully oxidized to form GO. A broad peak appeared at 24.8° (d = 3.59 Å), which implied that RGO formation was achieved by hydrazine reduction of GO. The graphene–PF NT hybrids contained a broad peak at approximately 25.3° (d = 3.52 Å), which corresponded to the furan intermolecular distance between the RGO–PF NTs. This result suggested that the PF NTs and the RGO sheet formed a composite

via π–π interactions.

GO exhibited characteristic oxide absorption bands, including the C=O stretching peak at 1733 cm^{-1}, the vibrational and deformation peaks of O-H groups at 3391 cm^{-1} and 1417 cm^{-1}, and the C-O (alkoyl) stretching peak at 1037 cm^{-1} (see Figure 31(c). Most of the peaks related to oxygen-containing functional groups vanished in the FTIR spectrum of RGO, thus indicating that the reduction of GO was successful. The spectrum of the RGO–PF NT composite material contained characteristic furan ring and graphene fundamental vibrations: 1598 cm^{-1} (C=C stretching); 1512 and 1498 cm^{-1} (C-C stretching); 1026 and 1001 cm^{-1} (C-O-C plane deformation); and 1149, 1096, and 1052 cm^{-1} (C-H bending and stretching).[23–25] The peaks in the spectrum of the RGO–PF NT composites were shifted compared with those of the separate PF NTs and RGO spectra due to interactions between the RGO layers and PF NTs.

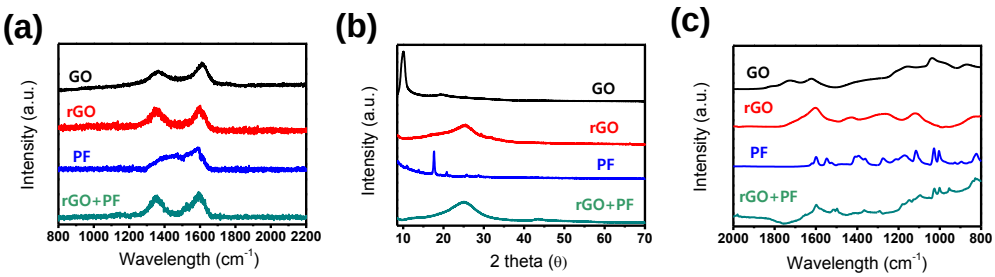

Figure 31. (a) Raman, (b) X-ray diffraction patterns, and (c) ATR-FT-IR spectra of GO, rGO, PF, and rGO+PF NT hybrids.

3.3.2. Electrical performance of RGO/PF NT hybrid materials

Measuring current–voltage (*I–V*) curves was used to characterize the electrical properties of the RGO, PF NTs, and RGO–PF NT hybrid materials on the patterned electrode substrate. Figure 32(a) shows linear *I–V* curves over a range of –0.6 V to +0.6 V, which means that Ohmic contacts were formed between samples and the gold electrodes. The conductivity of the RGO–PF NT hybrid was higher than that of RGO and PF NTs. This result proposed that RGO–PF NT hybrids exhibited effective electron transport between the PF NTs and the RGO, resulting in a decrease in the resistance. Despite excellent electrical properties of RGO sheet, the conductivity was highly anisotropic, and interlayer electron transport was slow. However, the PF NTs acted as conductive channels to connect the RGO layers, resulting in enhanced conductivity. To study the electrical characteristics of the RGO–PF NT conductive channels, we measured the source–drain current–voltage (I_{SD}–V_{SD}) characteristics of liquid-ion-gated transistors under various gate biases. For these measurements, V_g was varied from –1.0 V to +0.6 V in steps of 0.2 V, with a gate voltage sweep rate of 0.2 Vs^{-1}; the devices were in a phosphate-buffered saline (PBS) solution (pH 7.4), as shown in Figure 32(b). I_{SD} increased when a larger negative gate bias was applied, which is typical of *p*-channel transistors. Thus, the current in the device was attributable to hole transport and

that the modulation of I_{SD} resulted from control over the hole carrier density at the surface of the RGO–PF NT composites. PF NTs exhibited *p*-type semiconductor behavior (see Figure 33). Although unaltered graphene exhibits ambipolar properties in electrical devices, the graphene samples used herein exhibited hole-transporting behavior due to the absorption of oxygen and/or water from air to yield RGO–PF NT composites that behaved as enhanced *p*-type systems.[79] This behavior, in turn, results in higher stability and improved sensing performance relative to that of the individual components alone.

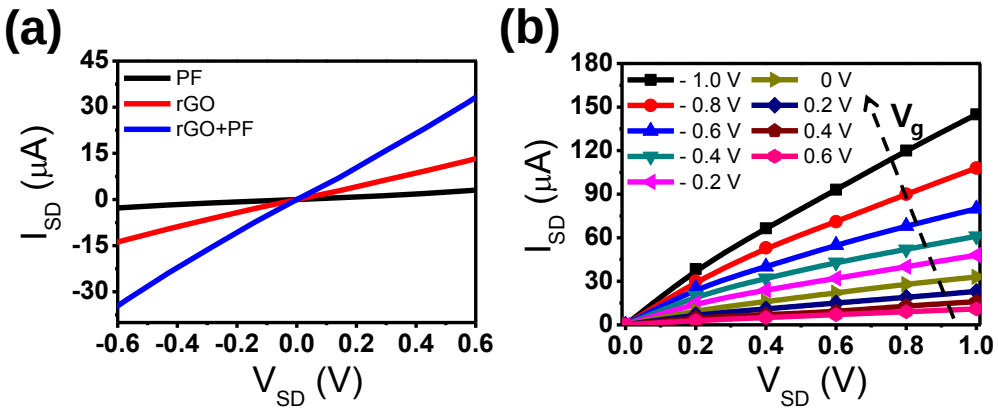

Figure 32. (a) Current−voltage (I−V) curves of PF NTs, rGO, and rGO-PF NT hybrids and (b) rGO-PF NT composites at V_g from –1.0 to +0.6 V in 0.2-V steps (Vsd: 0 to 1.0 V in 0.2-V steps).

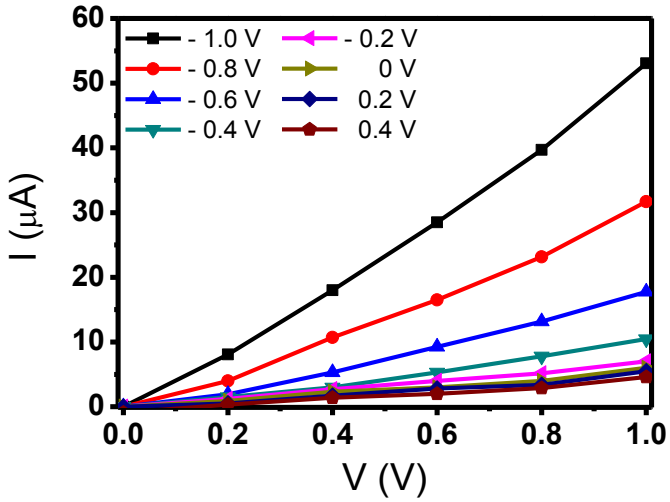

Figure 33. PF NTs at V_g from −1.0 to 0.4 V in 0.2-V steps (Vsd: 0 to 1.0 V in 0.2-V steps).

3.3.3. FET-type Hg^{2+} biosensor based on RGO/PF NT hybrid materials

Liquid-ion-gated FETs were fabricated and immersed in PBS electrolyte at pH 7.4, as shown in Figure 34(a). A remote electrode in the surrounding electrolyte provided good contact between the RGO–PF NT composites and the solution. This strategy enhanced the sensitivity via signal amplification. Using the FET-type sensor as a *p*-channel FET (with V_g = – 0.1 V), the real-time response to Hg^{2+} at various concentrations was observed. The lone-pair electrons on the oxygen atom of furan bind to the Hg^{2+}. As shown in Figure 34(b), the changes in I_{SD} were measured in response to variations in the Hg^{2+} concentration in the solution. The sensitivity was determined from the normalized change in the current $\Delta I_{SD}/I_0 = (I_{SD}–I_0)/I_0$, where I_0 is the initial current and I_{SD} is the measured real-time current following stabilization after adding the Hg^{2+} ion. The I_{SD} of the sensor increased in response to a gradual increase in the concentration of Hg^{2+}, which occurred due to the accumulation of *p*-type charge carriers at the surface of the RGO–PF NT hybrids. Moreover, the real-time responses of the FET-type Hg sensor were rapid (on a time scale of less than 1 s), and instantaneous signal changes were observed over a wide range of Hg^{2+} ion concentrations (10 pM to 100 nM).

The RGO–PF NT composites exhibited very sensitive responses to Hg,

with a detection limit of approximately 10 pM [signal-to-noise (S/N) ratio = 3.12]. Typically, S/N ratios of ≥ 3.0 are considered sufficiently high to indicate a significant signal. As shown in Figure 35, the S/N ratio at the 1 pM level was only 0.89 and thus too low to obtain a reliable signal measurement.[79] Thus, 10 pM is determined to be the detection limit in this system. On the other hand, the FET-type sensor based on PF NTs exhibited a detection limit of about 100 nM (S/N = 3.28). No change in the current after adding the Hg^{2+} was observed for the sensing device based on RGO material alone, thereby indicating that the PF functional groups are critical to sensing performance. Enhanced performance in the sensor based on the RGO–PF NT composites was attributed to the following: (i) an efficient response to Hg^{2+} occurred due to the enhanced surface area and conductivity on the RGO–PF NT hybrid materials, and (ii) the enhanced *p*-type semiconductor behavior improved signal transduction. Figure 4c shows the calibration curve; stronger signals were detected when the Hg^{2+} concentration increased. In all measurements, the FET sensors had rapid response times of less than 1 s and exhibited linear responses to current changes.

The selectivity of the RGO–PF NTs toward Hg^{2+} was evaluated using real-time monitoring of I_{SD} in the presence of various interfering metal ions (e. g., Zn^{2+}, Ce^{2+}, Na^{+}, Ni^{2+}, Pb^{2+}, Cu^{2+}, Co^{2+}, and Li^{+}), as shown in Figure 36. A

remarkable increase in the current was observed when Hg^{2+} ions were injected, even at far lower concentrations (two orders of magnitude) than the other compounds in the analyte (see Figure 34(d)). Exposure to other metal ions did not significantly alter the charge density on the surface of the RGO–PF NTs relative to the changes observed upon exposure to Hg^{2+}, because RGO–PF NTs have a greater binding affinity for Hg^{2+} than for the other metal ions.

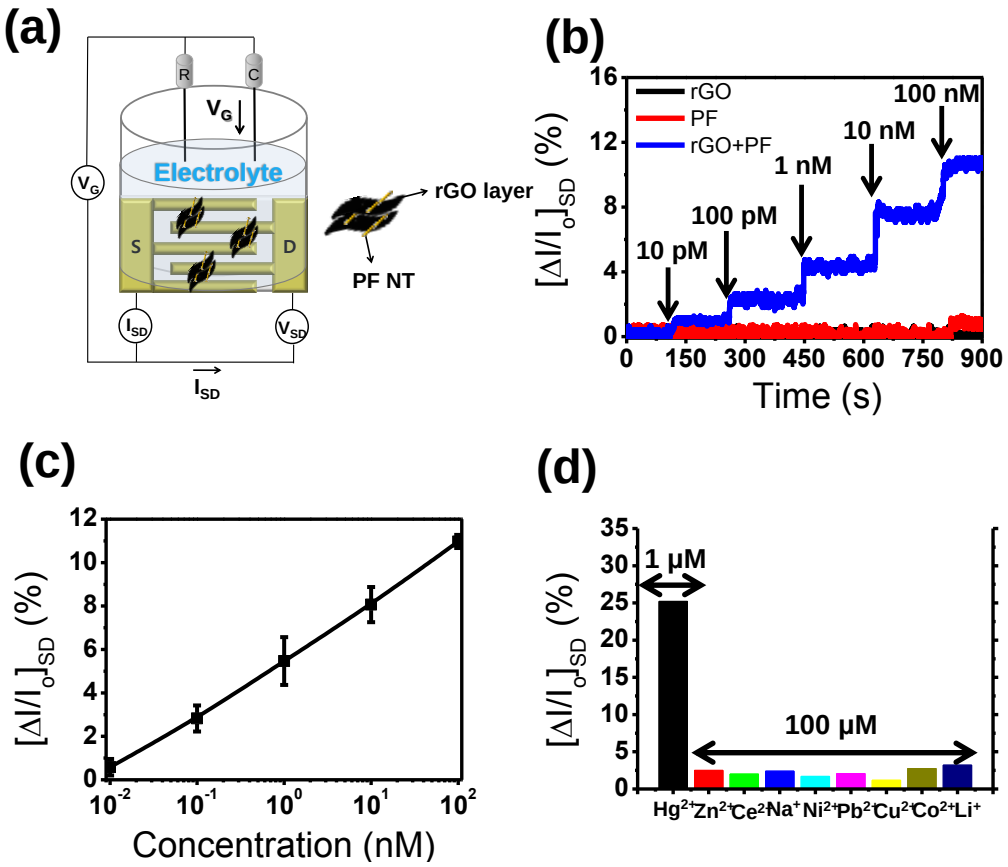

Figure 34. (a) A liquid-ion-gated FET-type sensor based on rGO-PF NTs. (Ag/AgCl reference electrode, R; platinum counter electrode, C; source and drain electrodes, S and D) (b) Real-time responses and (c) a calibration curve for Hg^{2+} based on rGO, PF NTs; rGO-PF NT composites were measured at Vsd = 10 mV (V_g = – 0.1 V) with Hg^{2+} concentrations of 10 pM to 100 nM. (d) A histogram of the sensitivity of the rGO-PF NT composites to Hg^{2+}, Zn^{2+}, Ce^{2+}, Na^{+}, Ni^{2+}, Pb^{2+}, Cu^{2+}, Co^{2+}, Li^{+}.

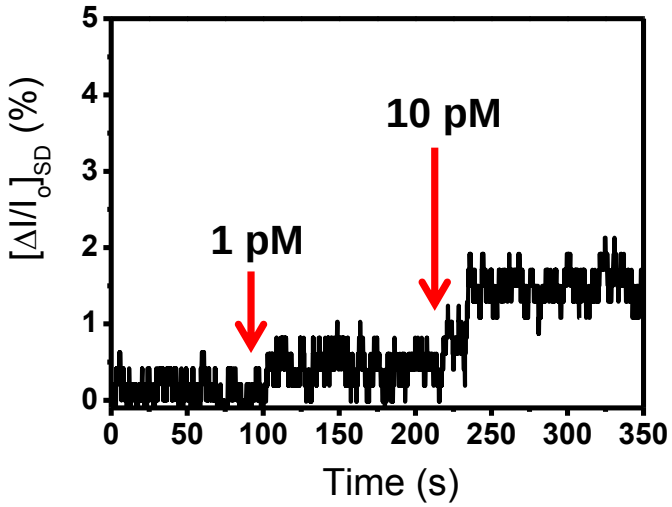

Figure 35. Real-time responses for Hg^{2+} sensor based on rGO-PF NT composites measured at V_{sd} = 10 mV (V_g = - 0.1 V) with a Hg^{2+} concentration of 1 pM to 10 pM.

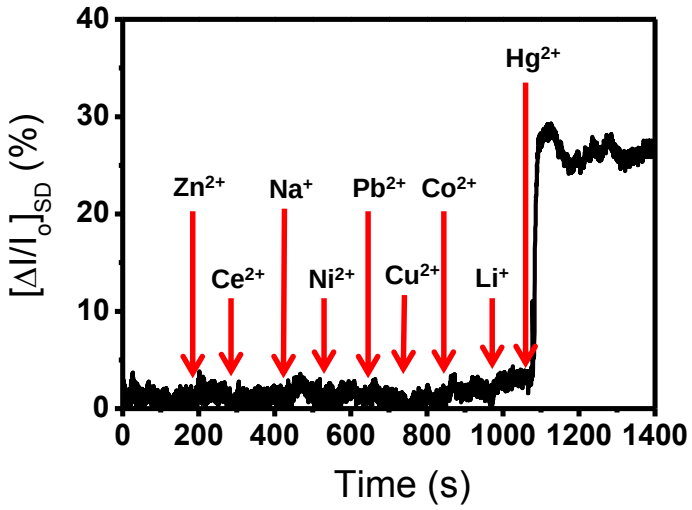

Figure 36. Real-time responses to Zn^{2+}, Ce^{2+}, Na^{+}, Ni^{2+}, Pb^{2+}, Cu^{2+}, Co^{2+}, Li^{+}, and Hg^{2+} measured at V_{SD}= 10 mV (V_g = - 0.1 V).

Table 3. Comparison of the mercury sensing performance of various sensor type devices.

Electrode materials	Sensor type	Sensitivity (μM)	Reference
CNT	Vapor	1	[180]
Ni/Au NHs	Vapor	0.1	[181]
PPy/Pd NHs	Vapor	1	[182]
CNT/Au NPs	Vapor	0.002	[183]
rGO/PF NHs	LE FET	0.000001	In this work

CNT = Carbon nanotube, NP = Nanoparticle, LE FET = Liquid electrolyte field effect transistor, NH = Nanohybrid

3.4. Fabrication of graphene/polyselenophene nanohybrid materials for highly sensitive and selective chemiresistive sensor

3.4.1. Fabrication of RGO/PSe nanohybrid materials

The morphology of the RGO/PSe nanohybrid material was characterized using FE-SEM and TEM. The FE-SEM images of RGO and RGO/PSe nanocomposites are shown in Figure 36(b) and (c). A rougher surface on the RGO/PSe nanocomposits than on the RGO sheets was observed, indicating that the PSe was coated onto the RGO layer. The morphology of the as-synthesized materials was confirmed using TEM. (See the insets of Figure 37(b) and (c).) The PSe was highly coupled to the graphene sheets, enabling the original morphology of the graphene sheets to be maintained. Scanning transmission electron microscopy (STEM) was conducted to obtain additional structural information about the graphene–PSe nanohybrid material. (See Figure 37(d)) Elemental analysis (Figure 36(e) and (f)) indicated uniform distribution of C and Se. (The greater intensity of the elemental C signal compared with that of Se was attributed to the fact that the TEM sample grid was C based.)

For greater insight into the structure of the RGO/PSe nanocomposites, Raman spectroscopy was carried out, as shown in Figure 38(a). The Raman spectrum of GO exhibited D peaks at 1364 cm^{-1}, and G peaks at 1610 cm^{-1}. On the other hand, the Raman spectrum of the RGO showed two prominent bands,

at 1356 cm^{-1} and 1602 cm^{-1}, corresponding to the D and G bands, respectively. These results clearly indicated perfect reduction of GO to RGO. The Raman spectrum of PSe exhibited C=C backbone stretching at ~1609 cm^{-1} and a ring stretching mode at 1372 cm^{-1}. The Raman spectrum of the RGO/PSe nanocomposites exhibited increased band intensity around 1357 cm^{-1}, indicating an interaction between PSe and the RGO sheets.

XRD patterns and ATR-FTIR were also conducted for structural analysis of graphene–PSe nanocomposites, as shown in Figure 38(b) and (c). The XRD pattern of GO exhibited a very sharp peak at 10.1° (d = 8.75 Å), indicating that the original graphite was successfully oxidized to form GO. A broad peak appeared at 24.8° (d = 3.59 Å), suggesting that RGO formation was achieved by reduction of GO using hydrazine. The RGO/PSe nanohybrids exhibited a broad peak at around 25.0° (d = 3.56), which corresponded to the PSe intermolecular distance in the RGO/PSe nanocomposites. This result is deduced that the PSe was successfully coated on the RGO layer via strong intermolecular π–π interactions.

ATR-FTIR spectra of the GO displayed characteristic absorption bands for oxide groups, including a C=O stretching peak at 1733 cm^{-1}, vibration and deformation peaks associated with O–H groups at 3391 cm^{-1} and 1417 cm^{-1}, respectively, and a C–O (alkoyl) stretching peak at 1037 cm^{-1} as shown in

Figure 38(c). Most of the peaks related to oxygen-containing functional groups were not evident in the FTIR spectra of RGO, indicating that the reduction of GO was successful. The spectra of the RGO/PSe nanohybrids exhibited characteristic bands for a selenophene ring and graphene fundamental vibrations, which occurred at 1624 cm^{-1} (C=C stretching), 1557 cm^{-1} (C–C stretching), 1196 cm^{-1} (C–Se stretching), and 1012 cm^{-1} (C–H deformation). [81] The RGO/PSe nanocomposite peaks were shifted compared with those of isolated PSe and RGO due to interactions between the RGO layers and PSe. Overall, the spectra indicated that the PSe materials were successfully coated onto the surface of the RGO layer.

The surface of RGO/PSe nanohybrids was further characterized by X-ray photoelectron spectroscopy (XPS), as shown in Figure 39. The XPS survey scan spectrum exhibited the principal C 1s, O 1s, Se 3d, and Cl 2p core levels, without any evidence of impurities. The O 1s peak was attributed to physisorbed oxygen on the RGO/PSe nanonetworks, even after reduction GO. Cl atoms doped the RGO/PSe nanocomposites during oxidation polymerization of the selenophene monomer, as confirmed by the Cl 2p XPS profiles. Therefore, the RGO/PSe nanohybrid material was successfully synthesized and characterized.

To quantify the amount of PSe in the rGO/PSe nanohybrid materials,

thermogravimetric analysis (TGA) analysis was carried out under air flow. Figure 40 shows the TGA curve of the rGO-PSe nanocomposites with thos of PSe and rGO when heated from 20 to 800 ℃ at a rate of 20 ℃/min under air flow. The PSe showed a 90.72 % weight loss at temperatures between 82 and 800 ℃ due to the evaporation of adsorbed water and decomposition of oligomers and the main backbone of PSe. There is around 8.9 wt% oxidant remaining. While the graphene powder displayed 12.6 % weight loss throughout the temperature range used for this experiment, the rGO-PSe nanohybrids exhibited a 32.79 % weight loss from 100 to 800 ℃, corresponding to the burning of PSe. Thus, it can be calculated that the weight percentage of PSe in this nanohybrids is 20.19 wt%.

To further evaluate the increased electrochemical properties, we conducted Brunauer−Emmett−Teller (BET) surface area measurements. (See Figure 41) Nitrogen isotherm adsorption measurement on the as-prepared PSe, rGO, and rGO/PSe nanocomposites revealed that graphene−PSe nanohybrids had a BET surface area of 95.06 $m^2 g^{-1}$, which was higher than that observed for pure PSe (19.57 $m^2 g^{-1}$) and rGO (63.5 $m^2 g^{-1}$). These results suggested that the rGO sheet served as a conductive channel, leading to enhanced conductivity (See Figure 42) and enlarged surface area.

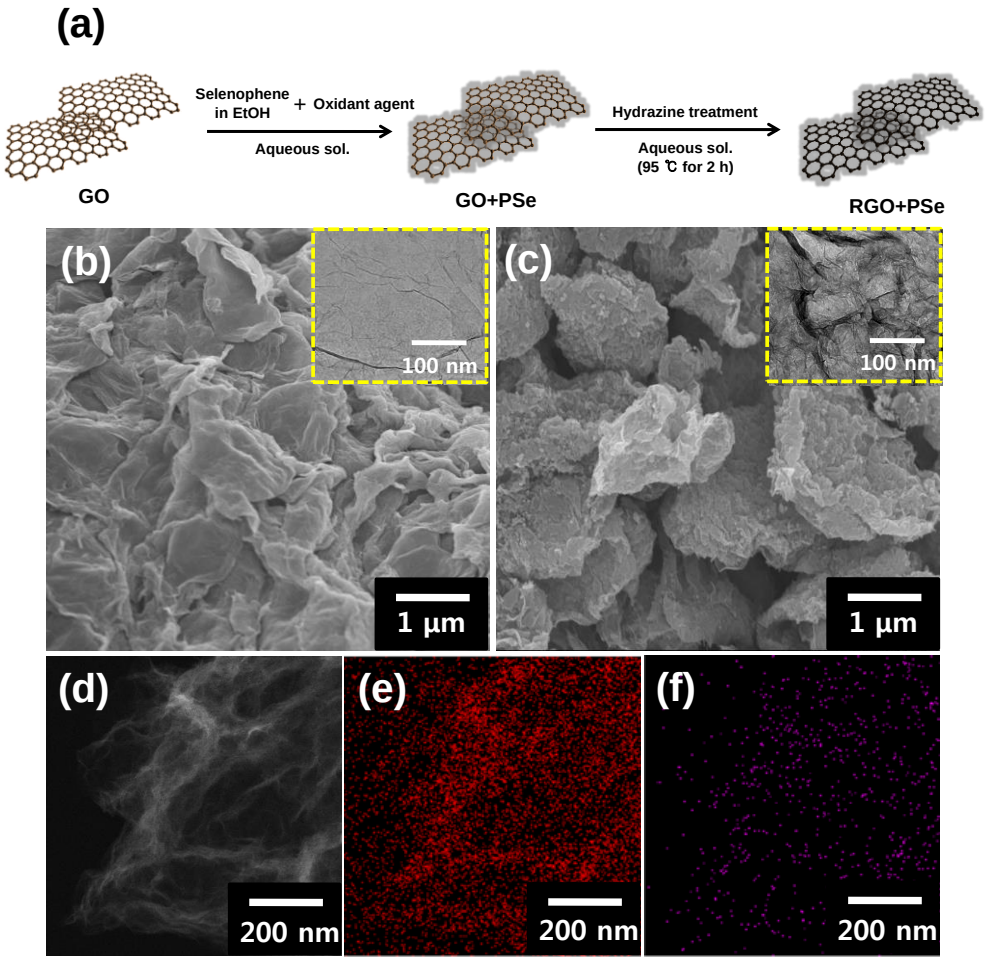

Figure 37. (a) Schematic illustration of the preparation of graphene–PSe nanocomposites. FE-SEM images of (b) rGO and (c) rGO/PSe nanocomposites. (Insets are the TEM images of rGO and rGO/PSe nanohybrid materials.) (d) Typical STEM image of graphene–PSe nanohybrids. Corresponding elemental mapping images of (e) C and (f) Se.

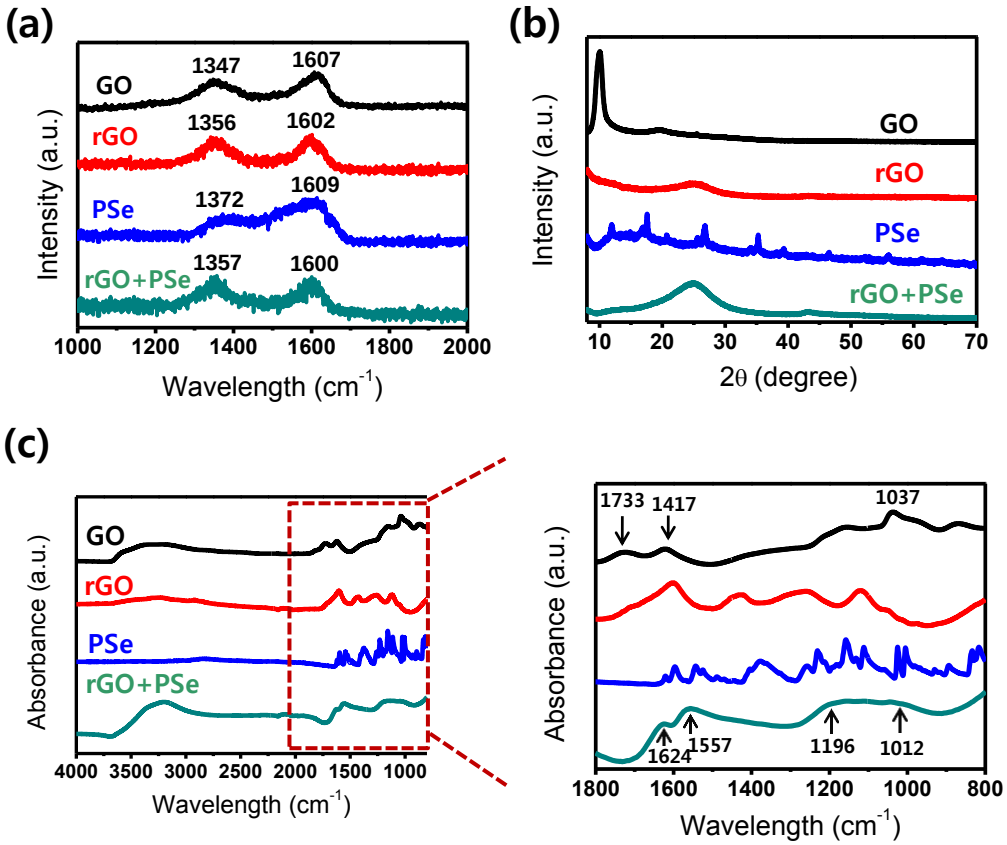

Figure 38. (a) Raman spectroscopy, (b) XRD patterns, and (c) ATR-FTIR spectra of GO, rGO, PSe, and rGO/PSe nanohybrids.

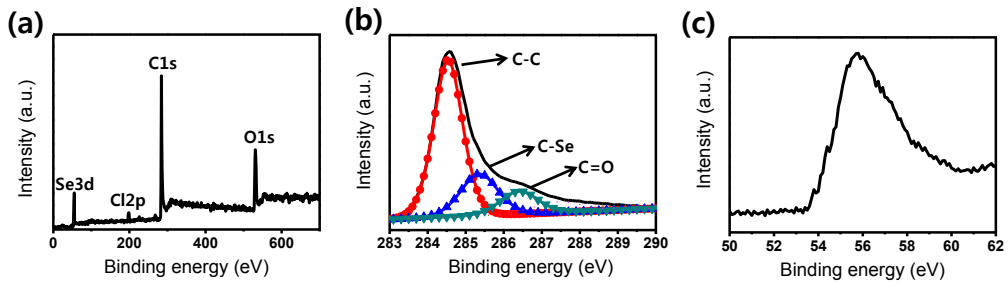

Figure 39. (a) Overall, (b) C 1s, and (c) Se 3d XPS profiles of rGO/PSe nanohybrids.

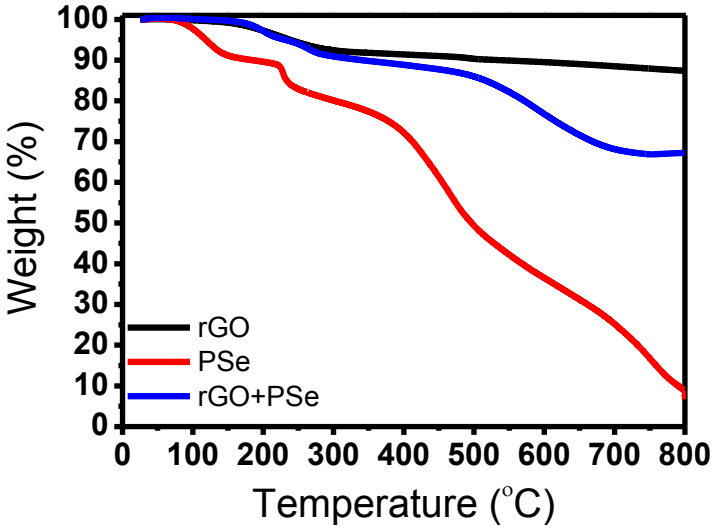

Figure 40. TGA curves of rGO, PSe, and rGO-PSe nanohybrid materials.

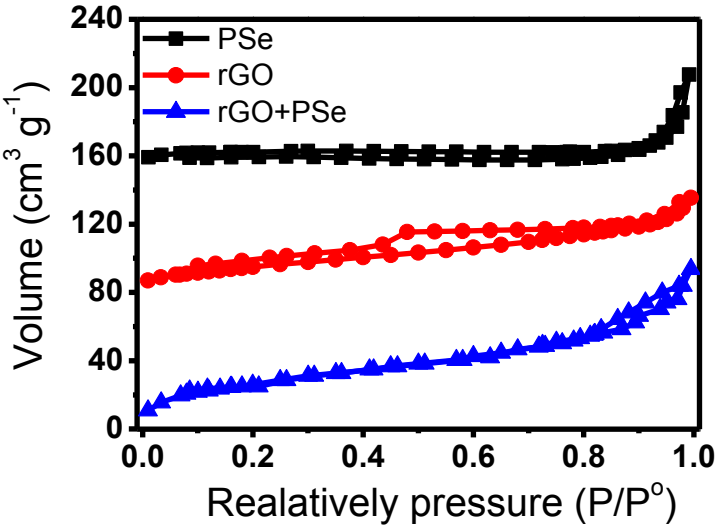

Figure 41. N_2 adsorption/desorption isotherms of PSe, rGO, and rGO/PSe nanohybrids.

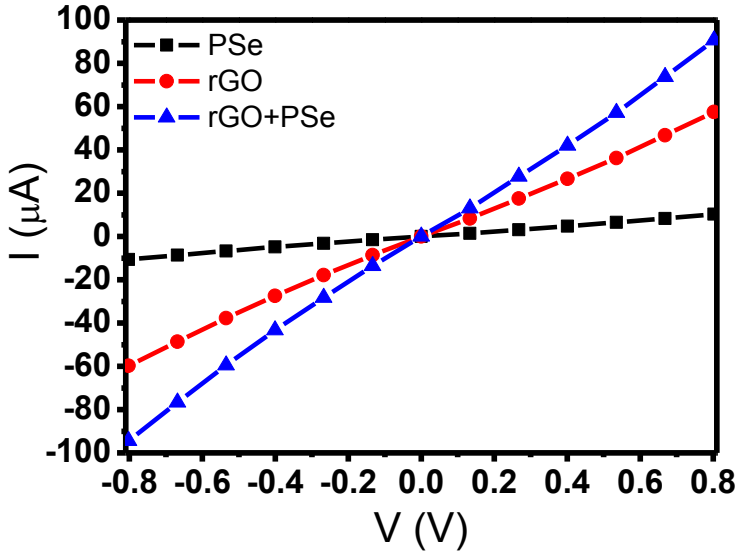

Figure 42. Current−voltage ($I-V$) curves of PSe, RGO, and RGO−PSe nanohybrid materials.

3.4.2. Fabrication of chemiresistive sensor based on RGO/PSe nanohybrid materials

RGO/PSe nanohbrid inks in chlroform solution were prepared and introduced on to the PET film by using screen printing method, as shown in Figure 43(a). Consecutively, building source and drain electrodes (PT, 100 nm) were pattered on the RGO/Pse film through shadow mask sputtering method. The optical microscopy images of RGO/PSe nanohybrid films were observed before and after Pt coated process, as shown in Figure 43(b) and (c). The resistance changes on the as-prepared electrode based on the RGO/PSe nanohybrid was measured via a source-meter connected to a computer. The chemiresistive sensor based on the RGO/PSe nanohybrid was placed in a vacuum chamber with a vapor inlet/outlet pressure of 100 Torr. Various concentrations of NH_3 (0.01–10 ppm), MeOH (1–100 ppm), and other organic gases were injected into the chamber using a mass flow controller (MFC, KNH Instruments). The real-time responses from the RGO/PSe nanohbyrid were systematically appraised by normalized resistance changes ($\triangle R/R_0$). The normalized resistance change ($\triangle R/R_0$) of the RGO/PSe based sensor was monitored in real-time during exposure to various gases at a constant applied current (10^{-6} A) until saturation was reached. $\triangle R/R_0$ of the RGO/PSe nanohybrid is given by the following equation:

$\Delta R/R_0 = (R - R_0)/R_0$ (1)

where R_0 is the initial resistance and R is themeasured real-time resistance, respectively.

After the RGO/PSe nanohybrids were exposed to various concentrations of NH_3 or MeOH gas for several minutes, the gas vapor was then replaced by compressed air to remove any molecules attached to the nanomaterials. This process was repeated several times. Vapor/air was supplied at various concentrate ranging from 2 to 8 slm and 1 to 5 sccm, as controlled by the MFC.

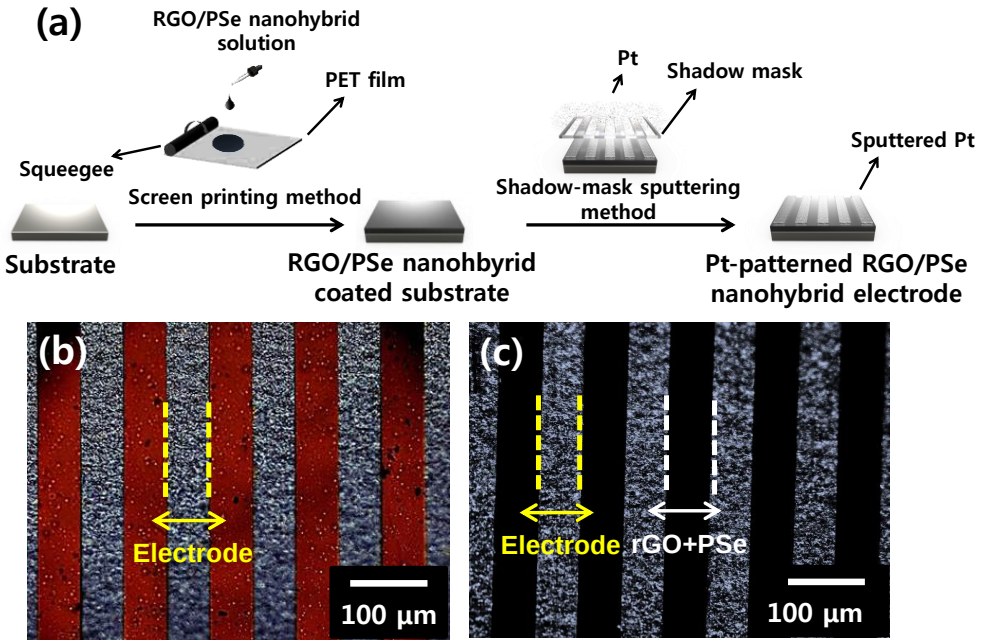

Figure 43. (a) Schematic illustration of RGO/PSe nanohybrid chemiresistive electrode. Optical microscopic images of fabricated electrode (b) before and (c) after RGO/PSe nanohybrid material coataing process.

3.4.3. Chemiresistive sensing performance of the RGO/PSe nanohybrid film

To investigate the sensing performance of the RGO/PSe nanohybrids, their electrical response (resistance changes) was recorded in real-time during exposure to various gases. When the chemiresistive sensor based on the RGO/PSe nanohybrid was exposed to various gases at room temperature, excellent sensitivity and rapid response/recovery times were observed. Figure 44(a) exhibits the response upon exposure to NH_3 and MeOH vapor as a function of analyte concentration. In particular, the sensing performance of devices based on the graphene nanohybird materials depends on the charge carrier density. The responses upon exposed gas molecules enable to change the charge carrier density in the RGO/PSe nanohbyrid structure. The electrical responses of the RGO/PSe nanohybrid sensor were different behavior for the two gases tested. The resistance increased after exposure to NH_3 and decreased after exposure to MeOH. This result proposes that the introduction of electron-donating molecules (NH_3) into the RGO/PSe nanohybrid backbone (p-type transducer) decreased the charge carrier density (hole density) via a redox reaction, resulting in the enhanced resistance of the transducer. In contrast, the electron-acceptor MeOH created new holes in the RGO/PSe nanohbyrid structure, leading to the opposite result. The limitation detection level (LDL) of

the RGO/PSe nanohybrid gas sensor was 0.01 and 1 ppm for NH_3 and MeOH, respectively. The LDL of both gases was within specifications offered by the Occupational Safety and Health Administration (NH_3: 25 ppm; MeOH: 200 ppm). The enhanced surface area of the RGO/PSe nanohybrids enabled not only fast diffusion of the analyte gas molecules for rapid response times, but also improved sensitivity compared with pure PSe nanomaterial, owing to the synergetic effects of RGO/PSe nanohybirds, leading to the increased the interaction between the target analyte and the nanohybrid material. To test the reproducibility and reversibility of the sensing performance, the electrical response of the chemiresistive sensor based on the RGO/PSe nanohybrid was monitored upon periodic exposure to 10 ppm of NH_3 and 100 ppm of MeOH at room temperature, as shown in Figure 44(b). The PSe nanomaterial displayed similar responses for both NH_3 and MeOH compared with the RGO/PSe nanohybrid material. Moreover, this gas sensor had excellent cycle stability (Figure 44(c)). Figure 44(d) exhibits the calibration curve of the sensor as a function of NH_3 and MeOH gas concentrations. The normalized resistance change was nearly zero at 0 ppm. At low concentrations (<1 ppm), the chemiresistive sensor displayed a nonlinear change in sensitivity. On the other hand, linear behavior was monitored over the concentration ranges of 0.01–0.1 ppm for NH_3 and 1–100 ppm for MeOH. Therefore, RGO/PSe nanohybrids can

be efficiently used for detecting NH_3 and MeOH gases of various concentrations. In addition, Figure 45 shows the sensitivity of RGO/PSe nanohybrids to several representative VOCs and toxic gases at 10 ppm. RGO/PSe nanohybrids showed remarkable signal changes in the presence of all of the selected gases evaluated except for hexane. Among all gases tested, the sensitivity and selectivity were greatest for NH_3. In addition, the LDL of NH_3 was 10–10^3 times higher than that of other gases.

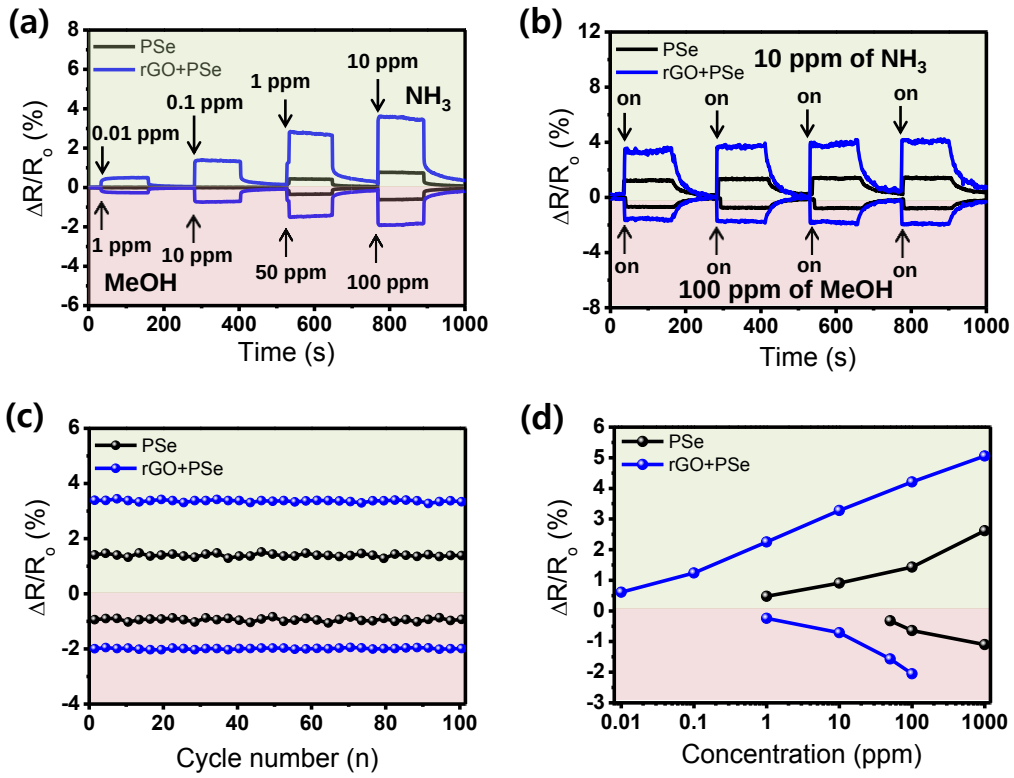

Figure 44. (a) Real-time responses of PSe and RGO/PSe nanohybrid materials upon sequential exposure to NH_3 (0.01 to 10 ppm) and MeOH (1 to 100 ppm). (b) Real-time responses of PSe and RGO/PSe nanohybrid materials on periodic exposure to 10 ppm of NH_3 and 100 ppm of MeOH. (c) Normalized resistance changes of PSe and RGO/PSe nanohybrids with periodic exposure to 10 ppm of NH_3 and 100 ppm of MeOH gases for 100 cycles. (d) Calibration curve of PSe and RGO/PSe nanohybrids as a function of NH_3 and MeOH concentration.

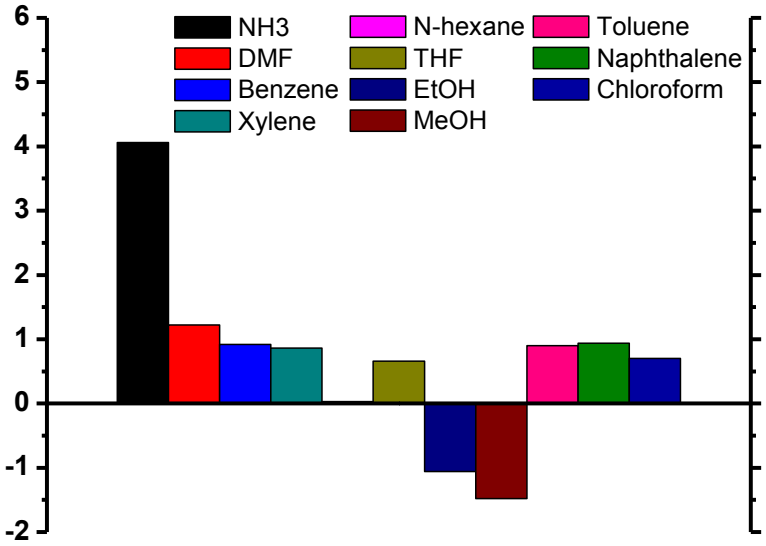

Figure 45. Sensing performance histrogram of RGO/PSe nanohybrid mateirals to 11 analytes: each analyte concentration was fixed at around 10 ppm.

3.5. Fabrication of graphene/free-standing nanofibrillar PEDOT/P(VDF-HFP) hybrid device for wearable and sensitive human motion detective piezo-resistive sensor

3.5.1. Fabrication of CVD graphene/free-standing nanofibrillar PEDOT/P(VDF-HFP) nanohbyrid devices

A schematic diagram of the fabrication process of the graphene/P(VDF-HFP)/V-PEDOT nanohybrid E-skin device was described, as shown in Figure 46. Single-layered graphene was synthesized on a copper foil substrate using CVD method. Then, a PMMA solution was poured and spin-coated (4000 rpm, 60 s) on the graphene film. Subsequently, the copper was removed by wet chemical etching process. A wet transfer method was used to transfer graphene on a flexible PDMS substrate. The PMMA was then removed using actone solution. The reason why PDMS was used is that this substrate has good flexibility, optical transparency, strength, and low weight.

To clearly understand the property of the graphene, atomic force microscopy (AFM) and HR-TEM were used. AFM showed the thickness of graphene to be 0.4 nm (Figure 47(a)) and HR-TEM proposed that it consisted of a single layer (Figure 47(b)). Figure 47(c) showed ultraviolet/visible (UV-Vis) spectra of a graphene film with dimensions in the range 400-800 nm. The optical transmittance measured following transfer of the graphene to the

flexible PDMS substrate, and was found to be 96.6% at 550 nm. The sheet resistance of the graphene was approximately 1 kΩ sq^{-1}. These results clearly indicate that CVD provides a monolayer of graphene.

The VDP process was conducted to vertically grow PEDOT nanofiber on the graphene surface. The resulting densely grown vertically aligned PEDOT islands on the graphene film were observed by FE-SEM, as shown in Figure 48(a) and (b). To clearly observe the formation of vertically growing PEDOT nanofibrillar deposition, SEM images according to vapor deposition reaction times were observed, as shown in Figure 49. Firstly, iron nanoparticles were formed on the surface of graphene. The iron/PEDOT nanofibers were clearly observed with increasing reaction time. After rinsing process was conducted several times, the optimized PEDOT islands were approximately 70 nm in diameter and 10 μm in length. Then, P(VDF-HFP) was deposited onto the V-PEDOT/graphene film by spin-coating at 3000 rpm for 60 s. To crystallize the P(VDF-HFP), the film was annealed at 150℃ for 2 h. The vertically aligned structure was preserved upon P(VDF-HFP) coating (See Figure 48(c)), suggesting that the structure was highly stable.

The properties of the graphene/V-PEDOT/P(VDF-HFP) nanohybrid film were compared to those of its component materials by Raman spectroscopy, as shown in Figure 50. The Raman spectrum of graphene exhibited G peak (at

~1600 cm^{-1}) and a 2D peak (at ~2700 cm^{-1}). This spectrum further confirms fabrication of single-layer graphene, as the 2D peak is sharper and more pronounced than the G peak. The Raman spectrum of PEDOT exhibited C=C backbone stretching peaks at 1541 cm^{-1} and 1573 cm^{-1}, symmetric C=C (–O) stretching at 1429 cm^{-1}, C–C stretching deformation at 1357 cm^{-1}, and a oxyethylene ring deformation feature at 988 cm^{-1}. The Raman spectrum of the P(VDF-HFP) exhibited peaks at 837 cm^{-1} and 910 cm^{-1}, indicating symmetric C–F_2 stretching of the crystalline beta phase.[184] The Raman spectrum of the graphene/V-PEDOT/P(VDF-HFP) nanohybrid film exhibited features of graphene and PEDOT, as well as P(VDF-HFP) fundamental vibrations, which were shifted compared with those of these materials in isolation due to interactions between them.

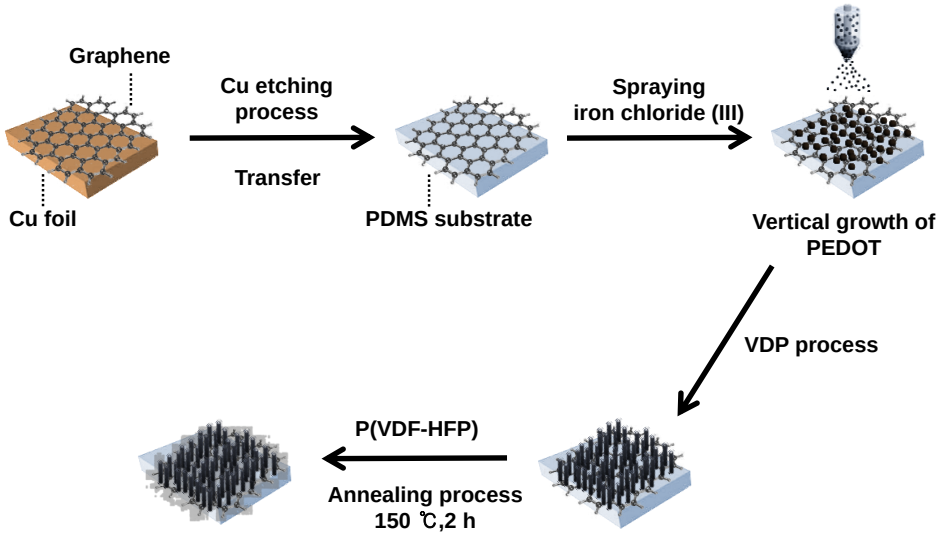

Figure 46. Schematic diagram showing the fabrication process of E-skin based on graphene/V-PEDOT/P(VDF-HFP) nanohybrid device.

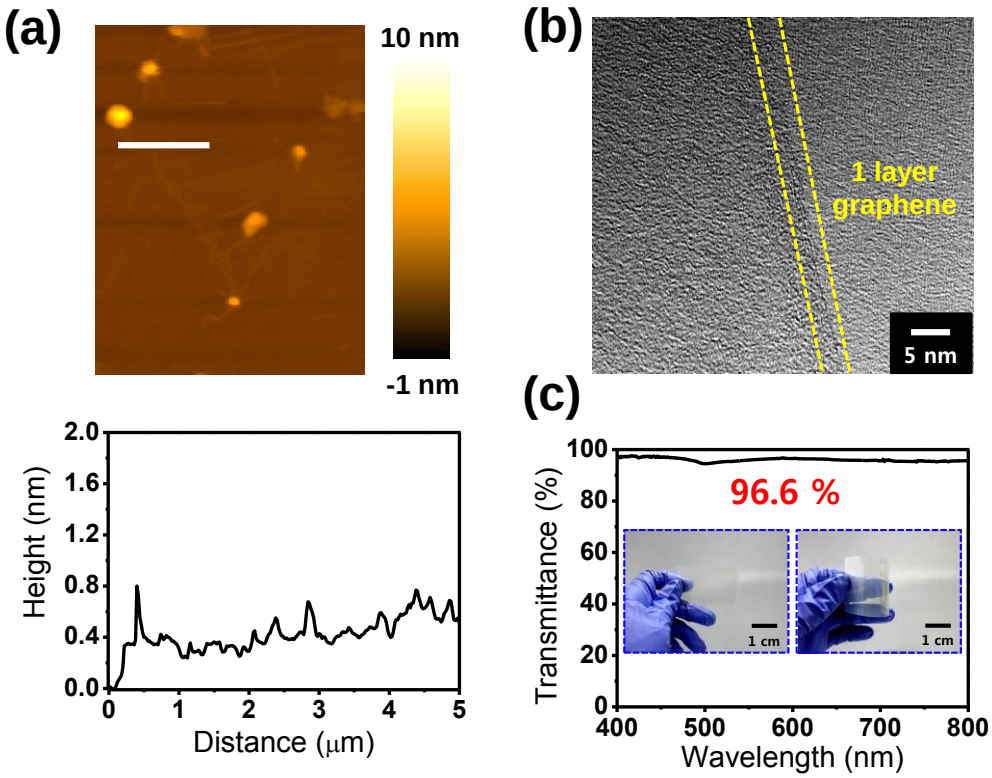

Figure 47. (a) AFM and (b) HR-TEM images of the single-layer graphene. (c) UV-Vis spectra of the graphene transferred onto the PDMS film. The inset shows a photograph of the flexible and transparent graphene film.

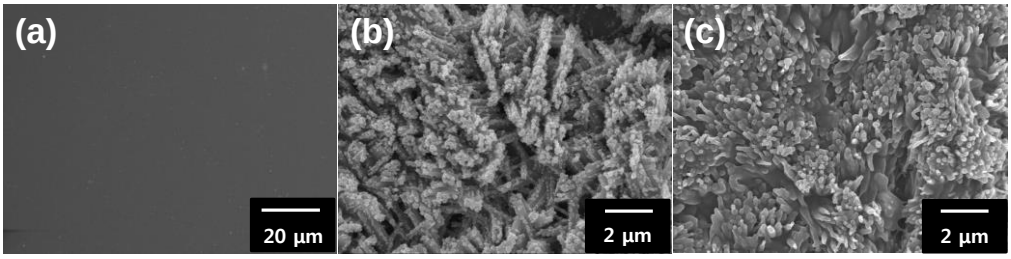

Figure 48. SEM image of the (a) graphene, (b) the vertically grown PEDOT (via VDP) nanofibers on the graphene, and (c) the fabricated P(VDF-HFP)/PEDOT/graphene films.

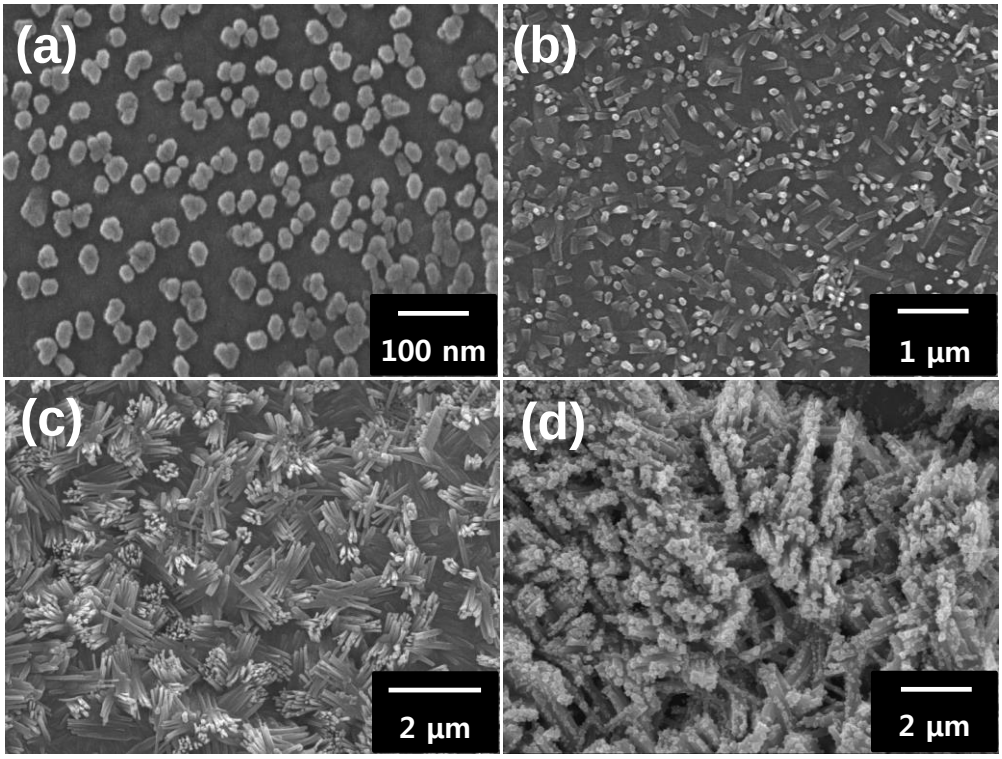

Figure 49. SEM images of V-PEDOT according to VDP reaction time (a) 0, (b) 15, (c) 30 min, and (d) 1h.

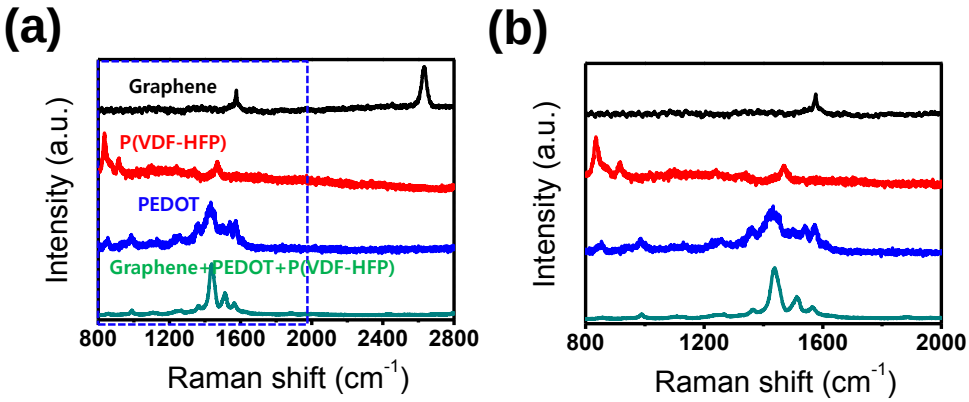

Figure 50. Raman spectra of graphene, P(VDF-HFP), PEDOT, and graphene/PEDOT/P(VDF-HFP) nanohybrid materials.

3.5.2. Sensing performance of E-skin device

The E-skin was constructed from two layers of graphene/V-PEDOT/P(VDF-HFP) films placed face to face, and Ag paste was placed at the edges of both films to form source and drain electrodes, as shown in Figure 51(a). The device's pressure response was first tested in real time by finger pressing. Then, response to pressure of varying force was tested. During these experiments, a thin glass slide (75×25 mm) was placed over the E-skin device to improve its stability. Signal (change in resistance) increased as the applied pressure increased from 5 to 30 Pa (See Figure 51(b)). The device's sensitivity was determined from the change in the resistance $\Delta R/R_0 = (R–R_0)/R_0$, where R_0 is the initial resistance and R is the measured real-time resistance following stabilization after application of pressure. The reason of change in E-skin resistance is a piezo-resistive effect, which may result from disturbances in conducting pathways, state changes in the nanohybrid material, or variation in tunneling effects between neighboring materials and the deformed graphene flakes. The detection limit of the fabricated novel E-skin was very low (0.5 Pa), indicating that it is almost 10-fold more sensitive than previous devices, as shown in Table 4. Interestingly, the piezo-resistivity of the graphene/V-PEDOT/P(VDF-HFP) nanohybrid device was larger than that of pure graphene or the graphene/P(VDF-HFP) device (See Figure 51(c)). To understand this

result, GF values of pure graphene, graphene/V-PEDOT, graphene/P(VDF-HFP), and graphene/V-PEDOT/P(VDF-HFP) nanohybrid devices were calculated, as shown in Figure 52. The GF was calculated according to:

$$GF = \frac{(R - R_o)}{R_o \times \varepsilon} \quad (1),$$

where R is resistance under mechanical strain, R_o is resistance without strain, and ε is mechanical strain.

With 0.2% tensile mechanical strain, the GF of each material was: pure graphene, 10,; graphene/V-PEDOT, 23; graphene/P(VDF-HFP), 34; and graphene/V-PEDOT/P(VDF-HFP), 67. With 2% tensile strain, the GF values were: pure graphene, 55; graphene/V-PEDOT, 83; graphene/P(VDF-HFP), 138; and graphene/V-PEDOT/P(VDF-HFP), 320. Interestingly, the GF of the graphene/V-PEDOT/P(VDF-HFP) nanohybrid device was up to sixfold greater than that of the simpler devices, suggesting that synergetic effects of the nanohybrid materials; i.e., enhanced piezo-resistive effect and contact area result in a large GF.

To test the electrical properties of the samples, current-voltage (*I-V*) curves were measured by using probe station (See Figure 53). In addition, the sheet resistance values of the samples were recoreded, as shown in Table 5. Firstly, the samples were fabricated on the gold patterned electrode substrate as the same method. Linear *I-V* curves were observed over a range of -0.6 V to +0.6

V. The conductivity of the graphene/V-PEDOT nanohybrid material was greater than that of the pure graphene, suggesting effective charge transport between the graphene and PEDOT. However, the graphene/V-PEDOT/P(VDF-HFP) nanohybrid device exhibited the smallest conductivity, which is attributed to the insulating properties of the P(VDF-HFP). Although the graphene/V-PEDOT/P(VDF-HFP) nanohybrid device showed reduced conductivity compared with graphene/V-PEDOT device, the high mechanical property of the P(VDF-HFP) maintains vertically grown PEDOT under strain stimulus, which leading to more durable, flexible, and stretchable character with large GF value.

Therefore, the graphene/V-PEDOT/P(VDF-HFP) nanohybrid E-skin device's highly sensitive strain-sensing behavior may be explained by the following factors: (i) the nano-scale vertically grown PEDOT provides increased contact surface area between the layers, (ii) the P(VDF-HFP) material reduces the number of conducting pathways, both of which lead to a larger strain-induced resistance change, and hence a larger GF, and (iii) high mechanical property of P(VDF-HFP) fixes free-standing PEDOT, responding more stable and sensible toward the pressure stimulus.

To investigate the pressure sensor's stability, its change in resistance was measured upon cyclic applied pressure of 30 Pa for more than 1,000 cycles at a

cycle length of 2 s (Figure 54). No defects or deterioration in performance were observed. This result indicates the E-skin device showed excellent stability and durability.

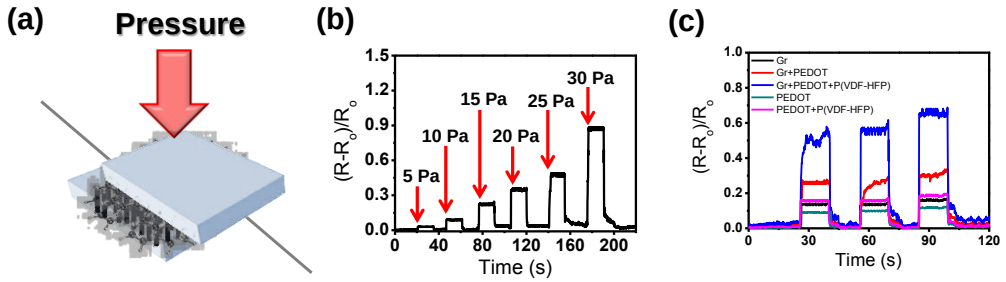

Figure 51. (a) Schematic diagram of the E-skin device. (b) Sensitivities to pressure with various stimuli. (c) Real-time change in resistance of the electronic skin devices as a function of the graphene, graphene/P(VDF-HFP), graphene/V-PEDOT/P(VDF-HFP), V-PEDOT, and V-PEDOT/P(VDF-HFP) material.

Table 4. Comparison between the detection limit performances of our flexible strain sensor and those of strain sensors based on other materials.

Material	GF	Ref
3D ZnO NW	3.5 kPa	185
Ag NPs	1 kPa	186
OFET	1 kPa	187
PT-coated polymer NFs	5 Pa	188
FE FET	2 Pa	189
ITO/PET film	3 Pa	190
Graphene/V-PEDOT/P(VDF-HFP) NC	0.5 Pa	This work

NW = Nanowire, NP = Nanoparticle, OFET = Oragnic Field-effect transistor, FE = Ferroelectret, NF = Nanofibre, NR = Nanoribbon, NC = Nanocomposite

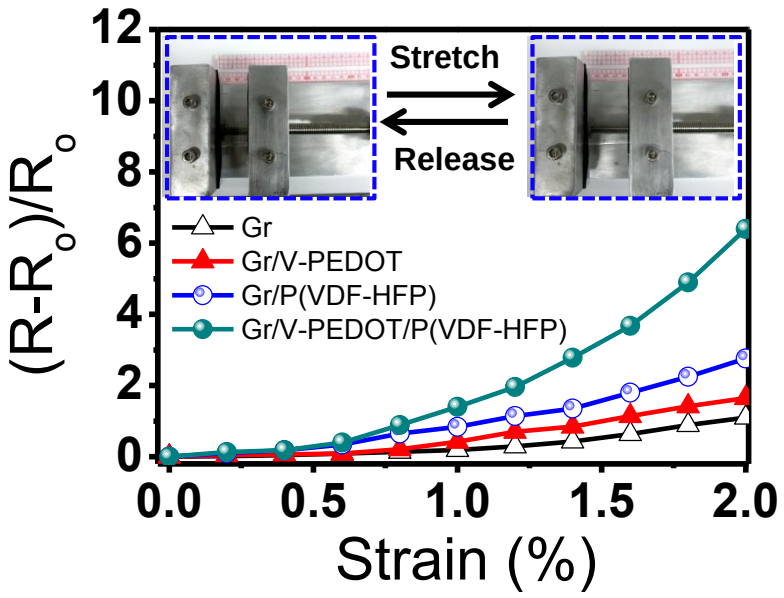

Figure 52. Resistance as a function of strain for graphene, graphene/V-PEDOT, graphene/P(VDF-HFP), and graphene/V-PEDOT/P(VDF-HFP) nanohybrid film.

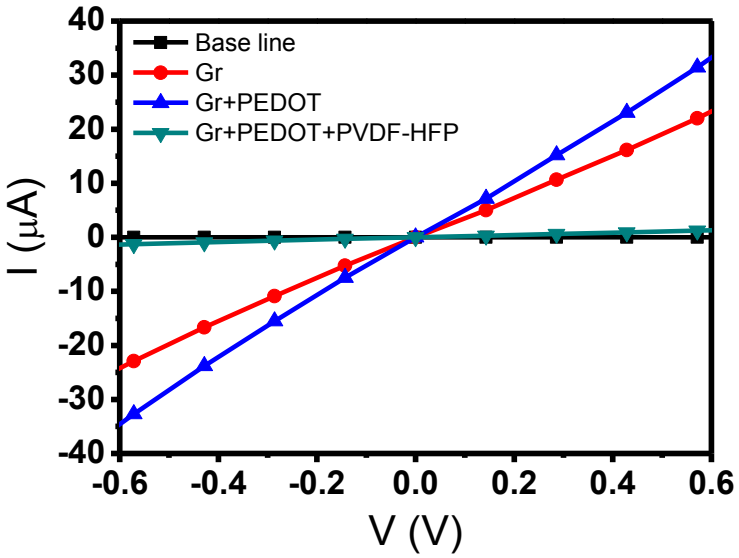

Figure 53. Current–voltage (*I*-*V*) curves of graphene, graphene/PEDOT, and graphene/PEDOT/P(VDF-HFP) nanohybrids.

Table 5. Comparison of the sheet resistance values based on graphene, graphene/V-PEDOT, and graphene/V-PEDOT/P(VDF-HFP) nanohybrids.

Samples	Resistance (kΩ)
Graphene	1.1
Graphene/V-PEDOT	0.43
Graphene/V-PEDOT/P(VDF-HFP)	4.5×10^2

Table 6. Comparison between the GF value of our E-skin device and those of strain sensors based on other materials

Material	GF	Ref
Single VO_2 NB	100	191
ZnO NW/PS film	116	192
ZnO – Paper NC	21.12	193
Graphene/PVDF NC	12.1	73
Polymer/CNT NC	117	195
Graphene/V-PEDOT/P(VDF-HFP) NC	320	This work

NB = Nanobeam, GF = Gauge factor, NW = Nanowire, PS = Polystyrene, NC = Nanocomposite, CNT = Carbon nanotube

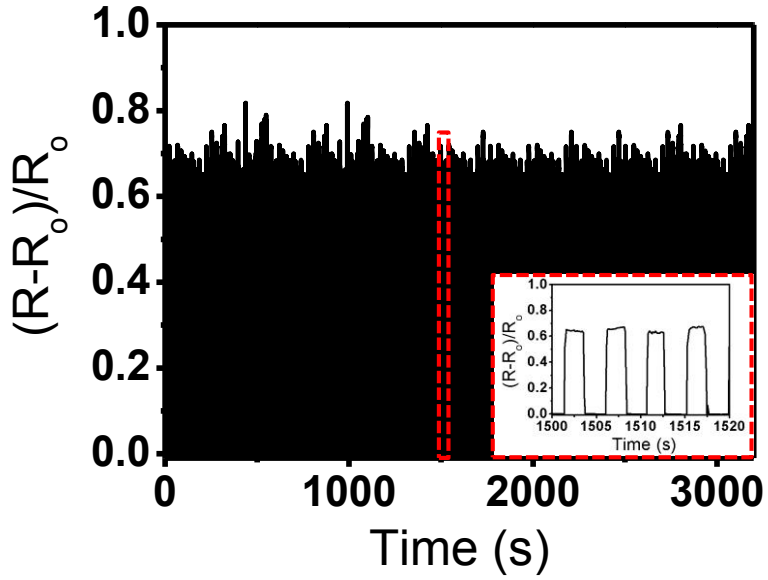

Figure 54. Real-time change in the resistance of the E-skin over more than 1000 loading cycles, with a cycle length of 2 s and an applied pressure of 30 Pa. The inset shows a magnified image in the red rectangular region.

3.5.3. Practical application of E-skin device

The GF value of graphene/V-PEDOT/P(VDF-HFP) nanohybrid E-skin device is much higher than that of other reported materials, as shown in Table 7. This extremely large GF value suggests that the device could detect very small strains associated with subtle motions, such as wrist pulse. Figure 55(a) exhibited the resistance change as a function of time in the wearable E-skin device during an *in situ* tensile test as the hand moved from an out-stretched to a clenched-fist position. The E-skin could provide an interesting and effective method for detecting human motion owing to ultra-sensitive and fast respond of the devices.

In modern medical practice, wrist pulse is an important indicator of arterial blood pressure and heart rate, providing useful information for non-invasive medical diagnosis. The E-skin fabricated, in this work, may be useful to measure wrist pulse in real time, as its rapid response (<1 s) gives sufficient resolution to measure pulse. Resistance change of the device as a function of time was observed when placed over the artery in the wrist reveals a pulse frequency of 75 bpm, as well as regular and repeatable pulse shapes (Figure 55(b)). This demonstrates potential biomedical applications.

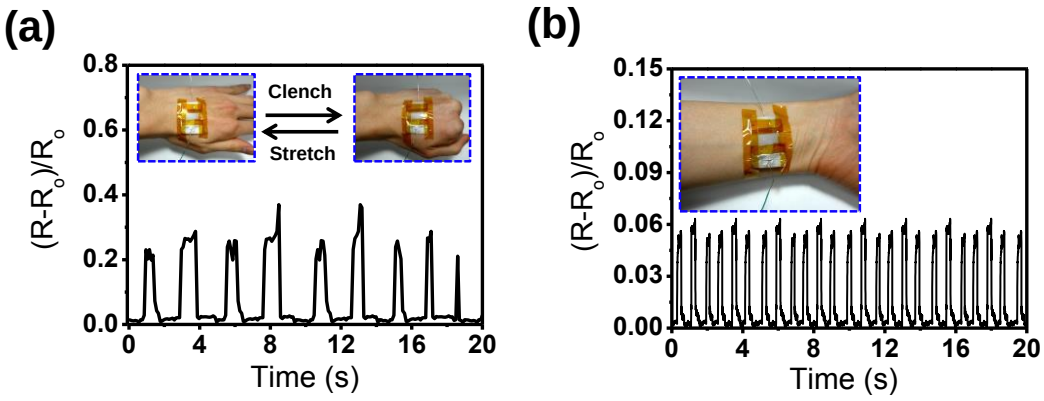

Figure 55. (a) Resistance as a function of time during motion of the hand from an outstretched to a clenched-fist position. (b) Resistance as a function of time while measuring the pulse in the wrist.

4. CONCLUSIONS

1. High sensitivity and specificity towards H_2O_2 using a liquid-ion-gated FET sensor based on RGO/PPy nanohybrid materials were demonstrated. Raman and ATR-FTIR spectroscopy were used for characterizing of the nanohybrid materials. The nanohybrid materials exhibited Ohmic contacts on the source and drain electrodes, which means the good contacts were formed between the materials and electordes. The FET devices based on the nanohybrid mateirals showed *p*-channel behavior, with excellent electrical conductivity. The fabricated FET devices exhibited *p*-channel behavior, with good electrical conductivity, and Ohmic contacts were formed with the source and drain electrodes. The fabricated FET devices were used in the biosensing applications, leading to a rapid response to changes in H_2O_2 concentration with a detection limit of 100 pM. These results are more attractive than those in previous reports for H_2O_2 biosensors. This FET-type biosensor displayed high reproducibility and stability in air condition. Furthermore, ultra-high sensitivity towards H_2O_2 was observed by testing the response of the biosensors in various biological fulids, such as UA, AA, and glucose. From the perspective of sensor performance, these FET-type biosensors based on RGO/PPy NTs may be utilized in environmental and food applications as alternative detecting methods of H_2O_2.

2. A liquid-ion-gated FET sensor based on RGO/C−PPy NT hybrid materials demonstrated high sensitivity and specificity with a rapid response time towards glucose. RAMAN, ATR-FTIR spectroscopy, and XRD were used for characterizing of the synthesized RGO/C−PPy NT hybrid materials. The synthesized nanohybrid mateirals showed synergetic effects of graphene and C−PPy NTs, such as enhanced conductivity and surface area. The FET devices based on the RGO/C−PPy NT hybrid materials display *p*-type semiconducting behavior. The fabricated FET-type biosensor showed a rapid response to electrical changes in glucose concentration with a detection limit of 1 nM (signal-to-noise = 3.22). These results are more attractive and 2–3 orders more sensible than those of previous reports of electrochemical biosensors for glucose detection. The fabricated biosensor had excellent reproducibility and stability in the air or liquid phases. In addition, high specificity towards glucose was demonstrated by testing the response of the biosensor in biological fluids containing UA and AA. These FET-type biosensors based on RGO/C-PPy NTs may be potential utilized as medical diagnosis, diabetes management, bioprocess monitoring, the beverage industry and environmental fields.

3. Liquid-ion-gated FET-type sensor based on the RGO–PF NTs was demonstrated for highly sensitive and selective Hg^{2+} detection. Interestingly, the synthesized RGO–PF NT hybrid materials bound specifically to Hg^{2+} ions

in the various metal ion mixed solution. The fabricated FET-type biosensor showed a rapid response (< 1 s) to electrical changes in Hg^{2+} concentration with a detection limit of 1 pM (signal-to-noise = 3.12). The fabricated biosensor showed excellent reproducibility and stability in the air/liquid phases. Furthermore, high specificity towards Hg^{2+} was demonstrated in real-time experiments in versatile metal ion solution. These FET-type sensors based on RGO–PF NTs could be potentially useful methods for the detection of Hg.

4. A new class of graphene–PSe nanohybrid materials were successfully synthesized and characterized for use as high-performance chemiresistive sensor application. The graphene–PSe nanohybrid materials were synthesized via a simple and facile *in situ* method. The synthesized nanohybrid materials showed the unique properties of both graphene and conducting polymers, such as high conductivity, excellent mechanical properties, and high surface area, which enhanced charge transport behavior and surface area, resulting in increasing the intereaction with the target analyte. These results were regarded as synergitic effects between the graphene and PSe materials. To the best of our knowledge, this is the first demonstration using in the chemiresistive sensing application based on graphene−PSe nanohybrid materials. The synthesized RGO/PSe nanohybrid materials were highly sensitive to various hazardous gases, especially NH_3 gas. The RGO/PSe nanohybrid gas sensor exhibited 10–

100 times greater sensing ability to various gases than that of pristine PSe sensor. In particular, RGO/PSe nanohybrid materials showed 0.01 ppm for NH_3 as limit of detection, which was higher than that observed for other chemical sensor decvice systems. Therefore, this research demonstrated an efficient method to fabricate graphene−PSe nanohybrid materials for use in high performance chemical sensors.

5. A new class of ultra-sensitive E-skin device using a graphene/V−PEDOT/P(VDF−HFP) nanohybrid material was successfully fabricated and developed. CVD method was used for fabrication of single-layer graphene, and nanofibrillar PEDOT was vertically grown on the graphene via vapor polymerization method. The uniform and well-aligned PEDOT nanofibers were clearly monitored by using experimental tool, such as FE-SEM. After deposition of P(VDF−HFP) material on the PEDOT nanofiber structure, the morphology of the PEDOT maintained, which means that the nanohbyrid materials was physically and chemically stable. This E-skin device based on graphene/V−PEDOT/P(VDF−HFP) nanohybrid materials showed werable and flexible properties, detecting strain or stretch with high sensitivity with fast response time, and good stability and durability. The E-skin had very large GF values: 320 at 2% tensile strain and 67 at 0.2% tensile strain, leading to the pressure detection limit was 0.5 Pa. These results are far more sensible and

higher value than those of other previous reports. Furthermore, monitoring human physiological signals, such as real-time monitoring wrist pulse, was demonstrated, suggesting utility for individual-centered health monitoring.

In summary, graphene/CP nanohybrid materials have been fabricated using in-situ polymerization and reduction from GO methods. These approaches were simple, facile, and possible to synthesize the uniform sheets based on the graphene/CP nanocomposites. Graphene/CP nanohybrid materials showed synergitic effects, including enhanced surface area, conductivity, and rapid charge carrier (electron or hole) transporting behavior, leading to high performance sensing performances. This strategy, using graphene/CP nanohybrid materials in the sensor application, may offer new opportunities of theoretical studies, as well as figure out the parameters determining performance of sensing devices. Thus, these findings were used not only general sensing devices, inlcuidng chemical/biological sensors, but also E-skin, such as pressure or strain sensors. Furthermore, this strategy, using graphene/CP nanohybrid materials in the sensor application, may offer new opportunities of theoretical studies, as well as figure out the parameters determining performance of sensing devices. Therefore, the graphene/CP nanohybrid materials have been successfully synthesized and utilized as various signal transducers in sensor platforms, suggesting that these materials could be potentially useful in many new types of applications related to electronic/optoelectronic devices, such as actuators, catalytic supports, energy storage/conversion, and drug delivery systems.

References

[1] M. R. Abidian, D. H. Kim, D. C. Martin, Advanced Materials 2006, 18, 405.

[2] R. Gangopadhyay, A. De, Chemistry of Materials 2000, 12, 608.

[3] M. Gratzel, Nature 2001, 414, 338.

[4] L. Groenendaal, F. Jonas, D. Freitag, H. Pielartzik, J. R. Reynolds, Advanced Materials 2000, 12, 481.

[5] A. Malinauskas, Polymer 2001, 42, 3957.

[6] N. Nuraje, K. Su, N.-l. Yang, H. Matsui, ACS Nano 2008, 2, 502.

[7] M. R. Arcila-Velez, M. E. Roberts, Chemistry of Materials 2014, 26, 1601.

[8] W. He, G. Li, S. Zhang, Y. Wei, J. Wang, Q. Li, X. Zhang, ACS Nano 2015, 9, 4244.

[9] A. T. Lawal, S. B. Adeloju, Biosensors and Bioelectronics 2013, 40, 377.

[10] H. C. Kang, K. E. Geckeler, Polymer 2000, 41, 6931.

[11] S. Kirchmeyer, K. Reuter, Journal of Materials Chemistry 2005, 15, 2077.

[12] B. Wei, J. Liu, L. Ouyang, C.-C. Kuo, D. C. Martin, ACS Applied Materials & Interfaces 2015, 7, 15388.

[13] H. Hlaing, X. Lu, C.-Y. Nam, B. M. Ocko, Small 2012, 8, 3443.

[14] F. C. Krebs, S. A. Gevorgyan, J. Alstrup, Journal of Materials Chemistry 2009, 19, 5442.

[15] S. Kirchmeyer, K. Reuter, Journal of Materials Chemistry 2005, 15, 2077.

[16] H. Hlaing, X. Lu, C.-Y. Nam, B. M. Ocko, Small 2012, 8, 3443.

[17] J. Ouyang, C. W. Chu, F. C. Chen, Q. Xu, Y. Yang, Advanced Functional Materials 2005, 15, 203.

[18] M. Vosgueritchian, D. J. Lipomi, Z. Bao, Advanced Functional Materials 2012, 22, 421.

[19] C. Li, H. Bai, G. Shi, Chemical Society Reviews 2009, 38, 2397.

[20] S. Nambiar, J. T. W. Yeow, Biosensors and Bioelectronics 2011, 26, 1825.

[21] J. Sekine, S.-C. Luo, S. Wang, B. Zhu, H.-R. Tseng, H.-h. Yu, Advanced Materials 2011, 23, 4788.

[22] R. J. Tseng, J. Huang, J. Ouyang, R. B. Kaner, Yang, Nano Letters 2005, 5, 1077.

[23] C. C. Ferron, M. C. R. Delgado, O. Gidron, S. Sharma, D. Sheberla, Y. Sheynin, M. Bendikov, J. T. L. Navarrete, V. Hernandez, Chemical Communications 2012, 48, 6732.

[24] O. Gidron, A. Dadvand, E. Wei-Hsin Sun, I. Chung, L. J. W. Shimon, M. Bendikov, D. F. Perepichka, Journal of Materials Chemistry C 2013, 1, 4358.

[25] O. Gidron, Y. Diskin-Posner, M. Bendikov, Journal of the American Chemical Society 2010, 132, 2148.

[26] A. Facchetti, M.-H. Yoon, C. L. Stern, H. E. Katz, T. J. Marks, Angewandte Chemie International Edition 2003, 42, 3900.

[27] R. Joseph Kline, M. D. McGehee, M. F. Toney, Nat Mater 2006, 5, 222.

[28] D. H. Kim, Y. D. Park, Y. Jang, H. Yang, Y. H. Kim, J. I. Han, D. G. Moon, S. Park, T. Chang, C. Chang, M. Joo, C. Y. Ryu, K. Cho, Advanced Functional Materials 2005, 15, 77.

[29] R. J. Kline, M. D. McGehee, E. N. Kadnikova, J. Liu, J. M. J. Fréchet, Advanced Materials 2003, 15, 1519.

[30] B. S. Ong, Y. Wu, P. Liu, S. Gardner, Journal of the American Chemical Society 2004, 126, 3378.

[31] A. Patra, M. Bendikov, Journal of Materials Chemistry 2010, 20, 422.

[32] M. Li, A. Patra, Y. Sheynin, M. Bendikov, Advanced Materials 2009, 21, 1707.

[33] B. Kim, H. Shin, T. Park, H. Lim, E. Kim, Advanced Materials 2013, 25, 5483.

[34] D. Astruc, F. Lu, J. R. Aranzaes, Angewandte Chemie International

Edition 2005, 44, 7852.

[35] C. Burda, X. Chen, R. Narayanan, M. A. El-Sayed, Chemical Reviews 2005, 105, 1025.

[36] B. D. Gates, Q. Xu, M. Stewart, D. Ryan, C. G. Willson, G. M. Whitesides, Chemical Reviews 2005, 105, 1171.

[37] N. L. Rosi, C. A. Mirkin, Chemical Reviews 2005, 105, 1547.

[38] R. H. Baughman, A. A. Zakhidov, W. A. de Heer, Science 2002, 297, 787.

[39] B. L. Cushing, V. L. Kolesnichenko, C. J. O'Connor, Chemical Reviews 2004, 104, 3893.

[40] W. W. Yu, L. Qu, W. Guo, X. Peng, Chemistry of Materials 2003, 15, 2854.

[41] X. Michalet, F. F. Pinaud, L. A. Bentolila, J. M. Tsay, S. Doose, J. J. Li, G. Sundaresan, A. M. Wu, S. S. Gambhir, S. Weiss, Science 2005, 307, 538.

[42] S. M. Bachilo, M. S. Strano, C. Kittrell, R. H. Hauge, R. E. Smalley, R. B. Weisman, Science 2002, 298, 2361.

[43] C. Dhand, M. Das, M. Datta, B. D. Malhotra, Biosensors and Bioelectronics 2011, 26, 2811.

[44] R. J. Tseng, J. Huang, J. Ouyang, R. B. Kaner, Yang, Nano Letters 2005, 5, 1077.

[45] Y. Wang, H. D. Tran, L. Liao, X. Duan, R. B. Kaner, Journal of the American Chemical Society 2010, 132, 10365.

[46] J. I. Lee, S. H. Cho, S.-M. Park, J. K. Kim, J. K. Kim, J.-W. Yu, Y. C. Kim, T. P. Russell, Nano Letters 2008, 8, 2315.

[47] M. Schierhorn, S. W. Boettcher, S. Kraemer, G. D. Stucky, M. Moskovits, Nano Letters 2009, 9, 3262.

[48] R. A. Potyrailo, Angewandte Chemie International Edition 2006, 45, 702.

[49] O. S. Kwon, S. J. Park, J. Jang, Biomaterials 2010, 31, 4740.

[50] H. D. Tran, D. Li, R. B. Kaner, Advanced Materials 2009, 21, 1487.

[51] X. Yang, Z. Zhu, T. Dai, Y. Lu, Macromolecular Rapid Communications 2005, 26, 1736.

[52] Y. Mao, W. L. Wang, D. Wei, E. Kaxiras, J. G. Sodroski, ACS Nano 2011, 5, 1395.

[53] J. C. Meyer, A. K. Geim, M. I. Katsnelson, K. S. Novoselov, T. J. Booth, S. Roth, Nature 2007, 446, 60.

[54] A. A. Balandin, S. Ghosh, W. Bao, I. Calizo, D. Teweldebrhan, F. Miao, C. N. Lau, Nano Letters 2008, 8, 902.

[55] K. S. Kim, Y. Zhao, H. Jang, S. Y. Lee, J. M. Kim, K. S. Kim, J.-H. Ahn, P. Kim, J.-Y. Choi, B. H. Hong, Nature 2009, 457, 706.

[56] Y. Zhang, Y.-W. Tan, H. L. Stormer, P. Kim, Nature 2005, 438, 201.

[57] S. Gilje, S. Han, M. Wang, K. L. Wang, R. B. Kaner, Nano Letters 2007, 7, 3394.

[58] S. Bae, H. Kim, Y. Lee, X. Xu, J.-S. Park, Y. Zheng, J. Balakrishnan, T. Lei, H. Ri Kim, Y. I. Song, Y.-J. Kim, K. S. Kim, B. Ozyilmaz, J.-H. Ahn, B. H. Hong, S. Iijima, Nat Nano 2010, 5, 574.

[59] Y. Zhu, S. Murali, W. Cai, X. Li, J. W. Suk, J. R. Potts, R. S. Ruoff, Advanced Materials 2010, 22, 3906.

[60] F. Xia, T. Mueller, Y.-m. Lin, A. Valdes-Garcia, P. Avouris, Nat Nano 2009, 4, 839.

[61] RamanathanT, A. A. Abdala, StankovichS, D. A. Dikin, M. Herrera Alonso, R. D. Piner, D. H. Adamson, H. C. Schniepp, ChenX, R. S. Ruoff, S. T. Nguyen, I. A. Aksay, R. K. Prud'Homme, L. C. Brinson, Nat Nano 2008, 3, 327.

[62] Z.-S. Wu, W. Ren, L. Wen, L. Gao, J. Zhao, Z. Chen, G. Zhou, F. Li, H.-M. Cheng, ACS Nano 2010, 4, 3187.

[63] H. Zhang, X. Lv, Y. Li, Y. Wang, J. Li, ACS Nano 2010, 4, 380.

[64] W. Chen, S. Li, C. Chen, L. Yan, Advanced Materials 2011, 23, 5679.

[65] J. R. Potts, D. R. Dreyer, C. W. Bielawski, R. S. Ruoff, Polymer 2011, 52, 5.

[66] L. Al-Mashat, K. Shin, K. Kalantar-zadeh, J. D. Plessis, S. H. Han, R. W. Kojima, R. B. Kaner, D. Li, X. Gou, S. J. Ippolito, W. Wlodarski, The Journal of Physical Chemistry C 2010, 114, 16168.

[67] Q. Wu, Y. Xu, Z. Yao, A. Liu, G. Shi, ACS Nano 2010, 4, 1963.

[68] K. Zhang, L. L. Zhang, X. S. Zhao, J. Wu, Chemistry of Materials 2010, 22, 1392.

[69] H. Chang, H. Wu, Energy & Environmental Science 2013, 6, 3483.

[70] Q. Su, S. Pang, V. Alijani, C. Li, X. Feng, K. Müllen, Advanced Materials 2009, 21, 3191.

[71] X. An, T. Simmons, R. Shah, C. Wolfe, K. M. Lewis, M. Washington, S. K. Nayak, S. Talapatra, S. Kar, Nano Letters 2010, 10, 4295.

[72] N. V. Kozhemyakina, J. M. Englert, G. Yang, E. Spiecker, C. D. Schmidt, F. Hauke, A. Hirsch, Advanced Materials 2010, 22, 5483.

[73] V. Eswaraiah, K. Balasubramaniam, S. Ramaprabhu, Nanoscale 2012, 4, 1258.

[74] X. Chen, X. Jia, J. Han, J. Ma, Z. Ma, Biosensors and Bioelectronics 2013, 50, 356.

[75] Y. Fan, J.-H. Liu, C.-P. Yang, M. Yu, P. Liu, Sensors and Actuators B: Chemical 2011, 157, 669.

[76] S. Liu, X. Xing, J. Yu, W. Lian, J. Li, M. Cui, J. Huang, Biosensors and

Bioelectronics 2012, 36, 186.

[77] J. W. Park, C. Lee, J. Jang, Sensors and Actuators B: Chemical 2015, 208, 532.

[78] J. W. Park, S. J. Park, O. S. Kwon, C. Lee, J. Jang, Analytical Chemistry 2014, 86, 1822.

[79] J. W. Park, S. J. Park, O. S. Kwon, C. Lee, J. Jang, Analyst 2014, 139, 3852.

[80] N. Ruecha, R. Rangkupan, N. Rodthongkum, O. Chailapakul, Biosensors and Bioelectronics 2014, 52, 13.

[81] J. W. Park, S. J. Park, O. S. Kwon, C. Lee, J. Jang, J. Jang, J. W. Park, S. J. Park, C. Lee, O. S. Kwon, Chemistry of Materials 2014, 26, 2354.

[82] S. K. Karan, D. Mandal, B. B. Khatua, Nanoscale 2015, 7, 10655.

[83] A. Midya, V. Mamidala, J.-X. Yang, P. K. L. Ang, Z.-K. Chen, W. Ji, K. P. Loh, Small 2010, 6, 2292.

[84] D. Yu, Y. Yang, M. Durstock, J.-B. Baek, L. Dai, ACS Nano 2010, 4, 5633.

[85] X.-D. Zhuang, Y. Chen, G. Liu, P.-P. Li, C.-X. Zhu, E.-T. Kang, K.-G. Noeh, B. Zhang, J.-H. Zhu, Y.-X. Li, Advanced Materials 2010, 22, 1731.

[86] Y. Cui, Q. Wei, H. Park, C. M. Lieber, Science 2001, 293, 1289.

[87] H. Liu, J. Kameoka, D. A. Czaplewski, H. G. Craighead, Nano Letters

2004, 4, 671.

[88] Y. Liu, X. Dong, P. Chen, Chemical Society Reviews 2012, 41, 2283.

[89] R. Martínez-Máñez, F. Sancenón, Chemical Reviews 2003, 103, 4419.

[90] D. T. McQuade, A. E. Pullen, T. M. Swager, Chemical Reviews 2000, 100, 2537.

[91] F. Schedin, A. K. Geim, S. V. Morozov, E. W. Hill, P. Blake, M. I. Katsnelson, K. S. Novoselov, Nat Mater 2007, 6, 652.

[92] N. Pinna, G. Neri, M. Antonietti, M. Niederberger, Angewandte Chemie International Edition 2004, 43, 4345.

[93] F. Schedin, A. K. Geim, S. V. Morozov, E. W. Hill, P. Blake, M. I. Katsnelson, K. S. Novoselov, Nat Mater 2007, 6, 652.

[94] Q. Wan, Q. H. Li, Y. J. Chen, T. H. Wang, X. L. He, J. P. Li, C. L. Lin, Applied Physics Letters 2004, 84, 3654.

[95] J. Xu, Q. Pan, Y. a. Shun, Z. Tian, Sensors and Actuators B: Chemical 2000, 66, 277.

[96] B. R. Azamian, J. J. Davis, K. S. Coleman, C. B. Bagshaw, M. L. H. Green, Journal of the American Chemical Society 2002, 124, 12664.

[97] K. Besteman, J.-O. Lee, F. G. M. Wiertz, H. A. Heering, C. Dekker, Nano Letters 2003, 3, 727.

[98] A. Bianco, K. Kostarelos, C. D. Partidos, M. Prato, Chemical Communications 2005, 571.

[99] S. M. Borisov, O. S. Wolfbeis, Chemical Reviews 2008, 108, 423.

[100] T. Kuila, S. Bose, P. Khanra, A. K. Mishra, N. H. Kim, J. H. Lee, Biosensors and Bioelectronics 2011, 26, 4637.

[101] V. S.-Y. Lin, K. Motesharei, K.-P. S. Dancil, M. J. Sailor, M. R. Ghadiri, Science 1997, 278, 840.

[102] M. Zhou, Y. Zhai, S. Dong, Analytical Chemistry 2009, 81, 5603.

[103] X. P. A. Gao, G. Zheng, C. M. Lieber, Nano Letters 2010, 10, 547.

[104] Y. Ohno, K. Maehashi, K. Matsumoto, Journal of the American Chemical Society 2010, 132, 18012.

[105] Z. Kuang, S. N. Kim, W. J. Crookes-Goodson, B. L. Farmer, R. R. Naik, ACS Nano 2010, 4, 452.

[106] H. Yoon, S. H. Lee, O. S. Kwon, H. S. Song, E. H. Oh, T. H. Park, J. Jang, Angewandte Chemie International Edition 2009, 48, 2755.

[107] D. Vione, V. Maurino, C. Minero, D. Borghesi, M. Lucchiari, E. Pelizzetti, Environmental Science & Technology 2003, 37, 4635.

[108] R. K. Gilpin, L. A. Pachla, Analytical Chemistry 2005, 77, 3755.

[109] J. Jia, B. Wang, A. Wu, G. Cheng, Z. Li, S. Dong, Analytical Chemistry 2002, 74, 2217.

[110] X. Shu, Y. Chen, H. Yuan, S. Gao, D. Xiao, Analytical Chemistry 2007, 79, 3695.

[111] J. Foreman, V. Demidchik, J. H. F. Bothwell, P. Mylona, H. Miedema, M. A. Torres, P. Linstead, S. Costa, C. Brownlee, J. D. G. Jones, J. M. Davies, L. Dolan, Nature 2003, 422, 442.

[112] J. D. Lambeth, Nat Rev Immunol 2004, 4, 181.

[113] P. Niethammer, C. Grabher, A. T. Look, T. J. Mitchison, Nature 2009, 459, 996.

[114] H. Sauer, G. Rahimi, J. Hescheler, M. Wartenberg, FEBS Letters 2000, 476, 218.

[115] C. Amatore, S. Arbault, D. Bruce, P. de Oliveira, M. Erard, M. Vuillaume, Chemistry – A European Journal 2001, 7, 4171.

[116] H. Ohshima, M. Tatemichi, T. Sawa, Archives of Biochemistry and Biophysics 2003, 417, 3.

[117] W. Maruyama, P. Dostert, K. Matsubara, M. Naoi, Free Radical Biology and Medicine 1995, 19, 67.

[118] K. Wang, Q. Liu, X.-Y. Wu, Q.-M. Guan, H.-N. Li, Talanta 2010, 82, 372.

[119] K. Sunil, B. Narayana, Bull Environ Contam Toxicol 2008, 81, 422.

[120] S. Xu, B. Peng, X. Han, Biosensors and Bioelectronics 2007, 22, 1807.

[121] Y. Wang, X. Chen, J.-J. Zhu, Electrochemistry Communications 2009, 11, 323.

[122] J. Bai, X. Jiang, Analytical Chemistry 2013, 85, 8095.

[123] A. K. M. Kafi, A. Ahmadalinezhad, J. Wang, D. F. Thomas, A. Chen, Biosensors and Bioelectronics 2010, 25, 2458.

[124] X. Sun, S. Guo, Y. Liu, S. Sun, Nano Letters 2012, 12, 4859.

[125] Y. Wang, X. Yang, J. Bai, X. Jiang, G. Fan, Biosensors and Bioelectronics 2013, 43, 180.

[126] C. Xu, X. Wang, J. Zhu, The Journal of Physical Chemistry C 2008, 112, 19841.

[127] J. Wang, Chemical Reviews 2007, 108, 814.

[128] R. Ballerstadt, A. Kholodnykh, C. Evans, A. Boretsky, M. Motamedi, A. Gowda, R. McNichols, Analytical Chemistry 2007, 79, 6965.

[129] N. C. Shah, O. Lyandres, J. T. Walsh, M. R. Glucksberg, R. P. Van Duyne, Analytical Chemistry 2007, 79, 6927.

[130] C. Shan, H. Yang, J. Song, D. Han, A. Ivaska, L. Niu, Analytical Chemistry 2009, 81, 2378.

[131] S. Hrapovic, Y. Liu, K. B. Male, J. H. T. Luong, Analytical Chemistry 2003, 76, 1083.

[132] J. A. Fernández, J. R. Aboal, A. Carballeira, Science of The Total

Environment 2000, 256, 151.

[133] J. K. Nicholson, M. D. Kendall, D. Osborn, Nature 1983, 304, 633.

[134] G.-B. Jiang, J.-B. Shi, X.-B. Feng, Environmental Science & Technology 2006, 40, 3672.

[135] C. Deng, D. Zhangb, X. Pan, F. Chang, S. Wang, Journal of Photochemistry and Photobiology B: Biology 2013, 127, 1.

[136] T. W. Clarkson, L. Magos, G. J. Myers, New England Journal of Medicine 2003, 349, 1731.

[137] S. Ekino, M. Susa, T. Ninomiya, K. Imamura, T. Kitamura, Journal of the Neurological Sciences 2007, 262, 131.

[138] D. A. Geier, M. R. Geier, Journal of Toxicology and Environmental Health, Part A 2007, 70, 837.

[139] M. Korbas, S. R. Blechinger, P. H. Krone, I. J. Pickering, G. N. George, Proceedings of the National Academy of Sciences 2008, 105, 12108.

[140] H. G. Sudibya, Q. He, H. Zhang, P. Chen, ACS Nano 2011, 5, 1990.

[141] T. H. Kim, J. Lee, S. Hong, The Journal of Physical Chemistry C 2009, 113, 19393.

[142] T. P. McNicholas, K. Zhao, C. Yang, S. C. Hernandez, A. Mulchandani, N. V. Myung, M. A. Deshusses, The Journal of Physical Chemistry C 2011, 115, 13927.

[143] L. Zhang, T. Li, B. Li, J. Li, E. Wang, Chemical Communications 2010, 46, 1476.

[144] S. V. Wegner, A. Okesli, P. Chen, C. He, Journal of the American Chemical Society 2007, 129, 3474.

[145] N. Dave, M. Y. Chan, P.-J. J. Huang, B. D. Smith, J. Liu, Journal of the American Chemical Society 2010, 132, 12668.

[146] T. Qian, S. Wu, J. Shen, Chemical Communications 2013, 49, 4610.

[147] T. Qian, C. Yu, S. Wu, J. Shen, Journal of Materials Chemistry A 2013, 1, 6539.

[148] Z.-Q. Zhao, X. Chen, Q. Yang, J.-H. Liu, X.-J. Huang, Chemical Communications 2012, 48, 2180.

[149] M. L. Hammock, A. Chortos, B. C. K. Tee, J. B. H. Tok, Z. Bao, Advanced Materials 2013, 25, 5997.

[150] D.-H. Kim, N. Lu, R. Ma, Y.-S. Kim, R.-H. Kim, S. Wang, J. Wu, S. M. Won, H. Tao, A. Islam, K. J. Yu, T.-i. Kim, R. Chowdhury, M. Ying, L. Xu, M. Li, H.-J. Chung, H. Keum, M. McCormick, P. Liu, Y.-W. Zhang, F. G. Omenetto, Y. Huang, T. Coleman, J. A. Rogers, Science 2011, 333, 838.

[151] J. Park, Y. Lee, J. Hong, M. Ha, Y.-D. Jung, H. Lim, S. Y. Kim, H. Ko, ACS Nano 2014, 8, 4689.

[152] A. N. Sokolov, B. C. K. Tee, C. J. Bettinger, J. B. H. Tok, Z. Bao,

Accounts of Chemical Research 2011, 45, 361.

[153] B. C. K. Tee, C. Wang, R. Allen, Z. Bao, Nat Nano 2012, 7, 825.

[154] X. Wang, Y. Gu, Z. Xiong, Z. Cui, T. Zhang, Advanced Materials 2014, 26, 1336.

[155] M. Madsen, K. Takei, R. Kapadia, H. Fang, H. Ko, T. Takahashi, A. C. Ford, M. H. Lee, A. Javey, Advanced Materials 2011, 23, 3115.

[156] J. Zhou, Y. Gu, P. Fei, W. Mai, Y. Gao, R. Yang, G. Bao, Z. L. Wang, Nano Letters 2008, 8, 3035.

[157] D. J. Lipomi, J. A. Lee, M. Vosgueritchian, B. C. K. Tee, J. A. Bolander, Z. Bao, Chemistry of Materials 2011, 24, 373.

[158] O. S. Kwon, S. J. Park, J.-Y. Hong, A. R. Han, J. S. Lee, J. S. Lee, J. H. Oh, J. Jang, ACS Nano 2012, 6, 1486.

[159] N. Hu, Y. Karube, M. Arai, T. Watanabe, C. Yan, Y. Li, Y. Liu, H. Fukunaga, Carbon 2010, 48, 680.

[160] A. D. Smith, F. Niklaus, A. Paussa, S. Vaziri, A. C. Fischer, M. Sterner, F. Forsberg, A. Delin, D. Esseni, P. Palestri, M. Ö stling, M. C. Lemme, Nano Letters 2013, 13, 3237.

[161] C. Yan, J. Wang, W. Kang, M. Cui, X. Wang, C. Y. Foo, K. J. Chee, P. S. Lee, Advanced Materials 2014, 26, 2022.

[162] H.-B. Yao, J. Ge, C.-F. Wang, X. Wang, W. Hu, Z.-J. Zheng, Y. Ni, S.-

H. Yu, Advanced Materials 2013, 25, 6692.

[163] W. Cai, Y. Huang, D. Wang, C. Liu, Y. Zhang, Journal of Applied Polymer Science 2014, 131, 39778.

[164] H. Gullapalli, V. S. M. Vemuru, A. Kumar, A. Botello-Mendez, R. Vajtai, M. Terrones, S. Nagarajaiah, P. M. Ajayan, Small 2010, 6, 1641.

[165] C. Pang, G.-Y. Lee, T.-i. Kim, S. M. Kim, H. N. Kim, S.-H. Ahn, K.-Y. Suh, Nat Mater 2012, 11, 795.

[166] W. S. Hummers, R. E. Offeman, Journal of the American Chemical Society 1958, 80, 1339.

[167] Y.-E. Miao, S. He, Y. Zhong, Z. Yang, W. W. Tjiu, T. Liu, Electrochimica Acta 2013, 99, 117.

[168] S. Liu, J. Tian, L. Wang, H. Li, Y. Zhang, X. Sun, Macromolecules 2010, 43, 10078.

[169] W. Zhao, H. Wang, X. Qin, X. Wang, Z. Zhao, Z. Miao, L. Chen, M. Shan, Y. Fang, Q. Chen, Talanta 2009, 80, 1029.

[170] Q. Wang, J. Zheng, Microchim Acta 2010, 169, 361.

[171] K. Cui, Y. Song, Y. Yao, Z. Huang, L. Wang, Electrochemistry Communications 2008, 10, 663.

[172] W. Zhao, H. Wang, X. Qin, X. Wang, Z. Zhao, Z. Miao, L. Chen, M. Shan, Y. Fang, Q. Chen, Talanta 2009, 80, 1029.

[173] L. Li, Z. Du, S. Liu, Q. Hao, Y. Wang, Q. Li, T. Wang, Talanta 2010, 82, 1637.

[174] Z. Yin, J. Wu, Z. Yang, Biosensors and Bioelectronics 2011, 26, 1970.

[175] Y. Li, Y. Chang, M. Jin, Y. Liu, G. Han, Journal of Applied Polymer Science 2012, 126, 1316.

[176] F. Xu, Y. Sun, Y. Zhang, Y. Shi, Z. Wen, Z. Li, Electrochemistry Communications 2011, 13, 1131.

[177] H. Teymourian, A. Salimi, S. Khezrian, Biosensors and Bioelectronics 2013, 49, 1.

[178] T. Zhang, R. Yuan, Y. Chai, W. Li, S. Ling, Sensors 2008, 8, 5141.

[179] X. Zhang, B. Qi, S. Zhang, Analytical Letters 2008, 41, 3100.

[180] A. Safavi, N. Maleki, M. M. Doroodmand, J. Hazard. Mater. 2010, 173, 622.

[181] Y. M. Sabri, S. J. Ippolito, A. J. Atanacio, V. Bansal, S. K. Bhargava, J. *J. Mater. Chem.*, **2012**, *22*, 21395.

[182] Y. M. Sabri, R. Kojima, S. J. Ippolito, W. Wlodarski, K. Kalantaradeh, R. B. Kaner, S. K. Bhargava, *Sens. Actuators B*, **2011**, *160*, 616.

[183] T. P. McNicholas, K. Zhao, C. Yang, S. C. Hernandez, A. Mulchandani, N. V. Myung and M. A. Deshusses, *J. Phys. Chem. C*, 2011, **115**, 13927.

[184] J. W. Park, J. Jang, Carbon 2015, 87, 275.

[185] W. Wu, X. Wen, Z. L. Wang, Science 2013, 340, 952.

[186] J. Lee, S. Kim, J. Lee, D. Yang, B. C. Park, S. Ryu, I. Park, Nanoscale 2014.

[187] J. Kim, T. Nga Ng, W. Soo Kim, Applied Physics Letters 2012, 101.

[188] C. Pang, G.-Y. Lee, T.-i. Kim, S. M. Kim, H. N. Kim, S.-H. Ahn, K.-Y. Suh, Nat Mater 2012, 11, 795.

[189] I. Graz, M. Kaltenbrunner, C. Keplinger, R. Schwödiauer, S. Bauer, S. P. Lacour, S. Wagner, Applied Physics Letters 2006, 89.

[190] S. C. B. Mannsfeld, B. C. K. Tee, R. M. Stoltenberg, C. V. H. H. Chen, S. Barman, B. V. O. Muir, A. N. Sokolov, C. Reese, Z. Bao, Nat Mater 2010, 9, 859.

[191] B. Hu, Y. Ding, W. Chen, D. Kulkarni, Y. Shen, V. V. Tsukruk, Z. L. Wang, Advanced Materials 2010, 22, 5134.

[192] H. Gullapalli, V. S. M. Vemuru, A. Kumar, A. Botello-Mendez, R. Vajtai, M. Terrones, S. Nagarajaiah, P. M. Ajayan, Small 2010, 6, 1641.

[193] X. Xiao, L. Yuan, J. Zhong, T. Ding, Y. Liu, Z. Cai, Y. Rong, H. Han, J. Zhou, Z. L. Wang, Advanced Materials 2011, 23, 5440.

[194] N. Hu, Y. Karube, M. Arai, T. Watanabe, C. Yan, Y. Li, Y. Liu, H. Fukunaga, Carbon 2010, 48, 680.

국문초록

그래핀/전도성 고분자 나노하이브리드 물질들은 향상된 표면적, 전하 운반체 이동속도, 열/전기적 전도율, 그리고 화학적/기계적 안정성 등과 같은 그들의 시너지 효과들 때문에 많은 관심을 받고 있다. 전자장치에 사용하기 위한 그래핀/전도성 고분자 나노하이브리드 물질들을 제조하기 위해서, 공유 그리고 비공유 합성법들이 소개되어 왔다. 비공유 합성법과는 달리, 공유 합성법은 그래핀과 전도성고분자 표면에 작용기를 먼저 도입시켜야 하기 때문에 시간소유와 까다로운 조건들을 요구하게 된다. 반면에, 비공유 합성법은 π–π 결합과 같은 이차적인 결합을 통해 그래핀/전도성 고분자 나노하이브리드 물지들을 쉽게 제조할 수가 있다. 비공유 합성법 중에 하나인 제자리 합성법은 균일한 나노하이브리드 물질을 얻을 수 있기 때문에 매우 유망하고 효과적인 제조법이다. 게다가, 그래핀/전도성 고분자 나노하이브리드 물질들의 형태와 모양을 전구체 물질들을 (그래핀 또는 전도성 고분자) 선택적으로 변형시킴에 따라 제어할 수 있다.

본 연구에서는, 다양한 그래핀/전도성 고분자 나노하이브리드 물질들을 제자리 합성법에 의해서 소개되었다. 합성된 나노하이브리드 물질들은 훌륭한 전기적/화학적 특성들을 보여주어, 센서응용분야에 활용할 수 있게 한다. 그래핀/전도성 고분자 나노하이브리드 물질들의 시너지효과들은 센서디바이스에서 전달체로 활용될 때, 굉장히 빠른 응답/복원 속도를

제공한다. 또, 그래핀/전도성 고분자 나노하이브리드물질들의 넓은 표면적은 향상된 목표 물질들과 상호작용을 제공하여, 고감도 센서 성능을 보여주게 된다.

주요어: 그래핀, 전도성 고분자, 나노하이브리드 물질, 전계-효과 트랜지스터, 센서 응용

학번: 2013-30778